



VNIVERSITAT
DE VALÈNCIA

Prof. D. Andrés Cantarero Sáez, Catedrático del Departament de Física Aplicada i Electromagnetisme de la Facultat de Física de la Universitat de València y **Prof. Dña. Clara María Gómez Clari**, Catedrática del Departament de Química Física de la Universitat de València.

Certifican:

Que el trabajo que presenta D. Mario Culebras Rubio en esta Memoria, bajo el título “Thermoelectric devices and supercapacitors based on nanostructured semiconducting polymers for energy production and storage” ha sido realizado bajo su dirección en el Institut de Ciència Molecular y en el Institut de Ciència dels Materials de la Universitat de València.

Y para que así conste, a efectos de su presentación para optar al Grado de Doctor Internacional en Química, expide la presente, que firma en
Paterna a 31 de Enero de 2017.

Handwritten signature of Andrés Cantarero Sáez in blue ink, underlined.

Fdo: Andrés Cantarero Sáez

Handwritten signature of Clara María Gómez Clari in blue ink, underlined.

Fdo: Clara María Gómez Clari

“A person who never made a mistake never tried anything new.”

Albert Einstein

UNIVERSITY OF VALENCIA

Abstract

Faculty of Chemistry

International Doctor in Chemistry

Mario Culebras Rubio

More than two third parts of the energy generated by conventional sources is lost as heat. Recovering those energy losses can help to create a more efficient way to produce energy for a sustainable development of our society. By using thermoelectric generators it is possible to produce energy from temperature gradients. Showing that, thermoelectricity can be a good strategy for energy harvesting and recovery. The thermoelectric efficiency is usually given by the dimensionless figure of merit, ZT . Currently, inorganic materials are commonly used in thermoelectric applications, however they present several disadvantages such as: scarcity of the raw materials and toxicity. Due to their interesting properties, organic materials, such as conducting polymers, have become an alternative to those inorganic materials. However, their thermoelectric efficiency is still very low compared with inorganic materials. For this reason, this thesis is focused on the synthesis and complete characterization of conducting polymers and hybrid materials for thermoelectric applications, developing new ways to increase the thermoelectric efficiency of organic materials. In addition, this thesis shows the fabrication of thermoelectric generators and supercapacitor devices using materials synthesized in our laboratories.

Acknowledgements

Me gustaría agradecer la realización de esta tesis doctoral en primer lugar a mis directores de tesis, Andrés Cantarero y Clara Gómez, por darme la oportunidad de cursar mis estudios de doctorado bajo su dirección, prestándome asesoramiento científico y un gran apoyo en todo momento.

Gran parte de los agradecimientos van hacia los compañeros del laboratorio tanto a los que siguen ahí como a los que se fueron: David, Toni, Alaina, Andrés, Paula, Regina, José, Ana, Raquel, Triana, Belén, Olaia, Carlos M, Sole y Carlos R ya que con ellos he compartido el día a día en el laboratorio y siempre me han prestado su ayuda de manera incondicional. También agradecer a María Jesús Sanchis y a Óscar Juan Durá por algunas de las medidas realizadas que forman parte de este trabajo. También agradecer a Antonio Madroño la preparación de algunas muestras que forman parte de esta tesis.

A todo el personal técnico y de administración: M^a Angeles, Toni y David Vie por toda la ayuda recibida a lo largo de estos años. Especial mención a los manitas: Pascual y Julián, por ayuda esencial en diseño y fabricación de los montajes experimentales desarrollados en esta tesis.

A Rafa Muñoz, Katharina Landfester y a la DAAD por brindarme la oportunidad de realizar una de mis estancias en el extranjero en el centro Max Planck Institute for Polymer Research.

Al profesor Jaime C. Grunlan por acogerme en su grupo de investigación durante mi estancia en la Universidad de Texas A&M en EE. UU. También a todos mis compañeros y amigos de Estados Unidos: Michelle, Merid, Chungyeon, Yixuan, Shuang, Marcus, Kevin H, Kevin W, Tyler, Alyssa, Chaowei y Ryan.

Al Ministerio de Educación, Cultura y Deporte por su financiación en el programa FPU/2012.

A todos mis amigos tanto de Barrax como de Valencia ya que gracias a ellos he podido desconectar del duro trabajo que suponen los estudios de doctorado. Especial mención merecen Ramón y Pau ya que la portada prácticamente es obra suya y sin duda agradecer a Miquel todo el apoyo recibido en nuestras largas conversaciones y debates.

Como no a mi familia, mis padres María y Aníbal y a mi hermano Aníbal, por ayudarme y apoyarme en todo momento ya que son ellos los responsables de que haya llegado hasta aquí, debido a la magnífica educación que he recibido por su parte.

Por último me gustaría agradecer a la persona que ha sido mi gran apoyo durante la recta final de la tesis. Ángela, gracias a tu amor y ánimos he conseguido llegar hasta el final.

Dedicated to my family

Contents

1	General introduction	1
1.1	The energy problem	1
1.2	Thermoelectricity	2
1.2.1	Thermoelectric efficiency	4
1.2.2	Thermoelectric materials	7
1.2.3	Applications of thermoelectricity	9
1.3	Energy storage	11
1.4	Objectives and structure of the thesis	11
2	Experimental	13
2.1	Electrical characterization techniques	13
2.1.1	Electrical conductivity	13
2.1.2	Seebeck coefficient	14
2.1.3	Power output	15
2.1.4	Thickness and mass deposition	16
2.1.5	Electrochemical measurements	16
2.2	Thermal analysis techniques	17
2.2.1	Differential scanning calorimetry	17
2.2.2	Thermogravimetric analysis	17
2.2.3	Thermal conductivity	17
2.3	Structural characterization techniques	18
2.3.1	X-ray diffraction analysis	18
2.3.2	Raman scattering	18
2.3.3	Fourier transform infrared spectroscopy	18
2.3.4	Uv-Vis spectroscopy	19
2.4	Morphological characterization techniques	19
2.4.1	Scanning electron microscopy	19
2.4.2	Transmission electron microscopy	19
2.4.3	Atomic force microscopy	19
3	Conducting polymers as organic thermoelectric materials	21

3.1	Introduction	21
3.1.1	Basic considerations of the synthesis of conducting polymers	23
3.1.2	Electronic transport in conducting polymers	25
3.1.3	Doping in conducting polymers	30
3.1.4	Electronic states of conducting polymers (solitons, polarons and bipolarons)	32
3.1.5	Secondary doping in conducting polymers	35
3.1.6	Nanostructuring in conducting polymers	36
3.2	Effect of the addition of dimethylsulfoxide on the thermoelectric properties in PEDOT:PSS solutions	39
3.2.1	Materials	39
3.2.2	Preparation of PEDOT:PSS films in presence of DMSO	39
3.2.3	Morphology of PEDOT:PSS films	39
3.2.4	Thermoelectric properties of PEDOT:PSS films	40
3.3	Effect of the chemical de-doping on PEDOT electrochemically synthesized in presence of different counter-ions	43
3.3.1	Materials	43
3.3.2	Synthesis of PEDOT films	43
3.3.3	Morphology of PEDOT films	44
3.3.4	Spectroscopy measurements of PEDOT films	46
3.3.5	Thermoelectric properties of PEDOT films	48
3.4	Electrochemical de-doping in PEDOT and polypyrrole	52
3.4.1	Materials	52
3.4.2	Synthesis of PEDOT	52
3.4.3	Synthesis of PPy	53
3.4.4	Electrochemical reduction of polymers	53
3.4.5	Morphology of PEDOT and PPy films	53
3.4.6	Cyclic voltametry of PEDOT and PPy films	53
3.4.7	Spectroscopy measurements of PEDOT and PPy films	55
3.4.8	Thermoelectric properties of PEDOT and PPy films	55
3.5	Nanostructuring of PEDOT using soft template methods	59
3.5.1	Materials	59
3.5.2	Synthesis of PEDOT nanoparticles using Lutensol AT50	59
3.5.2.1	Influence of EDOT:Fe-Tos	60
3.5.2.2	Influence of H ₂ O ₂ concentration	60
3.5.2.3	Influence of miniemulsion pH	60
3.5.3	Synthesis of PEDOT nanoparticles using DTAB	61
3.5.4	Morphology of PEDOT nanoparticles	62
3.5.5	Thermoelectric behavior of PEDOT nanoparticles	66
3.6	Nanostructuring of PEDOT using hard template methods	75
3.6.1	Materials	75
3.6.2	Synthesis of PEDOT nanowires	75
3.6.3	Morphology of PEDOT nanowires	76
3.6.4	Future application of PEDOT nanowires	77
3.7	Conclusions	78

4 Non conventional inorganic thermoelectric materials 79

4.1	Introduction	79
4.1.1	Alternative inorganic materials to bismuth, antimony, tellurium and lead compounds	80
4.1.1.1	Clathrates	80
4.1.1.2	Skutterudites	82
4.1.1.3	Metallic Oxides	83
4.1.1.4	Half-Heusler compounds	85
4.1.1.5	Carbonaceous materials	86
4.1.2	Low dimensional thermoelectric materials	87
4.2	Perovskite nanostructures: $\text{La}_{1-x}\text{Ca}_x\text{MnO}_3$ system	89
4.2.1	Materials	89
4.2.2	Synthesis of $\text{La}_{1-x}\text{Ca}_x\text{MnO}_3$ nanostructures	89
4.2.3	Morphology of $\text{La}_{1-x}\text{Ca}_x\text{MnO}_3$ nanostructures and temperature effects	90
4.2.4	Phase transition of $\text{La}_{1-x}\text{Ca}_x\text{MnO}_3$ during the calcination process	91
4.2.5	Thermoelectric behavior of $\text{La}_{1-x}\text{Ca}_x\text{MnO}_3$	93
4.3	Perovskite nanostructures: $\text{Nd}_{1-x}\text{Ca}_x\text{CoO}_3$ system	96
4.3.1	Materials	96
4.3.2	Synthesis of nanowires	96
4.3.3	Morphology of $\text{Nd}_{1-x}\text{Ca}_x\text{CoO}_3$ nanostructures and temperature effect	97
4.3.4	Phase transition of $\text{Nd}_{1-x}\text{Ca}_x\text{CoO}_3$ during the calcination process	98
4.3.5	Thermoelectric behavior of $\text{Nd}_{1-x}\text{Ca}_x\text{CoO}_3$ nanowires	99
4.4	Carbonaceous materials: application to carbon black	102
4.4.1	Materials	102
4.4.2	Structural analysis	103
4.4.3	Thermoelectric behavior of carbon black	103
4.5	Carbonaceous materials: application to charcoal	104
4.5.1	Materials	104
4.5.2	Charcoal treatments	104
4.5.3	Morphology and thermoelectric parameters	104
4.6	Carbonaceous materials: application to vitreous carbon	107
4.6.1	Materials	107
4.6.2	Thermoelectric behavior of vitreous carbon	108
4.6.3	X-ray analysis of vitreous carbon	108
4.7	Conclusions	112
5	Nanocomposites and hybrid materials for thermoelectric applications	115
5.1	Introduction	115
5.1.1	Carbon nanotubes	116
5.1.2	Graphene/Graphite	118
5.1.3	Inorganic nanoparticles	119
5.1.4	Common methods to prepare nanocomposites and hybrid materials	121
5.1.4.1	Surface modification of inorganic nanofillers	122
5.2	PEDOT:PSS/EG composites	123
5.2.1	Materials	123
5.2.2	Preparation of expanded graphite	124
5.2.3	Preparation of PEDOT:PSS/EG	124
5.2.4	Morphology of the PEDOT:PSS/EG composites	124

5.2.5	Thermal analysis of the PEDOT:PSS/EG composites	125
5.2.6	Thermoelectric properties of PEDOT:PSS/EG composites	127
5.3	Hybrid composites of NCCO perovskites/PEDOT	129
5.3.1	Materials	129
5.3.2	Synthesis of the perovskite nanoparticles	129
5.3.3	Preparation of the composites	130
5.3.4	Morphological and structural characterization of the NCCO/PEDOT perovskites nanocomposites	130
5.3.5	Thermoelectric properties of the NCCO/PEDOT hybrids perovskites composites	131
5.4	Combining multilayer carbon nanotube assembly and electrochemical polymerization for hybrid thermoelectric materials	133
5.4.1	Materials	133
5.4.2	Substrates	134
5.4.3	Assembly of MWCNT films	134
5.4.4	Electrochemical deposition of PEDOT	134
5.4.5	Morphology and characterization during the electrochemical deposition of PEDOT	135
5.4.6	Thermoelectric behavior of MWCNT-PEDOT hybrid films	140
5.5	Tellurium-PEDOT hybrid films synthesized by electrochemical synthesis	141
5.5.1	Materials	141
5.5.2	Synthesis of Te-PEDOT films	141
5.5.3	Morphology and characterization during the electrochemical deposition of Te	142
5.5.4	Thermoelectric behavior of Te-PEDOT films	147
5.6	Conclusions	148
6	Devices for energy production and storage using conducting polymers	151
6.1	Introduction	151
6.1.1	Thermoelectric modules	151
6.1.2	Power output and conversion efficiency	152
6.1.3	Thermoelectric module fabrication	153
6.1.4	Organic thermoelectric modules	155
6.1.4.1	State-of-the-art of organic thermoelectric modules	156
6.1.5	Conducting polymers as supercapacitors	158
6.2	A thermoelectric module fabricated by electrochemical polymerization	161
6.2.1	Materials	161
6.2.2	Device fabrication	161
6.2.3	Electrical measurements of the thermoelectric module	162
6.3	A cylindrical thermoelectric module fabricated using layer-by-layer assembly and electrochemical polymerization	165
6.3.1	Materials	165
6.3.2	Device fabrication	165
6.3.3	Characterization of the thermoelectric module	166
6.4	Thermal sensor based on a PEDOT film	168
6.4.1	Materials	168
6.4.2	Synthesis of PEDOT nanofilms	168

6.4.3	Sensor fabrication	168
6.4.4	Sensor characterization	169
6.5	Supercapacitor devices based on PEDOT nanocomposites	172
6.5.1	Materials	172
6.5.2	Assembly of supercapacitors based on PEDOT films	173
6.5.3	Preparation of MWCNTs-cotton fabrics	173
6.5.4	PEDOT synthesis over MWCNTs-cotton fabrics	173
6.5.5	MnO ₂ -PEDOT co-synthesis over MWCNTs-cotton fabrics	174
6.5.6	Assembly of devices based on cotton fabrics	174
6.5.7	Characterization of supercapacitors based on PEDOT films	175
6.5.8	Characterization of supercapacitors based on cotton fabrics	176
6.6	Conclusions	181
7	General conclusions	183
	Bibliography	185
	Abbreviations	207
	List of Figures	209
	List of Tables	217
A	Resumen en castellano	219
A.1	Motivación	219
A.2	Objetivos	221
A.3	Metodología y estructura de la tesis	221
A.4	Resultados y conclusiones más relevantes	221
B	Publication list	229

Chapter 1

General introduction

1.1 The energy problem

Nowadays, the sustainability of energy production is one of the most important challenges. Due to the increasing in the energy demand (see Figure 1.1), and inherent depletion of the fossil

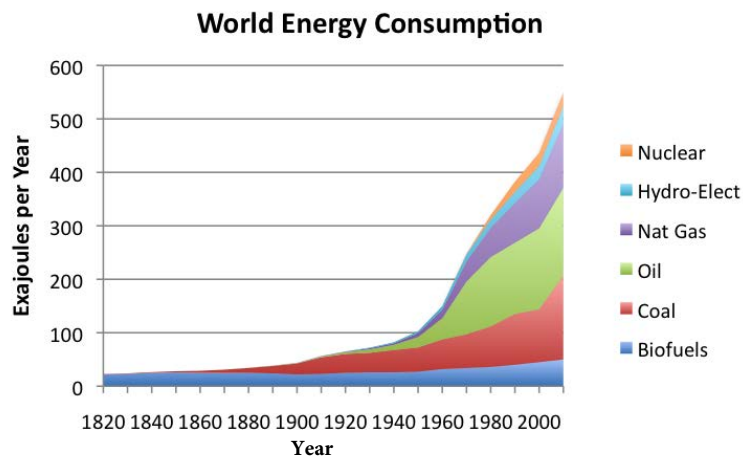


Figure 1.1 Historical energy demand. Image taken from BP Statistical Review of World Energy, London, 2015.

fuels, there is a great interest by the scientific and political community to develop new ways for the sustainability of energy production. One of the most important tasks for the coming years is to expand the amount of the renewable energy produced. This kind of energy is more important in some countries, however, according to Figure 1.1, it is less than the 15 % at the global scale. This percentage corresponds greatly with hydro-power and wood fuels in developed countries. Other kinds of renewable sources such as wind or solar energy only constitute a very small part of the total amount supplied.

Basically, attending the three following aspects, it is possible to achieve a sustainable energy development [1–3]. The first one is savings in energy demand. Reducing the amount of energy is crucial in order to achieve a sustainable development. For this reason, it is necessary to promote campaigns for energy saving in the society. The second aspect is to promote the development of the renewable energy sources. There are several renewable sources to be promoted such as: wind energy (onshore and offshore), photovoltaic, wave energy, hydro power, solar thermal, geothermal and biomass (straw, wood, waste, biogas, energy crops). The final aspect is the improvement of the efficiency in energy production. Figure 1.2 shows an example

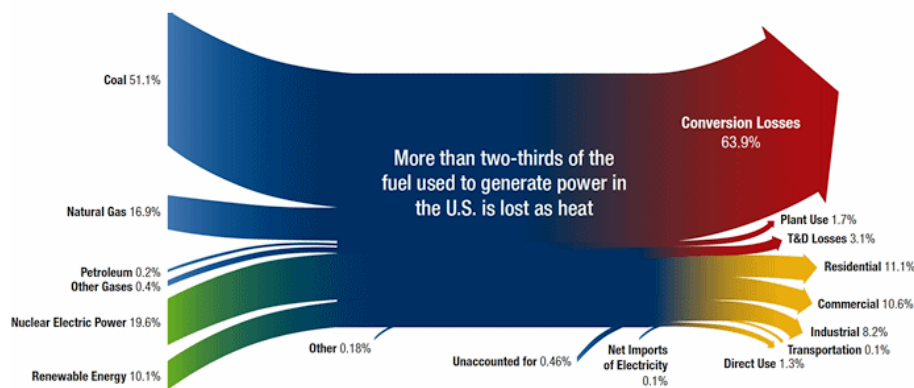


Figure 1.2 Diagram of energy losses. Image taken from U.S. Department of Energy Midwest.

of the importance of efficiency in energy. According to Figure 1.2, more than two-thirds parts of the energy produced is lost as heat. Therefore, it is very important to find ways to recover all these energy losses. Energy harvesting can recover all the energy that is wasted to environment and transform it in electric power. There are several ways to recover energy, for example: piezoelectricity [4, 5] which converts mechanical strain into electric current, or triboelectricity [6, 7], which through the frictional contact between different materials can produce electric power. However, from the point of view of energy recovering of heat losses, thermoelectricity has become the most promising way due to the possibility to recover energy from temperature gradients. The thermoelectricity is a property given in semiconductors and metals (more pronounced in semiconductors) which consists of transforming a temperature difference into an electric current and vice versa.

1.2 Thermoelectricity

In 1821 Thomas Johann Seebeck found that a circuit made from two different metals, with junctions at different temperatures would deflect a compass magnet [8]. Consequently, he observed that a temperature difference produces an electric potential across the junction which can drive an electric current in a closed circuit. Nowadays, this is known as the Seebeck effect. This fact

can be explained by considering the presence of free electrons or holes which carry both charge and heat in a thermoelectric material. In a simple approximation, the electrons and holes can be considered as charged particles of gas. If a neutral gas is in a box and a temperature gradient is applied (generating a hot and cold side), the gas molecules from the hot part will move faster than the molecules that are in the cold side. Since the molecules with higher temperature will diffuse beyond the molecules with lower temperature, it will generate a net accumulation of molecules at the cold side. Consequently, a density gradient will be generated and will produce a diffusion of the gas molecules to the hot side. When the stationary state is reached, the effect of the density gradient will be neutralized by the effect of the temperature gradient, consequently, there will not be net flow of molecules. Now by considering charged molecules, the charge accumulation at the cold side will also produce a repulsive electrostatic force, that is an electric potential that will move the charges back to the hot side (see Figure 1.3) [9]. The Seebeck

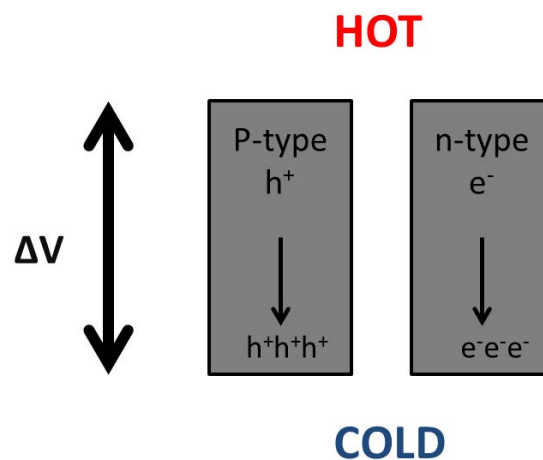


Figure 1.3 Scheme of the thermoelectric effect.

voltage is proportional to the temperature difference as shown in the following equation:

$$\Delta V = S \cdot \Delta T \quad (1.1)$$

where S is a proportional constant called Seebeck coefficient. The sign of the Seebeck coefficient determines the type of semiconductor, negative values are given for n-type semiconductors and positive values for p-type semiconductors. Using the Seebeck voltage it is possible to make thermoelectric generators. Figure 1.4 shows a single thermoelectric generator (TEG) based on a $p-n$ junction working as a Seebeck current supply. The thermoelectric elements in the module are electrically connected in series and thermally in parallel. The heat flow goes from the top to the bottom, while the current flows in the direction provided by the holes movement in the p-type semiconductor and by the electrons in the n-type.

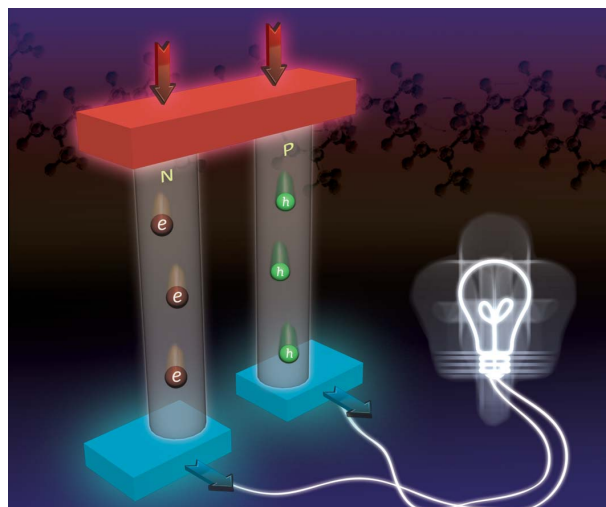


Figure 1.4 Thermoelectric module.

Moreover, the opposite effect that transforms a current flow into a temperature gradient, is called the Peltier effect. In 1834, a French watchmaker and part time physicist, Jean Charles Athanase Peltier found that an electrical current would produce heating or cooling at the junction of two dissimilar metals. The Peltier effect is used to make Peltier modules, usually employed in cooling systems.

1.2.1 Thermoelectric efficiency

A thermoelectric converter is a heat engine and like all heat engines obeys the laws of thermodynamics. The maximum thermoelectric efficiency of a thermoelectric generator is given by:

$$\phi_{max} = \frac{P_{out}}{Q_{in}} \quad , \quad (1.2)$$

where Q_{in} is the amount of heat which enters into the device and P_{out} is the power generated by the device, including the heat losses. In terms of the Carnot efficiency [10],

$$\phi_{max} = \phi_C \frac{\sqrt{1 + ZT_{av}} - 1}{\sqrt{1 + ZT_{av}} + T_h/T_c} \equiv \phi_C \gamma \quad , \quad (1.3)$$

T_h and T_c being the temperatures at the hot and cold ends, respectively, $T_{av} = (T_h + T_c)/2$, and the Carnot efficiency is given by $\phi_C = (T_h - T_c)/T_h$. The term γ represents the irreversible contribution to the efficiency. The quantity ZT is called dimensionless figure of merit and it can be shown to be [10]

$$ZT = \frac{S^2 \sigma}{\kappa} T \quad , \quad (1.4)$$

where S is the Seebeck coefficient, σ is the isothermal electrical conductivity and κ the thermal conductivity. The thermal conductivity has actually two contributions, $\kappa = \kappa_e + \kappa_p$. The

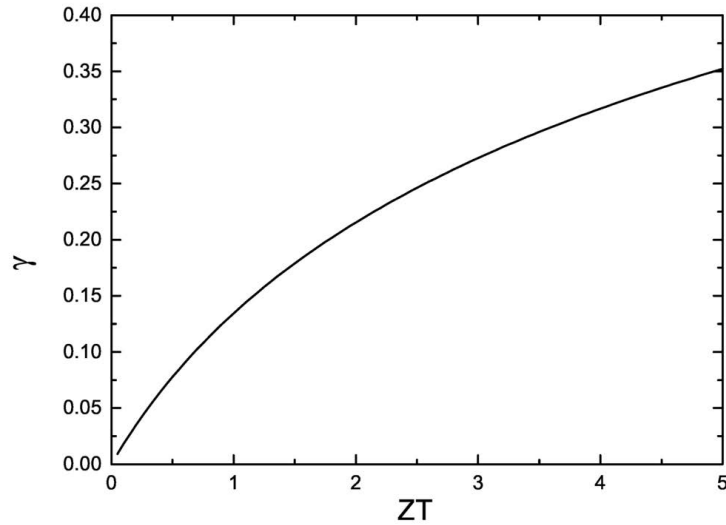


Figure 1.5 γ as a function of ZT .

electronic contribution κ_e is the most important in metals, while in semiconductors the phonon contribution κ_p is dominating.

From Eq. (1.3), it is clear that the maximum efficiency depends on both the Carnot efficiency and γ . As an example, if the cold end is at room temperature and the hot end at 1000 K, $\phi_C = 0.7 = 70\%$. In order to reach this efficiency, γ must be 1, which corresponds to $ZT \rightarrow \infty$. In Figure 1.5 we show the function $\gamma(ZT)$ from $ZT=0$ to $ZT=5$. Even in the case where $ZT=5$ the value of $\gamma = 0.42$, *i. e.* $\phi_{max} = 28\%$ following this example. With the state of the art in inorganic materials ($ZT \sim 2$), the maximum efficiency would be $\phi_{max} \sim 20\%$. These are some limiting cases and depending on the application, not always such temperature gradients are possible. Large temperature gradients can be produced in the exhaust of a car. In a Peltier modulus to cool a detector the temperature difference is of the order of 40 K. In the case of organic materials, the best values of ZT are half of the values obtained in inorganic materials and the Carnot efficiency will be lower than 40%, since temperature gradient can not be so high. Although the important factor to improve is not the figure of merit but the efficiency of the thermoelectric device, *i. e.* $\eta_C \gamma$, for a given application we should pay attention to the improvement of ZT .

The electrical, j and heat current, j_Q , can be written, respectively, as:

$$\begin{aligned} j &= e\mathcal{L}_{11} \left(e\mathbf{E} - T\nabla \frac{\mu}{T} \right) - e\mathcal{L}_{21} \nabla \ln T, \\ j_Q &= e\mathcal{L}_{21} \left(e\mathbf{E} - T\nabla \frac{\mu}{T} \right) - \mathcal{L}_{31} \nabla \ln T, \end{aligned} \tag{1.5}$$

where μ is the chemical potential ($\mu = \varepsilon_F$, the Fermi energy, at $T = 0$), \mathbf{E} is the electric field and the transport coefficients are defined as [11]:

$$\mathcal{L}_{ij} = \frac{4}{3m^*} \int \left(-\frac{\partial f}{\partial \varepsilon} \right) \tau^j \varepsilon^i D(\varepsilon) d\varepsilon, \quad (1.6)$$

being m^* is the effective mass, f the Fermi-Dirac distribution function and $D(\varepsilon)$ the electronic density of states (DOS). $\tau(\varepsilon)$ is the relaxation time, which depends on the scattering processes. In the absence of concentration and temperature gradients, the first term of Eqs. (1.5) provides the electrical conductivity, $\sigma = e^2 \mathcal{L}_{11}$. In open circuit, $j = 0$, and we can deduce from Eqs. (1.5) that the electric field is:

$$\mathbf{E} = \frac{1}{e} \nabla \mu - \frac{\mu \mathcal{L}_{11} - \mathcal{L}_{21}}{e \mathcal{L}_{11} T} \nabla T = -\nabla V \quad (1.7)$$

without gradients of concentrations, we arrive to the expression of the Seebeck coefficient:

$$S = \frac{\mu \mathcal{L}_{11} - \mathcal{L}_{21}}{e \mathcal{L}_{11} T} = \frac{k_B}{e \sigma} \int_{\varepsilon_c}^{\infty} \sigma(\varepsilon) \left(\frac{\varepsilon - \mu}{k_B T} \right) \left(-\frac{\partial f}{\partial \varepsilon} \right) d\varepsilon, \quad (1.8)$$

this last equation was provided by Mott [12]. Since Eq. (1.5) are only related to the electronic contribution, we can also deduce from them κ_e . One way to derive an expression for the phononic part is via the Boltzmann transport equation for phonons [11]. Equation (1.8) is valid for insulators or metals. In the case of a metal or a degenerate semiconductor, the derivative of the distribution function is basically a Dirac delta function produced at the Fermi energy and the transport coefficients can be written as:

$$\mathcal{L}_{ij} \approx \frac{4e^2}{3m^*} \tau^j(\varepsilon_F) \varepsilon_F^i D(\varepsilon_F). \quad (1.9)$$

Thus the Seebeck coefficient given by Eq. (1.8) can be written in the well known form [11, 12]

$$S = \frac{\pi^2 k_B^2 T}{3 e} \left. \frac{\partial \ln \sigma}{\partial \varepsilon} \right|_{\varepsilon = \varepsilon_F} = \frac{\pi^2 k_B^2 T}{3 e \varepsilon_F}. \quad (1.10)$$

This expression gives a Seebeck coefficient of the order of $1 \mu\text{V K}^{-1}$. It is a typical value for metals. Actually, this expression, although using Fermi integrals, was used by Hicks and Dresselhaus [13] to claim that the figure of merit of Bi_2Te_3 could be increased up to a factor of 13 by reducing the dimensionality (building a superlattice). In practice, ZT has been improved in the best of the cases by a factor of 3 by reducing the dimensionality [14]. The main goal to increase the figure of merit by decreasing the dimensionality is to engineer a material in such a way that the Fermi energy is just at the maximum of the density of electronic states. In this way, there will be a huge increase in the Seebeck coefficient, but of course there are other factors more difficult to engineer, mainly the thermal conductivity.

1.2.2 Thermoelectric materials

The ideal thermoelectric material would be one with a high electrical conductivity, high Seebeck coefficient and low thermal conductivity as shows Eq.(1.4). Basically, thermoelectric materials are semiconductors because the Seebeck coefficient is higher than metals and also it is possible to optimize the ZT value through the doping level. Figure 1.6 shows ZT val-

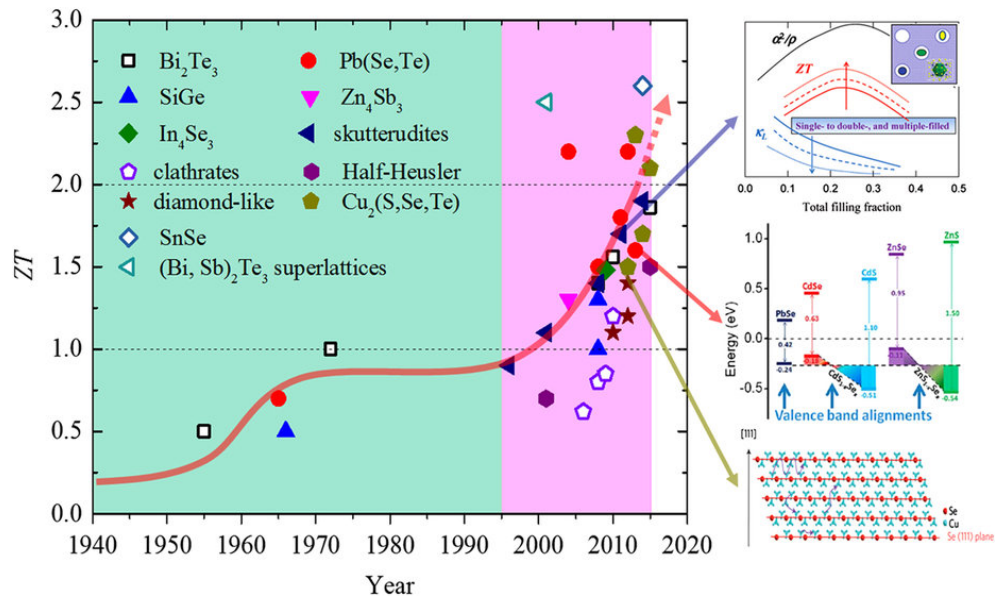


Figure 1.6 Evolution of ZT in some thermoelectric materials. Reproduced from [15] image under a Creative Commons CC-BY license .

ues of some thermoelectric materials during the last 75 years [15]. During the decade of 1950, Bi_2Te_3 was the reference thermoelectric material with a modest ZT value around 0.5 at room temperature. Moreover, materials based on PbTe were developed for medium range temperature applications [15]. In the case of high temperature range application, SiGe was employed [15], especially for aerospace generators used in space aircrafts. Since 1960 there was no change in the values of the thermoelectric efficiency, because research projects with the objective to increase ZT until values around 3 were rejected by the funding agencies as not possible. However, in middle of the 90's with the work of Hicks and Dresselhaus published in 1993 something changed [13]. They showed a path to increase the thermoelectric efficiency of a semiconductor: the reduction of the dimensionality [13]. Following their ideas, semiconductor superlattices such as $\text{Bi}_2\text{Te}_3/\text{Sb}_2\text{Te}_3$, [16] semiconductors alloys like PbSeTe [17] or, more recently, SiGe [18] have been shown to have ZT values around 2. However, there are several drawbacks in inorganic semiconductors. The first one is the high cost of production of semiconductors with good thermoelectric properties, for this reason a tiny amount of n- and p-doped Bi_2Te_3 , is used in commercial TEGs. The second problem is the high toxicity of some of the compounds, that contain Pb, for instance, and the scarcity of these materials. Consequently, many studies have

driven their efforts to search new and clean (“green”) efficient thermoelectric materials during the last few years [9, 15].

One kind of these new materials are organic semiconductors, especially, conducting intrinsic polymers (ICP). Conjugated polymers such as: poly(3,4-ethylenedioxythiophene) (PEDOT), polyaniline (PANI), (Poly(3-hexylthiophene-2,5-diyl)) (P3HT) or polypyrrole (PPy) have attracted the attention in thermoelectric applications during the last decade [19, 20]. The main advantage of these organic materials is the low thermal conductivity, compared to inorganic compounds. The thermal conductivity of most polymers is at least a factor of 10 smaller than that of inorganic compounds. In spite of the finding of Hicks and Dresselhaus [13], the figure of merit of inorganic compounds has increased by a factor of 3 or 4 in the last 20 years, and this increase was not exclusively due to the modification of the Seebeck coefficient, but also to other factors related to the lattice thermal conductivity like interface roughness or, in general, to surface effects [21]. There are several more advantages for using conducting polymers instead of inorganic materials such as: non scarcity of raw materials, non toxicity, possibility of using them in large area applications, good mechanical properties, easiness to fabricate them, etc. This last one is actually an important point, since as it has been commented previously, the total efficiency depends on the Carnot efficiency multiplied by ZT . In large area applications, it is possible, on one side, to increase the temperature difference and, on the other, to increase the total supplied power by building a large area single module. One example of large area application can be found in the module proposed by Wagner *et al.* [22] using SiGe alloys. However the Ge amount used in the module increases the cost of the device and it could not be developed in practice. Table 1.1 shows values of thermoelectric properties of the most representative conducting polymers. Some few works show ZT values around 0.2-0.4, for this reason more research is needed to increase the thermoelectric efficiency in conducting polymers. Different strategies have been employed in the past to improve and optimize ZT values (or the power factor, $PF \equiv S^2\sigma$) in intrinsically conducting polymers, but most of the strategies have been, unfortunately, hardly unexplored. One of the methods most oftenly used to optimize the doping level of ICPs is either chemical or electrochemical doping [23, 27, 28, 36, 37]. Using these methods, the thermoelectric performance of PEDOT has reached values of ZT in the range 0.20 – 0.40 [23, 27, 28, 36, 37]. However, these values are still lower than those corresponding to inorganic materials. The use of hybrid organic-inorganic materials could be a promising alternative to improve the thermoelectric properties of ICPs. Very high values of the PF have been obtained for polyaniline (PANI)/double wall carbon nanotube (DWCNT)/Graphene ($1750 \mu\text{W}/\text{m K}^2$)[38] and PANI/DWCNTs/PEDOT:PSS/Graphene ($2710 \mu\text{W}/\text{m K}^2$)[39] synthesized by means of layer by layer (LBL) assembly. The incorporation of semiconductor nanostructures such as Te nanorods [40–42], Te-Cu hybrids nanorods [43] or even Bi_2Te_3 nanoparticles [44–46] produce a large increase in the Seebeck coefficient of the polymer, delivering a high PF, since most of the times the thermal conductivity has not been measured. The incorporation

Table 1.1 Thermoelectric parameters of the most relevant conducting polymers at room temperature.

System	σ (Scm ⁻¹)	S (μ VK ⁻¹)	κ (W m ⁻¹ K ⁻¹)	PF (μ W/m K ²)	ZT	reference
PEDOT:Tos/ PEO- PPO-PEO electrochem. reduct.	~1200	~100		1270	~1.02	[23]
PEDOT:PSS + EG treat.	~980	~70	0.23	469	0.4	[24]
PEDOS-C6 elec- trochem. reduct.	~200	~110		354.7		[25]
PEDOT:PSS + EG treat. + hydrazine reduct.	~1300	~49	0.3	320	0.3	[26]
PEDOT:Tos + TDEA reduct.	~80	~290	0.37	324	0.25	[26]
PEDOT:BTfMSI + hy- drazine reduct.	~1080	~37	0.19	147	0.22	[27]
PEDOT:PSS elec- trochem. reduct.	~25	~90	0.17	23.5	0.041	[28]
PEDOT:PSS + DMSO 5%	298	12.65		4.78	~0.001	[29]
PANI/CSA-doping in m-cresol	220	~20		11		[30]
PANI doped with H ₃ PO ₄	40	~7		0.19		[31]
polyselenophene and its copolymers with 3-methylthiophene	0.1-54	20-98		2-12	0.034	[32]
Copolymer of 1,12- bis(carbazolyl) dode- cane and thieno[3,2- b]thiophene and its copolymers with 3-methylthiophene	4x10 ⁻⁵ -0.4	75-169		~0.17-0.33		[33]
Phenylenevinylene block copolymers and their blends with MEH-PPV	6x10 ⁻⁶ -14.4	7-531		~10 ⁻⁵ -1.33		[34]
PEDOT:PSS + Poly- thiophenes Bilayered nanofilms	125-200	11-17		~1.5-6		[35]

of inorganic nanostructures to an ICP matrix is not an easy path, due to the intrinsic incompatibility between the two components. In particular, Te nanostructures are not very stable in solution. Thus, non homogeneous films with a bad morphology are usually obtained and the thermoelectric performance of the final material has been hardly improved.

1.2.3 Applications of thermoelectricity

Power generation is one of the most important application of thermoelectric materials. Highlight their use in aerospace missions. Figure 1.7 shows the General-Purpose Heat Source-Radioisotope Thermoelectric Generator (GPHS-RTG) [47]. The GPHS-RTG uses 18 modules along with the same SiGe unicouple, with a longer converter filled with plutonium fuel. The

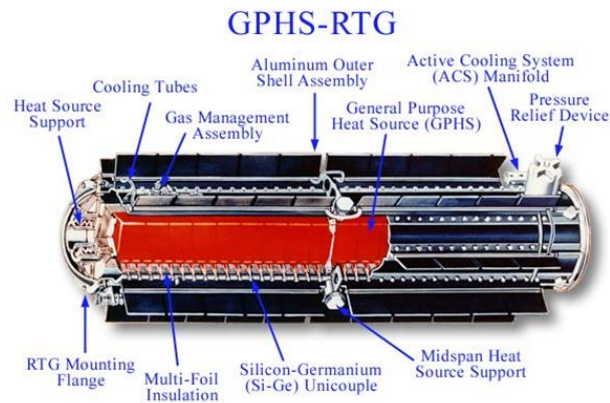


Figure 1.7 GPHS-RTG thermoelectric generator. Reproduced from [47] with permission of TAYLOR and FRANCIS.

hot-leg and cold-leg temperatures during operations are nominally 1273 and 566 K, respectively giving a specific power of 5.2 W/kg [47]. This generator was used in Galileo (1989), Ulysses (1990), and Cassini missions (1997).

Other promising application in terms of energy production is to use the body heat. The integration of thermoelectric generators into normal devices in contact with human body such as: clothes or watches will be able to supply enough energy to small portable devices [48].

The other main application of thermoelectric materials is their use in coolers and refrigeration systems using the Peltier effect. Peltier modules are the most common devices in terms of cooling. Currently, there are commercial refrigerators available using thermoelectric modules as shown in Figure 1.8. Another application can be thermal sensing, since using the Seebeck

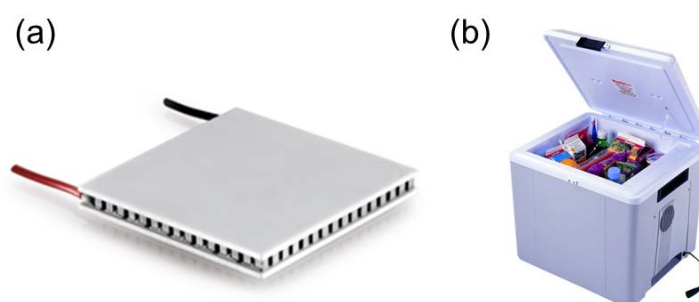


Figure 1.8 Commercial: (a) Peltier module and (b) portable thermoelectric refrigerator.

voltage it is possible to detect changes in temperature. In this work a thermoelectric sensor using organic semiconductors has been developed.

1.3 Energy storage

Not only the production of energy is highly important but also to find an efficient way to store it. Currently, there are several devices for energy storage such as: fuels cell, batteries, capacitors and supercapacitors [49]. From the point of view of organic semiconductors, the supercapacitors have become in the focus of many research due to their enormous potential as electrodes in devices for energy storage. Figure 1.9 shows excellent values of specific capacity using conducting

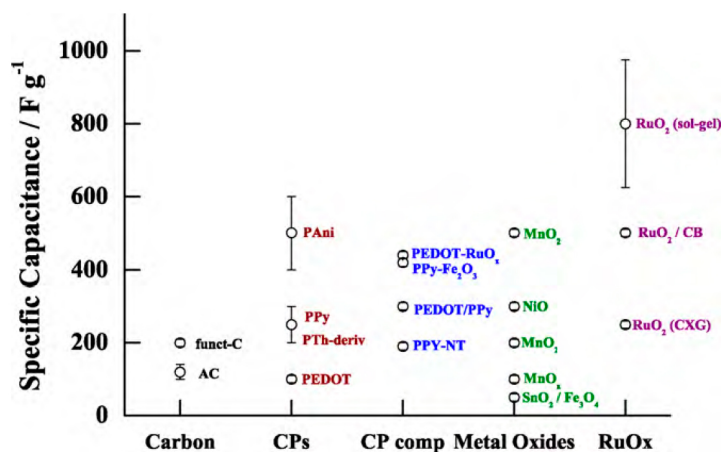


Figure 1.9 Specific capacitance of some materials. Reprinted from [49] with permission from Elsevier.

polymers such as: PANI, PEDOT or PPy [49]. The use of conducting polymers for supercapacitors presents a high potential due to its high capacity and its fast absorption and desorption of ions. Again, the formation of polymeric nanostructures can be the key to increase the performance of supercapacitors devices, since the use of nanostructured materials increase the surface area. Consequently, the interphase electrode-electrolyte is larger, increasing the charging and discharging velocity, due to a diminution in the electronic transport [50, 51].

1.4 Objectives and structure of the thesis

The principal objective of this work has been to investigate and develop organic materials to built efficient thermoelectric devices. Several partial objectives objectives have been successively attained such as:

1. Design, formulation and synthesis of conducting polymers and their complete properties characterization.
2. Design, formulation and synthesis of hybrid organic-inorganic materials and their complete properties characterization.

3. Synthesis of semiconducting nanostructures and their characterization.
4. Fabrication and testing of thermoelectric modules and supercapacitors devices.

Each chapter of this thesis, with the exception of the general introduction (Chapter 1) and the global conclusion (Chapter 7), is organized in the same way: an introductory part, which reviews the fundamental concepts to understand the chapter, followed by the results and discussion of different experiments, with experimental details, and finally the main conclusions of the chapter.

Chapter 3 is focused on the preparation and characterization of conducting polymers such as PEDOT and PPy. After a revision of the fundamental concepts of conducting polymers several experimental studies are described. The first one is the thermoelectric properties of PEDOT:PSS films made by solution a process. The second one is the effect of the chemical de-doping on PEDOT electrochemically polymerized using several counter ions. The third study was focused on the electrochemical de-doping in PEDOT and polypyrrole. The last experiment was the nanostructuration of PEDOT using soft and hard template methods. Chapter 4 is focused on the preparation and characterization of inorganic materials such as metallic oxides and carbon based materials. After a brief description of several groups of inorganic compounds for thermoelectric applications several experimental studies are presented. The first one is based on thermoelectric properties of Perovskite nanostructures, $\text{La}_{1-x}\text{Ca}_x\text{MnO}_3$ and $\text{Nd}_{1-x}\text{Ca}_x\text{CoO}_3$. The other experimental works are focused on the thermoelectric properties of carbon based materials such as: vitreous carbon, carbon black and charcoal. The synthesis and characterization of polymer hybrid materials are treated in Chapter 5, where the thermoelectric properties of PEDOT nanocomposites based on Perosvkite nanoparticles, expanded graphite, MWCNTs and Te are discussed. Chapter 6 is aimed to the fabrication of thermoelectric and supercapacitors devices. In this chapter the properties and the fabrication process of two thermoelectric modules, one thermal sensor and one supercapacitor based on PEDOT, cotton fabric-MWCNTs-PEDOT and cotton fabric-MWCNTs-PEDOT- MnO_2 are discussed. Finally, Chapter 7 summarizes the most relevant results of this thesis.

Chapter 2

Experimental

Content

In this chapter all the characterization techniques used to determine the properties of the different materials and devices developed in this thesis are explained. This chapter has been structured in four sections: electrical, thermal, morphological and structural characterization.

2.1 Electrical characterization techniques

2.1.1 Electrical conductivity

The electrical conductivity has been determined using the Van Der Pauw method with a home made equipment, where four contacts are used to eliminate the effect of the contact resistance [52]. The electrical conductivity can be obtained from two four-point resistance measurements independently either on contact resistances or on the specific geometry of the contact arrangement as shown in Figure 2.1(a) and (b). For the first resistance measurement, a current I_{AB} is driven from two contacts, named A and B , and the potential difference V_{CD} between the other two contacts, C and D was measured, giving the first resistance $R_1 = V_{CD}/I_{AB}$. The second resistance, $R_2 = V_{BD}/I_{AC}$, is obtained by driving the current from A to C and measuring the voltage between B and D (see Figure 2.1). The voltage and current values were plotted giving a lineal trend (see Figure 2.1c) according to the Ohms law. The conductivity of the sample is obtained by solving the Van Der Pauw equation [52]:

$$e^{-\pi d R_1 \sigma} + e^{-\pi d R_2 \sigma} = 1, \quad (2.1)$$

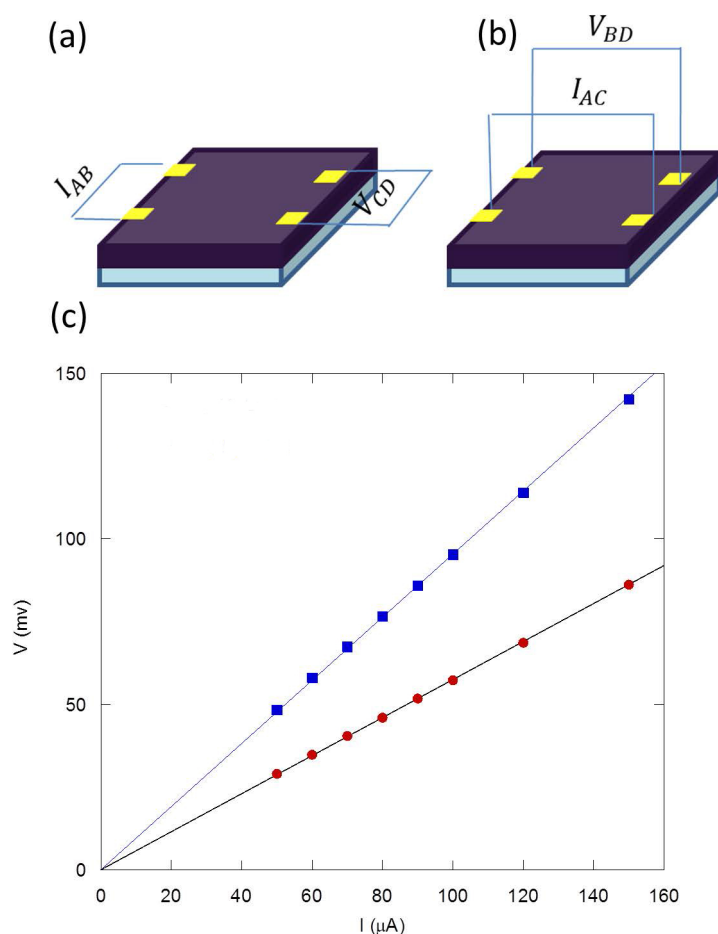


Figure 2.1 Contacts configurations to measure (a) R_1 , (b) R_2 and (c) voltage as function of the current for a PEDOT:PSS film.

where d is the sample thickness previously measured. A Keithley 2400 current source was used as driving source. For high temperature measurements the electrical characterization were performed by using a commercial MMR-Technologies system in the temperature range between 300 and 700 K. The electrical resistivity measurements were made on flat plates by applying the Van Der Pauw method previously described. For the case of PEDOT:Tos pellets samples the electrical conductivity measurements were carried out by using broadband dielectric relaxation spectroscopy in a Novocontrol Broadband Dielectric Spectrometer (Hundsagen, Germany).

2.1.2 Seebeck coefficient

For Seebeck effect measurements a home-made apparatus was fabricated. The experimental set-up consists of two copper blocks, one heated by an electrical resistance and the other cooled by water flow. The sample is placed in between these two blocks. A temperature difference is created across the sample and the resulting voltage is recorded. The Seebeck coefficient can be determined as the ratio between the electrical potential, ΔV , and the temperature difference, ΔT ,

that is:

$$S = \frac{\Delta V}{\Delta T} \quad (2.2)$$

The temperature is controlled by a Lakeshore 340 and two PT100 resistors previously calibrated. To record the potential data a Keithley 2750 Multimeter/Switching System was employed. Both instruments are controlled together using a Labview software. Figure 2.2(a) shows pictures of

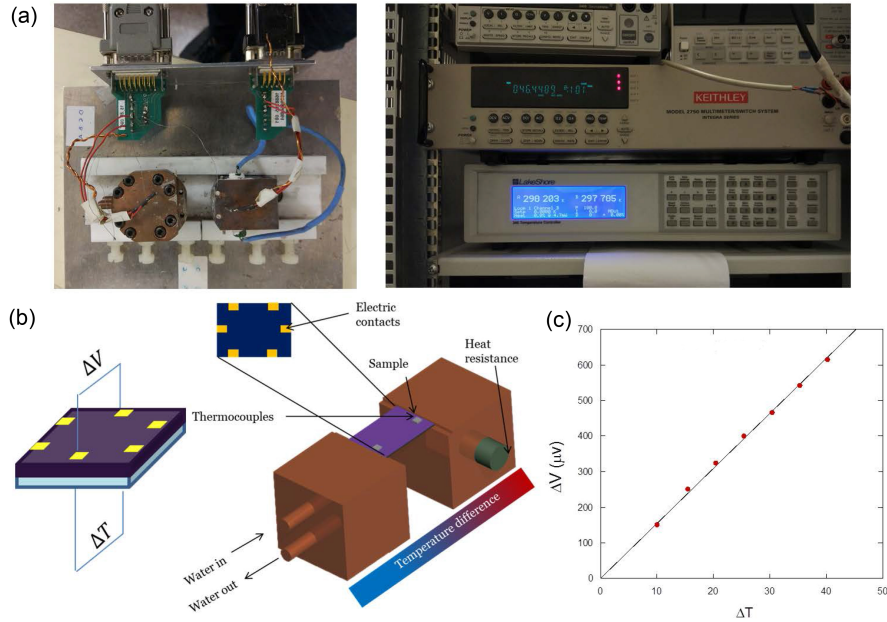


Figure 2.2 (a) Seebeck measurement system, (b) scheme of sample measurement and (c) Seebeck voltage as a function of the temperature gradient.

the home-made apparatus developed for the Seebeck coefficient measurements. The electric contacts are placed in the ends of the sample and the potential is recorded as a function of the temperature difference as shown in the scheme of Figure 2.2(b), obtaining a linear behaviour between the voltage and the temperature gradient (see Figure 2.2(c)).

For Seebeck coefficient measurements at higher temperatures a MMR-Technologies system in the temperature range between 300 and 700 K using a reference constantan wire was used.

2.1.3 Power output

The power output is the characteristic parameter for energy generators. The power supply was calculated using the basic equation

$$P = \frac{\Delta V^2}{R_L} \quad (2.3)$$

where V is voltage across the contacts and R_L the load resistance. For these measurements, an electric generator is connected to a variable resistor from 10Ω to $1 \text{ M}\Omega$ (see Figure 2.3). Several

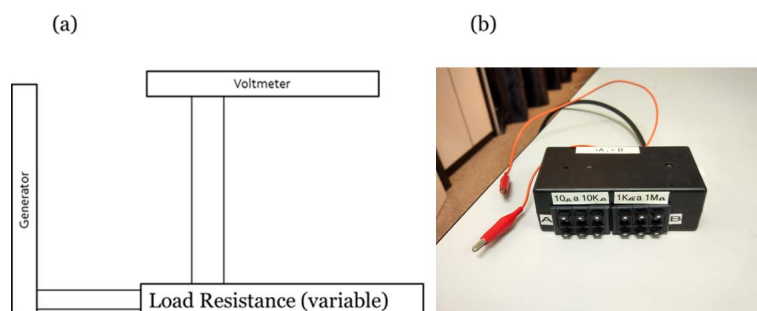


Figure 2.3 (a) Scheme of the power measurements, and (b) box with the connections for the load resistance.

temperature differences are applied to the thermoelectric generator and the potential is recorded as a function of the load resistance.

2.1.4 Thickness and mass deposition

The film thickness was measured with the aid of a profilometer (Optical Profilometer -Dektak 150) and reported values represent an average of at least 5 different measurements per film. The mass of the deposited layer on the Au/Ti crystals was measured with a Maxtek Research Quartz Crystal Microbalance (Cypress, CA). The quartz crystal was blown with compressed nitrogen gas prior to be left on the microbalance to analyse the mass change of LBL thin films.

2.1.5 Electrochemical measurements

All the electrochemical synthesis and characterization were carried out in a Ivium-n-Stat: multi-channel electrochemical analyzer as show Figure 2.4(a) . The electrochemical cell basically is

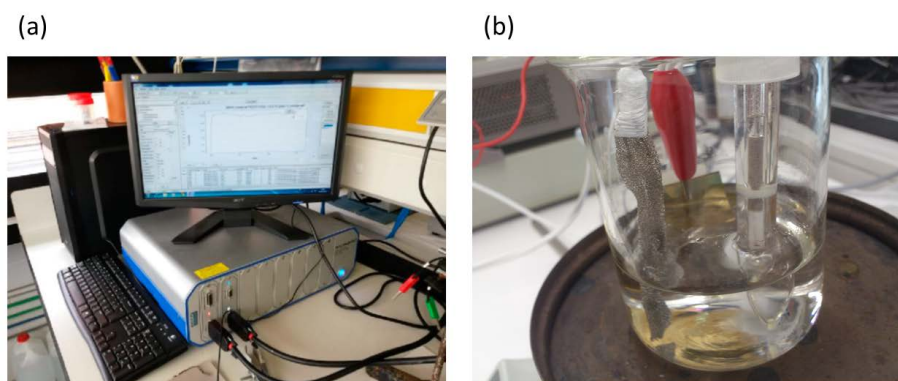


Figure 2.4 Picture of (a) Ivium-n-Stat: multi-channel electrochemical analyzer and (b) electrochemical cell with the three electrodes.

composed by three electrodes: the working electrode, the reference electrode and the counter electrode, as shown in Figure 2.4(b). All the synthesis of the conducting polymers were made

using the galvanostatic mode, keeping constant the current and recording the voltage, except in the tellurium electrodeposition which was carried out in the potentiostatic mode (applying a constant voltage). The cyclic voltamperometry was carried out applying a potential scan from an initial voltage to a different voltage and back again to the initial voltage using several scan rates.

2.2 Thermal analysis techniques

2.2.1 Differential scanning calorimetry

Differential scanning calorimetry (DSC) studies were performed on a Q-20 DSC from TA Instruments calibrated with indium. In this technique, the difference in the amount of heat required to raise the temperature of a sample and the reference is measured as a function of temperature or time. The measurements were carried out in the range of 90 to 220 °C at a heating rate of 20 °C/min under nitrogen atmosphere. Two scans have been made in each sample in order to delete the thermal history of the samples.

2.2.2 Thermogravimetric analysis

The thermogravimetric analysis basically consists of monitoring the mass of sample as a function of the temperature (dynamic mode) or as function of the time keeping constant the temperature (isothermal mode). Thermogravimetric analysis (TGA) was performed on a Setaram Setsys 16/18 TGA ATD analyzer. The samples were analyzed in platinum pans at a heating-cooling rate of 10 °C/min from 30 to 1000 °C under oxygen atmosphere. Samples masses ranged from 7 to 10 mg.

2.2.3 Thermal conductivity

The thermal conductivity was determined with the aid of modulated differential scanning calorimetry (MDSC) according to the ASTM E1952-11 standard test method. This method is valid to measure thermal conductivities of polymeric materials with values within the range 0.1 – 1 W m⁻¹K⁻¹. The MDSC measurements were performed in a DSC Q-20 TA Instruments calibrated with indium and sapphire. All MDSC measurements were carried out at 300 K in modulated conditions with a period of 80 s and ±1 K of temperature amplitude. The thermal conductivity is calculated from the equation:

$$\kappa = \frac{8LC^2}{C_p M d^2 p} , \quad (2.4)$$

where C_p is sample specific heat ($J/^\circ C \text{ g}$), L the sample length (m), d the sample diameter (m), M is the sample mass (g), C the apparent heat capacity ($J/^\circ C$) and p the period of the modulated scan.

For the case of perovskite samples, the thermal conductivity was determined from the measurements of the thermal diffusivity (α), specific heat (C_p) and density (ρ) using the $\kappa = C_p \alpha \rho$ relationship. The Dulong-Petit rule was used to estimate the value of C_p whereas α was measured with a commercial Linseis system (LFA 1000) between 300 and 500 K. All samples were covered with a graphite screen to ensure full absorption of the light at the front surface and highest emissivity from the backside. ρ was obtained through the Archimedes principle using water as immersion fluid.

2.3 Structural characterization techniques

2.3.1 X-ray diffraction analysis

The X-ray diffraction analysis was carried out using a Bruker AXS D5005 diffractometer. The samples were scanned at 4° min^{-1} using $\text{Cu K}\alpha$ radiation ($\lambda=0.15418 \text{ nm}$) at a filament voltage of 40 kV and a current of 20 mA. The diffraction scans were collected within the $20^\circ \leq 2\theta \leq 60^\circ$ range with a 2θ step of 0.01° .

2.3.2 Raman scattering

The Raman scattering measurements were carried out at room temperature in backscattering configuration using a Jobin Yvon T64000 spectrometer equipped with a liquid-nitrogen cooled open electrode charge-coupled device (OECCD camera). The excitation line of 514.53 nm was provided by an Ar/Kr laser focused onto the sample using a $100\times$ microscope objective with a numerical aperture $NA = 0.90$ (Olympus). This setup focuses the light on an area around $1\mu\text{m}$ on top of the sample. To avoid the sample heating during the experiment, special care was taken, limiting the power down to a few μW .

2.3.3 Fourier transform infrared spectroscopy

Fourier transform infrared spectroscopy (FTIR) measurements were performed in a Nicolet Nexus FTIR spectrometer over the range from 450 to 4000 cm^{-1} with the attenuated total reflectance accessory by co-addition of 60 scans with a spectral resolution of 2 cm^{-1} .

2.3.4 Uv-Vis spectroscopy

The Uv-Vis spectroscopy measurements were carried out in a Shimadzu UV-2501PC Uv-Vis spectrophotometer covering the range from 1100 to 300 nm. For the case of polymer films, the film accessory was used. However, for nanoparticles suspensions quartz, buckets were employed.

2.4 Morphological characterization techniques

2.4.1 Scanning electron microscopy

Scanning electron microscopy (SEM) was carried out in a Hitachi S-4800 microscope at an accelerating voltage of 20 kV and a working distance of 14 mm. Small pieces of sample were placed in the sample holder (2 inches). The samples were metallized with a Au-Pd coating before observation. The equipment has incorporated a RX Bruker retro-dispersed X-ray for microanalysis to determine the elemental composition of sample surface.

2.4.2 Transmission electron microscopy

Transmission electron microscopy (TEM) was carried out in a JEOL JEM-1010, coupled with a digital camera MegaView III at 100 kV. The samples for cross section analysis were prepared by embedding a small piece of coated PET in DurcupanTM ACM resin (SigmaAldrich, Munich, Germany), curing overnight and then cutting cross sections using an Ultra 45° diamond knife (Diatome, Hatfield,PA). Samples were imaged on copper grids. The particle size was analyzed from the TEM images using the software "Image J".

2.4.3 Atomic force microscopy

Surface topography was evaluated using atomic force microscopy (AFM) from NT-MDT in semicontact mode using cantilever NSG10/TiN tip (NT-MDT). AFM height images of each sample were captured in ambient air at 68% humidity and temperature at 23°C. Nova PX imaging software was used to analyze the resulting images.

Chapter 3

Conducting polymers as organic thermoelectric materials

Content

This chapter studies the thermoelectric behavior of conducting polymers, focusing on PEDOT with the principal objective of increasing its thermoelectric efficiency. The chapter has been divided in several sections. An introduction, where the most fundamental aspects of thermoelectricity in conducting polymers are described, other part with several studies carried out in PEDOT and polypyrrole such as: the effect of the addition of organic solvent to Poly(3,4-ethylenedioxythiophene)-poly(styrenesulfonate) (PEDOT:PSS) solutions, the optimization of the ZT of PEDOT and PPy trough chemical and electrochemical de-doping and the synthesis of PEDOT nanostructures (nanoparticles and nanowires).

3.1 Introduction

Traditionally, inorganic materials have been used in thermoelectric applications such as Bi_2Te_3 [53], PbTe [54] or SiGe [22, 55]. In the last years, most of the research in thermoelectricity has been concentrated in inorganic compounds. The main purpose was to find an inorganic material with a small lattice thermal conductivity. Besides the well known bismuth telluride, skutterudites [56] and half-Heusler compounds [57] have been studied in the last decade as good candidates for the development of TEGs. The strategy in the search of inorganic compounds with low thermal conductivity is to find materials with complex crystal structures and heavy atoms providing a low phonon propagation. However, this class of inorganic materials presents several drawbacks from the point of view of TEG fabrication. One of the most important is the

abundance of the raw materials. The commonly used elements in the thermoelectric module fabrication are Bi and Te [58], the abundance of them in the earth crust is 0.0025 ppm and 0.001 ppm. These values are insignificant compared with the abundance of other semiconductors such as silicon, 270,000 ppm. This fact increases the cost of thermoelectric generators. The other disadvantage is the toxicity, for example a big number of toxic effects have been attributed to bismuth compounds in humans: nephropathy, encephalopathy, osteoarthropathy, gingivitis, stomatitis and colitis [59, 60]. These facts make these materials unsuitable for thermoelectric applications in large scale.

Conducting polymers have become very interesting materials in the development of electronic devices such as: organic solar cells [61], transistors [28], supercapacitors [51, 62], light emitting diodes [63, 64], and recently thermoelectric modules [19, 20, 65]. The typical conducting polymers are summarized in Table 3.1. Table 3.1 shows the chemical structures of conducting polymers commonly used in thermoelectricity: PANI, polyalkyl thiophenes, PEDOT, polyacetylene, PPy and poly(2,7-carbazolyenevinylene).

Table 3.1 Molecular structures of typical conducting polymers.

Polymer	Structure
polyacetylene	
polyaniline	
PEDOT	
polypyrrole	
polyalkyl thiophenes	
Poly(2-7carbazoles)	

Conducting polymers compared with inorganic materials present several advantages. For example, organic materials are cheap, and also they offer the possibility to be used in large scale areas, because some of them are soluble, being easy to cover large areas through thin polymer films. Conducting polymers can offer other interesting properties such as: flexibility (making possible their integration in flexible devices), absence of toxicity and easier chemical modification.

However, the thermoelectric efficiency of these materials is very low compared with classical inorganic materials such as, Bi_2Te_3 or PbTe . For this reason researches all over the world dedicate a great effort to increase the ZT of organic materials.

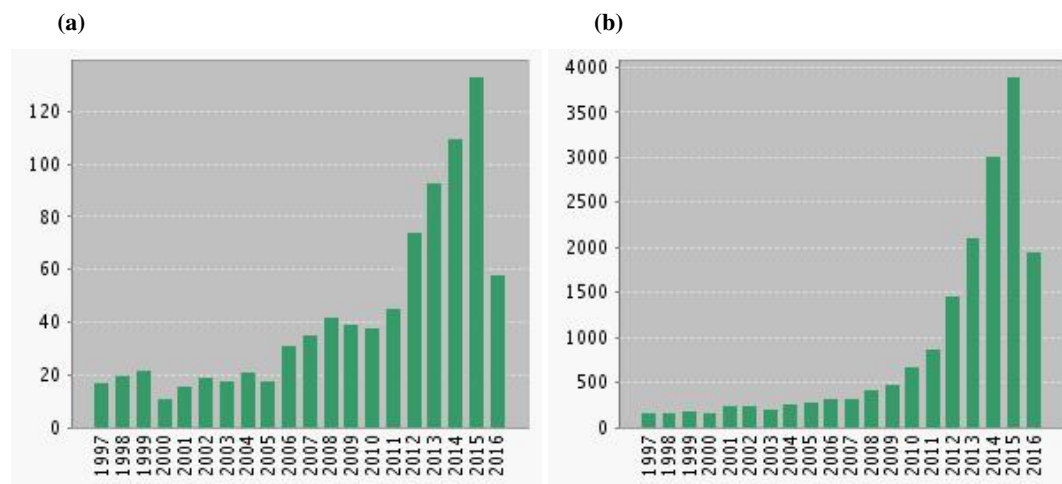


Figure 3.1 Conducting polymers (a) articles and (b) number of cites in thermoelectricity during the last 19 years. Data taken from Web of ScienceTM.

Figure 3.1 shows the number of papers and cites about thermoelectric properties of conducting polymers during the last 19 year. It is possible to observe an exponentially growth in both aspects (cites and papers) since 2012 corresponding with the beginning of this thesis. The real fact is that, while ZT in inorganic materials has increased around a factor of 3-4 in the last 20 years, even via nanostructuration, in the case of organic materials the increase in ZT has been of several orders of magnitude. Even more, 10 years ago the figure of merit of most conducting polymers were of the order of 10^{-4} , nowadays the best values are around 0.5. Although values of ZT have been increased 1000 times, there is still a lot of work to be done in order to get organic materials competitive with the traditional inorganic materials.

In this chapter, several methods to increase the thermoelectric efficiency of conducting polymers will be shown such as: secondary doping, chemical and electrochemical de-doping.

3.1.1 Basic considerations of the synthesis of conducting polymers

Typically, conducting polymers are synthesized by oxidative polymerization. The monomer with a conjugated π -bound structure is polymerized in the presence of an oxidant salt. Figure 3.2 shows the mechanism for 3,4-ethylenedioxythiophene (EDOT) polymerization using ammonium persulfate (APS) as oxidant. The oxidant remove electrons from the double bounds of the conjugated structure in order to form the polaronic form of EDOT. Then, two of these polaronic molecules are bonded together in order to form a dimer structure. This process repeats for the dimer, the trimer and all the species and finally, a polymeric materials is obtained

[66]. Generally, the polymer chains are oxidized during the polymerization, a fact that produces positive charges along the polymer chains, neutralized by the anion of the oxidant. This process is called doping in conducting polymers. As the positive charges along the polymer backbone increase, the doping level increases. Consecutively, as the polymer is deficient in electrons, they are in an oxidative state, generating a p-type semiconductor. Table 3.2 shows the most usual dopant molecules for typical semiconducting polymers used in thermoelectric applications. The counter-ion can play an important role in the chemical properties of the final conducting polymer. For example, PEDOT synthesized using iron(III) p-toluene sulphonate or LiClO_4 are insoluble, however when PEDOT is synthesized in presence of PSS is water soluble. Moreover, the mechanical and optical properties can be also dependent on the counter-ion [19, 27].

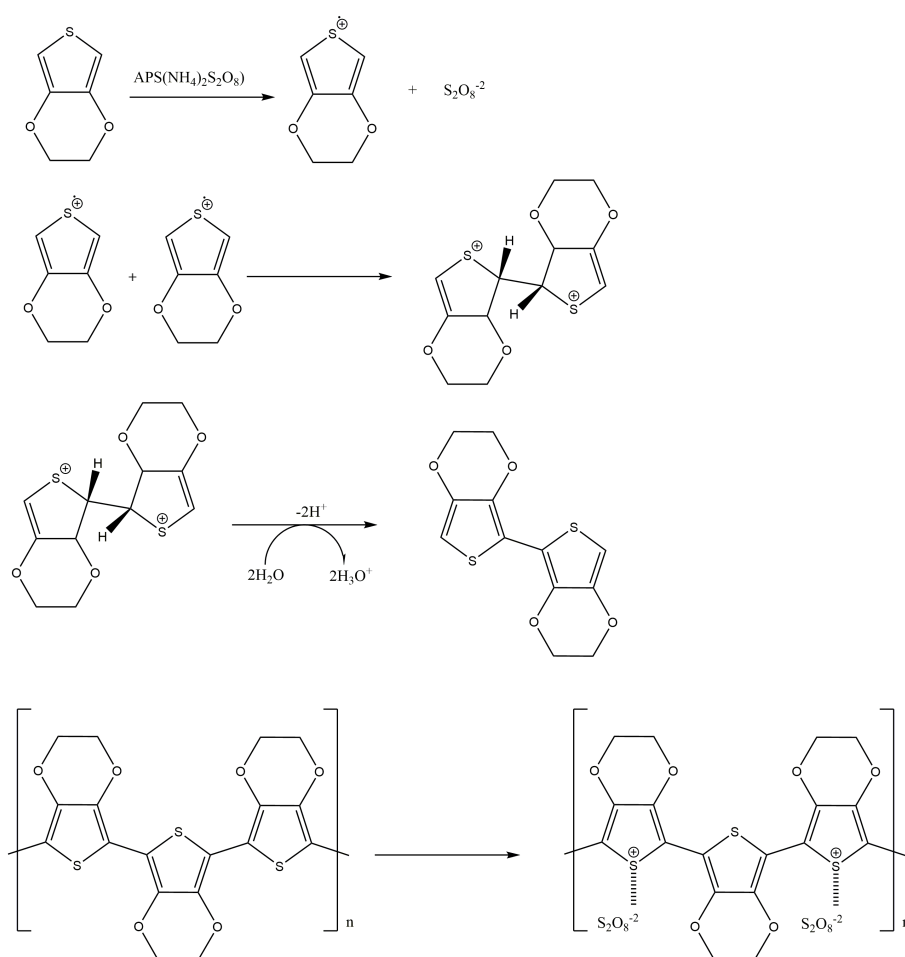
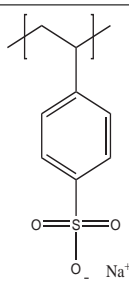
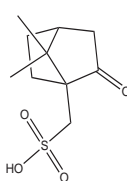
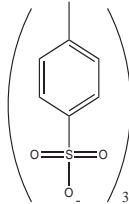


Figure 3.2 Mechanism for EDOT polymerization using APS as oxidant.

Other way to synthesize conducting polymers is through electrochemical oxidation in a electrochemical cell [19, 27, 37, 67–69]. Using this method, the polymerization occurs over the surface of the working electrode, obtaining a polymeric film after the synthesis. Controlling the current density and the polymerization time, it is possible to control the thickness of the film. The electrochemical method presents several advantages over the chemical oxidation such as:

in most cases the polymeric material is deposited on the working electrode as a film, absence of purification steps, the reaction is very simple to control and it allows to scale it to industrial applications. One of the main problem of the electrochemical synthesis of conducting polymers (from the point of view of the thermoelectric applications) is that after the synthesis, the film is deposited over a conductive surface. This fact makes the final materials electrically connected to a metallic surface, making impossible the electrical measurements in the plane of the film, due to the presence of the metallic substrate. For this reason, it is very important to obtain a conducting polymer film over an insulating surface. In this thesis, several ways to achieve conducting polymer films over an insulating surface after the electrochemical polymerization have been developed. One of these methods will be described in detail in this chapter.

Table 3.2 Dopants of the most typical semiconducting polymers .

Polymer	Dopant	Reference	Polymer	Dopant	Reference
PEDOT		[26, 28, 70–72]	PANI		[30, 73, 74]
		[23, 36, 70]		H ₂ SO ₄	[75, 76]
	LiClO ₄	[27, 61, 62]		HCl	[77]
	BF ₄	[78–80]		H ₃ PO ₄	[81]
	PF ₆ ⁻	[27, 61, 82]		polycarbazoles	FeCl ₃
polyalkyl thiophenes	FeCl ₃	[32]	polyacetylene	I ₂ vapour	[84, 85]
	I ₂ vapour	[32]			

The electrochemical polymerization also allows to use many dopants, instead of common electrolytes, such as ionic liquids.

3.1.2 Electronic transport in conducting polymers

For the case of small molecules with a defined number of atoms, the atomic orbitals are combined to produce molecular orbitals with discrete and well defined energy levels. The low energy orbitals are filled with electrons achieving a bonding character, however the orbitals with high energy level are empty, consequently, these orbitals present an antibonding behavior. When the

number of atoms increases forming a three-dimensional lattice, the molecular orbitals overlap in a band, consequently a gap between this two bands appears as it is shown in Figure 3.3. In

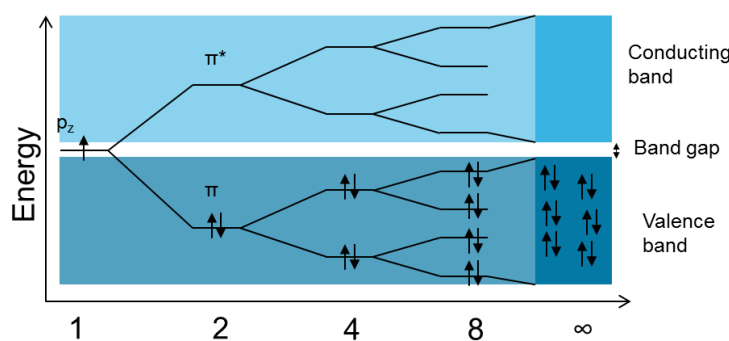


Figure 3.3 Diagram of energy levels in conjugated systems.

general, the electronic structure of conjugated polymers is divided in two parts: the bands originated from the bonding and anti-bonding energy level associated with the σ -bonds formed from the sp^2 wavefunctions, and the π -band that is originated due to the presence of delocalized p_z wavefunctions. The polymer backbone is kept together by the σ -bonds. For example, in the case of sp^3 carbon chains, such as polyethylene, the excitation of the σ -bonded electrons will promote electrons from the bonding σ -band to antibonding σ^* -band, in consequence a structural instability is generated. When this process appears, the degradation of the polymer chains occurs due to the fact that the electrons are not in the σ -bonding orbitals for holding the polymer chains together. Consequently, saturated polymers do not have any interesting electronic or optical properties. However, for the case of conjugated polymers, electronic transitions within the π -band does not mean breaking the polymer chain. For this reason, conjugated polymers are photoconductors instead of photoresistors [86].

It is possible to explain the band structure of the polyacetylene using the tight-binding approximation. For the uniform bond length of polyacetylene there is a single π -band which can accommodate $2N$ electron where N is the number of atoms in the polymer chain. Each carbon atom gives one p_z electron, so the π -band will be half-filled, consequently, the polyacetylene would be a metal. After the initial discovery of the metal-insulator transition in polyacetylene a theoretical description was proposed [86]. The construction of the remarkably successful Su-Schrieffer-Heeger (SSH) Hamiltonian was based on two assumptions: the first one is that the π -electronic structure can be treated in the tight-binding approximation with a transfer (hopping) interaction, t_0 sigma orbital and the local electron density through the length of the chemical bonds. The first assumption defines the lowest order transfer energy, which is responsible for the delocalization of the π -electrons along the polymer backbone. The second assumption gives the first order correction to t_0 , also two intuitive terms related to the lattice degrees of freedom: a harmonic "spring constant" term that is the increment in potential energy resulting from displacement from the uniform bond lengths in $(CH)_x$ and the kinetic energy term for the nuclear

motion. These two lattice parameters, coupled to the electronic via the bond-length dependent transfer term, are the origin of the nonlinear excitations of the polymer chain, solitons, polarons and bipolarons.

The SSH Hamiltonian is written as the sum of three terms:

$$H_{SSH} = \sum_{n,\sigma} [-t_0 + \alpha(u_{n+1} - u_n)] (c_{n+1,\sigma}^+ c_{n,\sigma} + c_{n,\sigma}^+ c_{n+1,\sigma}) + \sum_n \frac{P_n^2}{2m} + \frac{1}{2} K \sum_n (u_{n+1} - u_n)^2, \quad (3.1)$$

where $c_{n,\sigma}^+$ and $c_{n,\sigma}$ are the fermion creation of annihilation operators for site n and spin σ , P_n are the nuclear momenta, u_n are the displacements from the equilibrium, m is the carbon mass, and K is an effective spring constant of the σ -bond. The first term is the contribution to the electronic structure, and the second and the third terms are related with the vibrations of the nuclei respect to their equilibrium position. In the tight-binding approximation of the π -electron band structure, one assumes that the wavefunctions are linear combinations the p_z -orbitals, that there is a transfer or hopping interaction with magnitude, $-t_0$, that transfer an electron on site n to near neighbors sites $n \pm 1$, and that all contributions to the wavefunction from other atomic orbitals (such as the sp^2 atomic orbitals) can be neglected. To neglect the contribution from the sp^2 orbitals requires that $t_0/\Delta E_{\pi-\sigma} \ll 1$, where $\Delta E_{\pi-\sigma}$ is the $\pi - \sigma$ energy difference (the difference between energy of the non bonded P_z , the σ -bond and the σ^* -bond) an assumption that is consistent with the basic $\sigma - \pi$ orthogonality. The transfer energy arises from the attractive interaction between an electron on a carbon atom at site n along the chain and the nucleus of the carbon atom at site $n \pm 1$. Thus, the magnitude of $-t_0$ is roughly proportional to the ionization potential of the carbon atom, I_p . Since the ionization potential arises from the attraction of the electron to the nucleus of the same site, $-t_0$ is approximately $-2I_p$ time the overlap of the wavefunctions on close sites, that is:

$$t_0 \approx 2I_p S, \quad (3.2)$$

where $S = \langle n | n \pm 1 \rangle$ represents the overlap of the π -electron wavefunctions on the site n and the site $n \pm 1$. The factor 2 arises from the fact I_p has two contributions, potential energy and kinetic energy. For polyacetylene, electron energy loss measurements of the band dispersion yield $t_0 \approx 3$ eV. Since $I_p \approx 5$ eV, the implied overlap of the wavefunctions is relatively large, $S = \langle n | n \pm 1 \rangle \approx 0.3$. Thus, there is a strong tendency toward delocalization of the electrons along the conjugated chain of carbon atoms. The magnitude on the transfer interactions is strongly dependent of the distance between successive carbon atoms, that is:

$$S \sim \exp\{-[(a \pm \delta)/r_\pi]\} = S_0 \pm \alpha \delta + \text{terms of order } \delta^2, \quad (3.3)$$

where r_π is the effective radius of the p_z wavefunction, δ is the magnitude of the change in bond length ($a \rightarrow a \pm \delta$) and α is a constant. To include this coupling of the electronic structure to the molecular structure in the SSH Hamiltonian, the transfer term to include the bond-length dependent hopping interaction from site n to $n + 1$:

$$t_{n,n+1} = t_0 + \alpha(u_{n+1} - u_n), \quad (3.4)$$

where u_n is the displacement from equilibrium of the n the n^{th} carbon atom. This effectively couples the electronic states to the molecular geometry, giving the electron-phonon (el-ph) interaction term where α is the el-ph coupling constant. The precise form of $t_{n,n+1}$, in which the dependence of the hopping energy on the C-C distance is linearized for small deviations about t_0 , is then in a Taylor expansion. The bond-length dependence of the transfer energy is an essential feature of the description of conjugated polymers since the ground state bond alteration makes the hopping interaction across double bonds larger than the corresponding hopping interaction across the single bonds. Let us consider first only the tight-binding terms which describe the electronic structure of a $(\text{CH})_N$ chain with uniform bond lengths:

$$H_{TB} = -I_p \sum_{n,\sigma} [c_{n,\sigma}^\dagger c_{n,\sigma}] + t_0 \sum_{n,\sigma} [c_{n+1,\sigma}^\dagger c_{n,\sigma} + c_{n,\sigma}^\dagger c_{n+1,\sigma}], \quad (3.5)$$

where $c_{n,\sigma}^\dagger$ and $c_{n,\sigma}$ are the creation and annihilation operators for electrons on site n with spin σ (up or down) and $|\langle c_{n,\sigma}^\dagger c_{n,\sigma} \rangle|^2 = 1$, the average number of electrons per site in $(\text{CH})_N$ (N is the number of atoms in the chain). The tight-binding terms are readily diagonalized by Fourier transformation to k -space:

$$c_{n,\sigma}^\dagger = (1/Na)^{1/2} \sum_n e^{-ikn} c_{k,\sigma}^\dagger, \quad (3.6)$$

$$c_{n,\sigma} = (1/Na)^{1/2} \sum_n e^{-ikn} c_{k,\sigma}, \quad (3.7)$$

where $k=0, \pi/Na, 2\pi/Na, \dots, \pi/a, |\langle c_{n,\sigma}^\dagger c_{n,\sigma} \rangle|^2 = 1$. The Hamiltonian is given by:

$$H = \sum_{k,\sigma} [-I_p + (1 - 2 \cos ka)] c_{k,\sigma}^\dagger c_{k,\sigma}, \quad (3.8)$$

and the π -electron energies are given by:

$$E_\pi = \langle H \rangle = -I_p + (1 - 2 \cos ka), \quad (3.9)$$

where the energy is measured with respect to the vacuum. Figure 3.4 shows the band structure of the uniform chain.

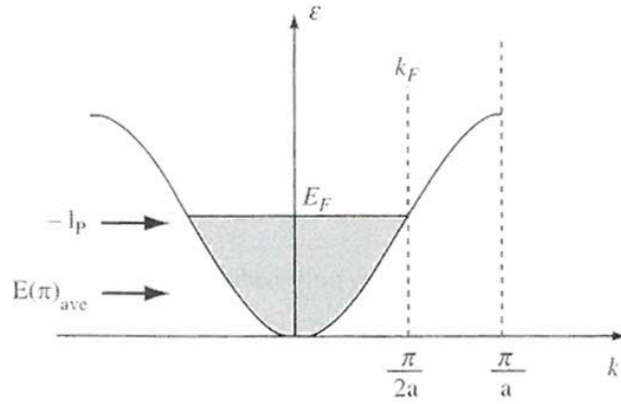


Figure 3.4 Tight-binding band structure of the uniform chain $(\text{CH})_N$. Reprinted from [86] with permission of Oxford University Press.

In the tight-binding approximation, the π -electron band structure of the uniform chain is a single band centered at $-I_p$ with a total bandwidth of $W = 4t_0$. The average energy of the π -electrons, $E(\pi)_{ave}$ (the average of the occupied states in Figure 3.4) in the metallic uniform $(\text{CH})_N$ chain is well below the center of the π -band.

Although the π -electrons in polyacetylene are delocalized along the polymer chain, this polymer is not a metal. The polymerization of acetylene produces a dimerized structure (bond alternating). The final polymer is insoluble and intractable. For this reason, the molecular weight cannot be directly measured. The molecular structure of polyacetylene has been shown in Table 3.1, this polymer has alternating single and double bonds that are, respectively, longer and shorter than the equilibrium value of the bond length in uniform $(\text{CH})_N$. In this structure, the π -electrons on neighboring carbon atoms form weaker and stronger $\pi - \pi$ bonds resulting in the bond alternating structure. The length of the alternating bonds can be determined experimentally using XRD and NMR. The resulting length for the shorter bond is 1.35 Å while for the longer bond is 1.45 Å. This alternating structure doubles the unit cell and consequently, a gap in the electronic structure is opened. For this reason, pristine polyacetylene is a semiconductor. Taking this into consideration, the SSH Hamiltonian reduces to

$$H = \sum_{n,\sigma} [-t_0 + \alpha(u_{n+1} - u_n)] (c_{n+1,\sigma}^+ c_{n,\sigma} + c_{n,\sigma}^+ c_{n+1,\sigma}) \quad (3.10)$$

where $u_n = \langle u_n \rangle = (-1)^n u$. Thus, $t_n = t_0 + (-1)^n 2\alpha u = t_0 + (-1)^n \Delta$, and

$$H = \sum_{n,\sigma} [-t_0 \pm \Delta] (c_{n+1,\sigma}^+ c_{n,\sigma} + c_{n,\sigma}^+ c_{n+1,\sigma}). \quad (3.11)$$

Diagonalization of the SSH Hamiltonian for dimerized $(\text{CH})_N$ produces a band structure as shown in Figure 3.5. Trans- $(\text{CH})_N$ is a semiconductor with energy gap $E_g = 2\Delta_0$.

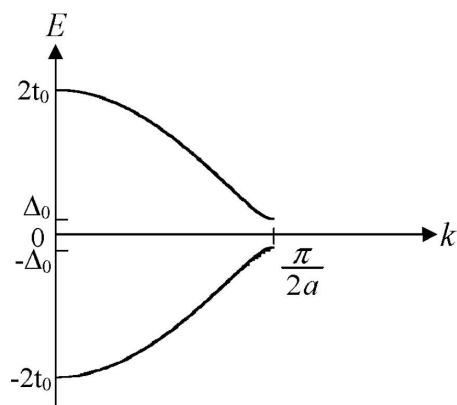


Figure 3.5 Tight-binding band structure of dimerized $(\text{CH})_N$. Reprinted from [86] with permission of Oxford University Press.

The energy versus wave number (k) is given by:

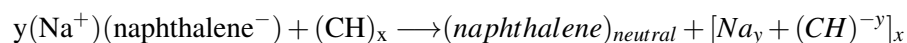
$$E_k = \pm \sqrt{\epsilon_k^2 + \Delta^2}, \quad (3.12)$$

where $\epsilon_k a = 2t_0 \cos ka$. In the traditional terminology of condensed matter, the π -band corresponds to the valence band and the π^* -band corresponds to the conduction band. All the states in the π -band are filled while the states in π^* -band are empty.

3.1.3 Doping in conducting polymers

For the polyacetylene molecule the gap is around 1.7 eV, so pristine polyacetylene presents not metallic behavior. In general, the conductivity of pristine polyacetylene is similar to very low doped semiconductors. The existence of relative low energy π -bonds into the polymer backbone creates the possibility of doping. It is possible to achieve this doping through electron acceptors molecules (oxidants). The electrons are transferred from the polymer backbone to the dopant, a fact that produces charge carriers (holes) and the electrical conductivity is increased, that is called chemical doping by charge transfer. An example of this phenomenon is the doping of polyacetylene with iodine. The dopant oxidizes the polymer chains removing electrons from the conjugated π -bond and increasing the conductivity until very high values, around 10^4 S/cm [84]. At very high doping levels there is a finite density of metallic states at the Fermi level, indicated by the presence of a temperature-independent Pauli susceptibility [87] and a linear electronic specific heat [88]. Then, the conductivity reaches very high values [89].

For the case of n-type doping, a reduction agent has to be used. An example of this is the following reaction [90]:



In this case, the naphthalene anion is the reducing agent and Na^+ is the counter-ion. In both cases, oxidative and reductive doping, mobile charges (charge carriers) are introduced in the π -electronic structure of the polymer chain. These charges are compensated by the counter-ions that diffuse into the polymer chains, the doped conducting polymers are similar to ionic salts.

Another method for doping conducting polymers is the electrochemical doping process. This doping is carried out in a three electrode cell with an electrolyte solution as shown in Figure 3.6. The conductive polymer is the working electrode where the oxidation/reduction process occurs. Generally, a platinum wire is the counter electrode and Ag/AgCl is the reference electrode.

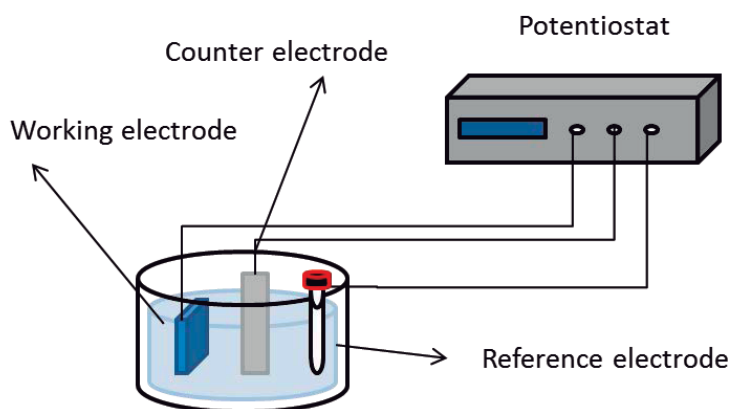


Figure 3.6 Scheme of the electrochemical cell.

The conjugated polymer is oxidized or reduced by the electrode and the counter-ion moves from the electrolyte into the polymer, again diffusing into the structure between chains. At high voltage, the chemical potential moves down in energy until the top of the π -band. When the chemical potential attains the top of the π -band, the oxidation process occurs, consequently, the counter-ion neutralizes this charge in the polymer chain. This fact generates a p-type semiconductor. When the voltage is negative, the chemical potential moves until the bottom of the π^* -band. When the potential achieves the π^* -band, the conducting polymer is reduced due to the incorporation of electron to the π^* -band. The negative charge is neutralized by cations from the electrolyte. This reduction process produces n-type semiconducting behavior in the conducting polymer.

Another kind of doping in semiconducting polymers can be the photoinduced doping. When the polymer is excited, an electron can go from the filled π -band to an empty π^* -band, it can be

considered as a local reduction and oxidation process. The photoexcitation can generate mobile charges producing negative and positive polarons. For this reason, conducting polymers can be photoconductive materials [86]. The photoinduced polarons can be in the same polymer chain or in a separated polymer chain by interchain electron transfer [86].

Controlling the doping in conducting polymers is very important in order to achieve the maximum thermoelectric efficiency. Figure 3.7 shows the evolution of electrical conductivity, See-

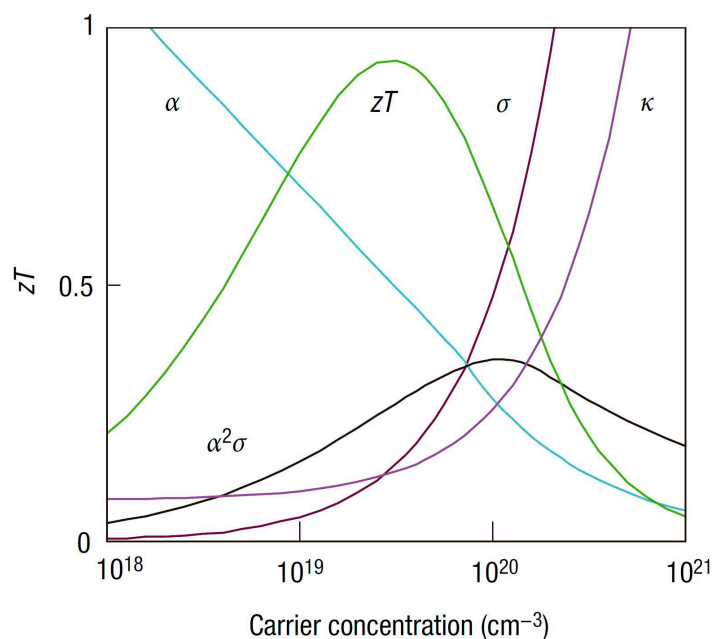


Figure 3.7 Electrical conductivity (σ), Seebeck coefficient (α), thermal conductivity (κ), PF and ZT as a function of the carrier concentration. Reprinted from [9] with permission of NPG.

beck coefficient, thermal conductivity, PF and ZT as a function of the carrier concentration for a semiconductor material such as Bi_2Te_3 . The electrical and thermal conductivities increase while the Seebeck coefficient decreases with the carrier concentration. Given these evidences it is very important to find the best compromise between the electrical conductivity, Seebeck coefficient and thermal conductivity, in order to get the maximum thermoelectric efficiency.

3.1.4 Electronic states of conducting polymers (solitons, polarons and bipolarons)

In order to understand the doping levels of conducting polymers, it is very important to know the possible electronic states that can be generated during the doping process. Considering polyacetylene, the most simple conducting polymer, it is possible to get two equivalent phases, depending on the position of the double bond, as it is shown in Figure 3.8. Now, imaging a polyacetylene chain with both phases on the same polymer chain, the resulting structure will contain a topological defect. This defect shown in Figure 3.8 has the properties of a soliton. The

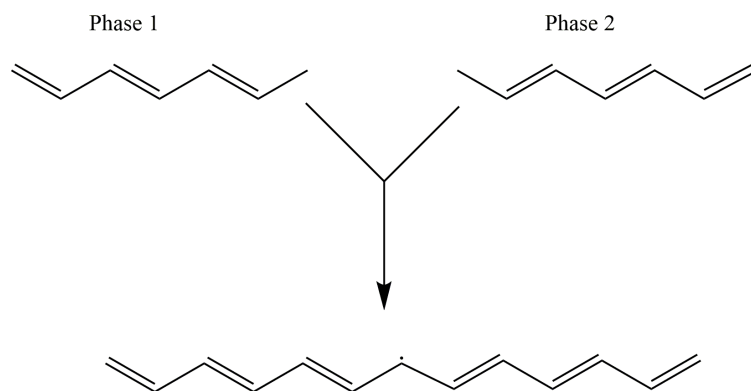


Figure 3.8 Structure of a soliton on a polyacetylene chain.

link between both phases is a neutral radical. The site of the radical there is no π -bond. As a result, the fourth electron is unpaired and exists in a nonbonding state. The unpaired electron is located in a nonbonding state at the center of the energy gap. Also, this electron is delocalized over several carbon atoms. The structural distortion generated, produces a change in the local electronic potential. This change leads to the formation of an electronic state in the energy gap called the "midgap" state [86]. The midgap state can be occupied by zero, one or two electrons. Figure 3.9 shows the band diagram of the left neutral soliton, center positive soliton

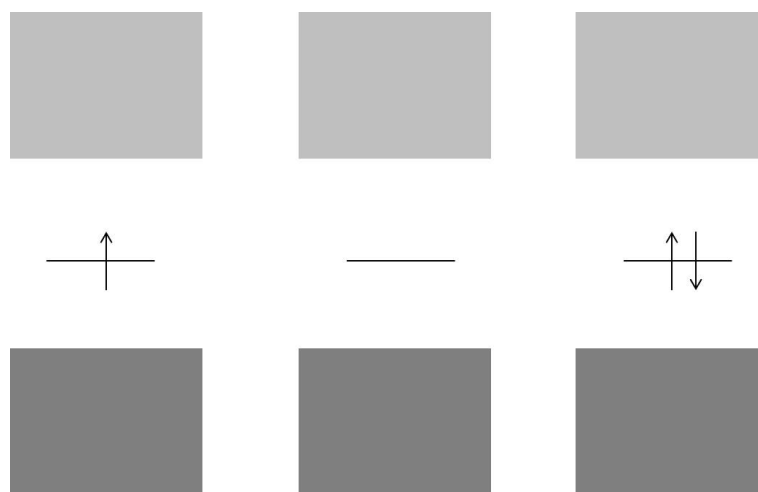


Figure 3.9 Band scheme of the midgap state associated with the soliton. Left neutral soliton, center positive soliton and right negative soliton.

and right negative soliton. When the midgap state is singly occupied, the soliton has zero charge and unpaired spin. The electron can be removed of the polymer chain by oxidation creating a positive soliton. The positive soliton has charge $+e$ and zero spin. Other option is to add an electron by a reduction process. This fact creates a negative soliton with a charge $-e$ and zero spin.

When two neutral solitons are attracted, because of the confinement energy, the electronic wave-functions overlap and two new bonding/antibonding pairs appear. As a consequence the energy

diagram has two states symmetrically placed between the band gap as shown in Figure 3.10.

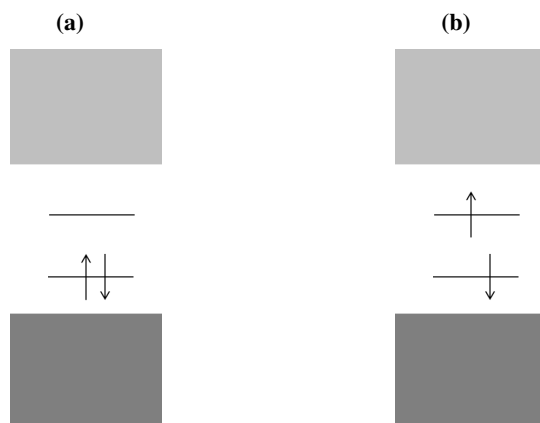


Figure 3.10 Bonding and antibonding pair of gap states associated with confined soliton pairs. (a) Lower gap doubly occupied and (b) two states occupied with electrons with a different spin.

The configuration shown in Figure 3.10(a) is unstable because the double occupied state is located close to the top of the π -band and the distance between the polarons approaches zero. That fact makes this configuration to disappear and the gap states to vanish. However, the configuration shown in Figure 3.10(b) where the two states are occupied, can be stable for the case of excited conjugated polymers.

Considering the combination of two solitons again, however one of them is a charged soliton, appears a stable "polaron". The polaron is a confined soliton pair with negative or positive charge and with spin 1/2. Figure 3.11 shows the energy structures of the polaronic states of poly-*p*-phenylene (PPP). When a soliton pair is combined, both having the same charge, that

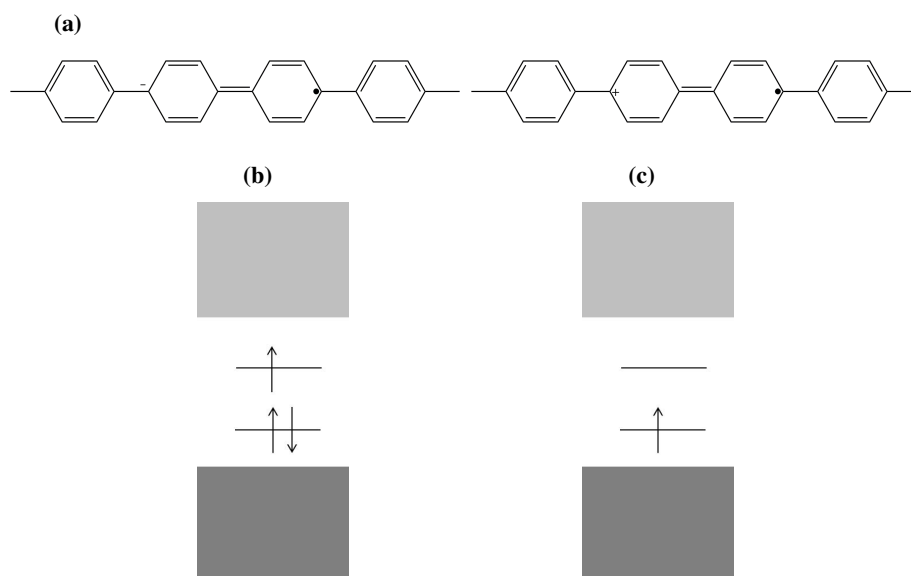


Figure 3.11 (a) Molecular structure of negative polaron (left) and positive polaron (right) in PPP. Electronic structures and gap state occupancies of the (b) negative polaron and (c) positive polaron.

means positive combined with positive or negative with negative, is called "bipolaron". Figure 3.12 shows the energy structures of the bipolaronic states of PPP. The charge of the bipolarons

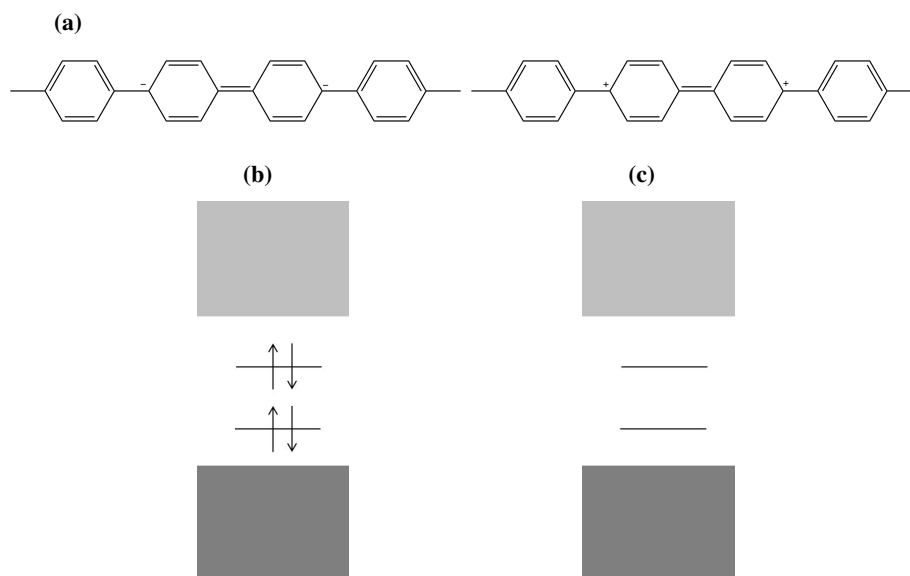


Figure 3.12 (a) Molecular structure of negative bipolaron (left) and positive bipolaron (right). Electronic structures and gap state occupancies of the (b) negative bipolaron and (c) positive bipolaron.

can be +2 or -2 and the spin is always 0. In general, during the doping process in the conducting polymer these electronic states appear. The electrical conductivity and the Seebeck coefficient are strongly dependent on these states. For this reason, if the number of bipolaronic states in the polymer material is high, the polymer will be in high oxidation level, that means high doping level, as consequence the electrical conductivity will be very high and the Seebeck coefficient will be very low. Thus, it is very important to find methods and mechanisms in order to control the doping level of the conducting polymer (polaronic and bipolaronic states).

The presence of polarons in conducting polymers can be determined by spectroscopic techniques such as electron spin resonance and, in the case of bipolarons, through Uv-Vis measurements.

3.1.5 Secondary doping in conducting polymers

Conducting polymers are structured in domains depending of the interaction between the polymer chains, consequently there are high ordered and disordered regions. That fact produces a high anisotropy in the electrical conductivity, because the high ordered regions are more conductive than the disordered ones. For this reason, there is another kind of doping in polymers called secondary doping. This doping is not electronic, it is related to the polymer chain conformation. Polymer conformation may play an important role in its physical properties, in particular in the conductivity. The electron-hole interaction leads to strongly bonded excitons (Frenkel excitons), which greatly affects the transport properties in conducting polymers. The electronic transport

is traditionally explained by the charge-energy-limited-tunneling model, proposed originally for highly disordered conducting polymers [71, 72] (for low electric fields, the voltage and the current are not proportional, since there is carrier injection). Amorphous polymer chains adopt a random coil conformation. The electrical conductivity of a random coil is lower than that of an extended coil/linear conformation (see Figure 3.13). Thus, the control of the polymer conformation is crucial to improve the electrical conductivity in order to obtain a high thermoelectric efficiency.

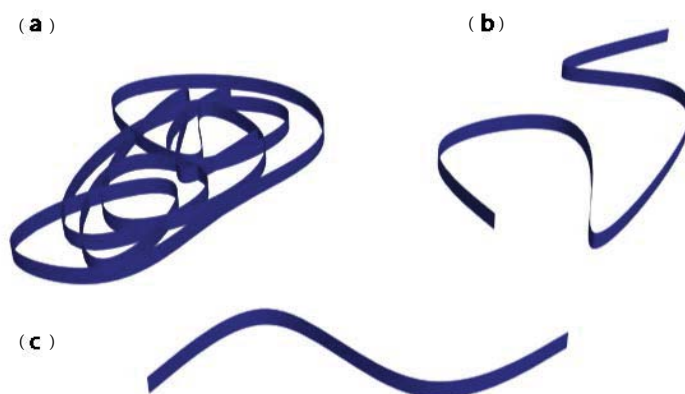


Figure 3.13 (a) Coil conformation, (b) extended coil conformation, and (c) linear conformation.

3.1.6 Nanostructuration in conducting polymers

Since the discover of the thermoelectric phenomenon by Thomas Johann Seebeck in 1821, materials such as Bi_2Te_3 have been used in thermoelectric applications. In the 50s thermoelectric materials have become very important in the development of thermoelectric generators for aerospace applications. However, values of ZT were close to 0.5. At this time, whatever project with the objective to increase the ZT until values higher than 1 would be rejected automatically. However, once the work of Hicks and Dresselhaus was published in 1993, something changed [13]. They showed a path to increase the thermoelectric efficiency of a semiconductor: the reduction of the dimensionality [13]. Following their ideas, semiconductor superlattices such as $\text{Bi}_2\text{Te}_3/\text{Sb}_2\text{Te}_3$ [16] semiconductors alloys like PbSeTe [17] or, more recently, SiGe [18] have been shown to have ZT values around 2. In the last years, the reduction of the dimensionality in Si by growing it in the form of nanowires has proven to be an effective way to decrease the phonon thermal conductivity. Si nanowires with rough surfaces favor a further decrease of the thermal conductivity by the appearance of back-scattering phonon processes. Since S and σ are somehow related in semiconductors, [91], the engineering to decrease κ is the most effective tool to increase ZT [92]. In spite of the efforts to increase ZT in inorganic materials, it seems

that the limit in the case of superlattices is of the order of 2, and there are no advances in the fabrication of TEG based on nanowires in the last years. In comparison with bulk, in nanostructured materials, the density of electronic states usually has sharp peaks and theoretically a large Seebeck coefficient can be reached if the Fermi level is located around a maximum in the electronic density of states. Also, the phonon dynamics and heat transport in a nanostructured system can be tailored.

These ideas also can be used for organic materials such as conducting polymers to obtain better properties compared with bulk materials. First of all, it has to be investigated synthetic methods to nanostructure conducting polymers. Currently, there are two kinds of methods to fabricate polymer nanostructures: top-down and bottom-up methods [93–96]. The top-down method is based on the reduction of components and structures from highest to lowest sizes. This type of nanotechnology is the most developed until now and also the most used in the field of electronics, since it is very powerful in the miniaturization of electronic components. In this method highlight the techniques called optical lithography and electron-been lithography [97]. The methods based in bottom-up techniques consist of the development of the nanostructures from the lowest to highest size. For example, the process can start form a molecule and with assembling reactions it is possible to generate a larger structure. This type of nanotechnology allows to create and control the size and the morphology in a very precise way. A process called polymerization facilitated by templates has been employed in this PhD thesis. Based on the nature of the template employed during the synthesis, there are two kinds of methods: soft and hard template. The nanostructuring by the soft template method is given under the presence of surfactants. In general, these systems are composed by two different phases, as shown in

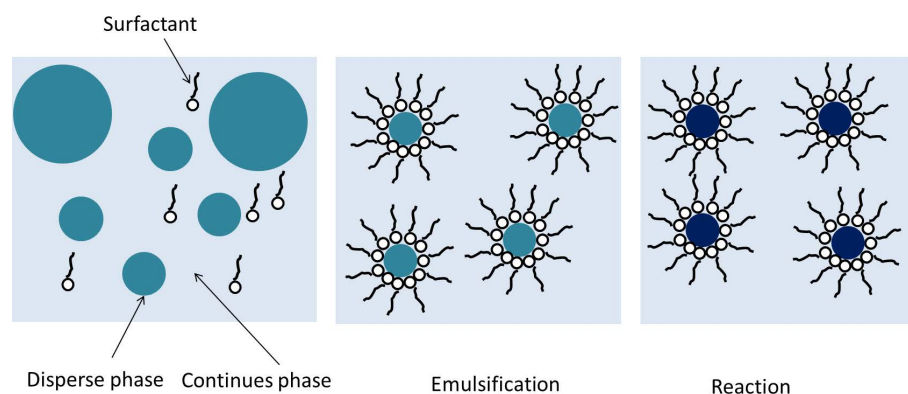


Figure 3.14 Scheme of a reaction using the soft template method.

Figure 3.14. One is the majority phase denoted as the continuous phase and the other one is the minority phase, called as the disperse phase (in the case of polymerization reaction is the monomer). The other component is the surfactant that can be anionic, cationic or not ionic. All the components are mixed together in order to create an emulsion, consequently, the disperse phase forms small drops, stabilized by the surfactant. The size of the the drops can be from 10

nm to 100 μm . Finally, the initiator of the reaction is added to the emulsion in order to start the reaction, which occurs inside of the drops. At the end, a nanostructured material is generated. In terms of emulsion polymerization, there are three types: macroemulsions, miniemulsions and microemulsions. The main differences between these processes are the size and the stability of the droplets. For the case of macroemulsions, the droplet size is around 1-100 μm and low stability is observed, only several minutes. The miniemulsions are characterized by a droplet size between 50-500 nm and a high stability from days or months. In general, ultrasounds or homogenizers are needed to achieve miniemulsions. Finally, microemulsions are translucent with a droplet size around 10-100 nm, and they are thermodynamically stable.

The hard template method is based on the synthesis of nanostructures inside the channels of a rigid template [98]. Anodized alumina membranes (AAOM) are the most common material used as a rigid template, since it is very easy to control the thickness and the pore diameter of the channels changing the experimental conditions. This method allows manufacturing quasi-one-dimensional nanostructures such as nanotubes, nanowires and nanorods with a relatively low cost and high versatility in terms of diameter and length. Figure 3.15 shows the pores structure

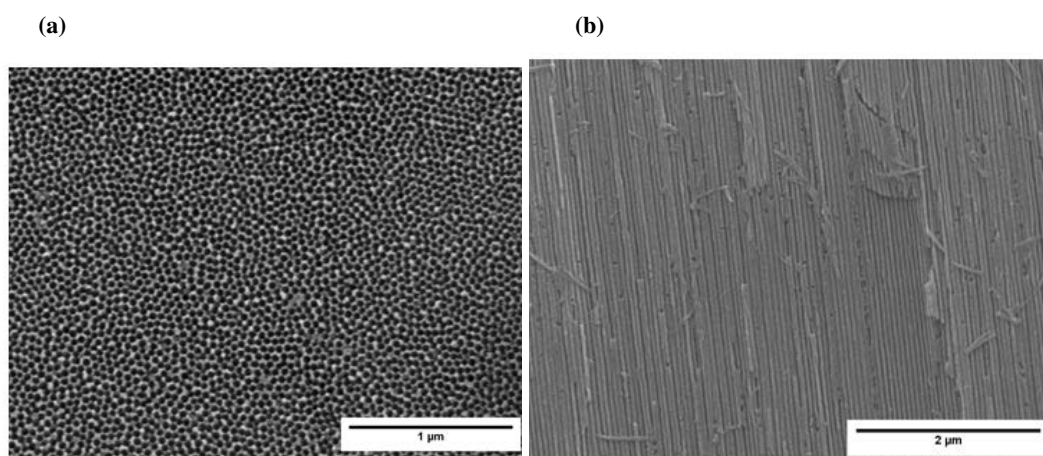


Figure 3.15 SEM images of AAOM: (a) top view and (b) cross section.

of one AAOM. The pores are parallel between them and the diameter of the channels is in the nanoscale range. Considering conducting polymers, the nanostructuring using these templates can be very simple by electrochemical polymerization [99]. In general, the electrochemical polymerization occurs over the surface of the working electrode, if the working electrode is the alumina template the polymerization will be inside the channels, producing a polymeric material with a nanowire shape. The use of AAOM as a working electrode requires an electrically conductive surface. For this reason, the bottom of the AAOM is covered by a metallic layer for example gold. Finally, the metallic layer, is connected to the potentiostat and dipped into the electrochemical solution. With this configuration, the polymerization only is carried out inside of the channels of the template. After the reaction, just removing the template, the nanostructures

are generated in a nanowire shape. The diameter of the nanowire will be given by the diameter of the AAOM pore and the length will be given by the time of polymerization and the thickness of the AAOM.

3.2 Effect of the addition of dimethylsulfoxide on the thermoelectric properties in PEDOT:PSS solutions

3.2.1 Materials

The materials used in this study were: PEDOT:PSS solution, 1.3% wt dispersion in H₂O content in PEDOT 0.5% wt and content in PSS 0.8% wt obtained from Sigma Aldrich (Madrid, Spain). Dimethylsulfoxide (98%) was purchased from Sigma Aldrich (Madrid, Spain). Microscope slides were obtained from Fisher Scientific (Madrid, Spain).

3.2.2 Preparation of PEDOT:PSS films in presence of DMSO

The films were prepared by adding DMSO to the commercial solution of PEDOT:PSS in a proportion of 5 % wt and 10 % wt. The mixture was magnetically stirred during 24 h. Finally, the solution was dropped on a glass slide (2.7×4.0 cm) and the solvent was evaporated at 60°C in vacuum during 4 h. After the films formation, six electric contacts were made on the film surface, for electrical measurements.

3.2.3 Morphology of PEDOT:PSS films

Figure 3.16(a) and (b) shows the SEM images of PEDOT:PSS films. The surface of the films after solvent evaporation was completely flat and homogeneous. The surface of PEDOT:PSS was flatter than other conducting polymers synthesized by different methods, for example synthesized by electrochemical polymerization, which typically shows a higher roughness [27, 37]. A possible explanation is that the film is composed also by PSS, the amorphous nature of this polymer, makes possible to achieve a flat surface, typical for insulating polymers films. Figure 3.16(b) shows the cross section of the PEDOT:PSS film. The thickness of the films was in the range of 10-13 μm after solvent evaporation. The films had a dark blue color with a bright surface as it is observed in Figure 3.16(c). The addition of DMSO did not change the morphology of the PEDOT:PSS films.

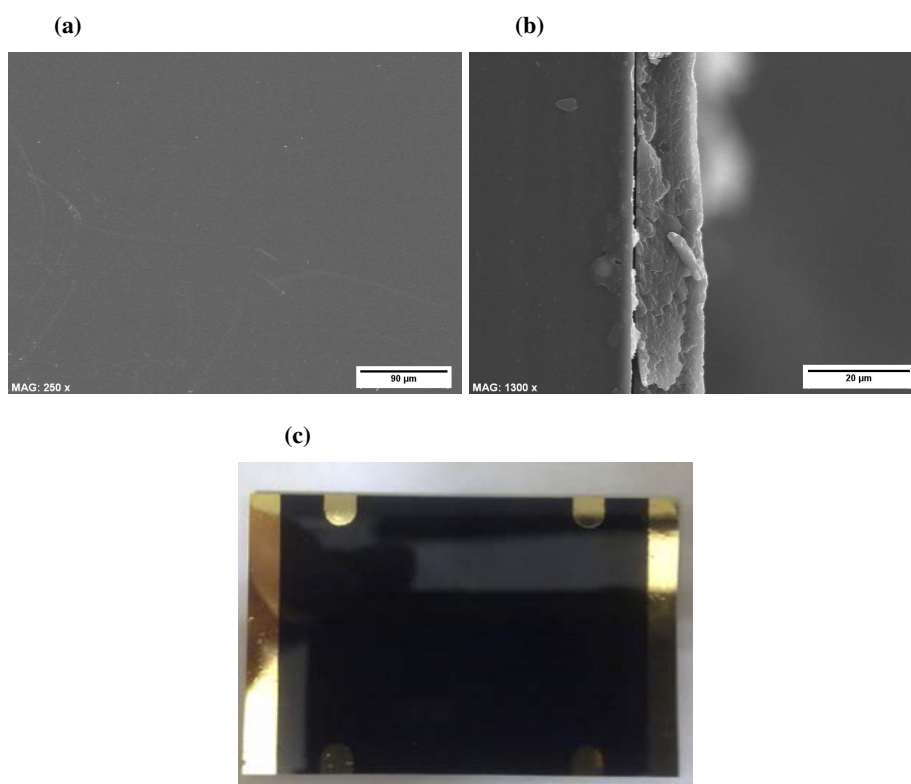


Figure 3.16 SEM images of PEDOT:PSS films (a) top view and (b) cross section. (c) Photograph of PEDOT:PSS film with gold contacts.

3.2.4 Thermoelectric properties of PEDOT:PSS films

Figure 3.17 shows the electrical conductivity of PEDOT:PSS as a function of the DMSO content.

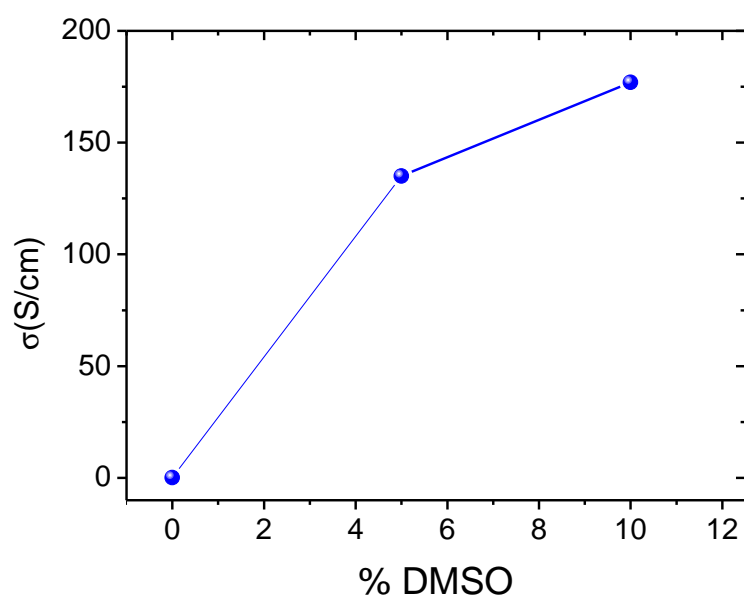


Figure 3.17 Electrical conductivity as a function of DMSO content.

The electrical conductivity increases from 0.14 S/cm to 177 S/cm. This fact means that with the addition of DMSO the electrical conductivity increases more than 1000 times compared to the pristine sample. Considering that DMSO does not have an oxidant power, the electronic doping level of the PEDOT is not affected, so the enhancement of the electrical conductivity is given by other factor. This behavior on the electrical conductivity is related with the secondary doping in conducting polymers [72], previously commented in the introduction. The electrical conductivity increases due to that the polymer chains are more elongated than in the pristine sample. The addition of DMSO to the PEDOT:PSS solution produces a change from the benzoid

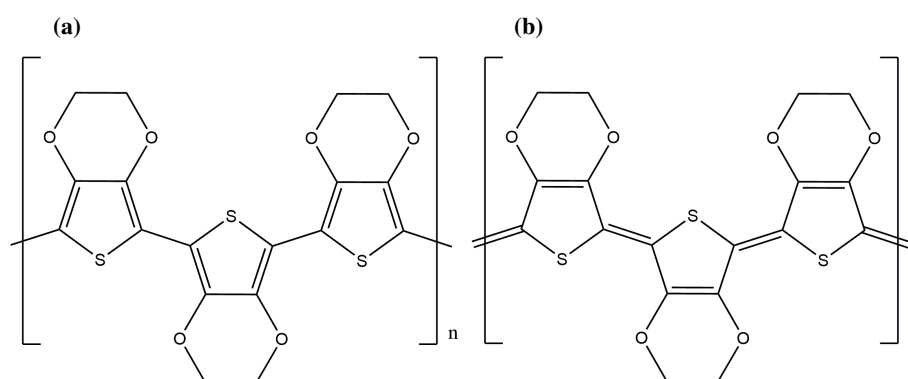


Figure 3.18 PEDOT at (a) benzoid and (b) quinoid conformation.

to the quinoid structure of the PEDOT:PSS chains (see Figure 3.18). The quinoid structure is more rigid than the benzoid structure, consequently the polymer chains change from coil conformation to linear or extended coil conformation, producing an increase in the electrical conductivity.

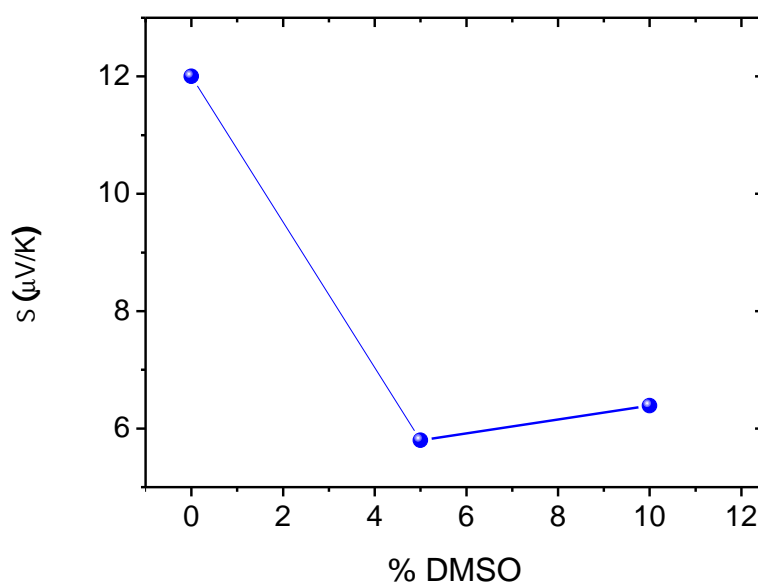


Figure 3.19 Seebeck coefficient of PEDOT:PSS films as a function of DMSO content.

The Seebeck coefficient is plotted in Figure 3.19. The Seebeck coefficient decreases with the addition of DMSO to the polymer solution. The values of the Seebeck coefficient are double in the pristine sample compared with the sample with 5 % of DMSO. The Seebeck coefficient is strongly affected by changes in the carriers concentration, however with the addition of DMSO to PEDOT:PSS solution the carrier concentration is not affected since DMSO is not an oxidant or reducing agent. Probably the increase in the electron mobility can be responsible for the changes of the Seebeck coefficient in this system [72].

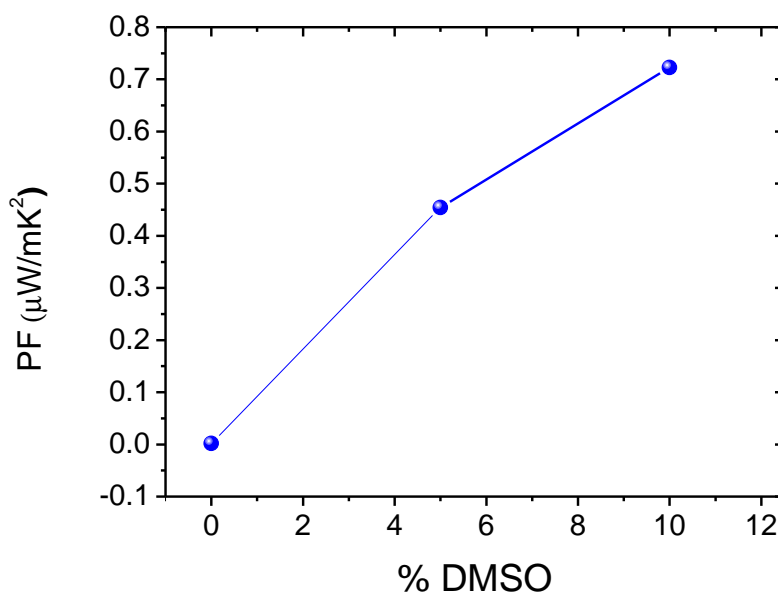


Figure 3.20 Power Factor of PEDOT:PSS films as a function of DMSO content.

The power factor has been calculated from the data of electric conductivity and Seebeck coefficient of the PEDOT:PSS films as a function of DMSO content in PEDOT:PSS solution (See Figure 3.20). The power factor increases from 0.002 to 0.722 $\mu\text{W}/\text{m K}^2$. The value of the PF increases two orders of magnitude with the addition of DMSO to the polymer solution. This increase of the thermoelectric efficiency is mainly dominated by the enhancement of the electrical conductivity due to the secondary doping produced in the PEDOT chains by the presence of polar organic solvents, such as DMSO.

3.3 Effect of the chemical de-doping on PEDOT electrochemically synthesized in presence of different counter-ions ¹

3.3.1 Materials

The reactants used in this study, EDOT, lithium perchlorate (LiClO_4), 1-butyl-3-methylimidazolium hexafluorophosphate, 1-ethyl-3-methylimidazolium bis(trifluoro- methylsulfonyl)imide (BTFMSI) and acetonitrile, were purchased to Sigma Aldrich Co (Madrid, España). Figure 3.21 shows the structure of these molecules.

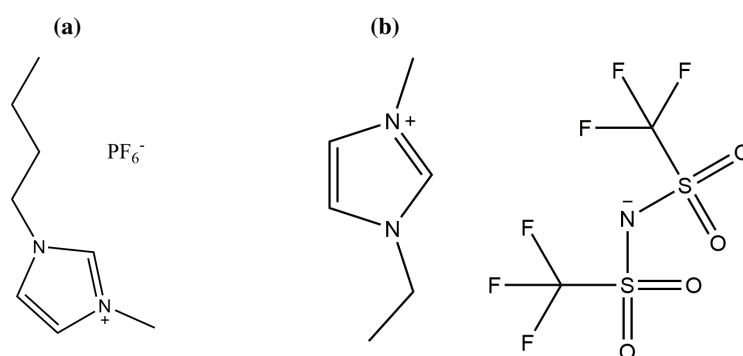


Figure 3.21 Molecular structure of (a) 1-Butyl-3-methylimidazolium hexafluorophosphate and (b) 1-Ethyl-3-methylimidazolium bis(trifluoromethylsulfonyl)imide.

3.3.2 Synthesis of PEDOT films

The films of PEDOT: ClO_4 , PEDOT: PF_6 and PEDOT:BTFMSI were synthesized through electrochemical polymerization on a gold surface (20 nm of thickness) previously deposited on a glass substrate ($2 \times 4 \text{ cm}^2$) by metal evaporation in a Univex 300 Evaporation system. The gold layer was, at the same time, the working electrode. The PEDOT: ClO_4 , PEDOT: PF_6 and PEDOT:BTFMSI were polymerized starting from a 0.01 M solution of EDOT and LiClO_4 0.1 M, 1-butyl-3-methylimidazolium hexafluorophosphate 0.01 M, 1-ethyl-3-methylimidazolium bis(trifluoro- methylsulfonyl)imide 0.01 M, respectively, in 100 mL of acetonitrile at -3 mA versus an Ag/AgCl reference electrode during 2 minutes. Under these experimental conditions, the thickness was 110-120 nm. A Pt grid was used as counter electrode and a Keithley 2400 power supply was employed. The gold layer was removed with an acid solution (HNO_3 : HCl ratio 1:3). The PEDOT derivatives thin films were washed several times with water and finally with

¹This section is based on the publication: "Enhanced thermoelectric performance of PEDOT with different counter-ions optimized by chemical reduction" M. Culebras, C. M. Gomez, A. Cantarero *Journal of Materials Chemistry A*, 26, 10109-10115 (2014)- Reproduced by permission of The Royal Society of Chemistry.

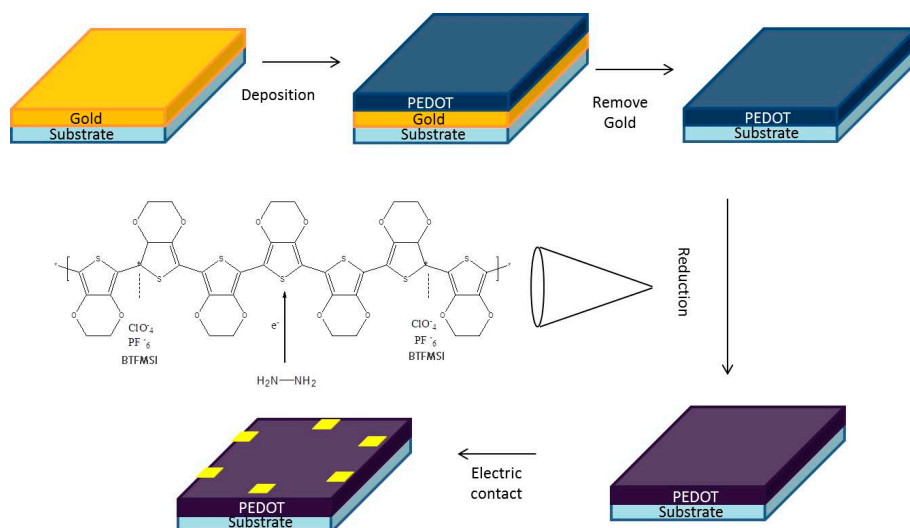


Figure 3.22 Scheme of the sample preparation sequence.

ethanol (with this treatment, the gold layer was removed keeping the polymer integrity and their properties).

The resulting films of PEDOT:ClO₄, PEDOT:PF₆ and PEDOT:BTfMSI were reduced by contact with hydrazine (N₂H₄) vapor during several seconds. In order to guarantee the reproducibility, the procedure was optimized keeping a constant hydrazine steam flow through the film surface, i.e. the film surface was in close contact with the hydrazine vapor. Figure 3.22 depicts a scheme of the polymer surface formation. In order to perform the electrical characterization, six gold contacts were coated on the polymer film surface by thermal evaporation; they were also used for the thermoelectric measurements.

3.3.3 Morphology of PEDOT films

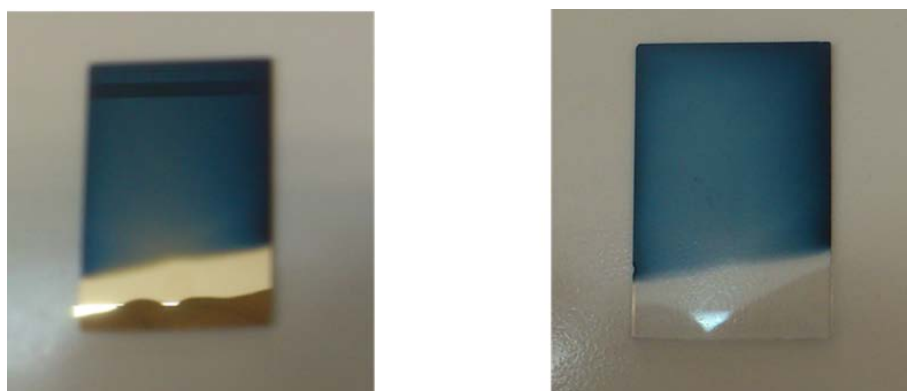


Figure 3.23 PEDOT:ClO₄ with the gold layer (left) and after removing the gold layer (right).

Figure 3.23 shows the polymer film on the glass substrate before and after the gold has been removed. No change in PEDOT appearance has been observed after the acid treatment. The blue

color of the PEDOT film was kept after the treatment, indicating not changes on the oxidation state. In addition, the film integrity was kept without cracks on the film surface.

For the morphological characterization of the film surface, we have used scanning electron microscope. Figure 3.24 shows the scanned (SEM) images of the three film surfaces under study.

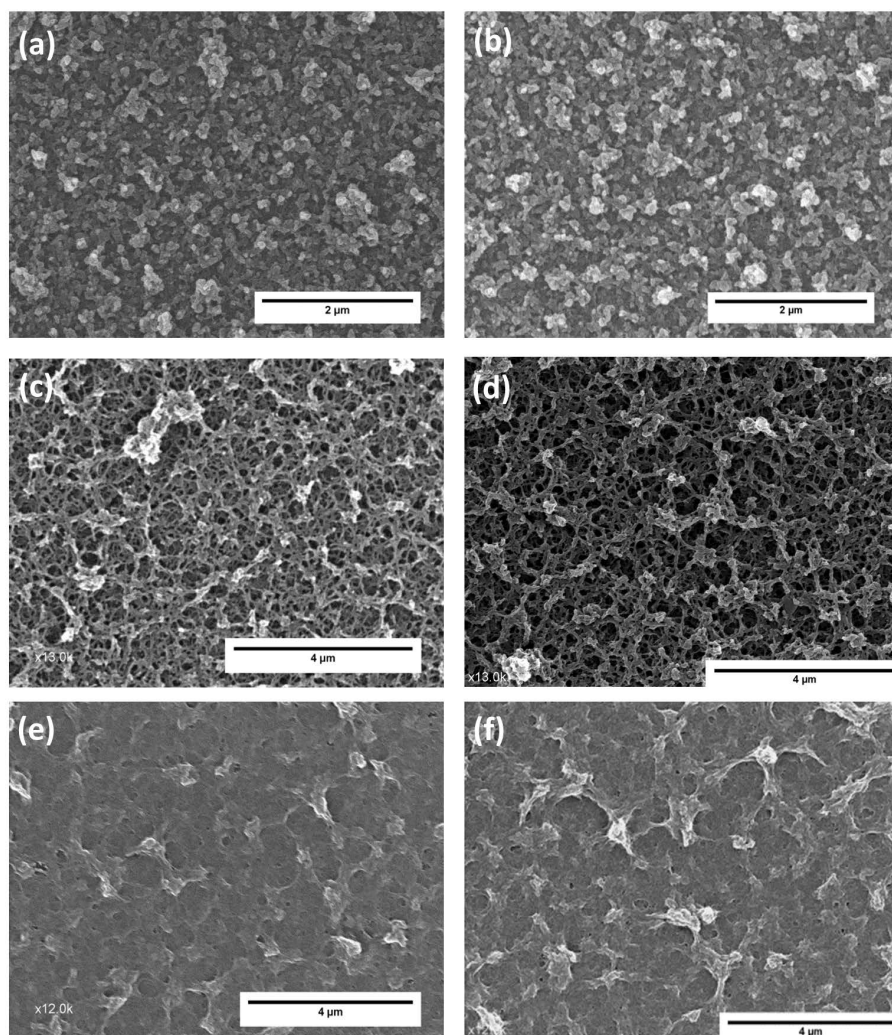


Figure 3.24 SEM images of (a) native PEDOT:ClO₄, (b) PEDOT:ClO₄ after 20s of reduction treatment, (c) native PEDOT:PF₆, (d) PEDOT:PF₆ after 20s of reduction treatment, (e) native PEDOT:BTfMSI and (f) PEDOT:BTfMSI after 20s of reduction treatment showing the different morphologies.

All the films appear to be homogeneous and compact with different roughness degree. Figures 3.24(a) and 3.24(b) (PEDOT:ClO₄) show a very rough surface, with well distinguished globules, homogeneously distributed all over the surface. This film resembles compact with ordered arrangements of cauliflowers-shaped granules, typical of electro-synthesized films. On the other hand, the Figures 3.24(c), 3.24(d), 3.24(e) and 3.24(f) (PEDOT:PF₆ and PEDOT:BTfMSI films) depict a smoother surface of nearly interconnected polymer chains and voids in between [72]. A smoother, more homogeneous and compact polymer film will clearly improve the electrical

conductivity and the electron transfer capability between chains due to a more stretched polymer structure. The reduction treatment does not alter the morphology of the films as shown in Figures 3.24(b), 3.24(d) and 3.24(f).

3.3.4 Spectroscopy measurements of PEDOT films

A Raman study (Figure 3.25) has been performed in the three polymers synthesized in this section in order to analyze the effect of the reduction on the vibrational modes of PEDOT also. The spectra depicts different vibrational modes, at 440, 576 and 990 cm^{-1} , the modes related to the oxyethylene ring deformation; the peak at 691 cm^{-1} corresponds to the symmetric C-S-C deformation; the C-O-C deformation corresponds to the mode appearing at 1100 cm^{-1} ; the $\text{C}_\alpha\text{-C}_\alpha$ (inter-ring) stretching mode is located at 1260 cm^{-1} ; the peak at 1361 cm^{-1} is related to the $\text{C}_\beta\text{-C}_\beta$ stretching; the symmetric stretching mode $\text{C}_\alpha=\text{C}_\beta(-\text{O})$ appears at 1430 cm^{-1} , and the asymmetric stretching of $\text{C}=\text{C}$ splits, as it is well known, into two Raman peaks at 1508 cm^{-1} and 1568 cm^{-1} , respectively. The frequencies of all the modes found in the Raman spectra are given in Table 3.3. These spectra are the indication test that PEDOT has been obtained after the electrochemical synthesis [100]. The normalized signals show a clear increase in the intensity

Table 3.3 Typical vibrational modes of PEDOT.

Raman shift (cm^{-1})	Assignment
440	Oxyethylene ring def
576	Oxyethylene ring def
691	sym C-S-C def
990	Oxyethylene ring def
1100	C-O-C def
1260	$\text{C}_\alpha\text{-C}_\alpha$ (inter-ring) str
1361	$\text{C}_\beta\text{-C}_\beta$ -str
1430	sym $\text{C}_\alpha=\text{C}_\beta(-\text{O})$
1508-1568	asym $\text{C}=\text{C}$ str

of the peaks centered at 1300-1500 cm^{-1} , respect to the background signal, with reduction time. This effect is due to the fact that the neutral segments of PEDOT are more active than the doped segments at the excitation line of 514.53 nm (green). Consequently, when the sample is subjected to the reduction treatment with hydrazine, the number of neutral segments increases, resulting in an increase of the Raman signal. These results are in agreement with the Raman studies of doping in PEDOT previously published by S. Garreau et al. [100, 101].

The UV-Vis-NIR absorption as a function of the reduction time is presented in Figure 3.26(a). The spectra obtained for highly reduced PEDOT: ClO_4 , PEDOT: PF_6 and PEDOT:BTfMSI (25 s of reduction time) show a broad absorption band centered around 600 nm, that corresponds to the $\pi - \pi^*$ transition (valence to conduction transition in a semiconductor), associated with

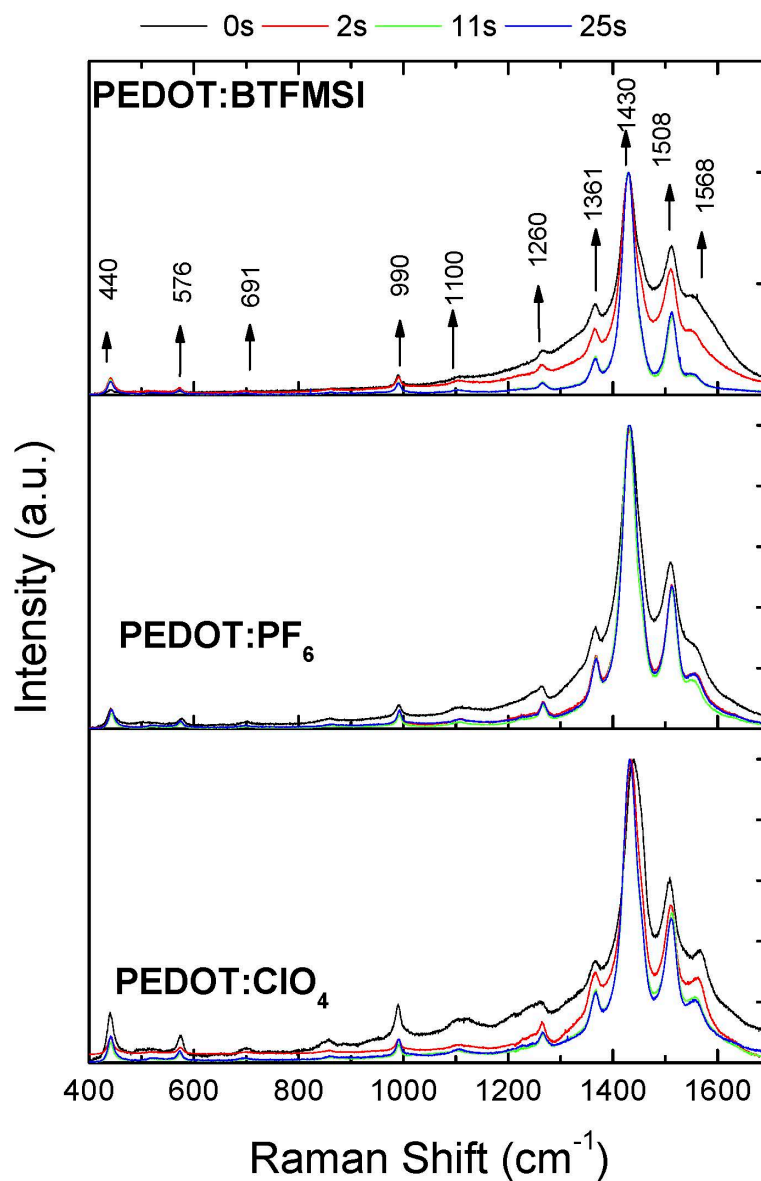


Figure 3.25 Raman spectra of PEDOT:ClO₄, PEDOT:PF₆ and PEDOT:BTfMSI at several reduction times.

the neutral segments in the PEDOT chains [101]. The other band observed in the Uv-Vis-NIR spectra appears around 900 nm. This band is related to the doping process of conducting polymers, actually due to bipolaron and polaron states [102]. The UV-Vis-NIR results indicate a clear influence of the reduction time with the doping level in the three polymers synthesized. In all cases the band centered around 600 nm increases with reduction due to the de-doping process, since they produce an increase of the neutral polymer segments. Also, the high NIR absorption in highly doped samples decreases with the reduction process, and it has been assigned to the decrease of bipolaron states [103].

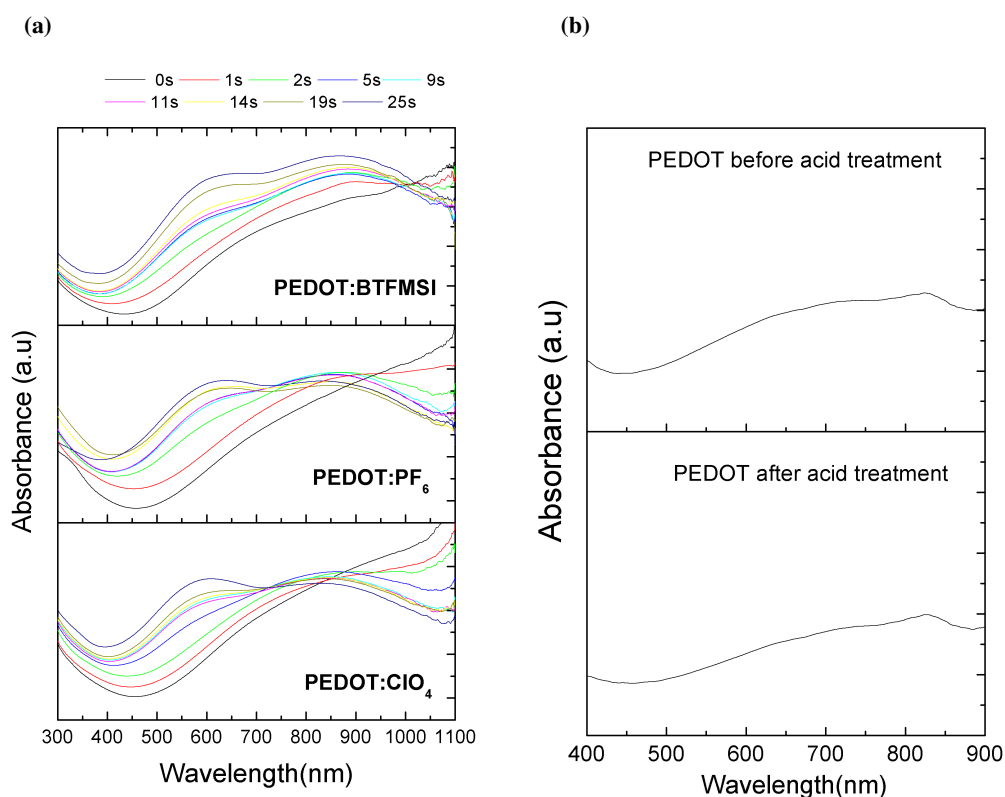


Figure 3.26 UV-Vis-NIRs spectra of: (a) PEDOT:ClO₄, PEDOT:PF₆ and PEDOT:BTfMSI at several reduction times and (b) PEDOT:ClO₄, before and after acid treatment.

Figure 3.26(b) shows the UV-Vis-NIR spectra of PEDOT:ClO₄ before and after removing the gold layer. The shape of the spectrum is conserved after the acid treatment indicating that the oxidation state of the polymer does not change with the acid treatment.

3.3.5 Thermoelectric properties of PEDOT films

Figure 3.27 depicts the values of σ , S and PF , of PEDOT:ClO₄, PEDOT:PF₆ and PEDOT:BTfMSI films as a function of the chemical reduction time. The samples tested using a reduction time up to 2 min, give the same values already obtained with 20 s. As shown in Figure 3.27, the electrical conductivity decreases with the reduction time until reaching a plateau due to the saturation of the doping level. After chemical reduction, the electrical conductivity changes from 753 to 230 S/cm for PEDOT:ClO₄, from 1000 to 312 S/cm in the case of PEDOT:PF₆ and from 2074 to 708 S/cm for PEDOT:BTfMSI. The opposite behavior has been observed in the variation of the Seebeck coefficient with the reduction time. Although the Seebeck coefficient is small, it increases with reduction time: from 9 to 35 $\mu\text{V/K}$ for PEDOT:ClO₄, from 11 to 34 $\mu\text{V/K}$ in the case of PEDOT:PF₆ and from 14 to 42 $\mu\text{V/K}$ for PEDOT:BTfMSI after 25 s of reduction time. These values are higher than those obtained for the PEDOT: PSS ($S \sim 15 \mu\text{V/K}$) [29, 72, 104] but lower than that of PEDOT:Tos (40-700 $\mu\text{V/K}$) [36]. In Figure 3.27, PF has been plotted

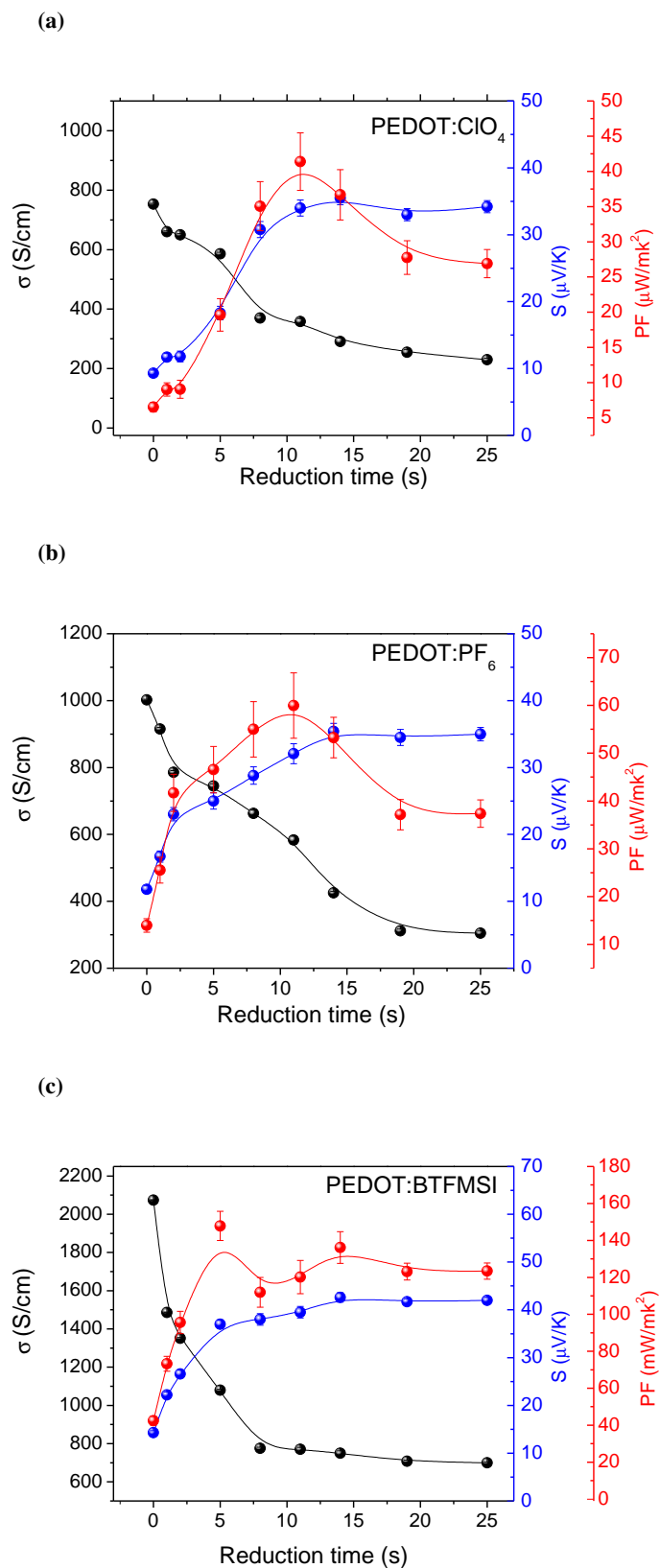


Figure 3.27 Electrical conductivity (σ), Seebeck coefficient S , and power factor (PF), of: (a) PEDOT:ClO₄, (b) PEDOT:PF₆ and (c) PEDOT:BTfMSI, as a function of chemical reduction time.

in order to show the optimum reduction time providing the highest thermoelectric efficiency. Figure 3.27 indicates that the optimum reduction time for the three polymers studied is around 11 s with $PF = 41 \mu\text{W}/\text{m K}^2$ for PEDOT:ClO₄; 11 s with $60 \mu\text{W}/\text{m K}^2$ for PEDOT:PF₆ and 5 s with $147 \mu\text{W}/\text{m K}^2$ for PEDOT:BTfMSI. As reported in the literature, polymeric materials with high doping level show a high electrical conductivity and a low Seebeck coefficient [23, 36]. When the doping level decreases, the Seebeck effect increases while the electrical conductivity decreases. The best compromise is given by the best power factor. PEDOT:ClO₄, PEDOT:PF₆ and PEDOT:BTfMSI are initially oxidized (highly doped). By reducing them with hydrazine, the doping level decreases up to reach the optimum PF. The reduction times, in our case, are of the order of a few seconds since we are dealing with undiluted hydrazine. These results are very exciting when compared with other conducting polymers [34, 105]. The electrical conductivity obtained for PEDOT:ClO₄, and PEDOT:PF₆ is very similar when compared with PEDOT:PSS doped with DMSO [24] (800-1000 S/cm), but in the case of PEDOT: BTfMSI is relatively high and of the same order of magnitude than PEDOT:Tos (2120 S/cm) [23]. The polymer conformation may play an important role in its physical properties, in particular in the conductivity. The electron-hole interaction leads to strongly bonded excitons (Frenkel excitons), which greatly affects the transport properties in conducting polymers. In the case of PEDOT, the electronic transport is traditionally explained by the charge-energy-limited-tunneling model, proposed originally for highly disordered conducting polymers [71, 72].

Looking at Figure 3.24 and the evolution of the electrical conductivity in the three polymers, clearly a great change from a typical coil conformation to a linear or expanded-coil conformation takes place in the presence of different counter-ions or dopants. The evolution of the chain conformation in presence of different counter-ions increases the compactness of the films, producing an increase of the electrical conductivity. Thus, the increasing order in the electrical conductivity (PEDOT:BTfMSI > PEDOT:PF₆ > PEDOT:ClO₄) is strongly related with the conformation of the PEDOT chains caused by the increase in the size of the three counter-ions used as shown schematically in Figure 3.28 .

In general, amorphous polymers adopt a random coil form. Thus, small anions such as perchlorates may lie smoothly neutralizing the positive charges of the chain, without modifying the coil structure. The increase in counter-ion size produces an extension of the polymer chain due to electrostatic interaction. An extended chain is more favorable for the neutralization of the positive charges of PEDOT by the BTfMSI anions, leading to an increase of the electrical conductivity. The fact that the extended chains are more conductive than random coil chains is well known in the literature. For example, PEDOT:PSS doped with DMSO or EG and PANI doped with m-cresol [72, 106]. The thermal conductivity of PEDOT samples has been measured using a MDSC system according to the ASTM E1952-11 standard. The values obtained at 25 °C were $0.35 \pm 0.02 \text{ Wm}^{-1}\text{K}^{-1}$ for PEDOT:ClO₄, $0.22 \pm 0.02 \text{ Wm}^{-1}\text{K}^{-1}$ for PEDOT:PF₆ and $0.19 \pm 0.02 \text{ Wm}^{-1}\text{K}^{-1}$ for PEDOT:BTfMSI. We have checked that the thermal conductivity

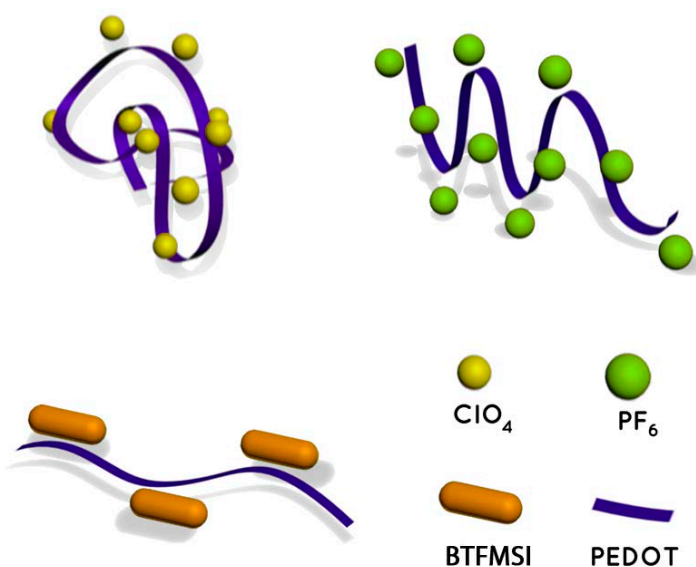


Figure 3.28 PEDOT conformation under the presence of different counter-ions.

does not change with the reduction level. These values are very similar to that calculated for PEDOT:Tos ($0.37 \text{ Wm}^{-1}\text{K}^{-1}$) and PEDOT:PSS ($0.20 \text{ Wm}^{-1}\text{K}^{-1}$) [36, 72]. The figure of merit for all samples as a function of the reduction time, is shown in Figure 3.29. The best value

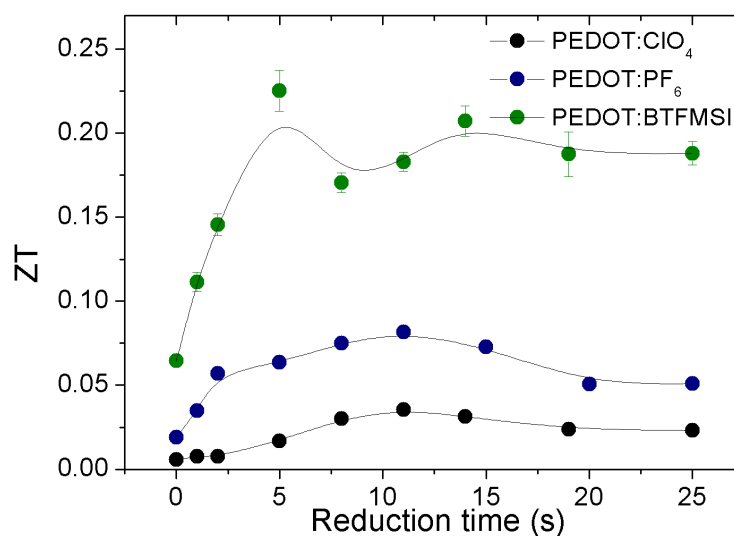


Figure 3.29 ZT values of PEDOT:ClO₄, PEDOT:PF₆ and PEDOT:BTFMSI as a function of chemical reduction time at 25 °C.

has been obtained for PEDOT:BTFMSI, $ZT \approx 0.22$. This value is one of the highest reported for

polymers in the literature, approaching to the record value obtained for a polymer [24] ($ZT=0.4$).

The importance of these high ZT values remains in the fact that they have been obtained with a simple polymer matrix, without the need of additional fillers. For this reason, it is interesting to compare our results with the most relevant data published on the thermoelectric performance in polymer composites. For example: in PANI/Bi nanocomposites $ZT\approx 0.4-1.3\cdot 10^{-3}$ [32], in PANI/SWCNTs [107], $ZT\approx 0.4-1.3\cdot 10^{-3}$, in poly(3-hexylthiophene)/ Bi_2Te_3 nanocomposites [108] $ZT\approx 1.7\cdot 10^{-2}$, in PEDOT:PSS/SWCNTs [109, 110], $ZT\approx 2\cdot 10^{-2}$ or PEDOT:PSS/CNT-stabilizers (PF 500 $\mu\text{W}/\text{mK}^2$). In addition, the suitable experimental process for manufacturing nanocomposites without purification stages indicates that PEDOT: ClO_4 , PEDOT: PF_6 and PEDOT:BTfMSI could be good candidates as polymer matrices in the production of high thermoelectric efficiency nanocomposites with high ZT values.

3.4 Electrochemical de-doping in PEDOT and polypyrrole²

3.4.1 Materials

The reactants used in this work, PPy, EDOT, lithium perchlorate, ethanol and acetonitrile, were purchased from Sigma Aldrich Co. (Madrid, España).

3.4.2 Synthesis of PEDOT

The electrochemical synthesis of PEDOT was carried out at room temperature in a three electrode cell following the procedure described in a previous section. The working electrode was a gold coated PET surface for SEM and transport measurements, while an ITO coated glass was used for cyclic voltammetry and absorbance measurements. A platinum grid acted as the counter-electrode and the Ag/AgCl electrode acted as the reference one. PEDOT was polymerized from a 0.01 M solution of EDOT and LiClO_4 0.1 M in acetonitrile. The electrochemical polymerization was made at a deposition intensity of 3 mA during 1.5 min over the working electrode surface. Films of 120-130 nm thickness were obtained. The gold layer of the corresponding working electrode was removed with an acid solution ($\text{HNO}_3:\text{HCl}$ ratio 1:3) after the film deposition. Finally, the deposited PEDOT films were rinsed several times with water and ethanol to remove the untreated monomer and then dried in air at room temperature.

²This section is based on the publication: "Controlling the thermoelectric properties of polymers: application to PEDOT and polypyrrole" M. Culebras, B. Uriol, C. M. Gómez, A. Cantarero, *Physical Chemistry Chemical Physics*, 17, 15140-15145 (2015) Reproduced by permission of the PCCP Owner Societies.

3.4.3 Synthesis of PPy

Polypyrrole films were also prepared at room temperature by the electrochemical polymerization method in a conventional three electrode system. The working electrode was a stainless steel electrode for SEM and transport measurements, while an ITO electrode was used for voltamperometry and absorbance measurements. A platinum grid acted as the counter-electrode and the Ag/AgCl electrode was used as reference. PPy was polymerized from a 0.01 M solution of pyrrole and LiClO₄ 0.1 M in acetonitrile. The electrochemical polymerization was made at a deposition intensity of 3 mA. The films, grown on the ITO electrode during 1.5 min, were 120-130 nm thick, whereas those obtained on stainless steel electrodes during 4 h were 100 μm. Finally, the deposited PPy films were rinsed several times with water and ethanol to remove the untreated monomer and then dried in air at room temperature. The layer of PPy was detached from the steel surface and transferred into a glass substrate for measurements purposes.

3.4.4 Electrochemical reduction of polymers

The electrochemical reduction of the polymeric samples was carried out in an Ivium-n-Stat: multi-channel electrochemical workstation under computer control. The three electrodes cell was formed by the ITO coated by the polymer (PEDOT or PPy) as the working electrode, the platinum grid as the counter-electrode, and the Ag/AgCl electrode as the reference one in a 0.1 M of LiClO₄ in acetonitrile solution. The polymer samples were subjected to several voltages vs the Ag/AgCl reference electrode, in order to determine the absorbance and the transport properties (electrical conductivity and Seebeck coefficient) at different reduction states.

3.4.5 Morphology of PEDOT and PPy films

SEM was used in order to characterize the surface morphology of the films. The images of the PEDOT and PPy films obtained after the electrochemical polymerization are depicted in Figure 3.30. The surface morphology of PEDOT (Figure 3.30(a)) shows a homogeneous and compact surface with a certain degree of roughness of nearly interconnected polymer chains and voids in between [27, 72]. The SEM surface image of PPy (Figure 3.30 (b)) shows typical granular (cauliflower) morphologies distributed over the substrate surface and densely packed [69, 111].

3.4.6 Cyclic voltammetry of PEDOT and PPy films

Cyclic voltammetry between -3 and +1.5 V at a rate of 20 mV/s was performed on the PEDOT and PPy films (Figure 5.25) in order to determine the voltage where the oxidation/reduction polymer species appear. The shape of the voltammogram with anodic (I) and cathodic (III) peaks

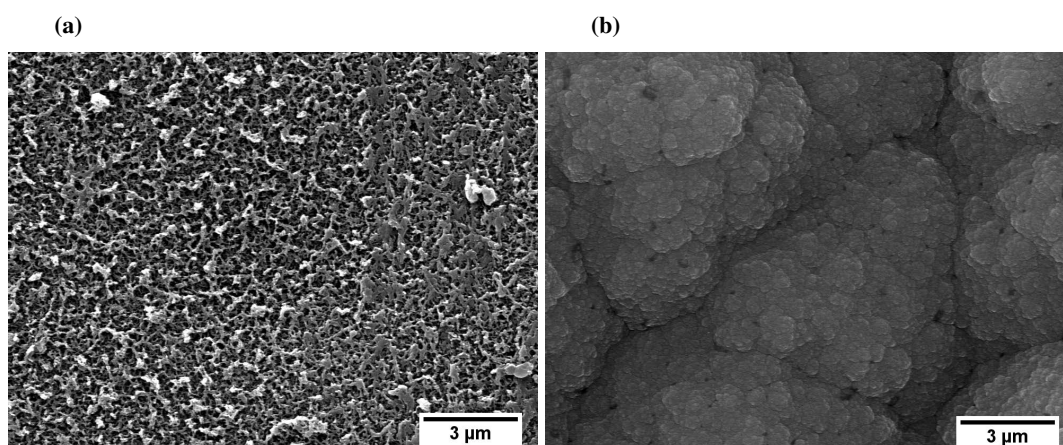


Figure 3.30 SEM images of: (a) PEDOT and (b) PPy films surfaces after electrochemical polymerization.

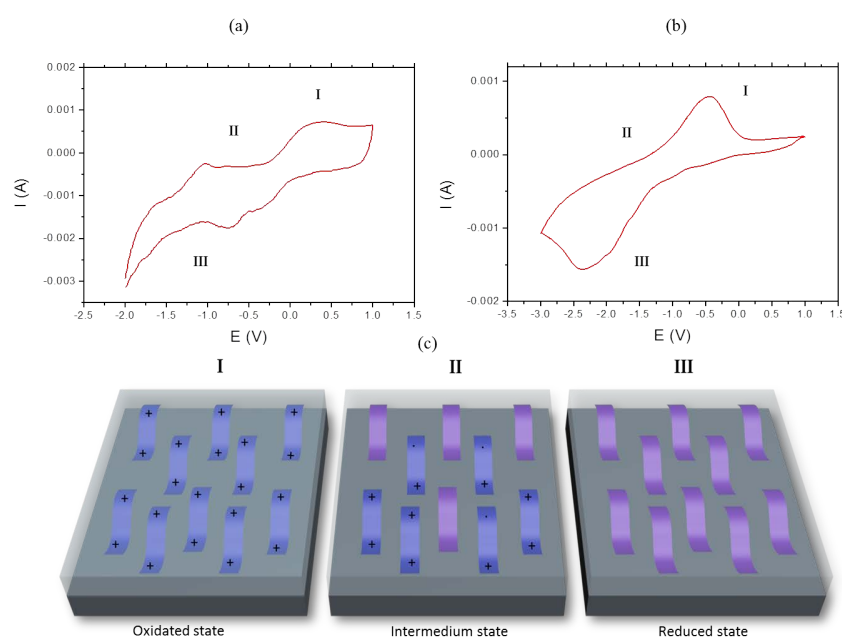


Figure 3.31 Cyclic voltammetry of: (a) PEDOT and (b) PPy. (c) Scheme of polymer electronic states as a function of the oxidation/reduction level.

related with the oxidation and reduction processes is similar to those reported in the literature [67, 68, 100, 101, 112–115]. The peak appearing at positive current values is related to the oxidation of the polymer, while that shown at negative currents is related to the reduction states (Figure 5.25). The reduction or cathodic peak appears in the range from -1.0 to $+0.2$ V while the oxidation peak is located in a potential range between 0 and 0.5 V (see Figure 5.25(a)) for PEDOT. Polypyrrole films depict a clear oxidation peak in the range from -1.0 to 0 V and a reduction peak in the range from -2.5 to -1.5 V (see Figure 5.25(b)). Figure 5.25(c) shows a scheme on the evolution of the electronic depending on the applied voltage. At oxidation potentials, the polymer chains are in a bipolaronic state, at intermediate potentials there is a

mixture between bipolaronic, polaronic and neutral states and finally at reduction potentials the chains are in their neutral states.

The nature of the doping states of conjugated polymers is still a matter of debate. A high doping level is desirable to improve the applications of conducting polymers; in the present case thermoelectric devices. Cyclic voltammetry has been performed to know the voltage values where the oxidized and reduced species appear. These voltages will change the doping state of the polymer and, as expected, the thermoelectric efficiency. In order to change the doping level of PEDOT and PPy, different voltages (V vs Ag/AgCl, taken as reference voltage) have been applied to the films, until the current remained unchanged. In this way, we have different doped polymers from neutral to bipolaron. Optical absorption, electrical and thermal conductivity, and Seebeck coefficient have been determined in those doped films.

3.4.7 Spectroscopy measurements of PEDOT and PPy films

Ultraviolet-visible (Uv-Vis) spectrochemical curves are shown in Figure 3.32 for PEDOT and PPy films deposited on an indium tin oxide (ITO) coated glass. The spectra depict different bands related with different oxidation states due to the electrochemical doping. A broad absorption band centered at 900 nm related with the oxidized PEDOT state ($0.0 < V < 1.0$ V) appears during the doping process and is related to polaron and bipolaron states [101]. However, an absorption band centered at 600 nm appears in the PEDOT reduced state ($V = -1.0$ V), that decreases its intensity as the applied voltage increases, that is, as the polymer changes from a reduced to an oxidized state, related to the $\pi - \pi^*$ transition [100–102, 114–116]. Thus, changing the doping states of the PEDOT chains from bipolarons/polarons to neutral states results in changes in the optical properties of the polymer. The color of the polymer changes from dark blue in the reduced state to light blue in the oxidized (bipolaron) state. Figure 3.32(b) shows the Uv-Vis spectrum of PPy films obtained at different doping levels. The absorption band between 500–900 nm at high applied voltages is related with the polaronic and bipolaronic (oxidized) states of PPy [115]. The band at 300–500 nm, related to the absorption of the neutral or reduced state of PPy [115], cannot be observed since it overlaps with the substrate signal (PET-ITO). The color of PPy changes from a neutral yellow form to blue-green for the fully oxidized, bipolaron state.

3.4.8 Thermoelectric properties of PEDOT and PPy films

Figure 3.33 shows the electrical conductivity, Seebeck coefficient and the power factor of PEDOT (Figure 3.33(a)) and PPy (Figure 3.33(b)) films as a function of the applied voltage vs (Ag/AgCl). In both cases, the electrical conductivity increases with the applied voltage or the

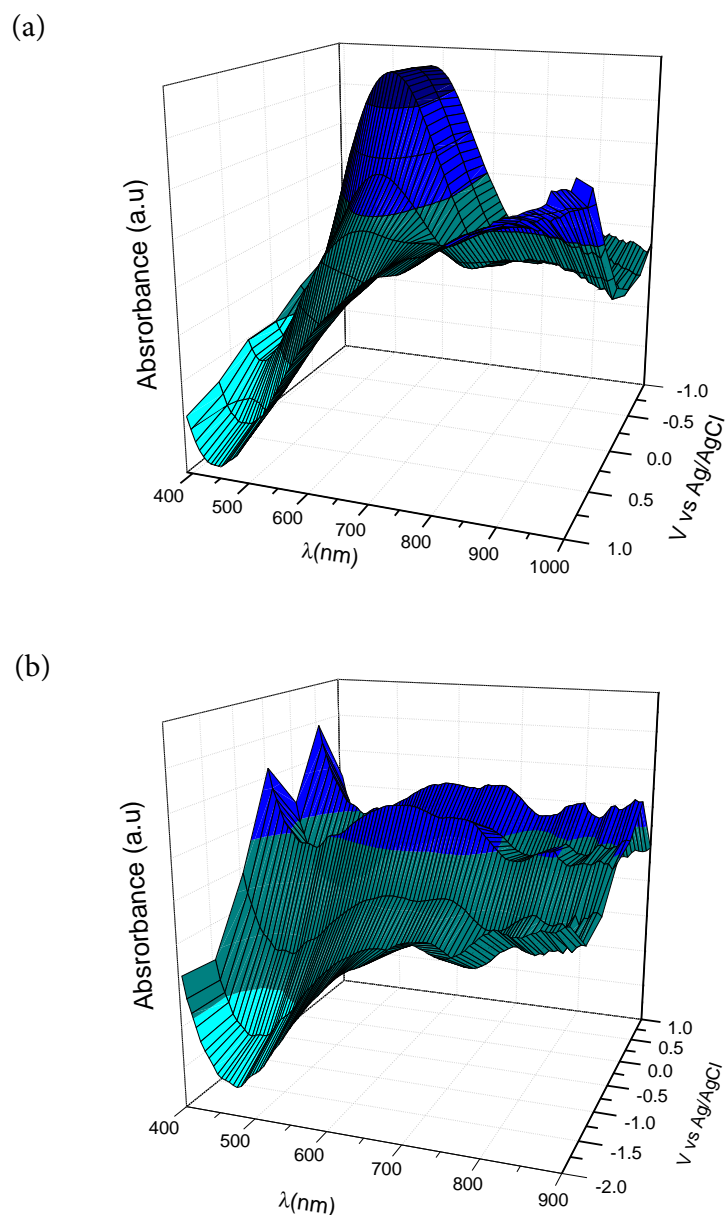


Figure 3.32 Uv-Vis spectra of: (a) PEDOT and (b) PPy as a function of different applied voltages vs Ag/AgCl on ITO coated glass electrodeposited polymer films.

oxidation state of the polymers. As the applied voltage changes from negative to positive, the polymers change from reduced to neutral and to an oxidized state, *i. e.* a bipolaron state as corroborated by cyclic voltammetry and Uv-Vis measurements. The electrical conductivity of PEDOT changes from 80 S/cm at -1.0 V to 766 S/cm at $+1.0$ V. These values are of the same order of magnitude than those found in the literature. For example, PEDOT:PSS doped with DMSO has an electrical conductivity between 500 and 1000 S/cm [24, 26, 29, 72]. The electrical conductivity of PPy increases from 15 S/cm at -2.0 V to 160 S/cm at $+1.0$ V. At the highest oxidation level, we obtain similar values to that reported for PPy:PF₆ (100 – 600 S/cm) [117], but higher than those obtained for PPy composites such as PPy/MWCNTs, 70 S/cm [118], or

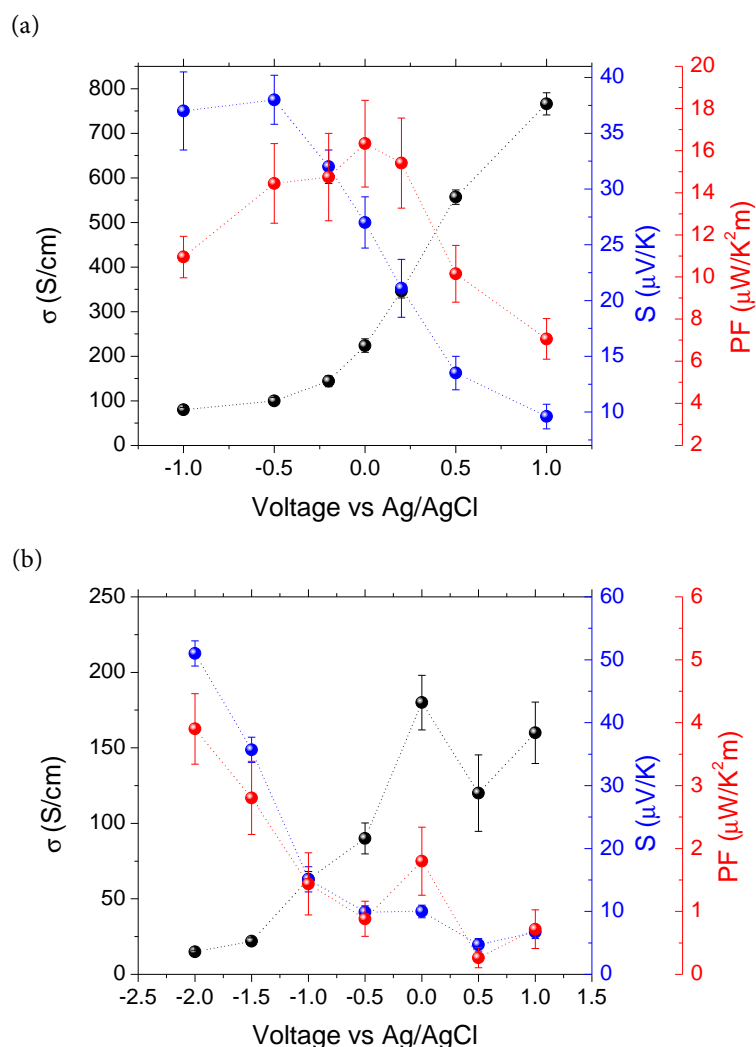


Figure 3.33 Electrical conductivity, Seebeck coefficient and power factor of (a) PEDOT and (b) PPy as a function of voltage referred to the Ag/AgCl electrode.

PPy/graphene nanosheets, 40 S/cm [119]. The opposite trend has been observed in the variation of the Seebeck coefficient (Figure 3.33). The Seebeck coefficient of PEDOT decreases from 37.0 $\mu\text{V/K}$ at -1.0 V to 9.6 $\mu\text{V/K}$ at $+1.0$ V whereas the Seebeck coefficient of PPy changes from 51.0 $\mu\text{V/K}$ at -2.0 V to 6.7 $\mu\text{V/K}$ at $+1.0$ V (always referred to the Ag/AgCl reference electrode). The values of S obtained for the PEDOT films are similar to those reported in the previous section. However, the values of the Seebeck coefficient obtained in this work for PPy are the highest values ever measured [20].

The PF corresponding to PEDOT and PPy has also been plotted in Figure 3.33. The maximum PF is 16.3 $\mu\text{V K}^{-1}\text{m}^{-2}$ for PEDOT at 0.01 V, while for the case of PPy the maximum value has been reached at -2.0 V, 3.9 $\mu\text{V K}^{-1}\text{m}^{-2}$. These values are related to an intermediate polaron structure for PEDOT and a reduced, neutral state for PPy due to the relationship between the Seebeck coefficient and the electrical conductivity.

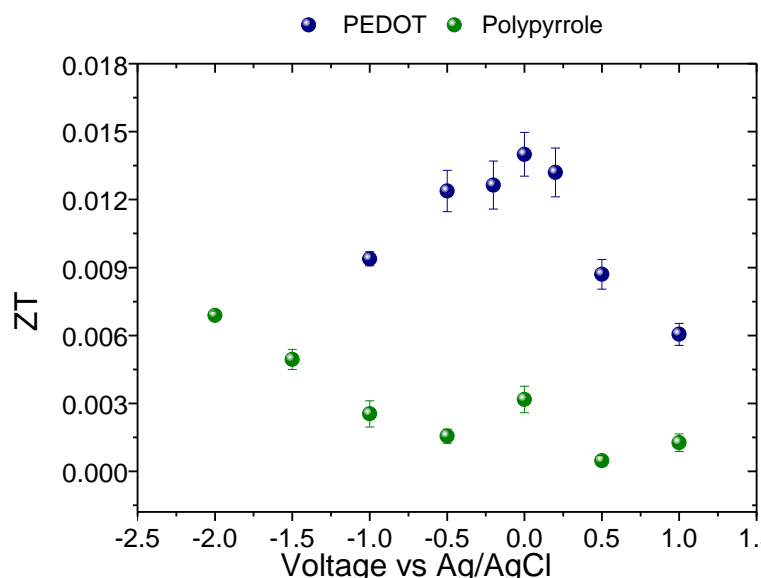


Figure 3.34 ZT of PEDOT and PPy as a function of applied potential at 300 K.

In order to calculate values of ZT, the thermal conductivity has been determined for the different samples, being independent of the doping level of the samples. The values obtained at 300 K were $(0.35 \pm 0.02) \text{ W m}^{-1}\text{K}^{-1}$ for PEDOT and $(0.17 \pm 0.02) \text{ W m}^{-1}\text{K}^{-1}$ for PPy. We have checked that the thermal conductivity does not change with the applied voltage. However, two recent papers reported an anisotropic thermal conductivity of PEDOT [120, 121] and a certain dependence with the electrical conductivity. The in-plane thermal conductivity increases with increasing σ , while the perpendicular thermal conductivity remains constant. In particular, the in-plane thermal conductivity of PEDOT is of the order of $1 \text{ W m}^{-1}\text{K}^{-1}$ for higher values of the electrical conductivity. This is probably because of the contribution of the electrons to the thermal conductivity. If the polymer chains are in-plane, the conductivity (both thermal and electrical) should be larger in-plane. Since we have measured the thermal conductivity using a DSC we have an average value, consistent with previous literature results [27, 36, 122]. But we do not expect an important anisotropy in our case, since we are dealing with very thin films of the order of 100 nm thick. Thus, we believe that our thermal conductivity data are confident.

The efficiency of a thermoelectric device has been plotted in Figure 3.34 for the different samples. The highest value of ZT was 6.8×10^{-3} for PPy and 1.4×10^{-2} for PEDOT, using the values of thermal conductivity obtained from our DSC measurements. These results are of the same order of magnitude as other recently reported on conducting polymers [19, 20].

3.5 Nanostructuring of PEDOT using soft template methods

3.5.1 Materials

The reactants used in this study were: EDOT (97%), Iron(III) p-toluenesulfonate hexahydrate (Fe-Tos) obtained from Sigma Aldrich. Hydrogen peroxide obtained from PanReac AppliChem. Decyltrimethylammonium bromide (DTAB) and Lutensol AT50 were used as surfactant, purchased from Sigma Aldrich and BASF respectively (see Figure 3.35).



Figure 3.35 Molecular structure of Lutensol AT50 and DTAB.

3.5.2 Synthesis of PEDOT nanoparticles using Lutensol AT50

The synthesis of the PEDOT nanoparticles was carried out using polymerization in miniemulsion. [123, 124] First, 0.05 g (2.03×10^{-5} moles) of Lutensol AT50 were dissolved in 40 mL of ultra-pure water. Then 0.2 mL (1.8×10^{-3} moles) of EDOT were added to the Lutensol solution. The mixture was magnetically stirred during 10 minutes. After that, the mixture was sonicated using a Branson 450-D sonifier with 70 % of amplitude in a pulsed mode (90 %) during 5 minutes. After this process, a white dispersion was obtained. The EDOT dispersion was transferred to the reaction flask in a oil bath thermostatted at 45°C. Finally, 25 mL of Fe-Tos solution was added to the reaction flask leaving the polymerization to take place during 24 hours.

The purification of PEDOT nanoparticles was carried out by centrifugation at 8000 rpm during 20 minutes. The process was repeated until the observation of a transparent color in the supernatant solution, indicating that all the Fe-Tos excess was completely removed. Finally, the purified nanoparticles was re-dispersed in 40 mL of ultra-pure water: the nanoparticles dispersion was sonicated for 30 minutes in a bath sonicator, then 20 minutes in a tip sonicator and finally 20 minutes in a bath sonicator.

In order to study the effect of the experimental conditions (EDOT:Fe-Tos molar ratio, the addition of H₂O₂ and the pH of the dispersion) on the final properties, such as morphology and thermoelectric parameters, several studies were realized.

3.5.2.1 Influence of EDOT:Fe-Tos

Table 3.4 summarizes the different reactants and molar ratios employed to study the EDOT:Fe-Tos reaction.

Table 3.4 Amounts of the reactants during the study of the EDOT:Fe-Tos molar ratio influence.

Reactant	EDOT:Fe-Tos molar ratio			
	1:0.5	1:1	1:2	1:3.5
Lutensol AT50 (g)	0.05	0.05	0.05	0.05
EDOT (mL)	0.2	0.2	0.2	0.2
Fe-Tos (M)	1.4×10^{-2}	2.8×10^{-2}	5.7×10^{-2}	1.0×10^{-1}

3.5.2.2 Influence of H₂O₂ concentration

For this study the molar ratio between EDOT and Fe-Tos was kept at 1:1 molar ratio. The amounts of the reactants used in this study are summarized in the Table 3.5. The addition of H₂O₂ was carried out one 1 hour after finishing the addition of Fe-Tos solution.

Table 3.5 Amounts of the reactants during the study of the H₂O₂ concentration influence.

Reactant	H ₂ O ₂ concentration (M)				
	0	7.5×10^{-3}	1.5×10^{-2}	3.7×10^{-2}	7.5×10^{-2}
Lutensol AT50 (g)	0.05	0.05	0.05	0.05	0.05
EDOT (mL)	0.2	0.2	0.2	0.2	0.2
Fe-Tos (M)	2.8×10^{-2}	2.8×10^{-2}	2.8×10^{-2}	2.8×10^{-2}	2.8×10^{-2}
H ₂ O ₂ (mL)	0.0	0.05	0.10	0.25	0.50

3.5.2.3 Influence of miniemulsion pH

For this study, the molar ratio between EDOT and Fe-Tos was kept at 1:1 and the volume of H₂O₂ was 0.5 ml. The amount of the reactants used in this study are summarized in Table 3.6. The addition of HCl to the reaction flask was carried out just after the addition of Fe-Tos.

Table 3.6 Amounts of the reactants during the study of the pH influence.

Reactant	HCl volume (mL)				
	0.0	0.5	1.0	2.5	5.0
Lutensol AT50 (g)	0.05	0.05	0.05	0.05	0.05
EDOT (mL)	0.2	0.2	0.2	0.2	0.2
Fe-Tos (M)	2.8×10^{-2}	2.8×10^{-2}	2.8×10^{-2}	2.8×10^{-2}	2.8×10^{-2}
H ₂ O ₂ (mL)	0.50	0.50	0.50	0.50	0.50

3.5.3 Synthesis of PEDOT nanoparticles using DTAB

The synthesis process of PEDOT nanoparticles using a cationic surfactant such as DTAB was carried out using a similar procedure as described in the previous section. Certain amount of DTAB was dissolved in 40 mL of ultra-pure water. Then 0.2 mL of EDOT was added to the cationic surfactant solution and the mixture was magnetically stirred for 10 minutes. After that, the mixture was sonicated using a Branson 450-D sonifier with 70 % of amplitude in a pulsed mode (90 %) during 5 minutes in a ice bath, in order to avoid the warming of the dispersion. After this process, a white dispersion was obtained. The EDOT dispersion was transferred to the reaction flask in a oil bath thermostatted at 45°C. Finally, 25 mL of Fe-Tos solution was added to the reaction flask leaving the polymerization to occur during 24 hours with constant magnetic stirring.

The PEDOT particles were purified by centrifugation. The raw reaction was centrifuged at 8000 rpm during 20 minutes, and then, the supernatant solution was removed. This process was repeated until the observation of transparent color in the supernatant solution. The resulting powder was re-dispersed in 40 mL of ultra-pure water following the following steps: the nanoparticles dispersion was sonicated for 30 minutes in a bath sonicator, then 20 minutes in a tip sonicator and finally, 20 minutes in a bath sonicator.

During this study, the influence of the DTAB concentration was carried out changing the amount of DTAB from 0.05 g to 3.0 g using two different molar ratio EDOT:Fe-Tos, 1:1 and 1:2. All the reactants amounts have been summarized in table 3.7.

Table 3.7 Reactants during the study of the DTAB influence on PEDOT polymerization with a molar ratios EDOT:Fe-Tos 1:1 and 1:2.

Molar ratio EDOT:FeTos 1:1				
Reactant	Amounts			
DTAB (g)	0.05	0.5	1.0	3.0
EDOT (mL)	0.2	0.2	0.2	0.2
Fe-Tos (M)	2.8×10^{-2}	2.8×10^{-2}	2.8×10^{-2}	2.8×10^{-2}
Molar ratio EDOT:FeTos 1:2				
Reactant	Amounts			
DTAB (g)	0.05	0.5	1.0	3.0
EDOT (mL)	0.2	0.2	0.2	0.2
Fe-Tos (M)	5.7×10^{-2}	5.7×10^{-2}	5.7×10^{-2}	5.7×10^{-2}

3.5.4 Morphology of PEDOT nanoparticles

The morphology of the PEDOT nanoparticles was studied by TEM. The particle size and shape of the nanoparticles are very important to keep the stability of the suspension, in order to be processed in solution for making devices or other applications. Figure 3.36 shows the morphol-

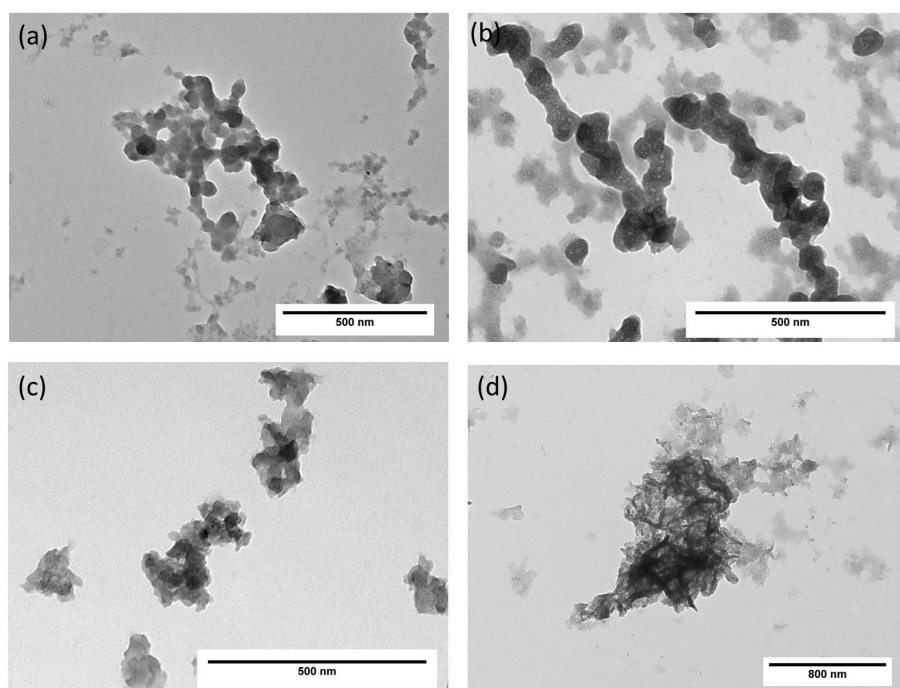


Figure 3.36 TEM images of PEDOT nanoparticles with a molar ratio: (a) EDOT:Fe-Tos 1:0.5, (b) EDOT:Fe-Tos 1:1, (c) EDOT:Fe-Tos 1:2, (d) EDOT:Fe-Tos 1:3.5.

ogy of the PEDOT nanoparticles with different molar ratio EDOT:Fe-Tos employed during the synthesis. The morphology is strongly related with the Fe-Tos content during the synthesis. Figure 3.36(a) shows nanoparticles aggregates composed by spherical nanoparticles with a size of (43 ± 20) nm at lower content of Fe-Tos (molar ratio 1:0.5). The aggregates size varies from several hundreds of nanometers to several microns. For the case of PEDOT nanoparticles obtained at molar ratio 1:1 (Figure 3.36(b)), a pseudo-spherical shape has been observed. Probably, the collisions between the unfinished polymerized drops give use to these branched aggregates observed in Figure 3.36(b). The particle size was (60 ± 10) nm. This increase of the particle size is an indication of the fact that the spherical shape is lost when the oxidant content increases. When the molar ratio EDOT:Fe-Tos increases until 1:2, the spherical morphology is completely lost as shown in Figure 3.36(c). The results, at this molar ratio, show particle aggregates composed of small amorphous particles. Finally, when the Fe-Tos content is very high (molar ratio 1:3.5), the particle morphology is not observed. Figure 3.36(d) shows that PEDOT is structured in big aggregates of flakes.

Figure 3.37 shows a simple scheme to explain the resulting morphology during the PEDOT polymerization. Initially, during the miniemulsion process, the PEDOT drops have a spherical

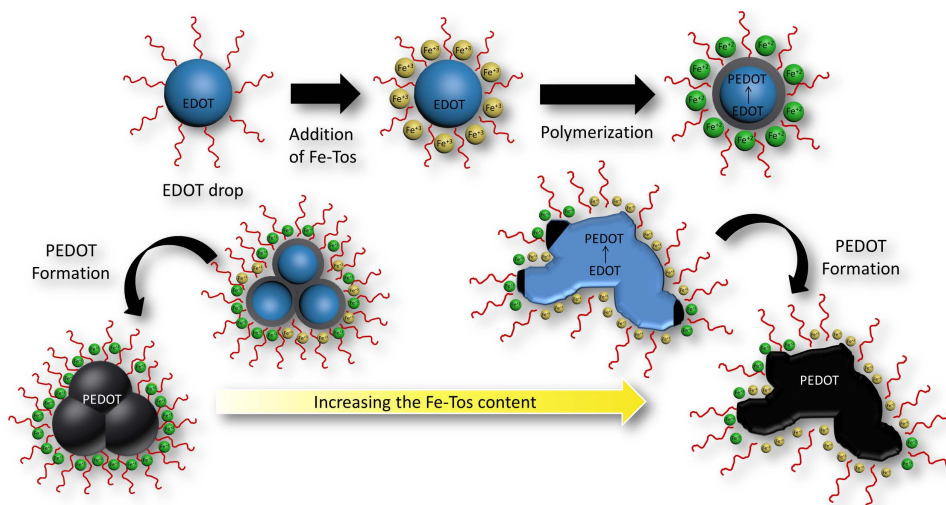


Figure 3.37 Scheme of PEDOT polymerization in miniemulsion.

morphology, when the oxidant (Fe-Tos) is added. The iron(III) ions go to the interphase EDOT-water to oxidize the monomer to form the polymer (EDOT to PEDOT), consequently a shell of PEDOT is created over the the EDOT drop. In addition the iron (III) ions are reduced to iron (II). These ions inhibit the EDOT polymerization inside of the drop. At this point, when the EDOT drops with the PEDOT shell crash, the drop is deformed and the EDOT monomers come out. This fact produces the polymerization of EDOT outside of the drop and is the responsible for the attachment of the particles between them. When Fe-Tos content is very high, the polymerization of EDOT after the collisions is very fast, consequently, a flake shape is generated.

Figure 3.38 shows the TEM images and particle size distribution of PEDOT nanoparticles synthesized at different concentrations of H_2O_2 . In these experiments, the molar ratio between EDOT:Fe-Tos was kept at 1:1. The addition of a small amount of H_2O_2 such as 0.05 ml (7.5×10^{-3} M) to the reaction flask, produces a spherical morphology in the final PEDOT nanoparticles as shown in Figure 3.38(a). This fact indicates that initial morphology of the EDOT drop is kept during the polymerization. It is possible to observe individual particles with a low level of aggregation. As the concentration of H_2O_2 , increases the spherical morphology of the PEDOT nanoparticles is not affected, as shown in Figure 3.38(b), (c) and (d). The particles were very similar in all cases and practically do not change with the H_2O_2 content, as shown in Figure 3.38(e). The particle size was (30 ± 5) nm, (32 ± 7) nm, (28 ± 5) nm and (36 ± 8) nm for 7.5×10^{-3} M, 1.5×10^{-2} M, 3.7×10^{-2} M and 7.5×10^{-2} M of H_2O_2 , respectively.

The role of the H_2O_2 during the polymerization has been summarized in the scheme of the Figure 3.39. The H_2O_2 addition was done 1 hour after the Fe-Tos addition. At this time, the initial PEDOT shell is already created, so the Fe^{+2} is surrounding the PEDOT shell. When the H_2O_2 is added to the reaction flask, the hydrogen peroxide oxidizes the surrounding Fe^{+2} to Fe^{+3} so the oxidation of EDOT (polymerization) can be realized. As the Fe^{+3} ions are

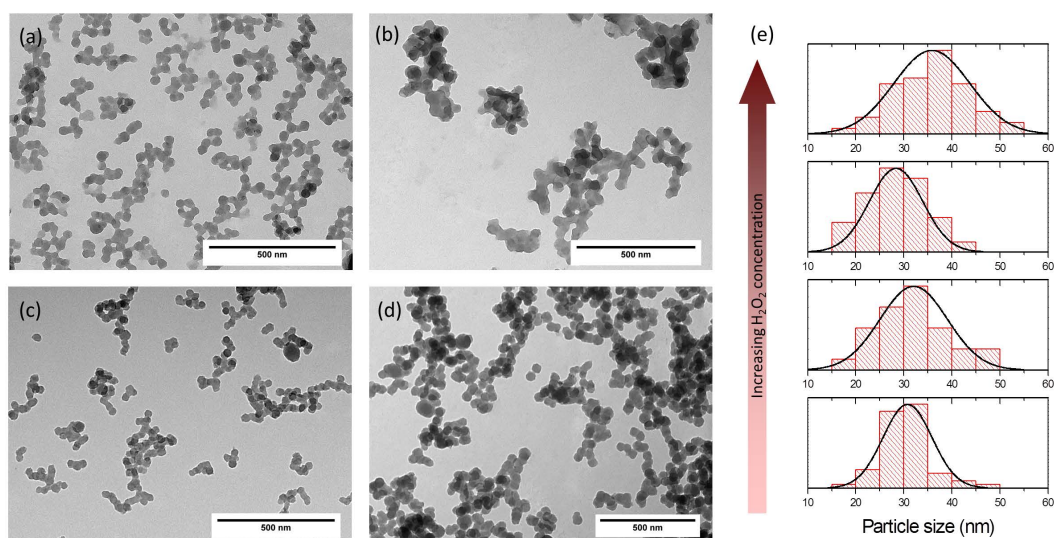


Figure 3.38 TEM images of PEDOT nanoparticles with H_2O_2 : (a) $7.5 \cdot 10^{-3}$ M, (b) $1.5 \cdot 10^{-2}$ M, (c) $3.7 \cdot 10^{-2}$ M, (d) $7.5 \cdot 10^{-2}$ M. (e) Particle size distribution.

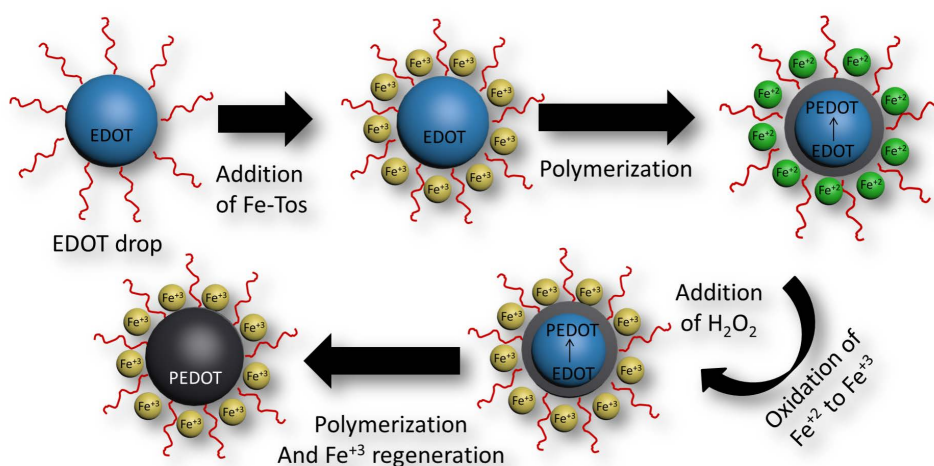


Figure 3.39 Scheme of PEDOT polymerization in miniemulsion with H_2O_2 .

polymerizing the EDOT, at the same time these ions are being regenerated due to the presence of H_2O_2 . This fact produces a fast polymerization keeping the spherical morphology of the EDOT. Consequently, in terms of stability of the final dispersion of PEDOT nanoparticles, the addition of H_2O_2 implicates a better stability than the nanoparticles synthesized without H_2O_2 . For example, the dispersion of PEDOT nanoparticles (molar ratio 1:1) without H_2O_2 was flocculated in a couple of hours. However, the dispersion of PEDOT nanoparticles (molar ratio 1:1) with H_2O_2 (0.05 ml) was kept stable during several weeks.

Figure 3.40 shows the morphology of the PEDOT particles with the addition of HCl during the synthesis. In general terms, the spherical morphology has not been observed in the samples. The addition of 0.5 ml of HCl to the reaction flask (Figure 3.40(a)) produces a distortion on the

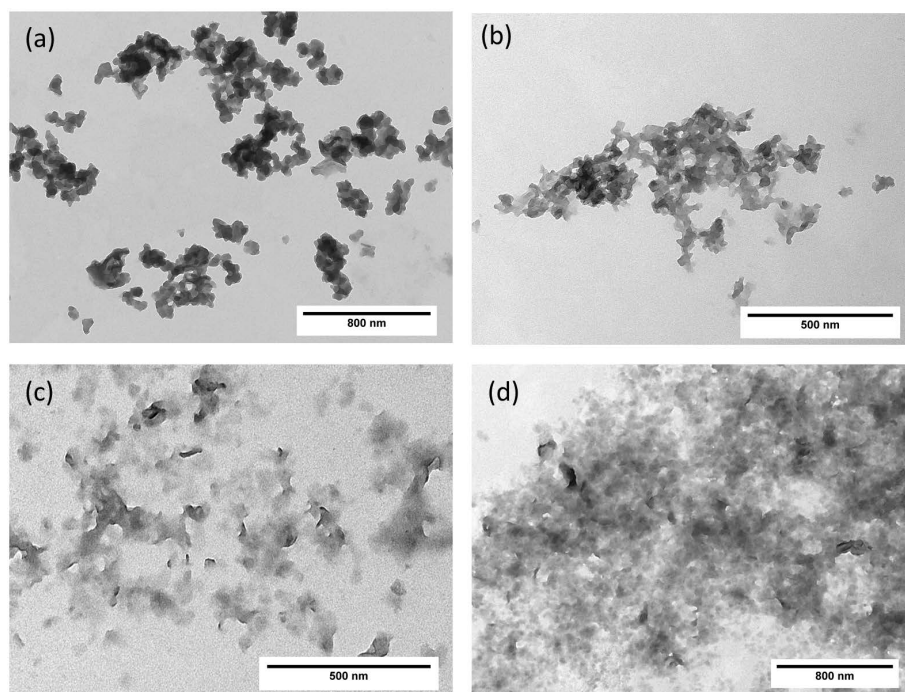


Figure 3.40 TEM images of PEDOT nanoparticles with 0.5 ml of H_2O_2 and: (a) 0.5 ml, (b) 1.0 ml, (c) 2.5 ml and (d) 5 ml of HCl.

nanoparticle morphology obtaining particle aggregates composed by pseudo-spherical nanoparticles. As the volume of HCl increases, the initial spherical morphology is lost. At high content of HCl a homogeneous film is obtained composed of particles with a shape of flakes as shown in Figure 3.40(d). This fact can be explained by two factors. One is the high ionic content, that destabilizes the miniemulsion, producing big aggregates of PEDOT particles, and the second one is that the oxidation process of EDOT is working better in acid media, consequently an increase in the polymerization rate is observed.

Figure 3.41 shows TEM images of the PEDOT nanoparticles obtained from the synthesis using DTAB as surfactant. All the nanoparticles presented flakey morphology independently of the amount of DTAB employed during the synthesis process. As happened in the experiments using lutensol as a surfactant during the polymerization process, the Fe^{+3} ions surround the EDOT drops, with the difference that, when DTAB is used as stabilizer the electrostatic repulsion between the positive charge from the DTAB and the Fe^{+3} , produces a detriment in the polymerization rate of EDOT, generating the morphology with a shape of flakes instead of spheres.

Figure 3.42 shows TEM images of PEDOT nanoparticles synthesized with different amounts of DTAB at a molar ratio EDOT:Fe-Tos 1:2. Similar morphology has been obtained for the case of molar ratio 1:2, however the aggregation level is higher compared to the particles obtained at molar ratio 1:1. This fact is normal since the oxidant content increases, with the molar ratio 1:2.

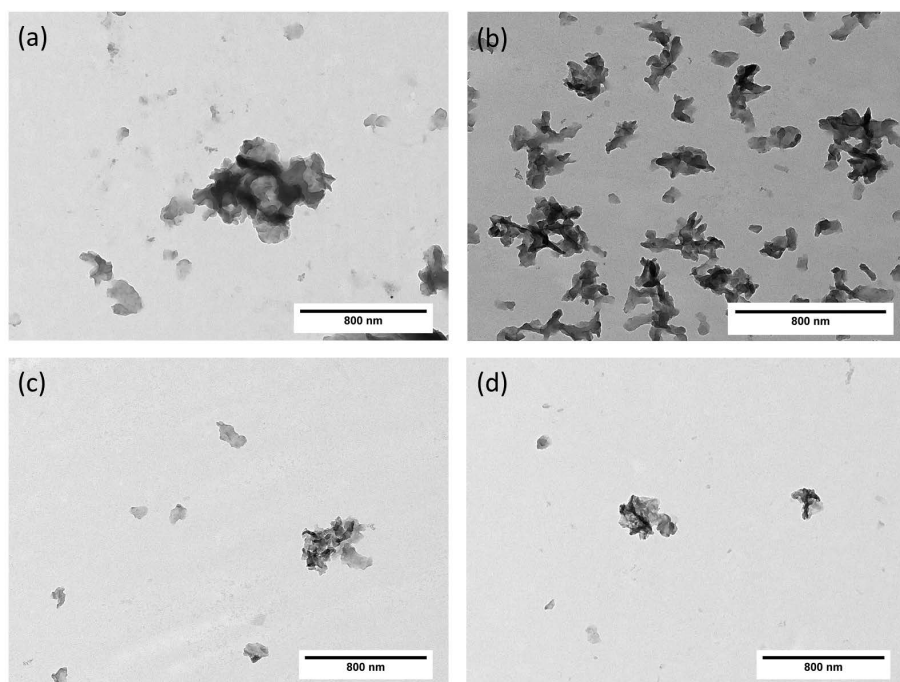


Figure 3.41 TEM images of PEDOT nanoparticles with a molar ratio EDOT:Fe-Tos 1:1 using: (a) 0.05 g, (b) 0.5 g, (c) 1.0 g and (d) 3.0 g of DTAB .

The stability of both systems was practically the same, independent of the molar ratio used during the polymerization. However, the suspension with 0.05 g of DTAB flocculates after a couple of days after the re-dispersion process, while the remaining dispersions were kept stable during weeks.

3.5.5 Thermoelectric behavior of PEDOT nanoparticles

In order to measure the thermoelectric properties of the PEDOT nanoparticles as a function of the concentration of Fe-Tos used during the synthesis, several films were made. The PEDOT films were prepared by drop-casting using PET as a substrate. The substrates were coated with the PEDOT suspension and the solvent (water) was evaporated at 60°C in vacuum. The electrical conductivity of these samples was measured using the Van Der Paw method, described in the experimental section. Figure 3.43 shows the electrical conductivity and the Seebeck coefficient of the PEDOT nanoparticles as a function of the Fe-Tos concentration. The electrical conductivity increases from 2.1×10^{-6} S/cm to 2.6 S/cm with the Fe-Tos concentration. The increment in Fe-Tos during the synthesis creates a higher oxidation level in the PEDOT chains, producing a doping process in the PEDOT nanoparticles [27, 37]. The Seebeck coefficient at 0.014 M was impossible to measure with the experimental setup described in Chapter 2 of this thesis due to the high electrical resistance of the sample. The measurements show a big noise making impossible to get a value of the Seebeck coefficient. However, the measurements for the samples prepared with a higher contraction of Fe-Tos gave a very clear measurement. The Seebeck

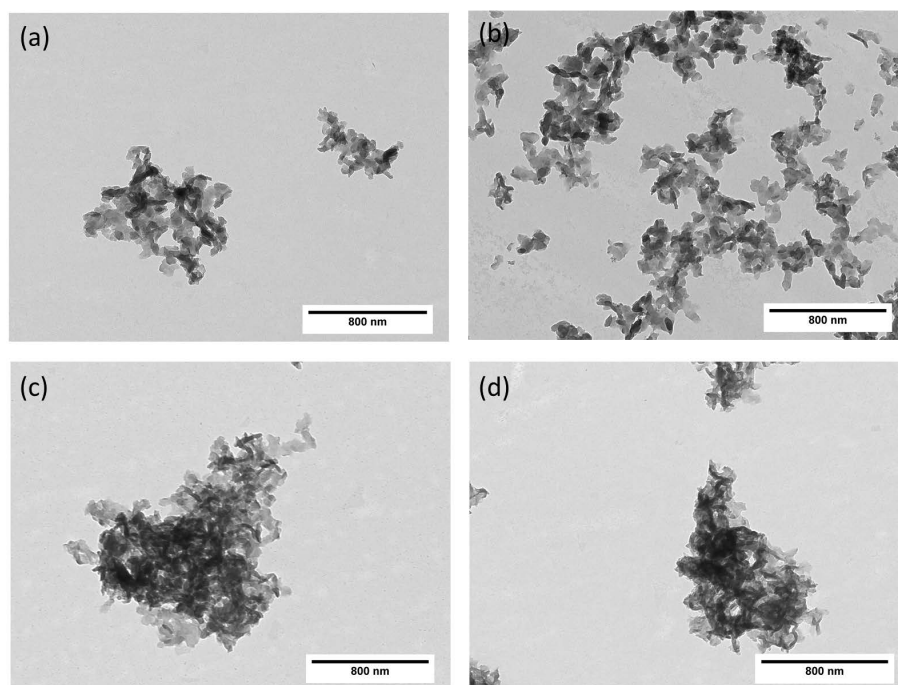


Figure 3.42 TEM images of PEDOT nanoparticles with a molar ratio EDOT:Fe-Tos 1:2 using: (a) 0.05 g, (b) 0.5 g, (c) 1.0 g and (d) 3.0 g of DTAB .

coefficient was around $30\text{--}35 \mu\text{V/K}$ for the particles synthesized with a Fe-Tos concentration between $0.028\text{--}0.057 \text{ M}$. These values correspond with low doped PEDOT. At higher concentration of Fe-Tos the Seebeck coefficient was around $12.6 \mu\text{V/K}$. This value is very similar to highly doped PEDOT films [27, 37]. This fact means that using 0.1 M of Fe-Tos is possible to obtain PEDOT with a high doped level.

In order to study the doping degree of the PEDOT nanoparticles, the samples were analyzed by Raman and Uv-Vis spectroscopy. Figure 3.44(a) shows the Raman spectra of PEDOT nanoparticles at different content of Fe-Tos. No Raman signal has been observed at low concentration of Fe-Tos (molar ratio EDOT:Fe-Tos 1:0.5) indicating a low polymerization degree. The Raman intensity increases when the concentration of Fe-Tos used during the synthesis is low (molar ratio EDOT:Fe-Tos 1:1) indicating a low doping level in PEDOT. The Raman signal is high when the number of neutral π -bonds increases in the polymer backbone [100, 101]. However, the Raman signal decreases at higher content of Fe-Tos because the final material presents a higher doping level. The same trend has been observed in the Uv-Vis results as it is shown in Figure 3.44(b). The spectrum of the sample prepared at EDOT:Fe-Tos molar ratio 1:0.5 is different from the others. Probably, the absorption is given by oligomeric species of EDOT, explaining its low electrical conductivity. However, the spectrum for the PEDOT nanoparticles prepared at higher molar ratios than 1:0.5 presents the typical shape of PEDOT. The absorption related with the polaronic and bipolaronic states ($800\text{--}1000 \text{ nm}$) [102] increases at higher concentration of Fe-Tos while the absorption responsible for the neutral π -bonds increases at lower concentration of Fe-Tos [102].

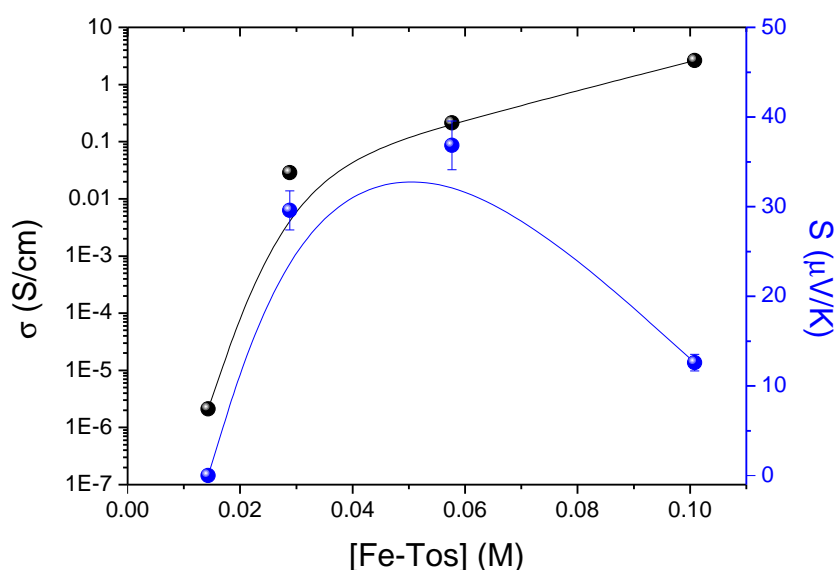


Figure 3.43 Electrical conductivity, and Seebeck coefficient of PEDOT nanoparticles as a function of Fe-Tos concentration.

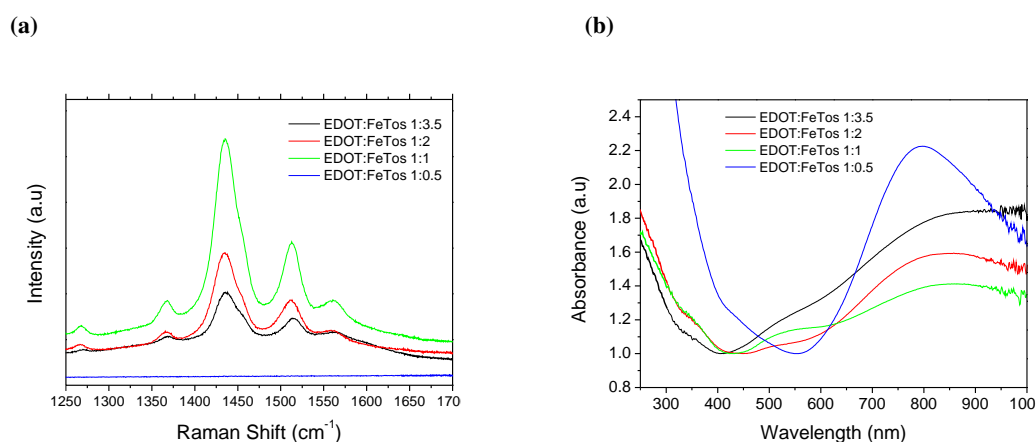


Figure 3.44 (a) Raman and (b) Uv-Vis spectra of PEDOT at different EDOT:Fe-Tos molar ratios.

For the case of the nanoparticles prepared with H_2O_2 , the electrical conductivity has been determined in a film and pellet conformation. The electrical conductivity has been obtained by the Van Der Pauw method for the case of film while for the case of pellet the values were obtained using broadband dielectric spectroscopy. Figure 3.45(a) shows the electrical conductivity for both, pellets and films, as a function of the H_2O_2 concentration employed during the synthesis. The electrical conductivity decreases from 0.028 to 4.39×10^{-6} S/cm with the H_2O_2 concentration, for the case of pellets. The same trend has been observed for the case of films, however the values of the electrical conductivity were higher compared to the pellets due to the large number

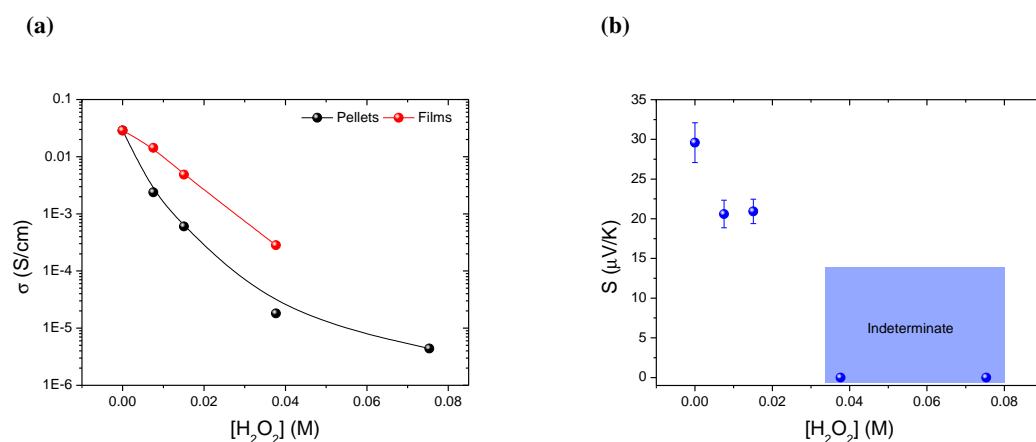


Figure 3.45 (a) Electrical conductivity and (b) Seebeck coefficient of PEDOT as a function of H_2O_2 concentration.

of defects and interphases in pellets. This fact produces more difficulties for the electric transport across the pellet compared with the thin film. The decrease of the electrical conductivity can be generated by molecular changes on the PEDOT structure. The values of the Seebeck coefficient are plotted in Figure 3.45(b). At higher concentrations of H_2O_2 the Seebeck coefficient could not be measured due to the insulating nature of the PEDOT nanoparticles. At low concentration, the Seebeck values were lower than the particles obtained without H_2O_2 . This trend is not normal because the electrical conductivity and the Seebeck coefficient decreases at the same time. So, this fact indicates that the H_2O_2 is not producing a de-doping process but instead some changes into the molecular structure of PEDOT that generates a depletion of the electrical conductivity.

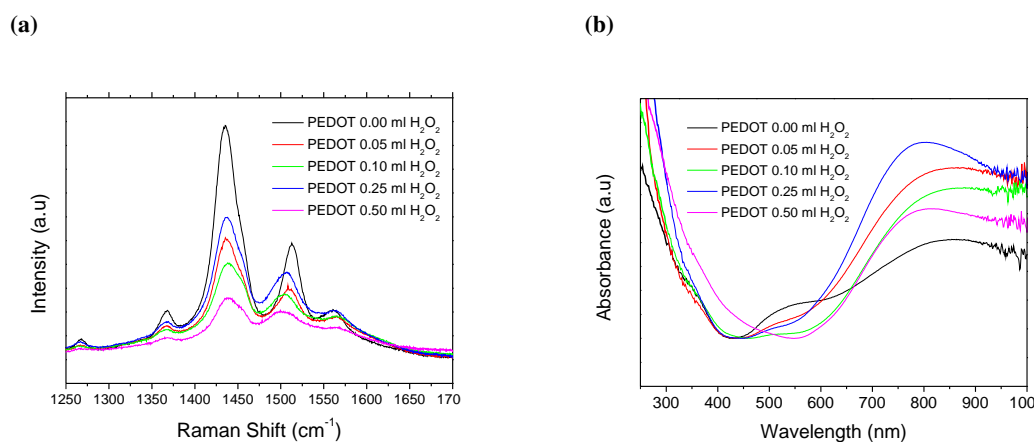


Figure 3.46 (a) Raman and (b) Uv-Vis spectra of PEDOT at different H_2O_2 content H_2O_2 .

Figure 3.46(a) shows the Raman spectra of PEDOT nanoparticles at different H_2O_2 volumes added during the synthesis. The spectra show the typical vibrational modes of PEDOT in the region between 1250-1700 cm^{-1} . The intensity of the Raman signal decrease with the presence of

H_2O_2 , indicating a decrease of the number of neutral π -bonds along the polymer backbone. Also a shift of the signal related with the asymmetric $\text{C}=\text{C}$ stretching is observed. This fact is also an indication of the decrease in the electrical conductivity, given by some changes in the conjugation of the PEDOT chains. Figure 3.46(b) shows the Uv-Vis spectra of PEDOT nanoparticles at different H_2O_2 volumes added during the synthesis. The absorption of the oxidized states is observed in all cases indicating a high oxidation in the polymer chains. However, the absorption related with the conjugated neutral π -bond is very low and decreases with the addition of H_2O_2 . A reason that could explain this trend is that during the polymerization process the radicals generated in the conjugated neutral π -system can interact with the $\cdot\text{OH}$ radicals from the H_2O_2 . The hydroxyl radicals are bonded to the polymer backbone breaking the conjugation of the PEDOT chain, as shown in the molecular structure of PEDOT with OH bond in their backbone (Figure 3.47). The break of the conjugation in the polymer backbone produces a big decrease in the

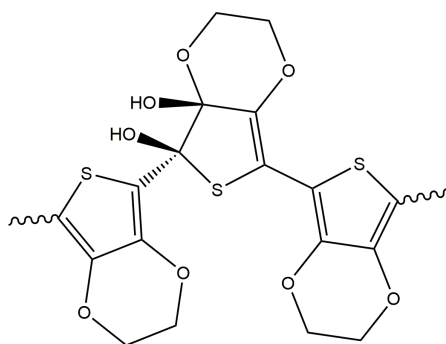


Figure 3.47 Broken conjugation of PEDOT due to the $\cdot\text{OH}$ radicals .

electrical conductivity, since the polymer chains are not able to propagate charge along their structure. For this reason, the electrical conductivity decreases five orders of magnitude with the addition of 0.5 ml of H_2O_2 .

As an evidence of the presence of hydroxyl groups in the polymer back bone, FTIR analysis has been made in the PEDOT nanoparticles. Figure 3.48 shows the FTIR spectra of PEDOT nanoparticles, with 0.5 ml and without H_2O_2 from 4000 cm^{-1} to 400 cm^{-1} and a zoom in the region between $3500\text{-}2500\text{ cm}^{-1}$. The typical vibrational modes of PEDOT have been observed. At 1328 cm^{-1} the $\text{C}=\text{C}$ stretching appears, the band at 1200 , 1142 and 1073 cm^{-1} correspond with the C-O-C bond stretching in the ethylene dioxy (alkylenedioxy) group. Also the CS bond in the thiophene ring was observed by the presence of bands at 960 and 837 cm^{-1} [125]. In the region between $3500\text{-}2500\text{ cm}^{-1}$, the band related with the C-H stretching has been observed at 2928 cm^{-1} in the sample without H_2O_2 . However, in the nanoparticles prepared with 0.5 ml of H_2O_2 a broad band in the range of $3300\text{-}3000\text{ cm}^{-1}$ has been observed. This indicates the presence of hydroxide groups in the polymer chains.

Figure 3.49 shows the electrical conductivity and the Seebeck coefficient for PEDOT nanoparticles synthesized using several concentrations of HCl . The electrical conductivity increases five

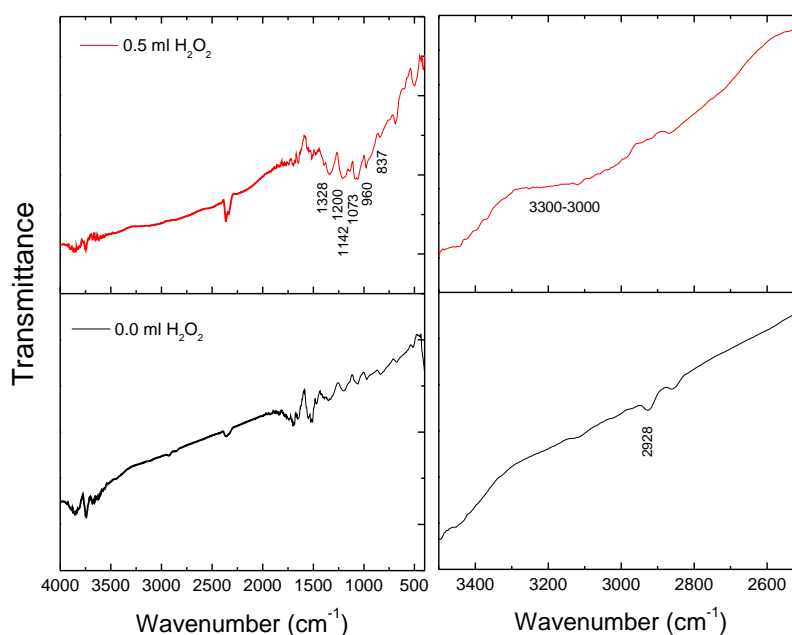


Figure 3.48 FTIR spectra of PEDOT nanoparticles with 0.5 ml and without H_2O_2 .

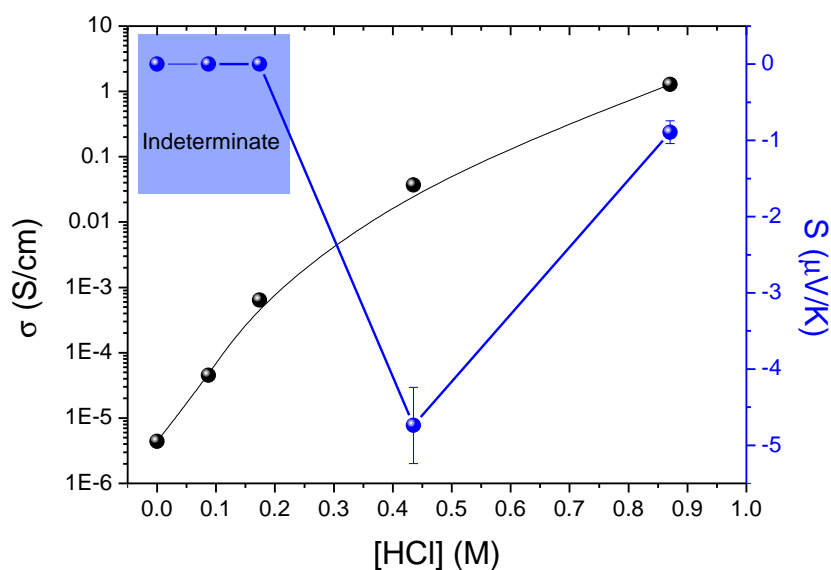


Figure 3.49 Electrical conductivity, and Seebeck coefficient, of PEDOT nanoparticles as a function of HCl concentration.

orders of magnitude with the addition of HCl during the synthesis. The electrical conductivity increases from 4.39×10^{-6} to 1.27 S/cm. This fact indicates that the polymerization of EDOT is more favorable in acid media since protons are required for the oxidation of EDOT. Other effect can be the morphology. At higher concentrations of HCl, the particle morphology is lost, becoming in particles with a flake shape. This kind of morphology produced during the film formation can help to the electrical transport along the film. Because this shape produces less

defects compared with a film made by spherical particles. The Seebeck coefficient was only determined for the samples at 0.4 M and 0.8 M, since the samples prepared with a smaller amount of HCl were insulators. The values of the Seebeck coefficient were very low (-5 and $-1 \mu\text{V/K}$), in the same range of metallic compounds and negative indicating a n-type behavior.

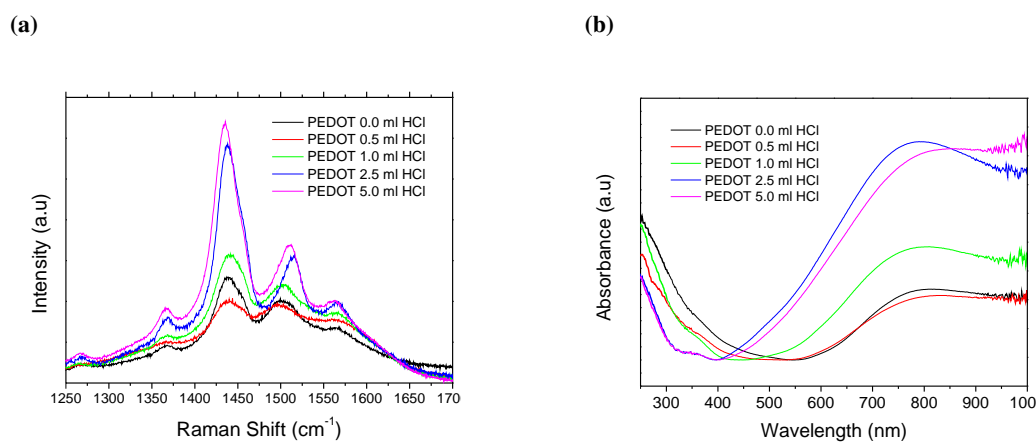


Figure 3.50 (a) Raman and (b) Uv-Vis spectra of PEDOT as a function of HCl volume added during the synthesis.

Figure 3.50(a) shows the Raman spectra of the PEDOT nanoparticles synthesized with HCl. The Raman intensity increases with the HCl concentration, indicating a higher polymerization degree with HCl. The absorbance increases in the polarionic and bipolaronic region with the HCl concentration as shown in Figure 3.50(b). This fact indicates a big number of polymer chains in an oxidation state, for this reason the increment in Raman is not due to the presence of neutral π -bonds but also by the increase in the polymerization degree of PEDOT.

The electrical conductivity and the Seebeck coefficient have been measured in the PEDOT nanoparticles films synthesized using DTAB as a surfactant. The results are plotted in Figure 3.51. The electrical conductivity decreases with the DTAB concentration in both cases, when the molar ratio EDOT:Fe-Tos is 1:1 (Figure 3.51(a)) and 1:2 (Figure 3.51(b)), being, in general terms, the electrical conductivity higher at a molar ratio 1:2. This behavior is due to an increase in the doping level of the PEDOT chains. However, the reason of the decrease of the electrical conductivity as a function of the DTAB concentration can be explained looking at the polymerization process. The DTAB stabilizes the EDOT drop in the miniemulsion, so this drop are positively charged due to the presence of DTAB in the interface. As the oxidant (Fe^{+3}) is also positively charged, there are electrostatic repulsion that makes difficult the approximation of Fe^{+3} to EDOT drop, so consequently the polymerization is inhibited as the DTAB concentration increases. The Seebeck coefficient describes a very rare behavior. For the case of the PEDOT nanoparticles at molar ratio EDOT:Fe-Tos 1:1 the Seebeck coefficient is positive, $22 \mu\text{V/K}$ at DTAB concentration of 0.0035 M , however when the concentration of DTAB increases to 0.035 M the Seebeck coefficient change to negative values, indicating a strong change in the

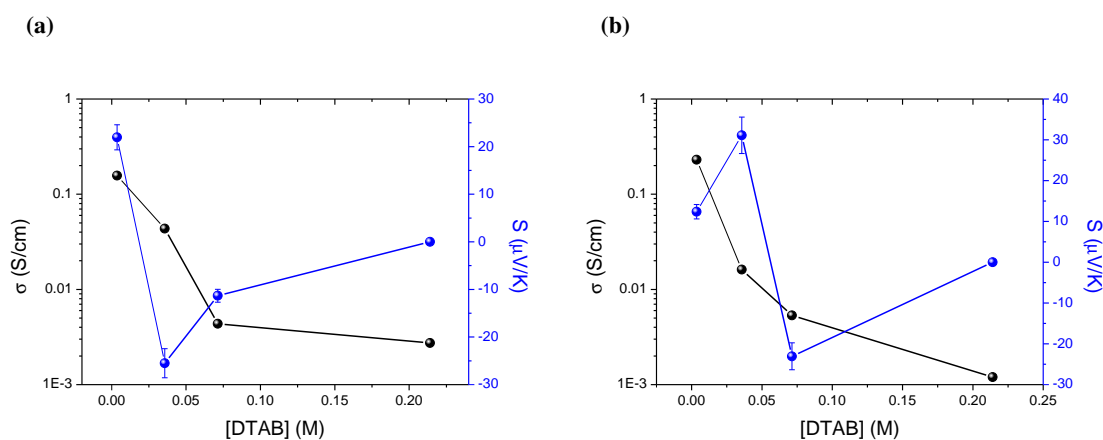


Figure 3.51 Electrical conductivity and Seebeck coefficient of PEDOT nanoparticles as a function of DTAB concentration using a molar ratio EDOT:Fe-Tos (a) 1:1 and (b) 1:2.

semiconducting behavior to n-type semiconductor. Then, the Seebeck coefficient decreases until indeterminable values. Similar trend has been observed for the case of PEDOT nanoparticles at molar ratio EDOT:Fe-Tos 1:2. The Seebeck coefficient was around $12 \mu\text{V/K}$ at 0.0035 M of DTAB, typical value for highly doped PEDOT [27, 37]. At 0.035 M of DTAB the Seebeck increases until $31 \mu\text{V/K}$, due to the decrease in the doping level of the PEDOT nanoparticles. However, when the concentration of DTAB was 0.07 M a change from p-type and n-type semiconductor is produced, achieving a Seebeck coefficient around $-23 \mu\text{V/K}$. The n-type behavior in PEDOT is not normal because during the polymerization an oxidation process is produced over the PEDOT chains, so electron are removing from the polymer generating holes and not electrons. This n-type behavior can be explained by the stabilization of an intermedium oxidation state with free electrons as charge carriers.

Figure 3.52 shows the Raman spectra of PEDOT nanoparticles PEDOT nanoparticles synthe-

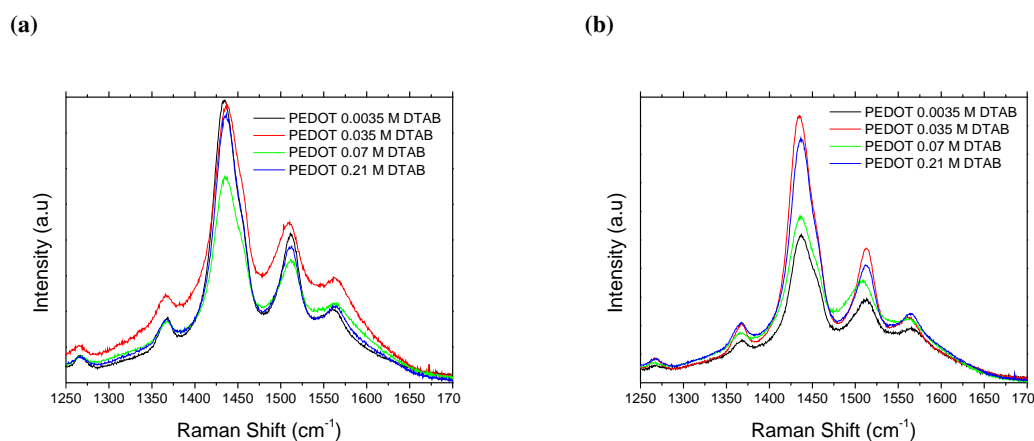


Figure 3.52 Raman spectra of PEDOT nanoparticles as a function of DTAB concentration using a molar ratio EDOT:Fe-Tos: (a) 1:1 and (b) 1:2.

sized using DTAB as surfactant with different EDOT:DTAB molar ratios. For the case of the samples using a molar ratio 1:1 (Figure 3.52(a)), the Raman intensity between the samples is very similar indicating the presence of neutral π -bonds typical for medium doped PEDOT. However, the sample with 0.07 M of DTAB presents lower intensity than the other samples, probably due to a some electronic alteration in the π -bond conjugated system. Figure 3.52(b) shows the Raman spectra of PEDOT nanoparticles at molar ratio 1:2. The particles synthesized at 0.0035 M of DTAB presents the lowest Raman intensity due to the lack of neutral π -bonds along the polymer chains, indicating a high doping level of PEDOT. This fact is normal due to a double content of iron in the solution. At 0.035 M of DTAB the intensity increases indicating de-doping process along the PEDOT chains, for this reason the Seebeck coefficient is higher at this concentration. However, when the concentration of DTAB increases, until 0.7 M the Raman intensity decreases again. That fact indicates that the conjugated π -bonds can be affected for another oxidation process, generating the change to n-type semiconductor as has been evidenced in the Seebeck coefficient measurements.

Figure 3.53 shows Uv-Vis spectra of PEDOT nanoparticles as a function of DTAB concentration

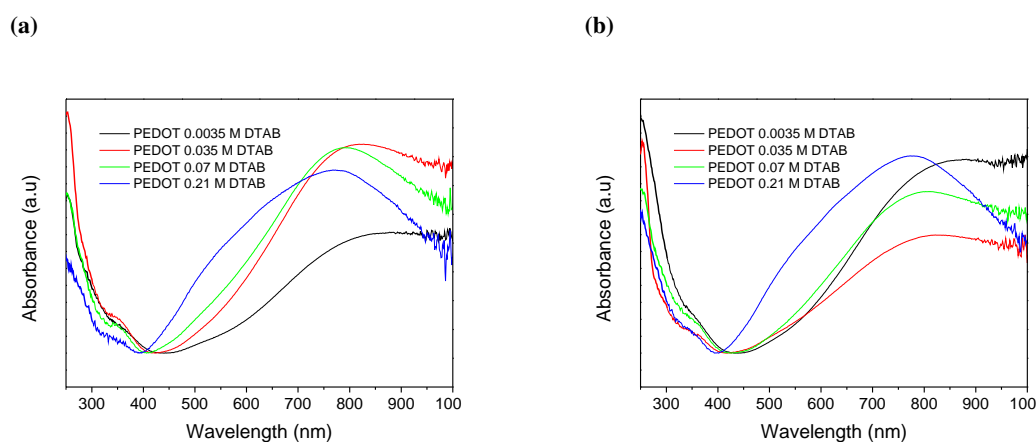


Figure 3.53 Uv-Vis spectra of PEDOT nanoparticles as a function of DTAB concentration using a molar ratio EDOT:Fe-Tos: (a) 1:1 and (b) 1:2.

using a molar ratio EDOT:Fe-Tos 1:1 and 1:2. The PEDOT nanoparticles synthesized at 0.21 M of DTAB show higher absorption in the region between 500-600 nm corresponding with the electronic transition of the electrons in the neutral π -bonds, indicating a very low doping level compared with the remaining samples. In general terms, the absorption in the region between 500-600 nm is higher in the samples prepared with a molar ratio 1:2. This trend is normal since a higher concentration of the oxidant implies higher doping level as has been observed in the previous results. In the polaronic and bipolaronic region, 800-1000 nm, a strong absorbance has been observed for the PEDOT nanoparticles in both cases. However, the films with a n-type behavior show a shift of the maximum in the polaronic and bipolaronic region to lower wavelengths.

3.6 Nanostructuring of PEDOT using hard template methods

3.6.1 Materials

EDOT, lithium perchlorate (LiClO_4), ethanol and sodium hydroxide were purchased from Sigma Aldrich and used as received without further purification.

3.6.2 Synthesis of PEDOT nanowires

PEDOT nanowires were synthesized by an electrochemical polymerization method in porous alumina templates (Whatman anodisc 13) previously covered on one side with a gold layer (thickness of 20 nm). A solution with 0.01 M of EDOT and 0.1 M of LiClO_4 was prepared in acetonitrile. The electropolymerization was carried out in an IVIUM n-stat multi potentiostat at 3 mA. The alumina template was used as the working electrode, a platinum grid was used as a counter electrode and an Ag/AgCl electrode was used as the reference one. After the reaction, the alumina template was removed by using a 6 M NaOH aqueous solution. Finally, the PEDOT nanowires were dispersed in ethanol by ultrasonic treatment and the solvent was evaporated in vacuum conditions at room temperature. The synthesis process is summarized by scheme of Figure 3.54 .

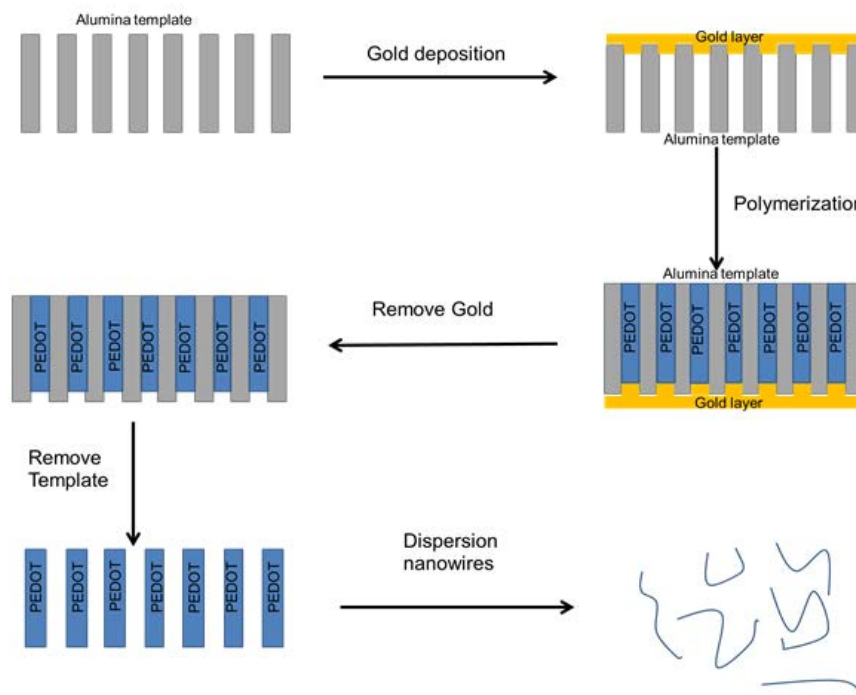


Figure 3.54 Scheme of PEDOT-NW synthesis.

3.6.3 Morphology of PEDOT nanowires

The polymerization of PEDOT was carried out inside of the alumina template porous. For this reason the final morphology is given by the shape of the porous of the alumina membrane. The alumina templates used in this study, had a pore diameter around 200 nm and their thickness was 60-70 μm . So, the diameter of the nanowires was fixed at 200 nm and the length was controlled depending on the experimental conditions during the synthesis.

Figure 3.55(a) shows SEM images of the alumina membrane before the synthesis of PEDOT. It

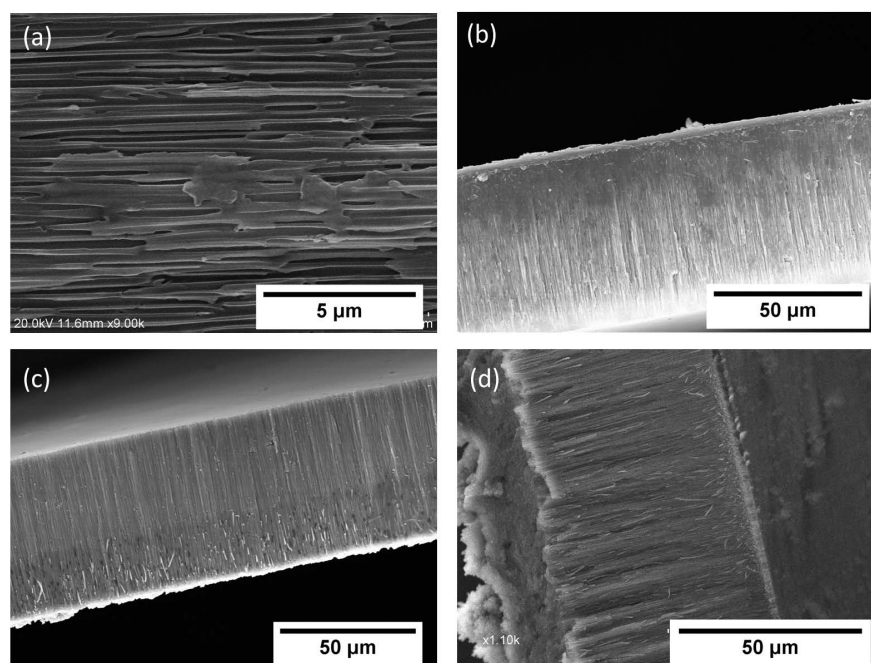


Figure 3.55 SEM images of the cross section of the alumina templates used in the PEDOT nanowires synthesis: (a) native membrane, (b) 4 hours at 3 mA, (c) 8 hours at 3 mA and (d) 8 hours at 6 mA.

is possible to observe how the channels are completely parallel in the template. Figure 3.55(b) shows the cross section after 4 hours of PEDOT synthesis at 3 mA. Only a small part of the template has been filled with the nanowires, achieving a length around $(13 \pm 1) \mu\text{m}$. The length, when the polymerization time was 8 hours, was $(22 \pm 2) \mu\text{m}$. However, in order to attain higher length of the nanowires using less polymerization time, the intensity during the synthesis was increased to 6 mA achieving a completely filled alumina after 8 hours of polymerizations, as shown in Figure 3.55(d). At this time the polymerization process occurs also on the top of the membrane, outside the channels creating a continue PEDOT film on the top of the alumina membrane.

Figure 3.56 shows the SEM images of the PEDOT nanowires synthesized during 8 hours at 3 mA after template removal using NaOH 6M. The PEDOT nanowires show a homogeneous

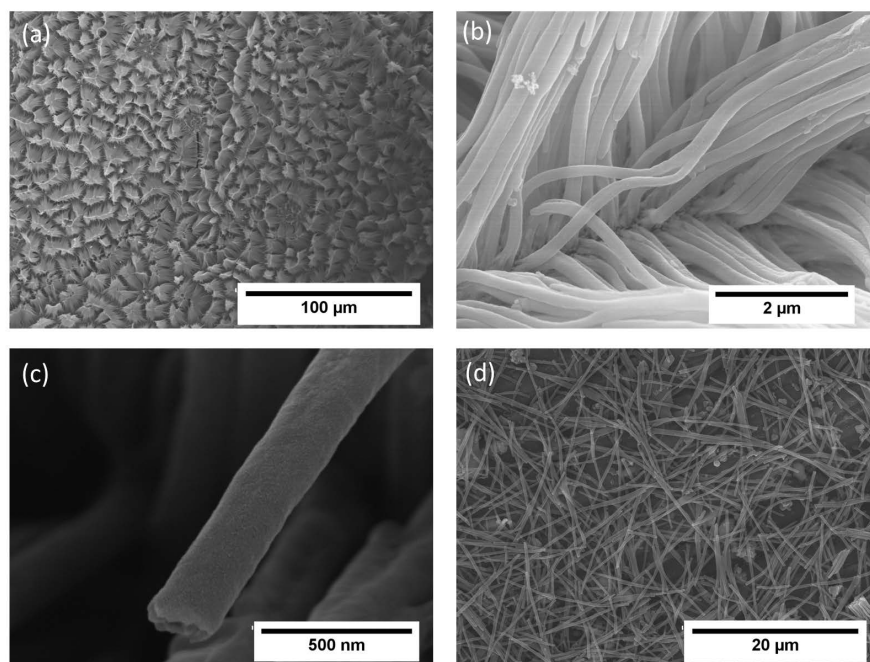


Figure 3.56 SEM images of PEDOT nanowires (a), (b), (c) after template removal and (d) after dispersion.

distribution in large surface as shown in Figure 3.56(a). This fact is very important in order to incorporate these structures in devices where a large surface area is needed. Figures 3.56(b) and (d) show the PEDOT nanowires in a higher magnification. It is possible to observe how the diameter is almost the same in all the nanowires, indication of monodispersity in terms of diameter (200 nm). The dispersion treatment using ultrasounds produces single nanowires as shown in Figure 3.56(d). However, the initial length of the nanowires ($22 \pm 2 \mu\text{m}$) is reduced until 8-16 μm due to the ultrasound treatment.

3.6.4 Future application of PEDOT nanowires

Using the hard template method, PEDOT nanowires have been synthesized. The nanowire structure can be very interesting from the point of view of thermoelectric generators due to the reduction of the thermal conductivity of the thermoelectric elements in the thermocouples. Also, the nanowires can be used in the miniaturization of thermoelectric generators. The problem is how to characterize the thermoelectric properties of a single nanowire. Fortunately, using lithographic techniques it is possible to fabricate electronic chips in the nanoscale capable to measure the electrical conductivity and the Seebeck coefficient for a single PEDOT nanowire. Figure 3.57 shows a scheme of the future measurement chips to characterize a single PEDOT nanowire. The image of the left represents a 4 electrical contacts with the mission to measure the electrical resistance using the 4 wire method in order to avoid the resistance of the electric contacts. The scheme of the right can be used for the measurement of Seebeck coefficient in

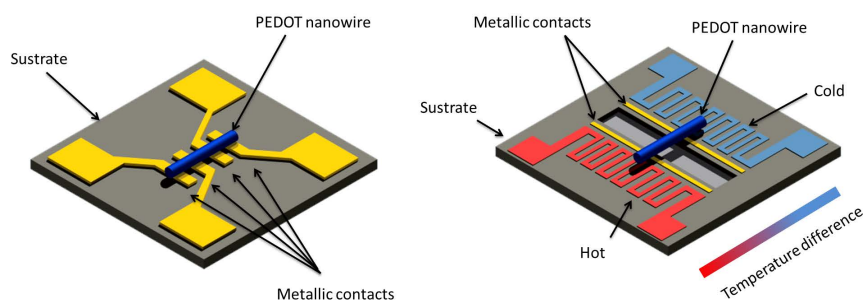


Figure 3.57 Scheme of electrical conductivity (left image) and Seebeck coefficient (right image) measurement of a single PEDOT nanowire.

a single PEDOT nanowire. The chip consists of two electrical resistors one is for heating and the other one is used as a heat sink, so it is possible to generate a temperature difference using this electrical resistors along the PEDOT nanowire. The voltage associated to this temperature difference can be recovered by the two metallic contacts.

3.7 Conclusions

In this chapter several routes to increase the thermoelectric efficiency of conducting polymers have been studied. The addition of DMSO to PEDOT:PSS solutions produces an increase in the electrical conductivity of the PEDOT:PSS films due to the secondary doping of the PEDOT chains. PEDOT and PPy films have been synthesized by electrochemical polymerization. The electrical conductivity decreases with the reduction time, while the Seebeck coefficient increases. A maximum ZT has been obtained for 11 seconds of reduction in the case of PEDOT:ClO₄ and PEDOT:PF₆ and 5 seconds for PEDOT:BTfMSI. These reduction times give Seebeck and electrical conductivity optimum values for a maximum thermoelectric efficiency, corresponding to the best PF. For the case of electrochemical de-doping the electrical conductivity increases at oxidative potentials for PEDOT and PPy films, while the Seebeck coefficient is higher at reduction potentials. The maximum thermoelectric efficiency has been obtained at 0.01 V for PEDOT and at 2.0 V for PPy. PEDOT nanoparticles have been obtained using polymerization in miniemulsion. The electrical conductivity increases with the contraction of Fe-Tos. The spherical morphology is only obtained with the presence of H₂O₂ during the synthesis. However, the electrical conductivity of the nano-spheres decreases with the concentration of H₂O₂ due to secondary reactions between the hydroxide radicals and the PEDOT chains. The synthesis of PEDOT nanoparticles using a positive charged surfactant (DTAB) produce a transition between p-type to n-type semiconductor. In addition, higher concentrations of DTAB inhibits the PEDOT polymerization. Finally, PEDOT nanowires with a 200 nm of diameter have been synthesized using alumina templates.

Chapter 4

Non conventional inorganic thermoelectric materials

Content

This chapter addresses the study of the thermoelectric properties of inorganic materials that are uncommon in thermoelectric applications such as metallic oxides (perovskites) and carbonaceous materials (carbon black). The chapter has been divided in four sections: an introduction, an experimental study of two types of perovskite nanostructures ($\text{Nd}_{1-x}\text{Ca}_x\text{CoO}_3$ and $\text{La}_{1-x}\text{Ca}_x\text{MnO}_3$), other experimental work devoted to carbonaceous materials (charcoal, vitreous carbon and carbon black) and finally, the conclusions.

4.1 Introduction

Inorganic semiconductors and semiconductor compounds are the most common materials used in thermoelectric applications. Among these compounds, semiconducting alloys and intermetallic materials are predominant over the rest. As it can be observed in Figure 4.1, ZT has been increased by a factor of 2 in the last ten years [126]. Values of ZT higher than 2 ($\sim 15\%$ of efficiency) are necessary for the fabrication of competitive thermoelectric generators. The most predominant semiconductor compounds used in nowadays thermoelectric devices are based on Bi, Te, Pb and Se. The use of these kind of chemical elements in the fabrication of semiconductor compounds or alloys generates serious problems as it has been commented in the previous chapters. Bismuth and tellurium are rare elements and their abundance in the Earth crust is very low, what implies high cost of the raw materials. Lead is one of the most toxic metals prodding abdominal pain, constipated, tired, headache, irritable, loss of appetite, memory loss, pain or

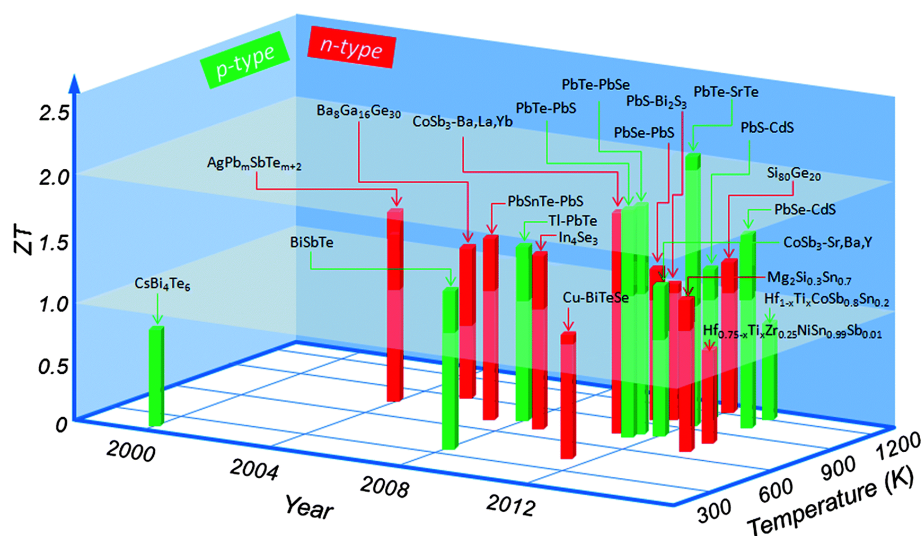


Figure 4.1 ZT of inorganic thermoelectric materials used for different temperature applications over the years. Reprinted from [126] with permission from The Royal Society of Chemistry.

tingling in the hands and/or feet and weak in short-term overexposure to lead [127]. Selenium can be also very toxic for humans, the adverse effect over the human health highlights: the toxic effect on the synthesis of thyroid hormones, hepatotoxicity, gastrointestinal disturbances, hair loss and dermatitis. From the drawbacks given below, it is clear that new methods of synthesis have to be explored in order to produce non-toxic and low cost thermoelectric devices with a high figure of merit.

4.1.1 Alternative inorganic materials to bismuth, antimony, tellurium and lead compounds

As it has been commented in the previous section, there is a high interest to find new thermoelectric materials capable to compete with the most traditional materials, semiconducting alloys of Bi, Sb, Te and Pb. In this subsection, we will discuss the fundamental aspects of clathrates, skutterudites, half Heusler compounds, metallic oxides and carbonaceous materials.

4.1.1.1 Clathrates

The inter-metallic compounds, called clathrates, have attracted the attention of many researchers in the last years due to their high potential in thermoelectric applications. These compounds are bulk solids with tetrahedrally bonded atoms in a framework of cages enclosing guest metal atoms. The clathrates have been known since the work of Cros. *et al* [128] and Kasper. *et al* [129] on $\text{Na}_8\text{Si}_{46}$ and $\text{Na}_x\text{Si}_{136}$ [129]. They have crystal structures closely related to those of type I and type II clathrate hydrates with compositions such as $(\text{Cl}_2)_8(\text{H}_2\text{O})_{46}$ and $(\text{CO}_2)_{24}(\text{H}_2\text{O})_{136}$, respectively. The type I structure can thus be represented by the general formula $\text{X}_2\text{Y}_6\text{E}_{46}$ while

the type II structure by $X_8Y_{16}E_{136}$. Here, X and Y are “guest” atoms encapsulated into two different polyhedra while E represents Si, Ge, or Sn. Figure 4.2 shows the type I and type II

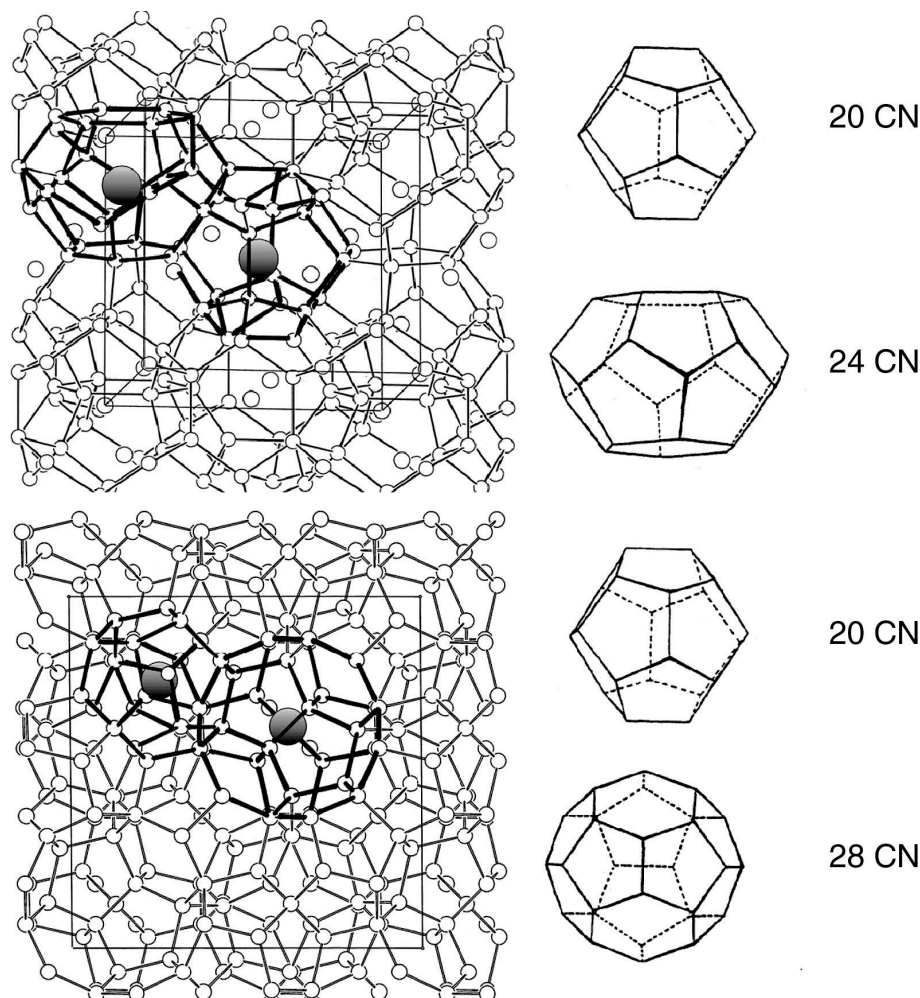


Figure 4.2 The building-blocks of the type I (top) and II (bottom) clathrates with guest atoms inside the polyhedra that form the unit cell of these two structure types. Reproduced from [47] with permission of TAYLOR and FRANCIS.

structures [47]. The type I structure is formed by two pentagonal dodecahedra (middle) and six lower symmetry tetrakaidecahedra in the cubic unit cell connected by shared faces. The type II structure is formed by 16 dodecahedra and eight hexakaidecahedra (middle). The open circles represent group-IV atoms that comprise the framework while the dark circles inside the polyhedra represent guest atoms. It is instructive to think of these structures as being constructed from two different face-sharing polyhedra: two pentagonal dodecahedra, and six tetrakaidecahedra per cubic unit cell in the case of the type I structure, and 16 dodecahedra and eight hexakaidecahedra for the type II compounds [47].

The typical way to synthesize these compounds is through direct reaction of the elements or pre-reacted binary precursors at high temperatures via solid-solid, solid-liquid, or gas-solid-liquid reactions. Alternative to the classical solid state reaction, it is possible to use other

method to synthesize these inter-metallic compounds such as thermal decomposition of metal-rich precursors, soft chemical routes or synthesis using high pressure [130].

In terms of thermoelectric properties of clathrates, highlights their low thermal conductivity smaller than $2 \text{ W/m}^{-1}\text{K}^{-1}$ due to their complex structure that increases the phonon scattering. The maximum ZT of these compounds is given at medium and high temperature, achieving values between 0.5-1.4 for $\text{Ba}_8\text{Ga}_{15.8}\text{Cu}_{0.02}\text{Sn}_{30.1}$, $\text{SrGa}_{16}\text{Ge}_{30}$, $\text{Eu}_8\text{Ga}_{16}\text{Ge}_{30}$, $\text{Sr}_8\text{Al}_{16.3}\text{Ga}_{10.3}\text{Ge}_{29.4}$, $\text{Ba}_8\text{Ga}_{16}\text{Ge}_{30}$ and $\text{Ba}_8\text{Al}_{14}\text{Si}_{31}$.

4.1.1.2 Skutterudites

The skutterudites (name from a small mining town, Skutterud, in Norway) compounds correspond with the composition MX_3 where M is a metal atom such as Co, Rh, or Ir, and X represents a pnictogen atom such as P, As, and Sb. Skutterudites present a body-centered-cubic structure form belonging to the space group $Im\bar{3}$. The structure is often depicted as in Figure 4.3 where

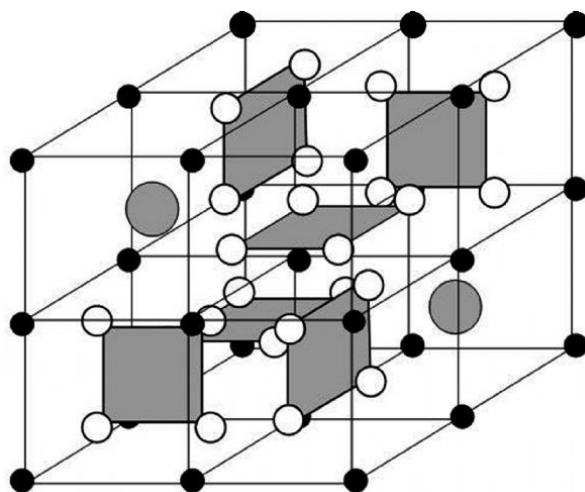


Figure 4.3 Crystal structure of skutterudites with the metal atoms M (open circles), the pnictogen atoms X (solid circles) arranged in planar, near-square four-membered rings. The other two circles are voids, which are often found by other elements to form a completely filled structure. Reprinted from [131].

the unit cell is displaced by a one-quarter distance along the body diagonal [131]. In this form it is easy to understand the open nature of the structure — only six of the available eight small cubes contain planar near-rectangular rings of pnictogen atoms. Two of the eight cubes remain empty, forming the voids of the structure. The open structural nature of skutterudites creates a big versatility, since filling the voids with foreign species, such as ions of rare-earths can develop a huge number of compositions. The filling process results in the formation of filled skutterudites, which facilitates the modification of the electronic and lattice properties, and greatly

enhances the figure of merit. A general formula describing a filled skutterudite compound is $R^{4+}[T_4X_{12}]^{4-}$, where R is an electropositive filler ion and the exponents indicate the charge balance. The resulting charge in $[T_4X_{12}]^{4-}$ comes when the group IX cobalt-like metals of binary skutterudites are replaced with the group VIII metals such as Fe, Ru, or Os. While binary skutterudites with the group VIII metals do not form because of the obvious charge imbalance, the filler ion R supplies the missing electrons, saturates the bond, and electrically neutralizes the structure. Also, it is possible to modify the charge compensation exchanging the pnictogen atoms for group IV elements such as Ge or Sn. These modifications creates the possibility of a big number of compounds with a large variety of properties such as superconductivity, [132] long-range magnetic order,[133] heavy fermion behavior [134], non Fermi-liquid state [135], mixed valence [136] and others.

To synthesize the skutterudites compounds, the solid state reaction is the most used method. The key to have a successful crystal growth is a thorough understanding of the respective phase diagram that describes thermodynamic equilibrium between various phases of the system. Polycrystalline structures can also be synthesized by the solid-liquid sintering process. This consists of sealing stoichiometric amounts of the constituent elements in an evacuated quartz ampule and heating the mixture for a prolonged time at temperatures just below the peritectic temperature. Other method such as chemical vapor transport can be employed to synthesize skutterudites.

From the point of view of the thermoelectric properties, the skutterudites have achieved very interesting values in terms of ZT in both n and p-type semiconductors. For the case of n-type highlights $Sr_{0.09}Ba_{0.11}Yb_{0.05}Co_4Sb_{12}$ with a ZT around 1.8 and for p-type highlights $CeFe_{3.5}Co_{0.5}Sb_{12}$ with a ZT around 1.4 in the temperature range 700-900°C.

4.1.1.3 Metallic Oxides

Metallic oxides have become very important from the point of view of thermoelectric application due to their many advantages such as: non toxicity, thermal stability, high oxidation resistance, etc. Since the discovery of Na_xCoO_2 , cobalt-oxide-based layer-structured crystals and their derivative compounds [137, 138], it has been considered a great thermoelectric materials achieving ZT values close to 1 or higher. Layered cobalt oxides are able to control the thermoelectric properties, high electrical conductivity, large thermopower, and low thermal conductivity simultaneously through the concept of the nanoblock integration. In these oxides, CoO_2 nano-sheets possess a strong way for electronic transport layers, while sodium ion nanoblock layers or calcium cobalt oxide misfit layers are perfect regions for phonon scattering giving low thermal conductivity. The nanoblock integration can generate high thermoelectric performance from hybrid crystals that are composed by periodic combinations of nano-blocks or nano-sheets possessing different role in the thermoelectric properties [139]. Figure 4.4 shows the scheme of

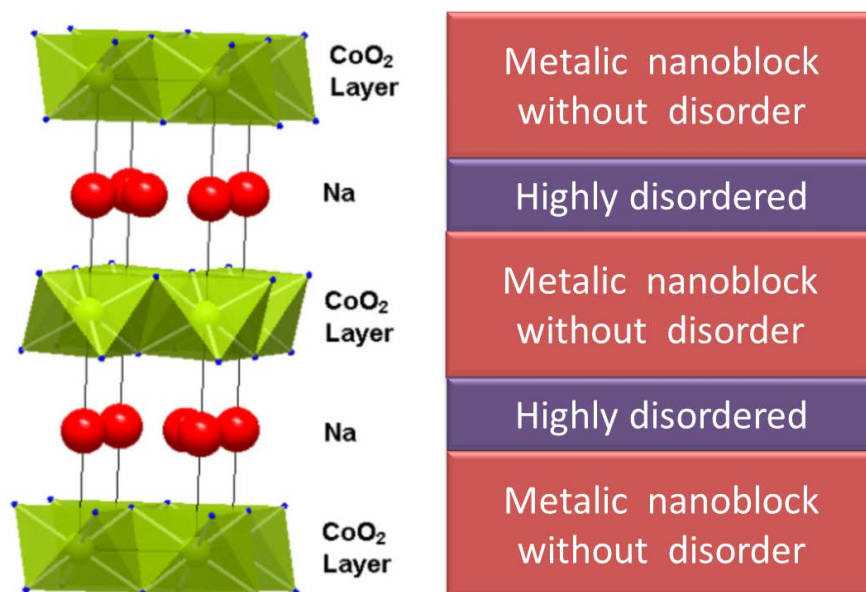


Figure 4.4 Crystal structure of layered cobalt oxides Na_xCoO_2 . Reprinted from [138] with permission of Elsevier.

the nanoblock integration in the Na_xCoO_2 crystalline structure. A cobalt ion is in the center of a distorted oxygen octahedra with little vacancies, while a Na^+ ion is in the prism site between the CoO_2 blocks. The Na^+ ions randomly occupy the site, and are highly disordered.

Other kind of oxides, called perovskite oxides, have also been attracted the attention due to their potential as thermoelectric materials. The ideal perovskite is given by the stoichiometry ABO_3 , where A is typically a rare-earth, alkaline-earth or alkali cation and B is a 3d, 4d, or 5d transition metal. The crystal structure of perovskite oxides is shown in Figure 4.5 for the case of SrTiO_3 .

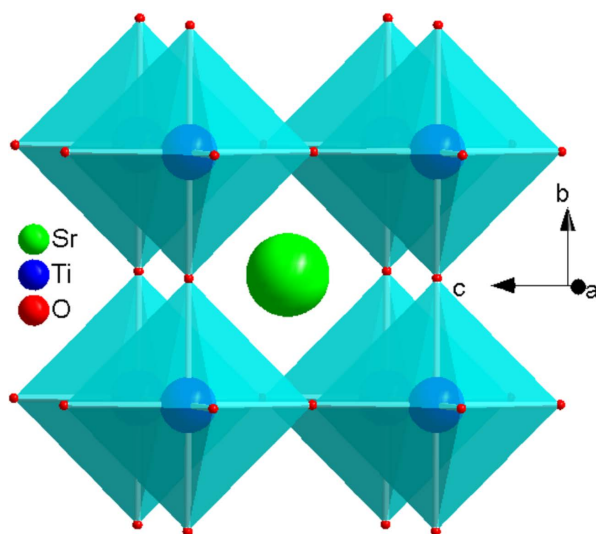


Figure 4.5 Crystal structure of SrTiO_3 perovskite. Reprinted from [139] with permission of Springer.

The cation A is located in the center of the unit cell while the cation B is located in the vertex of the unit cell coordinated with O atoms in an octahedral environment [139].

Perovskite oxides have very interesting properties such as high-temperature superconductivity, colossal magnetoresistance, ferroelectricity, and thermoelectricity due to their flexible crystal structure. Perovskite such as cobaltates, titanates, and manganates have achieved high thermoelectric properties at high temperatures since it is possible to dope through the substitution of the A and B cationic sites. Other characteristic property is their high Seebeck coefficient around 800-1000 $\mu\text{V/K}$ for the case LaCoO_3 or NdCoO_3 [140, 141]. Through the doping by changing the A metal, it is possible to control the semiconductor behavior (n-type and p-type). For example, the LaMnO_3 is typically a p-type semiconductor, however when La is exchanged by Ca the material becomes a n-type semiconductor [142]. Other kind of perovskites can be employed in thermoelectric applications such as: double perovskite with the general formula $\text{A}_2\text{B}'\text{B}''\text{O}_6$ or $\text{A}_3\text{B}'\text{B}''_2\text{O}_9$, where B' and B'' are different cations in octahedral coordination, or layered perovskite oxides. These oxides consist of infinite two-dimensional (2D) slabs of ABO_3 -type structures which are separated by some motif, for example the compound $(\text{SrO})(\text{SrTiO}_3)_m$. Following the nanoblock integration in these compounds, it is possible to achieve very interesting values of ZT [47].

The synthesis of these compounds can be done using several methods. One of those is the traditional ceramic method using solid state reactions. The metallic precursors are mixed together and heated at higher temperatures during long times. However, it is possible to use solution methods to prepare these metallic oxides, for example hydrothermal synthesis [143, 144] or colloidal methods (inverse emulsion, inverse mini-emulsion or inverse micro-emulsion) [145].

4.1.1.4 Half-Heusler compounds

The first Heusler compound was synthesized in 1903 by Heusler with the composition Cu_2MnAl [146]. This material and its derivative compounds are known as Heusler and half-Heusler. One class of these compounds present semiconducting behavior making very interesting their use in thermoelectric applications. Their band gaps can readily be tuned from 0 to 4 eV by changing their chemical composition. Compounds with eight valence electrons per formula unit are closely related to classical semiconductors, such as silicon and GaAs. However, the design of unconventional semiconductors based on 18 valence electrons for half-Heusler compounds or 24 for Heusler compounds is also possible, resulting in band gap widths of more than 1 eV. The half-Heusler compounds have a ternary stuffed variant of classical electron closed-shell semiconductors which crystallize in a zinc-blende lattice. The 8 valence electrons are distributed along three atoms instead of two. This produces that the third atom occupies the octahedral vacancies in the ZnS-type lattice. Consequently, a rocksalt-like sublattice is formed with ionic

bonding interaction. The Heusler compounds contains transition metals with almost completely filled d-electron. Nowadays, in the field of thermoelectricity highlights compounds based on NiTiSn for the n-type and CoTiSb for the p-type materials, showing very high values of ZT at medium range temperature. The composition Sb-doped NiTi_{0.50}Zr_{0.25}Hf_{0.25}Sn achieved a ZT of 1.5 at 700 k being the highest value for these compounds [147].

4.1.1.5 Carbonaceous materials

Recently, low dimensional carbon structures such as graphene and CNTs or C₆₀ have been attracting the attention in thermoelectric applications [148]. Most of the studied are centered in the use of these carbon materials as a filler in a conductive polymer matrix [20] in order to increase the thermoelectric performance of the final materials. Basically, the problem of these compounds to be used alone (not as filler in a polymer matrix) is their high thermal conductivity (1000-3000 Wm⁻¹K⁻¹) [149] and also their high cost. However, there are other carbon materials such as carbon black or graphite, cheaper than the low dimensional carbon materials, with interesting thermoelectrical properties. Carbonaceous materials are of special interest in the field of thermoelectricity since they can be doped and behave as an n- or p-type semiconductors [150, 151]. Hydrogen is a simple element which can be added to the carbonaceous material and alter its electrical and thermoelectric properties [152]. The hydrogen present in a carbonaceous material can be either existent in the raw material or be incorporated in the production process [151, 153]. Actually, hydrogen is capable of converting a n-type carbonaceous material into p-type [154, 155]. One interesting way of incorporating hydrogen in a carbonaceous material is to insert the material into an over-pressurized hydrogen atmosphere. The absorption process is mainly controlled by the porosity of the material [154, 156], thus the typical process consists of an acid etching of the surface [155, 157] producing pitting and thus an increase of the hydrogen storage capacity [156, 158]. The restriction of this chemical treatment is the fact that the etching commonly acts only on the material surface. Therefore, the absorber materials should be very fragmented and it generally supposes an increase of production costs. Thus, the possibility to irradiate the carbons with γ -rays could be interesting because such irradiation activates the surface of carbons [159]. Beside of this, γ -irradiation produces damages in the inner crystalline structure of the solids [157, 160, 161]. Therefore, the irradiation can be used to promote simultaneously a hydrogenation in the surface and in the bulk of the material [158, 162, 163]. It is remarkable that a hydrogen bond on a carbon surface takes place just on a small breakage of the crystal structure [159, 164], and during an activation with γ -rays nano-defects of this type are produced. In this chapter, the thermoelectric behavior of three different carbons materials, carbon black, glass carbon and charcoal, have been studied under the influence of several treatments such as: γ -rays irradiation or acid etching.

4.1.2 Low dimensional thermoelectric materials

The thermoelectric area was developed rapidly in the 1950s when the basic science of thermoelectric materials was well established, the role of doped semiconductors as thermoelectric materials was accepted, the apparition of bismuth telluride and its development for commercialization, and the thermoelectric industry was launched. At that time, it was established that the thermoelectric efficiency could be described in terms of the dimensionless thermoelectric figure of merit. During the next three decades, 1960 to 1990, small increment were done in ZT, with Bi_2Te_3 becoming the best material with a ZT value close to the unit. During this period, the research in thermoelectric received little attention from the scientific world. In the decade of 1990, the US Department of Defense showed interest in the potential of thermoelectricity for new types of applications and technology, consequently, many researches become interested in thermoelectric materials. So, two different research approaches were taken for developing the next generation of new thermoelectric materials, one using new families of bulk materials and the other using low-dimensional materials systems [47].

There are several ways to increase the thermoelectric performance using the concept of low-dimensional material. Since the electrical conductivity, the Seebeck coefficient and thermal conductivity are related and dependent in conventional three-dimensional (3D) crystalline systems, thus it is very difficult to control these variables independently in order to increase ZT. However, if the dimensionality is reduced, the new variable of size becomes available. As the size approaches nanometer length scales, it is possible to cause dramatic differences in the density of electronic states (DOS) as shown in Figure 4.6. This fact creates new ways to modify the Seebeck coefficient, electrical and thermal conductivity independently. In addition, the introduction of many interfaces increase phonon scattering more than electron scattering; consequently the electrical conductivity is no affected so much. However, the thermal conductivity decreases by interface scattering processes. One of the most used ways to increase ZT for low-dimensional materials is based on strategies to reduce the thermal conductivity, for example by increasing the presence of interfaces which scatter phonons more effectively than electrons. However, the ZT increase by a high factor is not only important to decrease the thermal conductivity, but it is important factor to increase is the power factor. There are several ways to increase the PF. For example to use bulk materials with a large maximum in the electronic density of states (DOS), such as transition metals or heavy fermion systems, and then moving the Fermi level forwards the maximum in the DOS. By reducing the dimensionality in bulk materials, it is possible to achieve the metal to semiconductor transition (Mott transition). When the quantum well width or quantum wire diameter decreases below a critical size, a semimetal semiconductor transition takes place [165]. Using this evidence, bismuth, with a very low thermoelectric efficiency (in bulk), can be a very good low-dimensional thermoelectric material. Bi has a very low band overlap energy, so the transformation to semiconductor can be given by preparing it as a nanowire.

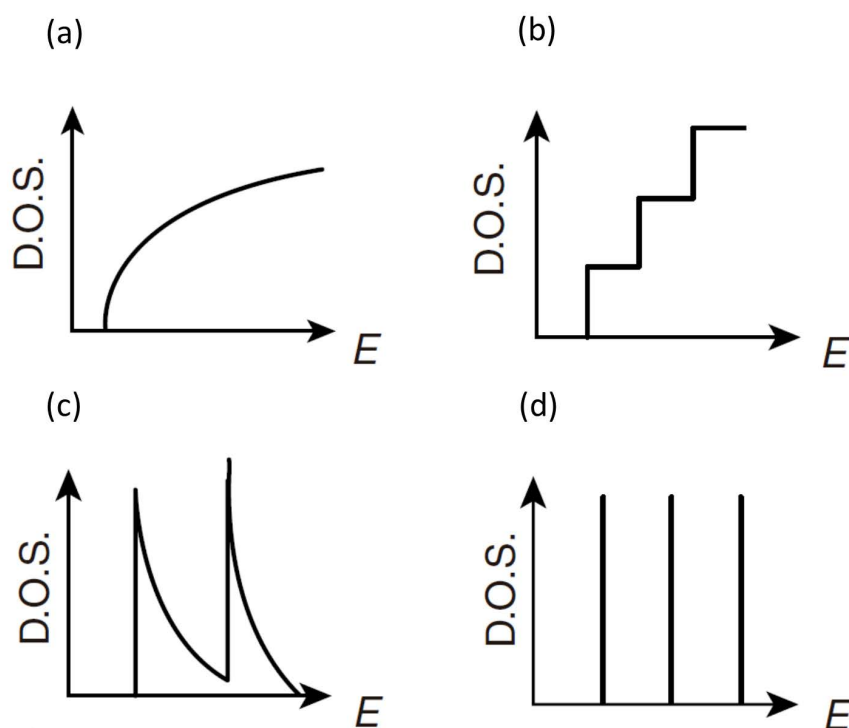


Figure 4.6 Density of states for (a) a bulk 3D crystalline semiconductor: (b) a 2D quantum well, (c) a 1D nanowire or nanotube, and (d) a 0D quantum dot. Reproduced from [47] with permission of TAYLOR and FRANCIS.

Nanowire nanostructures give rise to quantum confinement and subbands through the superlattice periodicity. For this reason, if subbands are formed in the valence and conduction bands, the lowest lying subband for the conduction band rises in energy as the quantum confinement length (as for example, the nanowire diameter) decreases, and likewise the highest lying valence subband falls in energy, until these subbands eventually cross and a semiconductor is formed [47]. Figure 4.7 shows the Seebeck coefficient of Bi nanowires, synthesized by vapor growth method using hard templates with a different pore diameter, as a function of temperature. The Seebeck coefficient strongly depends on the diameter of the nanowire. Compared with bulk material, the nanowires with a very low diameter present a very high Seebeck coefficient [47]. This experiments are the prove of that, the PF can be increased just trough the nano-structuration of bulk materials. Theoretical calculations of n-type bismuth nanowires show predictions of ZT in 1D achieving very high values, for example ZT can be increased until 6 for a 5 nm Bi nanowire [166].

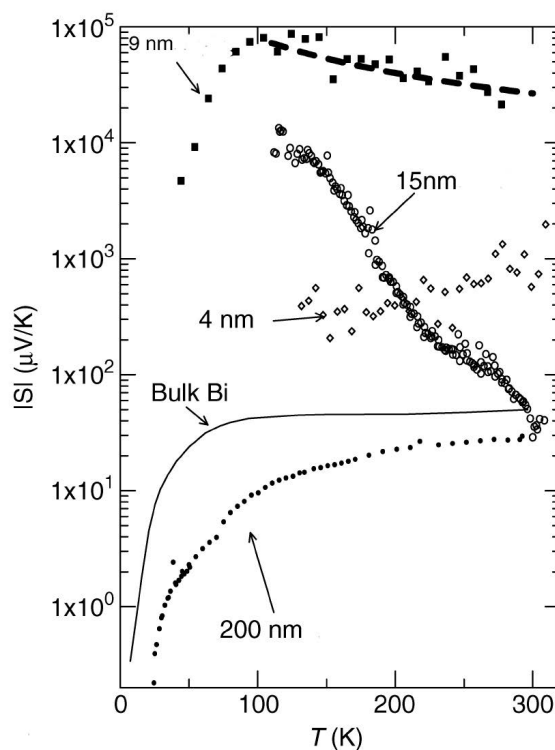


Figure 4.7 Seebeck coefficient of Bi nanowires of various diameters. Reproduced from [47] with permission of TAYLOR and FRANCIS.

4.2 Perovskite nanostructures: $\text{La}_{1-x}\text{Ca}_x\text{MnO}_3$ system³

4.2.1 Materials

The reactants, $\text{MnCl}_2 \cdot 4\text{H}_2\text{O}$, $\text{Ca}(\text{NO}_3)_2$, $\text{La}(\text{NO}_3)_3$, KMnO_4 and KOH , were purchased to Sigma Aldrich Co., Madrid, Spain.

4.2.2 Synthesis of $\text{La}_{1-x}\text{Ca}_x\text{MnO}_3$ nanostructures

$\text{La}_{1-x}\text{Ca}_x\text{MnO}_3$ samples with $x = 0.005, 0.05, 0.1$ and 0.5 have been prepared by a conventional hydrothermal treatment [144, 167, 168]. Stoichiometric amounts of reactants were used to have an aqueous solution 0.55 M in cations (Mn^{7+} , Mn^{2+} , Ca^{2+} and La^{3+}) by keeping a molar ratio between KMnO_4 and $\text{MnCl}_2 \cdot 4\text{H}_2\text{O}$ according to the average valence of Mn ions in $\text{La}_{1-x}\text{Ca}_x\text{MnO}_3$. The pH of the solution was adjusted to 13 by adding KOH . After ultrasonic stirring, the solution was transferred into a Teflon autoclave reinforced with a steel holder (see Figure 4.8) for 30 h at 230°C . Then, the reactor was cooled down to room temperature and the obtained solid was washed with distilled water and ethanol, and dried at 230°C for 12 hours.

³This section is based on the publication: "La_{1-x}Ca_xMnO₃ semiconducting nanostructures: morphology and thermoelectric properties" M Culebras, R Torán CM Gómez, A Cantarero *Nanoscale Research Letters*, 9, 415 (2014).



Figure 4.8 Photograph of a Teflon autoclave with its steel holder .

The powder was subjected to different temperatures, 650°C and 900°C, during 12 h. The powder obtained after 900°C was pressed to form compact pellets (1/2 inch of diameter) by using a pellet die at 490 MPa. The Pellet was sinterized at 900 °C for 24 h being the thickness of the Pellet in the range of 0.3-0.4 mm.

4.2.3 Morphology of $\text{La}_{1-x}\text{Ca}_x\text{MnO}_3$ nanostructures and temperature effects

Scanning electron microscopy images show the evolution of the morphology as a function of temperature treatment (Figures 4.9(a), (b) and (c)). The first temperature treatment was carried out at 230°C during 12 hours (drying treatment); the resultant morphology after this treatment is shown in Figure 4.9(a). A fibrillar morphology has been observed with the treatment, with an average diameter of (120 ± 50) nm. The second treatment was carried out at 650°C during 12 hours, leading to a change in morphology, from fibrillar to aggregated nanoparticles as shown in Figure 4.9(b). In addition, some parts of the powder retain the fibrillar morphology. Finally, the last treatment was carried out at 900°C during 12 hours, as shown in Figure 4.9(c), all the material depicts a nanoparticle structure. This evolution of the morphology with temperature is similar to other materials as $\text{La}_{1-x}\text{Sr}_x\text{CoO}_3$, previously reported in the literature [169]. Figure 4.9(d) shows the surface morphology of the pellet after the sintering process, the powder obtained after 900°C treatment were compacted and treated at 900°C again during 24 hours. The surface shows a nanostructured morphology with spherical domains around (251 ± 45) nm. The sintering process helps to get a good contact between the nanoparticles that form the pellet, creating a better path for electric transport around the compacted material, in other words, just a simple compacted powder produces a big number of interfaces creating a discontinuous path for electric transport.

Figure 4.10 shows the evolution of the morphology after the different temperature treatments

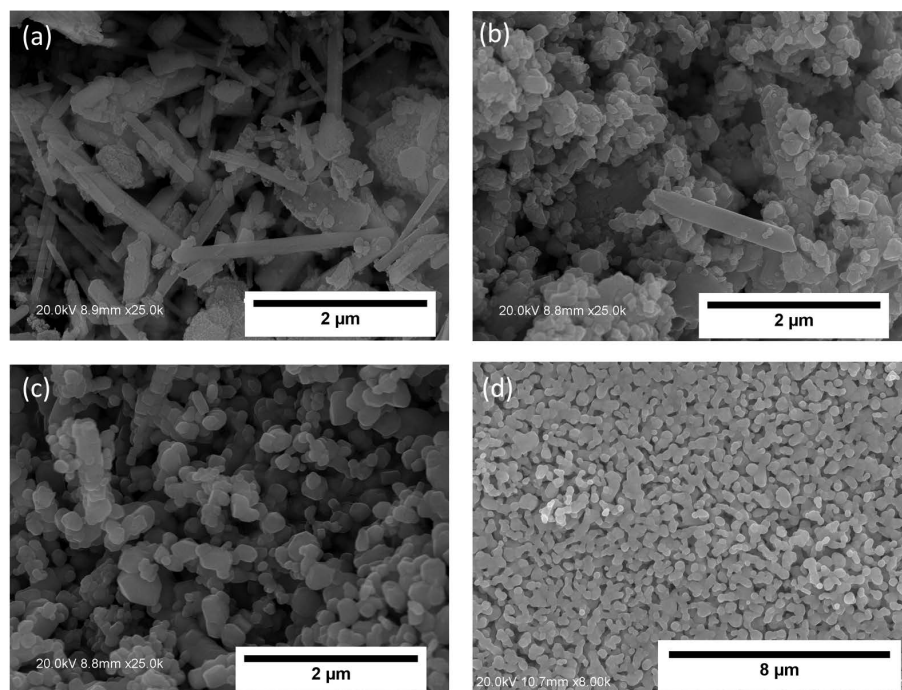


Figure 4.9 SEM images of $\text{La}_{1-x}\text{Ca}_x\text{MnO}_3$ ($x=0.05$) after different temperature treatments during 12 h: (a) 230 °C, (b) 650 °C, (c) 900 °C and (d) after sintering.

observed by TEM. As shown in the previous results observed by SEM, after the hydrothermal synthesis at 230 °C (see Figure 4.10(a)) the morphology of the nanostructures was in a nanowire shape. Figure 4.10(b) shows an histogram of the size distribution in terms of the diameter of the nanowire. The analysis of the size was carried out using several TEM images and the diameter was measured by the software "Image J", analyzing hundreds of nanowires. The maximum of size distribution of the nanowires was around 40-45 nm, as it can be observed in Figure 4.10(b). After the treatment at 650 °C the morphology change to spherical shape (Figure 4.10(c)) although it is possible to observe the presence of some perovskite nanowires. Figure 4.10(d) shows the size distribution of the nanostructures after the treatment at 650 °C, indicating a maximum around 100-120 nm. Finally, the nanowire shape was lost after the calcination at 900 °C as shown in Figure 4.10(e). As it has been observed in the SEM analysis, there were only particles with a diameter around 180 nm in the sample treated at 900 °C. The evolution of the nanostructure morphology with the calcination temperature has been observed in similar materials [169]. This fact can be explained due to the diffusion of the ions around the material changing its morphology since the calcination treatment occurs at elevated temperatures during a long time.

4.2.4 Phase transition of $\text{La}_{1-x}\text{Ca}_x\text{MnO}_3$ during the calcination process

The X-ray diffraction patterns for the $\text{La}_{1-x}\text{Ca}_x\text{MnO}_3$ ($x = 0.05$) powder, resulting from the thermal treatment at 230 °C, 650 °C, and 900 °C are depicted in Figure 4.11a. XRD analysis has

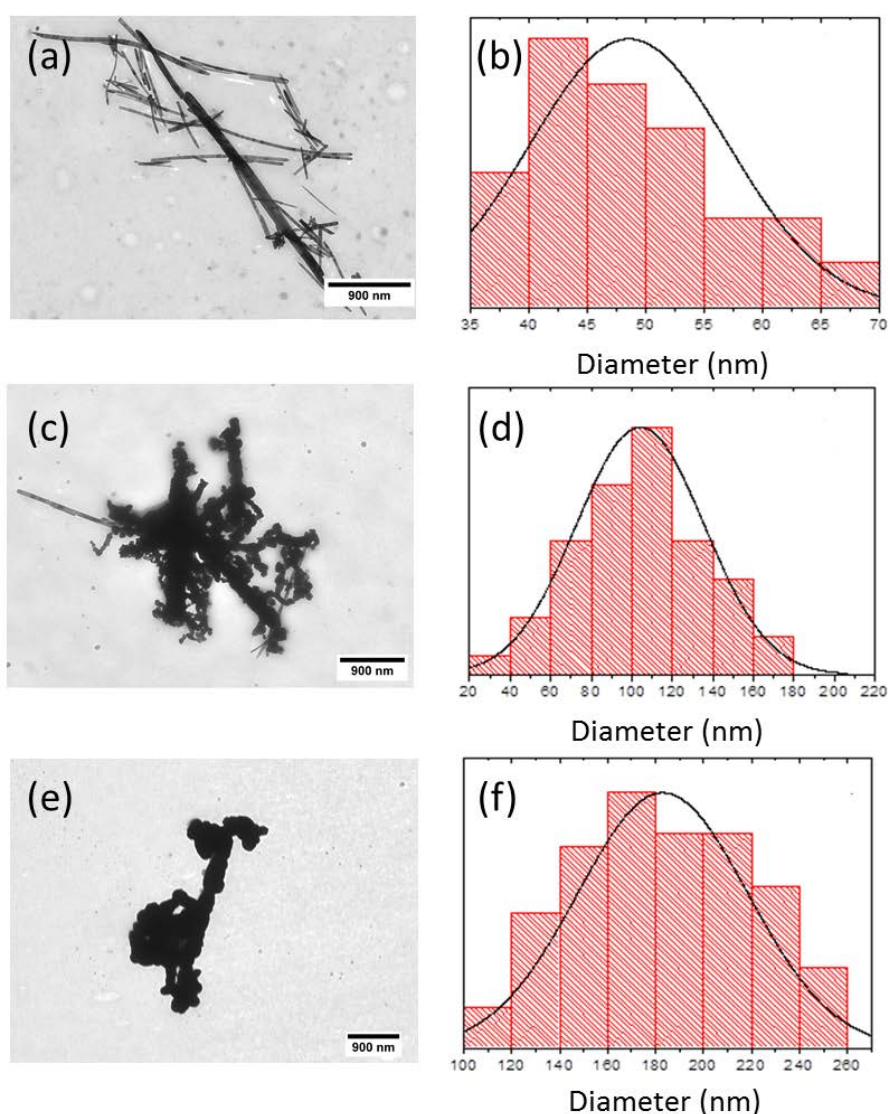


Figure 4.10 TEM images and particle size distribution of $\text{La}_{1-x}\text{Ca}_x\text{MnO}_3$ ($x=0.05$) after different temperature treatments during 12 h: (a) and (b) 230°C , (c) and (d) 650°C , (e) and (f) 900°C .

been made in order to know when the perovskite phase appears because only this phase presents thermoelectric activity [143, 170, 171]. At 230°C the perovskite phase was not obtained, resulting in an insulating material. The diffraction peaks observed at 230°C are related to segregated metallic oxides of Ca, La and Mn (CaO , Mn_3O_4 , CaMn_2O_4 , ...). At 650°C , the XRD spectrum indicates that the perovskite-type structure was obtained. The material obtained after this treatment was a semiconductor. The XRD spectrum of the sample heated at 900°C is the same to that obtained at 650°C , indicating that the perovskite-phase is maintained. The perovskite phase is attained at 650°C , however the electrical conductivity of the compacted powder (without sintering) produced at 650°C and 900°C is very low (around 10^{-3} S/cm). In addition, the sample size and shape are more homogeneous after the treatment at 900°C . Thus, in order to use these

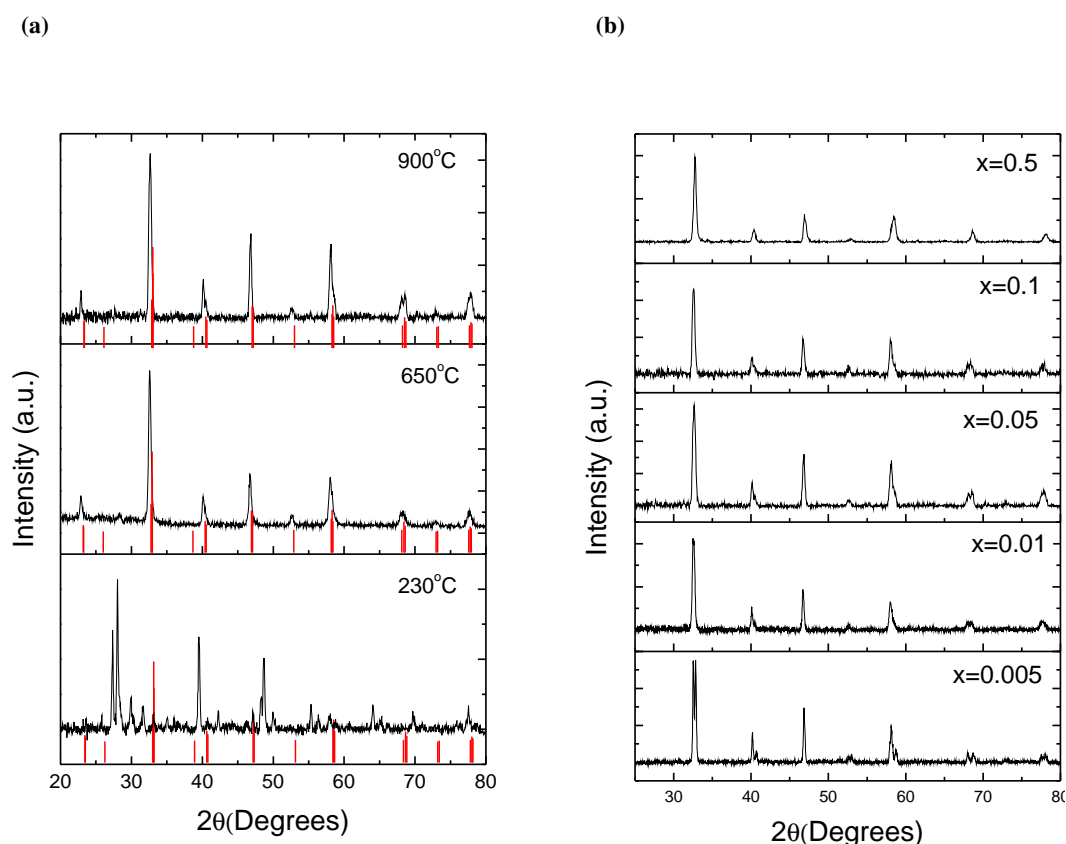


Figure 4.11 X-ray diffraction spectra of $\text{La}_{1-x}\text{Ca}_x\text{MnO}_3$ nanostructures (a) as a function of the calcination temperature ($x = 0.05$) and (b) as a function of the composition. The red lines refer to the perovskite phase diffraction pattern.

materials for thermoelectric applications, it has been realized a sintering process by keeping the compact pellet at 900°C for 24 h. Similar diffraction patterns are obtained for the remaining samples as shown the Figure 4.11(b). The results indicate that the perovskite phase has been attained in all the compositions.

4.2.5 Thermoelectric behavior of $\text{La}_{1-x}\text{Ca}_x\text{MnO}_3$

The electrical conductivity was measured in the compacted powder after the treatment at 900°C (without sintering) and also it was measured in the same pellet subjected to a sintering process at 900°C during 24 hours. The results for the sample with $x = 0.05$ are plotted in Figure 4.12(a). The electrical conductivity increases 3 orders of magnitude in the pellets subjected to the sintering process. This process produces an intimate contact between the particles decreasing the contact boundaries between them and also producing a better path for electric transport along the pellet. The electrical conductivity of the samples after the sintering process has been plotted in Figure 4.12(b). An increase of 3 orders of magnitude with respect to the samples

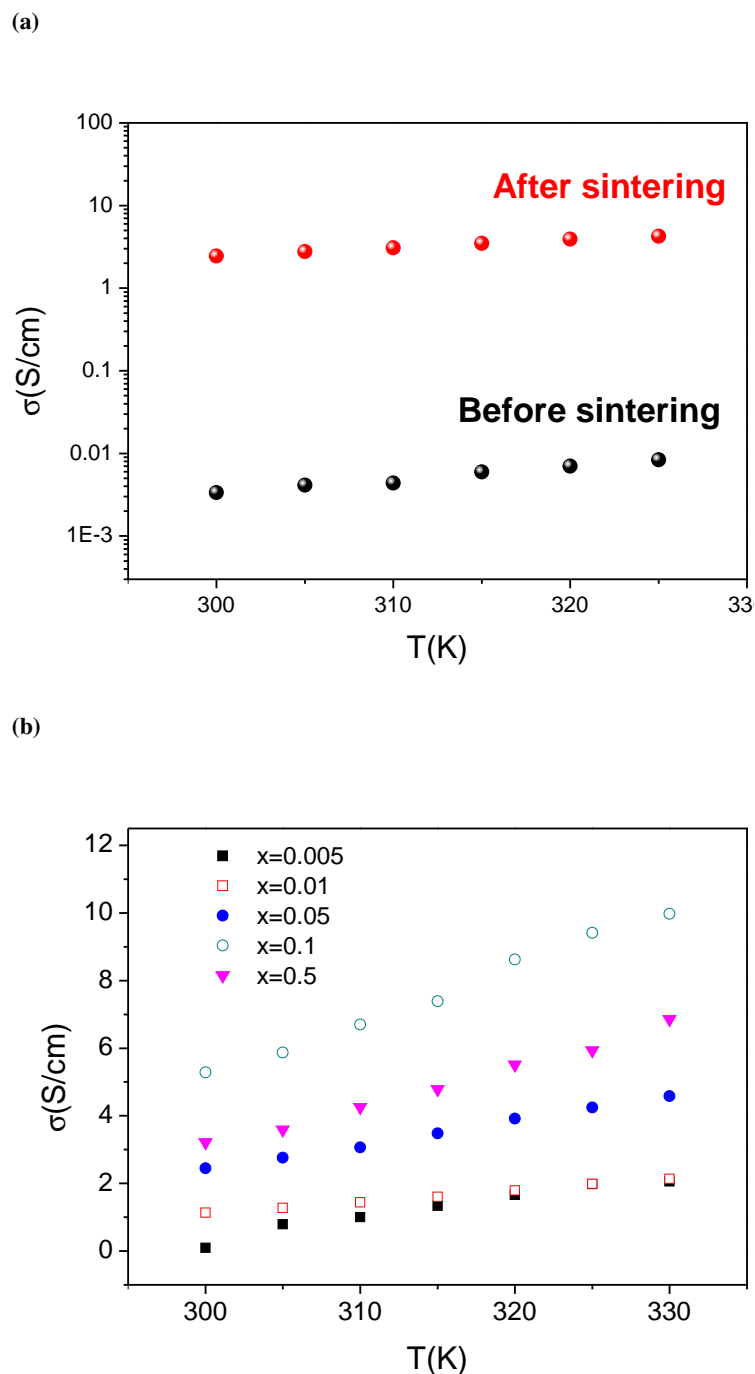
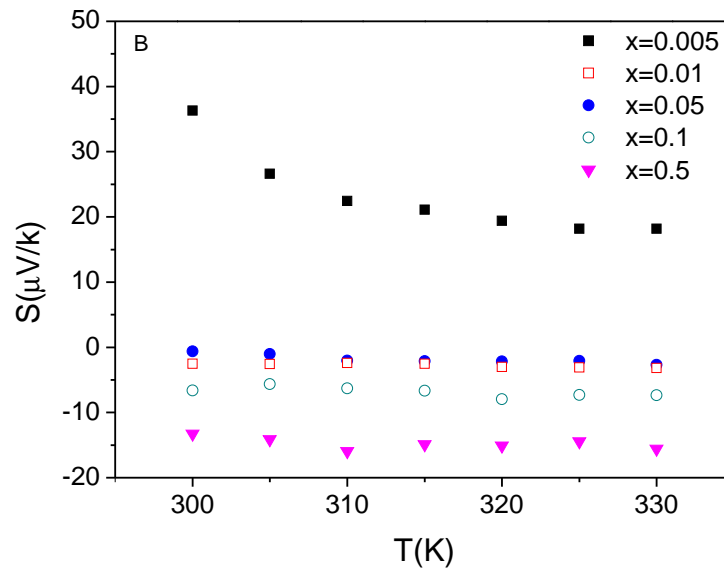


Figure 4.12 Electrical conductivity of $\text{La}_{1-x}\text{Ca}_x\text{MnO}_3$ (a) ($x = 0.05$) before and after sintering and (b) for different Ca contents as a function of the temperature.

before the sintering process is observed. This fact can be explained by the reduction of the interfaces and grain boundaries during the sintering process. The electrical conductivity increases with temperature; this trend is normal in this kind of semiconducting materials [172, 173]. The maximum value of the electrical conductivity, 10 S/cm, has been obtained for $\text{La}_{0.9}\text{Ca}_{0.1}\text{MnO}_3$ at 330 K. The increase of the calcium content in the nanostructured material produces an enhancement of the electrical conductivity, with the exception of $\text{La}_{0.5}\text{Ca}_{0.5}\text{MnO}_3$. Figure 4.13(a)

shows the variation of the Seebeck coefficient with the temperature and Ca content. The values

(a)



(b)

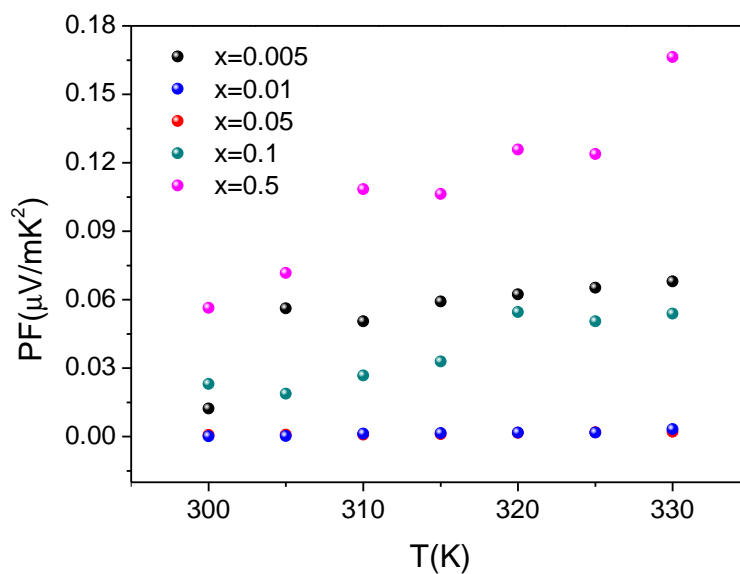


Figure 4.13 (a) Seebeck coefficient and (b) power factor of $\text{La}_{1-x}\text{Ca}_x\text{MnO}_3$ for different calcium contents as a function of the temperature.

of S change from positive to negative at high Ca content, denoting a change from p-type to n-type conduction. The dependence of S with temperature is negligible except for the lower Ca content ($x = 0.005$). Generally, p-type conductivity is observed in LaMnO_3 [174, 175]. This behavior is related to the presence of oxygen excess ($\text{LaMnO}_{3+\delta}$). Consequently, the number of Mn^{+3} ions decreases and the content of Mn^{+4} ions increases to compensate the oxygen excess

[174, 175]. In the case of CaMnO_3 n-type conductivity is observed [176, 177]. This fact is due to the presence of oxygen vacancies ($\text{CaMnO}_{3-\delta}$) in such a way the charge of these vacancies are compensated by the Mn^{+3} ions [176]. For this reason the increase of calcium content on $\text{La}_{1-x}\text{Ca}_x\text{MnO}_3$ produces a change of the conduction mechanism from, p to n-type. The substitution of La^{+3} by Ca^{+2} reduces the number of Mn^{+3} (d^4) ions and increases the number of Mn^{+4} (d^3) ions, to compensate the presence of Ca^{+2} ions in the crystalline structure [143, 170, 171]. The conduction mechanism can be explained by the octahedral coordination of the Mn atoms. When the Mn is octahedrally coordinated, the bonding states are $3t_{2g} \uparrow 2e_g \uparrow$, while the antibonding states are that with opposite spin. The $t_{2g} \uparrow$ states have a lower energy than the $e_g \uparrow$ states (in a tetrahedrally coordinated configuration the $e_g \uparrow$ states have a lower energy than the $t_{2g} \uparrow$ levels). In the case of Mn^{+4} , there are three electrons in the three $t_{2g} \uparrow$ states and one electron in the $e_g \uparrow$ states.

The electronic configurations of d orbitals in Mn^{+3} and Mn^{+4} are $(t_{2g} \uparrow)^3, e_g \uparrow$ and $(t_{2g} \uparrow)^3$ respectively, in such a way that the hopping conduction takes place in $e_g \uparrow$ level [171]. At high calcium content ($x = 0.5$), the electrical conductivity decreases and the Seebeck coefficient is clearly negative (n-type conduction), indicating a change on the conducting mechanism. This effect appears in related compounds such as, LaSrMnO_3 , LaNaMnO_3 LaRbMnO_3 [143]. This fact may be attributed to the conduction on the $t_{2g} \downarrow$ level [171].

Figure 4.13(b) shows the power factor calculated in order to have an idea of the thermoelectric efficiency in this kind of materials at 330 K. The best power factor, $0.16 \mu\text{W/m K}^2$ has been obtained for $\text{La}_{0.5}\text{Ca}_{0.5}\text{MnO}_3$. The values obtained in this work are similar to that obtained for some organic semiconductors [33, 178].

4.3 Perovskite nanostructures: $\text{Nd}_{1-x}\text{Ca}_x\text{CoO}_3$ system⁴

4.3.1 Materials

The reactants: $\text{Co}(\text{NO}_3)_2 \cdot 6\text{H}_2\text{O}$, $\text{Ca}(\text{NO}_3)_2$, $\text{Nd}(\text{NO}_3)_3$ and KOH , were purchased from Sigma Aldrich Co., Madrid, Spain.

4.3.2 Synthesis of nanowires

A solution with 0.55 M in cations (Co^{2+} , Ca^{2+} and Nd^{3+}) was prepared in deionized water, and the pH of the mixed solution was adjusted to 13 by adding KOH . After ultrasonic stirring,

⁴This section is based on the publication: "Synthesis of $\text{Nd}_{1-x}\text{Ca}_x\text{CoO}_3$ perovskite nanowires for thermoelectric applications" M. Culebras, A. Gómez, F. Sapiña, C. M. Gómez, A. Cantarero *Journal of Electrical Engineering*, 2, 59-64 (2014).

the solution was transferred into a teflon autoclave for hydrothermal treatment [144, 167, 168] for 48 h at 230°C. After the autoclave was cooled down to room temperature, the obtained solid products were washed with deionized water and ethanol, and subsequently dried overnight. Finally, the solid was heated at 650°C during 4 h to obtain the perovskite phase. The diameter of the nanowires was around 30–40 nm. Several compositions changing the calcium content were studied: $\text{Nd}_{0.995}\text{Ca}_{0.005}\text{CoO}_3$, $\text{Nd}_{0.97}\text{Ca}_{0.03}\text{CoO}_3$ and $\text{Nd}_{0.9}\text{Ca}_{0.1}\text{CoO}_3$. Finally, the powder was compacted using a pellet die (0.5 inch of diameter) and sintered at 900°C during 24 hours.

4.3.3 Morphology of $\text{Nd}_{1-x}\text{Ca}_x\text{CoO}_3$ nanostructures and temperature effect

In order to analyze the morphology obtained in the hydrothermal synthesis, the samples were analyzed by SEM and TEM. Figure 4.14(a) shows, the morphology of the $\text{Nd}_{0.995}\text{Ca}_{0.005}\text{CoO}_3$

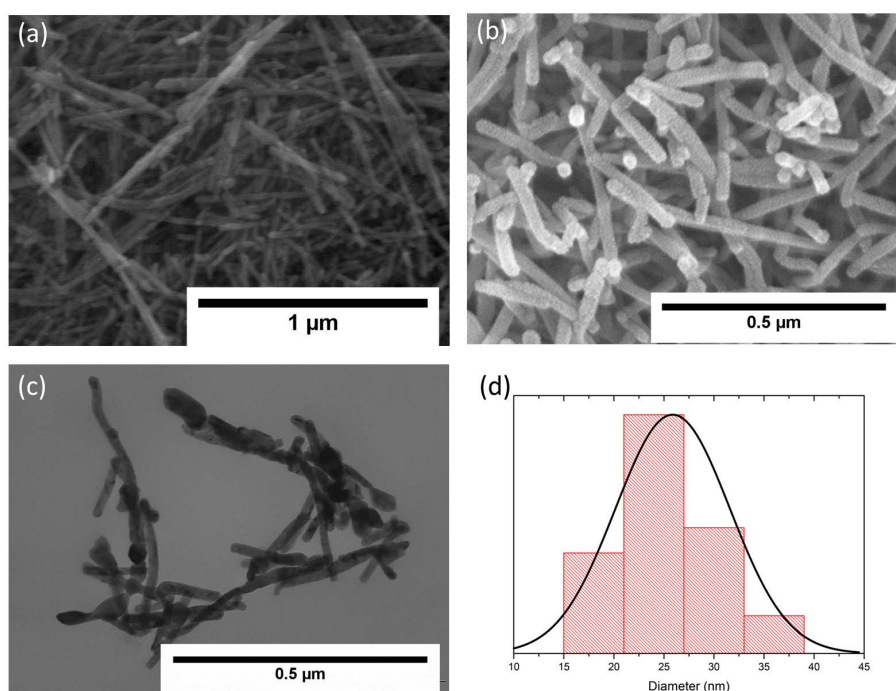


Figure 4.14 SEM images of $\text{Nd}_{1-x}\text{Ca}_x\text{CoO}_3$ ($x=0.005$) at: (a) 230 °C and (b) 650 °C. (c) TEM images of $\text{Nd}_{1-x}\text{Ca}_x\text{CoO}_3$. (d) Histogram of the diameter of the nanowires.

nanowires after the hydrothermal synthesis at 230°C. It is possible to observe a nanowire shape in the sample. This morphology is kept after the treatment at 650°C as it shown in Figure 4.14(b). The calcination treatment is not enough to change the morphology of the nanoparticles as has been observed in the $\text{La}_{1-x}\text{Ca}_x\text{MnO}_3$ perovskites. However, some deformation is observed in the TEM images of the nanowires calcinated at 650°C (Figure 4.14(c)). This fact indicated that the system is in the limit of stability since, a higher temperature treatment can change the morphology of the nanowires. Figure 4.14(d) shows the size distribution of the nanowires after the treatment at 650°C, the results show a maximum in the range of 25 nm. Similar trends have been observed for the remaining compositions.

4.3.4 Phase transition of $\text{Nd}_{1-x}\text{Ca}_x\text{CoO}_3$ during the calcination process

DRX analysis was realized in order to study the crystalline phase of the $\text{Nd}_{1-x}\text{Ca}_x\text{CoO}_3$ nanowires. Figure 4.15(a) shows the X-ray diffraction spectra after the hydrothermal synthesis at 230°C for

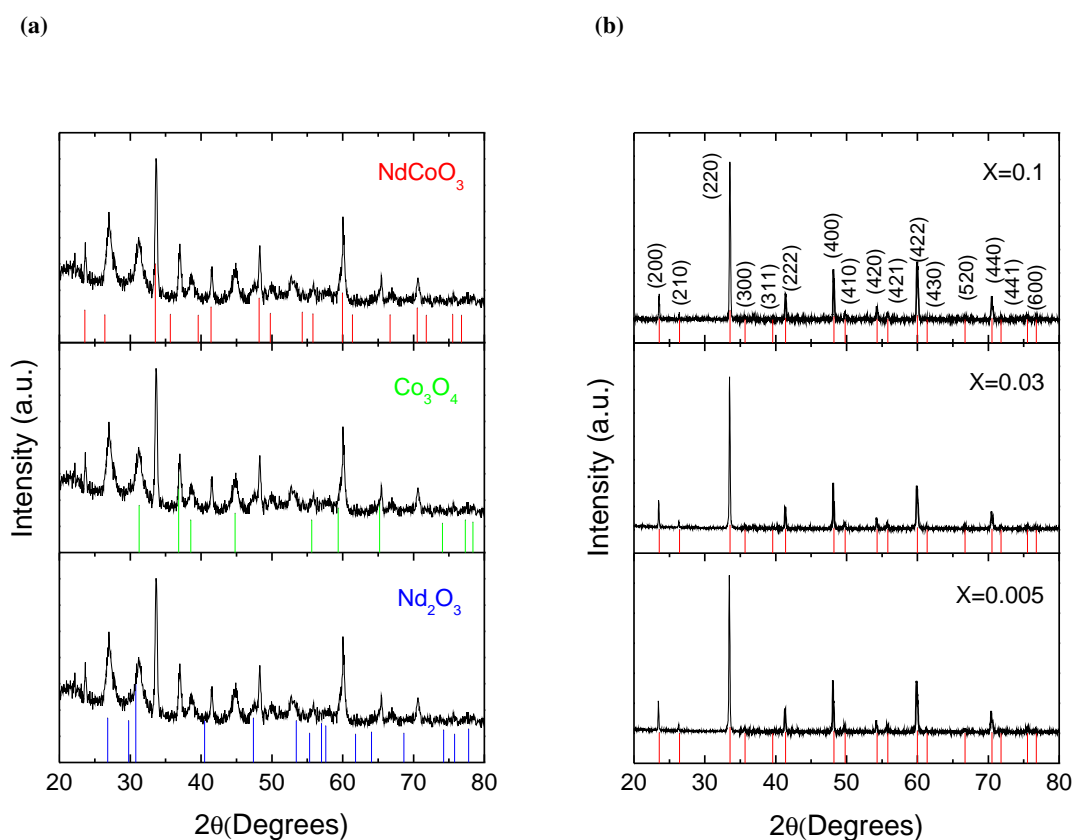


Figure 4.15 X-ray diffraction spectra of $\text{Nd}_{1-x}\text{Ca}_x\text{CoO}_3$ nanostructures (a) at 230°C for the composition $x = 0.005$ and (b) at 650°C as a function of the composition. The vertical lines correspond to the diffraction patterns.

$\text{Nd}_{0.995}\text{Ca}_{0.005}\text{CoO}_3$. After the synthesis, the nanowires present a lot of diffraction peaks indicating that the perovskite phase was not attained. However, it is possible to observe some diffraction peaks corresponding with the NdCoO_3 perovskite phase (vertical red lines). Thus, the results show that after the reaction some of the nanowires got the perovskite phase and others were composed by other oxides of Nd and Co. Comparing with the diffraction patterns of Nd_2O_3 and Co_3O_4 , there are some matches, since probably the remaining nanowires correspond with these two oxides. After the post treatment at 650°C the perovskite phase is attained as shown the Figure 4.15(b). Similar diffraction spectra have been obtained for all the compositions studied in this work. The XRD spectra indicates the cubic perovskite-type structure.

4.3.5 Thermoelectric behavior of $\text{Nd}_{1-x}\text{Ca}_x\text{CoO}_3$ nanowires

Figure 4.16 shows the electrical conductivity of the compacted powder obtained at 650°C before and after the sintering process in the same pellet at 900°C during 24 hours. The electrical

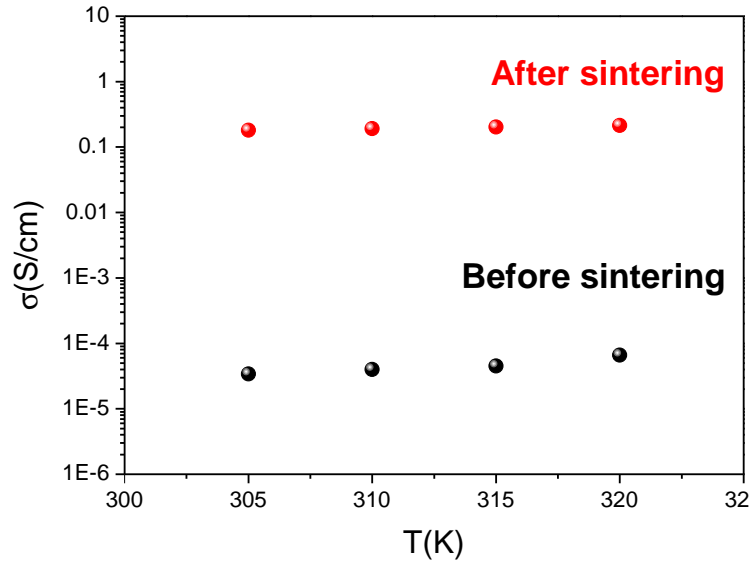


Figure 4.16 Electrical conductivity of $\text{Nd}_{1-x}\text{Ca}_x\text{CoO}_3$ ($x = 0.005$) before and after sintering.

conductivity increases four orders of magnitude. Before the sintering process the electrical conductivity was in the range of 10^{-5} S/cm, however after the sintering treatment the electrical conductivity increased until values around 0.1 S/cm. As happened in the previous system ($\text{La}_{1-x}\text{Ca}_x\text{MnO}_3$) the sintering process produces an intimate contact between the nanowires, decreasing the boundaries between them and also producing a better path for electric transport around the pellet.

The electrical conductivity values as a function of temperature for all the compositions studied in the $\text{Nd}_{1-x}\text{Ca}_x\text{CoO}_3$ system have been plotted in Figure 4.17(a). The electrical conductivity increases with temperature until values around 1.92 S/cm for $\text{Nd}_{0.995}\text{Ca}_{0.005}\text{CoO}_3$, 1.02 S/cm for $\text{Nd}_{0.97}\text{Ca}_{0.03}\text{CoO}_3$ and 0.55 S/cm for $\text{Nd}_{0.9}\text{Ca}_{0.1}\text{CoO}_3$. This trend is normal in semiconducting inorganic materials, since the electrical conductivity is related with the temperature by the following equation:

$$\sigma = \frac{A}{T} e^{-E_a/kT}, \quad (4.1)$$

where A is a constant of the material, E_a is the activation energy of the conduction process and k is the Boltzmann constant. When the temperature increases, the carrier concentration and the carrier mobility also increases producing this increment in the electrical properties of the $\text{Nd}_{1-x}\text{Ca}_x\text{CoO}_3$ perovskite nanowires. The electrical conductivity increases at lower Ca content, indicating that the Ca produces a de-doping effect in the perovskite nanowires.

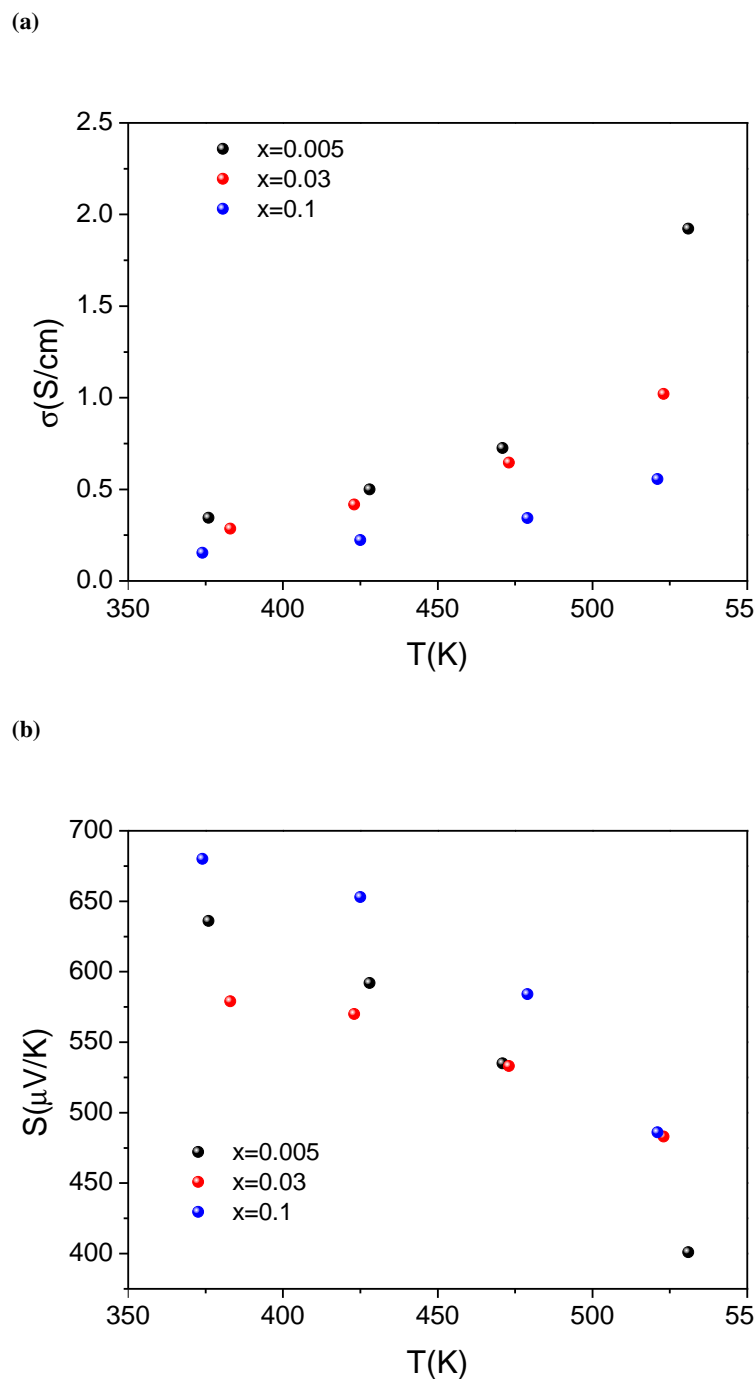


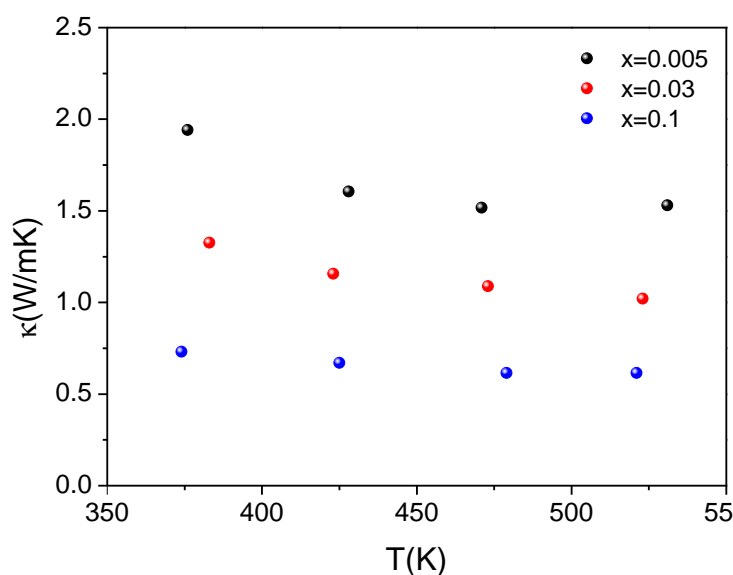
Figure 4.17 (a) Electrical conductivity and (b) Seebeck coefficient of $\text{Nd}_{1-x}\text{Ca}_x\text{CoO}_3$ as a function of the temperature.

Figure 4.17(b) shows the Seebeck coefficient of the $\text{Nd}_{0.995}\text{Ca}_{0.005}\text{CoO}_3$ nanowires as a function of temperature. The Seebeck coefficient decreases with the temperature for all the samples. This trend is the usual one for semiconducting materials since, at higher temperatures the carrier concentration increases, producing a decrease of the Seebeck coefficient. Very high values have been obtained for the nanowires, being larger in the sample with a $x = 0.1$ with a value around $680 \mu\text{V/K}$. The Seebeck values obtained for these nanostructured materials were higher than

the bulk corresponding ones [141]. This enhancement could be attributed to the increase of the number of interfaces in nanostructured materials.

The thermal conductivity has been measured in the $\text{Nd}_{1-x}\text{Ca}_x\text{CoO}_3$ nanowires as shown in Figure 4.18(a). It is strongly related with the calcium content and decreases with its content. This

(a)



(b)

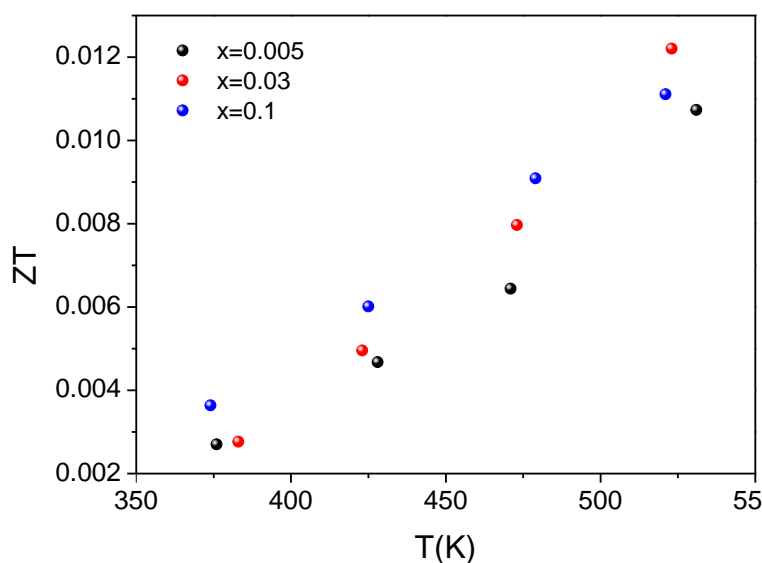


Figure 4.18 (a) Thermal conductivity and (b) ZT of $\text{Nd}_{1-x}\text{Ca}_x\text{CoO}_3$ as a function of the temperature.

fact can be attributed to a doping effect at lower calcium content which increases the electron contribution to the thermal conductivity. Compared with the bulk materials, a decrease of the

thermal conductivity has been achieved employing nanostructures such as nanowires, since the thermal conductivity of these kind of compounds in bulk is around $2\text{-}5 \text{ Wm}^{-1}\text{K}^{-1}$ [179]. As it has been observed in nanostructured alloys, the decrease of the thermal conductivity is given by the noticeable interfaces in the nanowires producing a strong phonon scattering [47]. The ZT values have been calculated as it is shown in Figure 4.18(b). ZT increases with the temperature mainly dominated with the increase of the electrical conductivity at high temperatures. The best value of ZT was 0.012, given by the composition $\text{Nd}_{0.97}\text{Ca}_{0.03}\text{CoO}_3$. ZT value in nanostructured materials is moderated, however, these materials can be good at high temperatures due to their good thermal stability and electrical properties.

4.4 Carbonaceous materials: application to carbon black ⁵

4.4.1 Materials

The chosen material for this study was Black Pearls 1400 carbon black, manufactured by Cabot (Boston, Massachusetts, USA). According to the manufacturer's information, the specific surface of this material is $560 \text{ m}^2/\text{g}$. The choice of an adequate carbon black was carefully made. The surface energy of commercial carbon blacks are from $70\text{-}200 \text{ m}^2/\text{g}$ [180] and the value of the surface area is a liable identifier of carbons with a good capacity for hydrogen adsorption [181]. Two different treatments were made in the samples, hydrogenation and irradiation. Hydrogenation was carried out in a pressured hydrogen atmosphere at 20 bar and room temperature for 180 min. In these conditions, hydrogen adsorption on the carbon black powder took place. The used hydrogen was Ultrapure Plus X50S (99,9992 %), supplied by Carburros Metálicos. In the irradiation process the sample was exposed to a 504-kGy irradiation with ^{60}Co isotopes. The sample exposition to radioisotope was carried out by immersion in a water well where the radioisotopes were located. The location was the Nayade facility, existing at the Centre of Energy,

Table 4.1 Treatments in the carbon black samples.

Sample	Treatment
TN-sH	without treatment
TN-H	Hydrogenation
CN-sH	Irradiation
CN-H	Irradiation and hydrogenation

Environment and Technology Research (Centro de Investigaciones Energéticas, Medioambientales y Tecnológicas, CIEMAT), in Madrid, Spain. For this study, four samples were prepared in order to study hydrogenation and irradiation effects in the samples as summarized in Table 4.1.

⁵This section is based on the publication: "An Approach on the Hydrogen Absorption in Carbon Black after Gamma Irradiation" A. Madroño, M. Culebras, A. Cantarero, C. Gómez, C. Mota, J. Amo and J. Robla *Advances in Materials Physics and Chemistry*, 3, 295-298 (2013).

4.4.2 Structural analysis

The treatment effect in the crystalline structure of carbon black has been studied using X-ray diffraction analysis. In Figure 4.19(a), referred to non-hydrogenated samples, it is possible

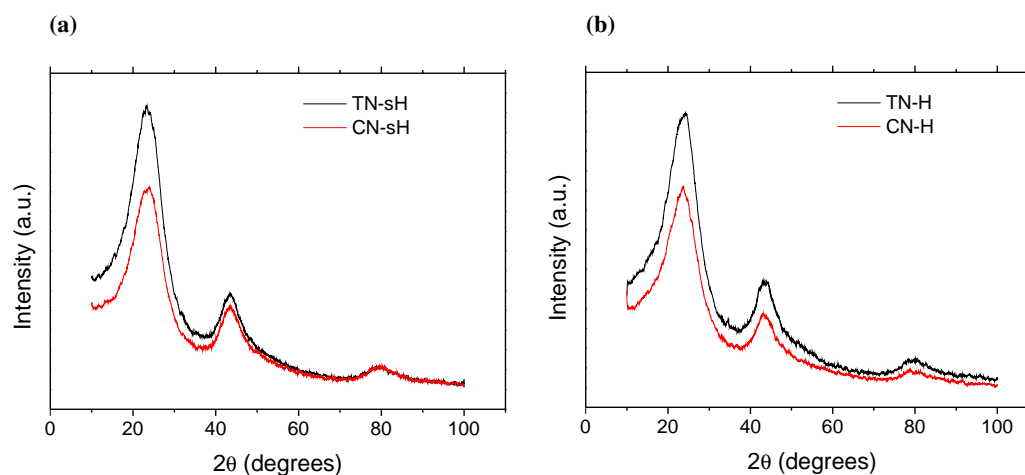


Figure 4.19 XRD plot of (a) non-hydrogenated samples and (b) hydrogenated samples.

to see that the effect of the irradiation is to decrease the crystalline perfection displayed as an impairing of the slenderness of the diffraction peak; the irradiated carbon black becomes more similar to an amorphous sample. The fact that γ -irradiation increases the hydrogen intake in carbon materials is in agreement with the knowledge that amorphous carbons are better absorbers than crystalline carbon [182]. Similar results can be observed in Figure 4.19(b) for the hydrogenated samples. Actually, the diffraction is a powerful tool to distinguish between irradiated and non-irradiated materials, but not very reliable to evaluate the level of over hydrogenation. In the same way, if we proceed to evaluate the crystalline size L_c using Scherrer's formula [183], as shown in Table 4.2 the effect of the irradiation is to decrease L_c . Similar evolution of the XRD diffractograms are known in carbon nanotubes irradiated with γ -rays [183].

Table 4.2 Determination of crystalline size using Scherrer's formula.

Sample	L_c [Å]
CN-H	6.8
CN-sH	7.3
TN-H	7.1
TN-sH	7.3

4.4.3 Thermoelectric behavior of carbon black

The electrical properties of the samples have been obtained using the Van der Paw technique described before and the results are shown in Table 4.3, where it is observed that the absorption

of hydrogen decreases the electrical conductivity, as it is known for similar materials [184]. The influence of the irradiation process is effective regarding the change in the Seebeck coefficient. Table 4.3 shows how the irradiation improves the Seebeck coefficient, but it is also remarkable that the intake of hydrogen increases that coefficient.

Table 4.3 Results of the measurements of electric conductivity and Seebeck effect on the carbon black samples.

Sample	σ (S/cm)	S (V/K)
TN-sH	2.00	0.87 ± 0.01
TN-H	1.49	4.20 ± 0.20
CN-sH	1.41	2.63 ± 0.05
CN-H	1.09	3.25 ± 0.05

4.5 Carbonaceous materials: application to charcoal

4.5.1 Materials

The material used in the present study is commercial charcoal produced from the wood of "Eucalyptus Melliodora" (commonly known as yellow box). The samples have a parallelepiped shape of $10 \times 10 \times 1 \text{ mm}^3$.

4.5.2 Charcoal treatments

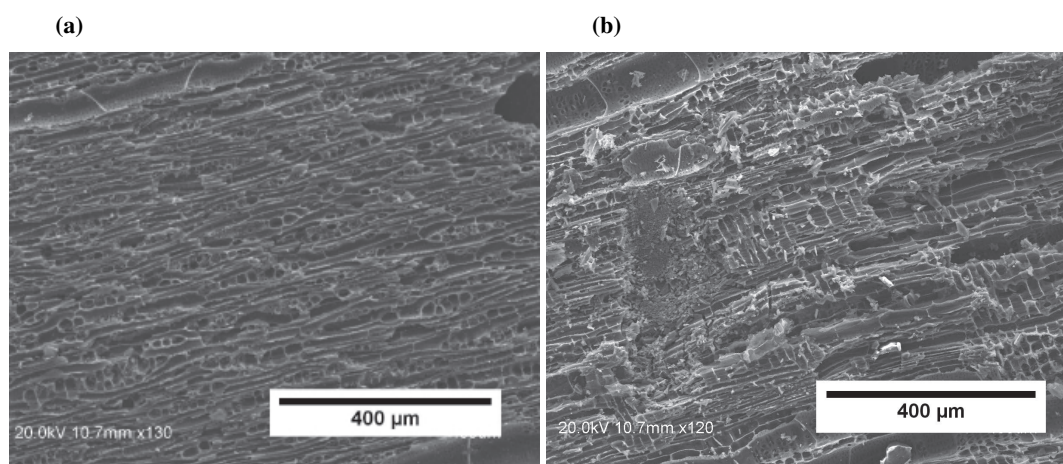
The charcoal samples have been subjected to different treatments in order to investigate their influence on the thermoelectric efficiency. These are: a) hydrogenation, carried out in a tubular steel reactor in a pure hydrogen atmosphere at 20 bars over-pressure during 3 hours at room temperature; b) the irradiation process on the samples was performed with doses up to 504 kGy irradiation with ^{60}Co . The sample exposition to the radioisotope was carried out by immersion in a water well where the radioisotopes were located. The irradiation was performed in the Náyade Facility, belonging to CIEMAT; and finally c) acid etching was performed by immersion in chronic acid during 130 min at 373 K with a further reduction using a hydrazine-water solution. The samples used in this study are summarized in the Table 4.4

4.5.3 Morphology and thermoelectric parameters

Figure 4.20 shows SEM micrographs of the charcoal samples before and after different treatments. Figure 4.20(a) shows the surface of the raw charcoal sample, sample P, where the typical

Table 4.4 Treatments performed on the charcoal samples.

Sample	Sequence of treatments
P	no treatment
PH	hydrogenation
PI	irradiation
PA	acid etching
PIH	irradiation and hydrogenation
PAI	acid etching and irradiation
PAIH	acid etching, irradiation and hydrogenation
PAHI	acid etching, hydrogenation and irradiation
PAHIH	acid etching, hydrogenation, irradiation and a further hydrogenation

**Figure 4.20** SEM images of: (a) the surface of sample P, (b) the surface of sample PA.

wood structure is still observable. Figure 4.20(b) shows the surface of sample P after acid etching, sample PA, where a clear erosion of the wood network due to the acid etching treatment appears. In the images a large number of pores and channels can be observed, legacy of the wood structure.

Figure 4.21 plots the electrical conductivity for the different samples under study. The irradiation of the samples with γ -rays causes a sharp increase in the conductivity, up to five orders of magnitude. The influence of the other treatments by themselves in the electrical conductivity is small in comparison with the irradiation process. This effect results from the fact that during irradiation, Compton scattering produces up to 5-6 vacancies per collision [185]. As a result, we observe that the effect of the irradiation with γ -rays is the production of structural defects in carbon materials as the tilt of crystalline planes [160]. These nanocrystalline alterations work as enclosures for the hydrogen storage [186], and it is assumed that the hydrogen located in defects and grain boundaries convert the carbon materials into semiconductors. The acid etching and hydrogenation improves the irradiation effect, increasing the conductivity of the samples as shown in Figure 4.21. Hydrogen incorporation causes an increase of charge carriers which results in an improvement on electrical conductivity of the charcoal samples. The Seebeck effect,

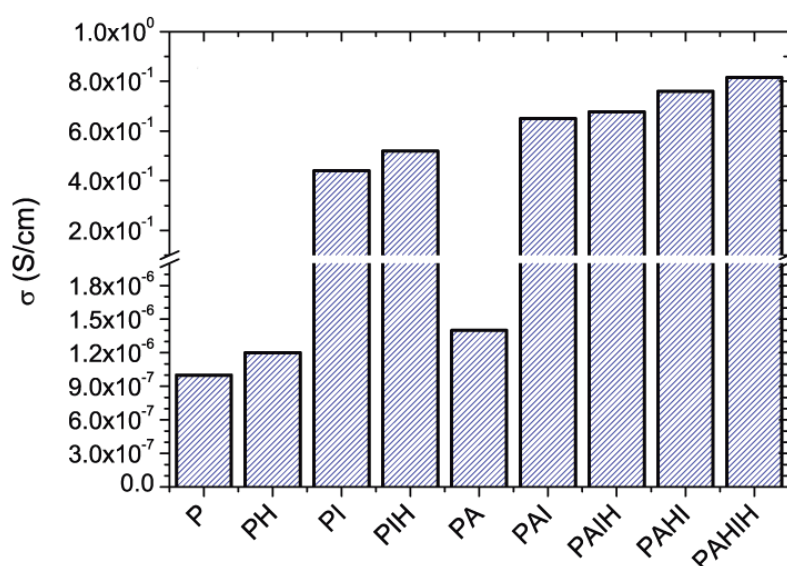


Figure 4.21 Electrical conductivity of charcoal samples as a function of the treatment.

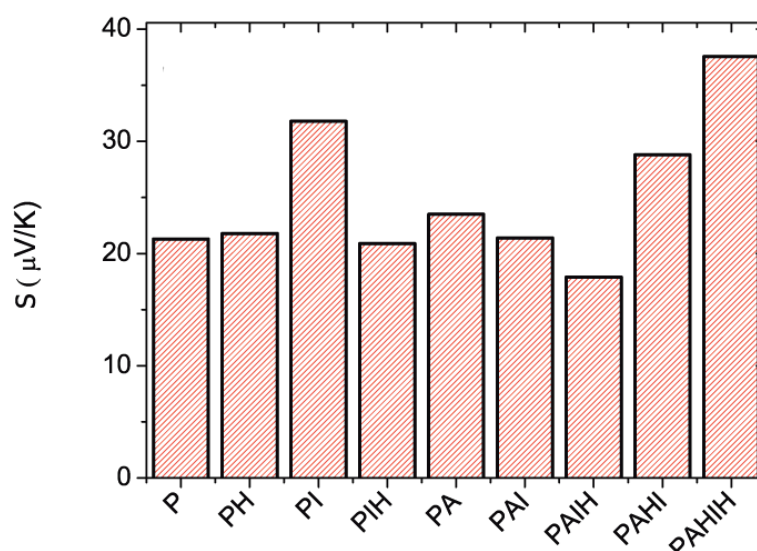


Figure 4.22 Seebeck coefficient of charcoal samples as a function of the treatment.

as shown in Figure 4.22, also increases when γ -irradiation takes place (except for sample PA), with a small influence of the other treatments such as hydrogenation and acid etching. The effect of acid etching and hydrogenation on the irradiated samples does not produce a drastic change in the value of Seebeck coefficient in opposite with the electrical conductivity that increases. This tendency is normal because when the number of charge carriers increases, the Seebeck coefficient decreases and the conductivity increases [9]. In contrast, acid etching previous to hydrogenation, irradiation and a second hydrogenation process (sample PAHIH) causes the largest

increase in the Seebeck coefficient. The thermoelectric efficiency in charcoal samples given by PF, indicates that all the irradiated samples show an increase of four orders of magnitude, as shown in Figure 4.23, being more accentuated for the PAHIH sample, as expected.

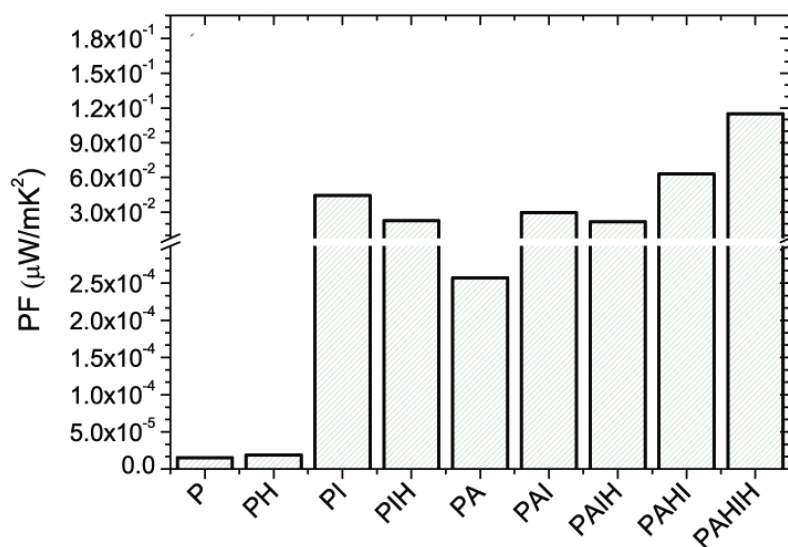


Figure 4.23 PF of charcoal samples after the different treatment.

4.6 Carbonaceous materials: application to vitreous carbon⁶

4.6.1 Materials

To perform this work, samples of vitreous carbon sized $10 \times 10 \times 1$ mm were prepared. They were cut with a diamond blade from vitreous carbon plate SIGRADUR®, manufactured by HTW Hochtemperatur-Werkstoffe GmbH (Germany). The samples received different treatments in order to see their influence on thermoelectrical parameters of our material (see Table 4.5). The hydrogenation was carried out in a tubular steel reactor in a pure hydrogen atmosphere at 20 bars of over-pressure during 3 hours at room temperature. The irradiation process on the samples was performed with doses up to 504 kGy irradiation with ^{60}Co . The irradiation was performed in the Náyade Facility, belonging to CIEMAT.

Table 4.5 Treatments performed on the samples.

Sample	Sequence of treatments
G	without treatment
GI	irradiation
GIH	irradiation and hydrogenation
GHI	hydrogenation and irradiation
GHIH	hydrogenation, irradiation and hydrogenation

Table 4.6 Results of electrical conductivity and Seebeck effect in vitreous-carbon samples subjected to different treatments.

Sample	σ (S/cm)	S ($\mu\text{V}/\text{m K}^2$)
G	4620	-0.37 ± 0.03
GI	2332	-1.95 ± 0.03
GIH	1854	1.26 ± 0.08
GHI	2255	-1.35 ± 0.02
GHIH	3909	1.37 ± 0.02

4.6.2 Thermoelectric behavior of vitreous carbon

The results of electric conductivity and Seebeck coefficient are shown in table 4.6. The electric conductivity is very high as it is normal in graphite compounds. The highest value is for pristine sample; the irradiation decreases the electrical conductivity probably because it reduces the number of charge carriers in the conduction band. This effect results from the fact that during irradiation, Compton scattering produces up to 5-6 vacancies per collision as already mentioned [185]. The Seebeck coefficient increases in absolute values for the treated samples (irradiation and or hydrogenation). Positive values, indicating p-type conduction, and negative values, indicating n-type conduction, are obtained. P-type conduction is observed when the last treatment is hydrogenation, whereas n-type conduction is obtained when the last treatment is irradiation. This is a good procedure to obtain either n- or p-type semiconductors based on carbon materials. This effect has also been observed in carbon microfibers [187].

4.6.3 X-ray analysis of vitreous carbon

Figure 4.24 shows the diffractograms of the samples under study. Two diffraction peaks, peak 1, at $2\theta \simeq 26^\circ$ and peak 2, at $2\theta \simeq 53^\circ$ are clearly distinguished. Peak 1 and peak 2 in Figure 4.24 are attributed to the diffraction in planes (002) and (110) by comparing with the data base Powders Diffraction File, in particular, with the diffractogram 23-0064 corresponding to graphite.

⁶This section is based on the publication: "Changes in the thermoelectric response of vitreous carbon due to the irradiation by γ -rays", M. Culebras, A. Madroñero, C. Mota, C. Gómez, J. Amo, A. Cantarero *Radiation Effects and Defects in Solids*, 169, 620-627 (2014) with permission of Taylor and Francis.

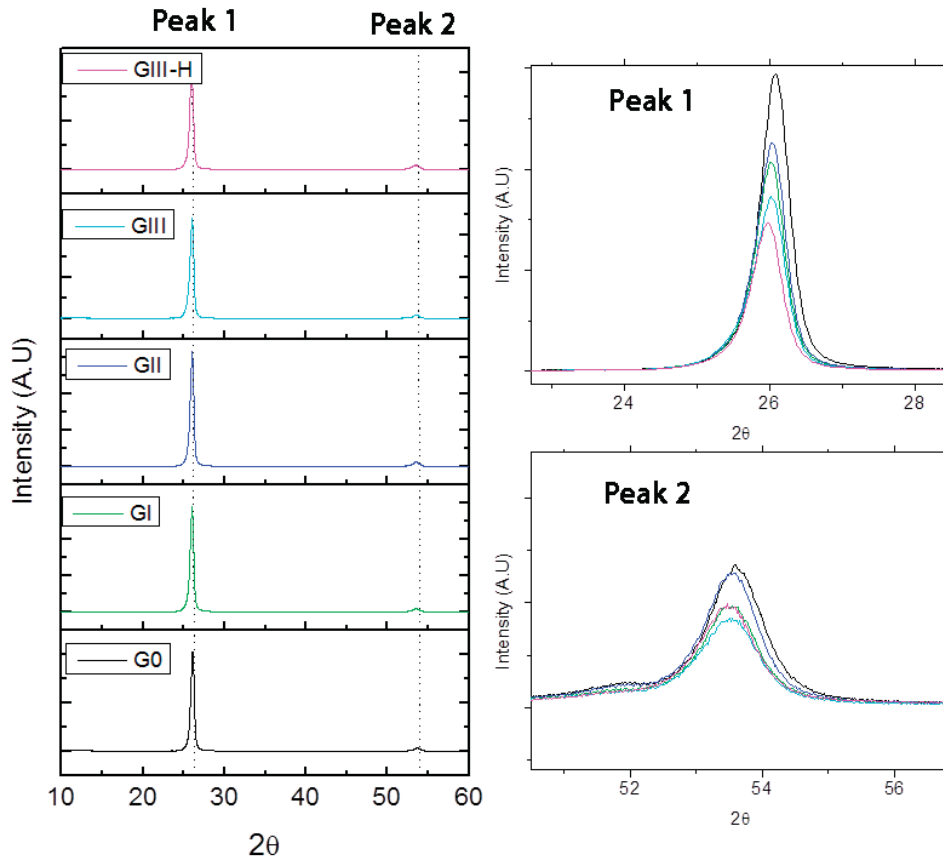


Figure 4.24 X-Ray results for glassy-carbon.

Then, it is possible to calculate the layer distances $d_{(002)}$ and $d_{(110)}$ from the Bragg's equation [188]:

$$d_{(002)} = \frac{\lambda}{2 \cdot \sin \theta_{(002)}} \quad , \quad (4.2)$$

$$d_{(110)} = \frac{\lambda}{2 \cdot \sin \theta_{(110)}} \quad , \quad (4.3)$$

where the wavelength is $\lambda = 0.154056$ nm because the monochromatic radiation used to perform the diffraction tests was $\text{CuK}\alpha$. It is also known that for hexagonal lattices the Bragg law are the following relationship between the lattice parameters and the Miller's indices [189]:

$$d_{(hkl)} = ((4/3a^2)(h^2 + hk + k^2) + (1/c)^2)^{-1/2} \quad , \quad (4.4)$$

Now, for the particular case of $2\theta = (002)$ and $2\theta = (110)$ we can take $h = 0$, $k = 0$ and $l = 2$ and on the other hand $h = 1$, $k = 1$ and $l = 0$ in Eq (4.4). Then we can obtain in (4.4)

$$c = 2d_{(002)} \quad (4.5)$$

and

$$a = 2d_{(110)} \quad (4.6)$$

By substitution of (4.2) and (4.3) into (4.5) and (4.6) the unit cell parameters a and c are obtained. It is also interesting to know the crystallite size or grain size (the samples are polycrystalline materials) using Scherrer's equation. For this purpose we can evaluate the crystalline parameters as shown in [190]:

$$L_c = \frac{0.9\lambda}{W_{(002)} \cos \theta_{(002)}} \quad , \quad (4.7)$$

$$L_a = \frac{1.84\lambda}{W_{(110)} \cos \theta_{(110)}} \quad , \quad (4.8)$$

where L_c and L_a are the crystallite parameters, λ is the wavelength ($\lambda = 0.15418$ nm), and W is the full width at half maximum of each peak in radians. The calculated diffraction parameters for all the samples are shown in Table 4.7. For an adequate identification of each parameter we define θ as the diffraction angle of each peak in degrees, H is the figure of counts in the height of each peak, W is the full width at half maximum of each peak in radians. These three numbers can be read in each diffractogram. After that, a simple calculation yielded the remaining parameters; s is (H/W) and represents the sharpness of the peak, d is the distance between crystallographic planes according to the Bragg's law and it is calculated from (4.2) and (4.3). On other side the lattice parameters a and c are obtained from (4.5) and (4.6). L_c and L_a is the crystallite parameters in nm and it is obtained from (4.7) and (4.8). Finally, r is L_c/L_a and represents the acuteness aspect of the crystallites, and sz is the stack size with two variations, $sz_a = L_a/a$ and $sz_c = L_c/c$. To make easier the comparisons, we will use $\Delta = sz_c/sz_a$ and represents the number of unit cell that constitutes a crystallite, in direction of crystallographic axis and in the basal direction.

Table 4.7 XRD parameters of all samples.

Sample	2θ	H	W	s	d	a	c	L_c	L_a	r	sz_a	sz_c	Δ
G	26.08	205935	0.0082	$2.510 \cdot 10^7$	0.34	—	0.68	17.92	1.96	—	26.25	0.98	
	53.59	6776	0.0176	$3.843 \cdot 10^5$	0.17	0.34	—	9.10	1.96	26.62	—	0.98	
GI	26.06	144991	0.0080	$1.806 \cdot 10^7$	0.34	—	0.68	18.31	2.01	—	26.75	1.00	
	53.52	4801	0.0176	$2.723 \cdot 10^5$	0.17	0.34	—	9.10	2.01	26.60	—	1.00	
GIH	26.03	157910	0.0083	$1.885 \cdot 10^7$	0.34	—	0.68	17.55	1.92	—	25.65	0.96	
	53.54	6378	0.0176	$3.618 \cdot 10^5$	0.17	0.34	—	9.10	1.92	26.61	—	0.96	
GHI	26.02	120902	0.0087	$1.385 \cdot 10^7$	0.34	—	0.68	16.85	1.96	—	24.61	0.98	
	53.52	4205	0.0186	$2.252 \cdot 10^5$	0.17	0.34	—	8.59	1.96	25.11	—	0.98	
GHIH	25.97	102318	0.0089	$1.149 \cdot 10^7$	0.34	—	0.68	16.51	1.85	—	24.08	0.92	
	53.46	4921	0.0179	$2.737 \cdot 10^5$	0.17	0.34	—	8.92	1.85	26.05	—	0.92	

Using these results, it is possible now to have information about some changes that the gamma irradiation and the absorption that hydrogen produces. Comparing with the hydrogenation, the effect of γ -irradiation is less pronounced but observable, taking into account the change of sz from G to GI. The variations of the lattice parameters a and c are not relevant, but the change in the crystallite size is observable as suggests the variation of the parameter Δ . This is in accordance with the results of experiments reported in the literature [191] referred to irradiation with neutrons of a set of graphite material. In all these results, irradiated materials show a marked increase in c-axis lattice strain, while changes in the lattice parameters are very small. The γ -irradiation produces an increasing of L_c without a decreasing in L_a , according with already known results [192]. The final crystallite appearance, if we compare r in GHIH with G, is a brocaded crystallite. The parameters Δ tell us when a crystallite grows irregularly with larger increase in ratio L_c/c than L_a/a or vice versa. This is similar to the results of neutron irradiation of pyrolytic carbons [193] that studies the dimensional behavior of pyrolytic carbon under irradiation by averaging methods to describe the anisotropic distortion of the bulk in terms of its preferred orientation and the shape change of the individual crystallites. Finally, we can conclude that the hydrogenation alone produces an enhancing of the amorphous grade of the material whilst the irradiation changes the crystallite shape and size. It is an advantageous aspect that the irradiation simultaneously produces changes in the bulk material, and improves the activity of the surface. The results from the point of view of the thermoelectric properties are also interesting. Therefore, it seems reasonable to accept that in the horizon of thermoelectricity there are some glasses with possibilities to improve the vitreous carbon characteristics [194], but the most interesting is that according to the change in the sign of the Seebeck's coefficient, the incorporated hydrogen works as a charged carrier. As the hydrogen was absorbed from a gaseous atmosphere of pure molecular hydrogen, the dissociation of the molecule takes place.

4.7 Conclusions

In this chapter, several non conventional inorganic materials for thermoelectric application have been studied. For the case of the perovskite nanostructures $\text{La}_{1-x}\text{Ca}_x\text{MnO}_3$ a morphology change was observed from nanowires to nanoparticles with the calcination temperature. The perovskite phase was obtained at 650°C . The electrical conductivity increased several orders of magnitude after the sintering process and a change from p-type to n-type conduction has been observed depending on the calcium content in the $\text{La}_{1-x}\text{Ca}_x\text{MnO}_3$ nanoparticles, p-type for $x = 0.005$ and n-type for $x = 0.01$ to $x = 0.5$. $\text{Nd}_{1-x}\text{Ca}_x\text{CoO}_3$ perovskite nanowires were synthesized achieving the perovskite phase at 650°C . The electrical conductivity increased with the sintering process. Very high values of the Seebeck coefficient were obtained from, 600-700 $\mu\text{V/K}$ at room temperature. The electrical conductivity depends on the calcium content

in $\text{Nd}_{1-x}\text{Ca}_x\text{CoO}_3$ perovskite nanowires, being higher at lower calcium contents. ZT was calculated from the values of PF and the thermal conductivity, achieving values around 0.012 at 520°C. For the case of carbonaceous materials, the irradiation process can alter the thermoelectric properties due to changes in the semiconductor behavior. For example the samples of vitreous carbon change from p-type to n-type after irradiation.

Chapter 5

Nanocomposites and hybrid materials for thermoelectric applications

Content

This chapter studies the thermoelectric behavior of several nanocomposites and hybrid materials based on PEDOT and inorganic fillers. Two kinds of materials were prepared attending to the nature of the filler. On the one hand, materials with carbon derivative fillers were prepared such as: PEDOT/expanded graphite, and PEDOT/multiwall carbon nanotubes (MWCNTs). On the other hand materials with inorganic additives such as: PEDOT/ Perovskite nanoparticles and PEDOT/Te were prepared.

5.1 Introduction ⁷

As it has been shown in previous chapters, the thermoelectric properties of conducting polymers are very low. Basically, this fact is because in general terms when the polymer is highly conductive (1000 S/cm) the Seebeck coefficient is extremely low ($\sim 5 \mu\text{V/K}$), consequently the resulting Power Factor is not very good. The same fact happens when the polymer has a high Seebeck coefficient ($S > 100/K$), in this case the electrical conductivity decreases until values between 10^{-2} - 10^{-4} S/cm. It is possible to obtain intermediate values of electrical conductivity and Seebeck coefficient with the optimization of the doping level, as has been demonstrated in Chapter 3. However, the resulting values of the PF are not as high as the traditional inorganic materials. For this reason, it is very important to find other ways to increase one of the

⁷This section is based on the publication: "Review on polymers for thermoelectric applications M Culebras, CM Gómez, A Cantarero *Materials*,7, 6701-6732 (2014).

thermoelectric parameters (σ or S) without detriment the rest. One way can be the synthesis of nanocomposites or hybrid materials. The combination of two different materials with low thermoelectric efficiency by themselves can generate a hybrid material with a higher thermoelectric efficiency compared with the raw materials. For example, the combination of a material with high electrical conductivity and high thermal conductivity (graphite) and other material with low electrical conductivity and low thermal conductivity (polymers) will result in a material with intermedium values; consequently, the thermoelectric efficiency will increase. In the following sections a brief summary of the thermoelectric properties of the most representative nanocomposites and hybrids materials investigated until now will be shown.

5.1.1 Carbon nanotubes

MWCNT, single wall carbon nanotube (SWCNT) or DWCNT, functionalized or not, are being extensively used to improve electrical conductivity and mechanical properties of polymeric matrices [195].

Choongho *et al.* have devoted several papers [109, 110, 196, 197] to investigate the influence of CNTs on the thermoelectric performance of a polymer matrix. They started by studying composites of CNT and poly(vinyl acetate) (PVAc) from aqueous solutions [196]. The highest thermoelectric performance was attained at a 20 wt % content of CNTs, with an electrical conductivity of 48 S cm^{-1} , thermal conductivity of $0.34 \text{ W m}^{-1}\text{K}^{-1}$ and a thermoelectric figure of merit larger than 6×10^{-3} at room temperature. Lately, by using a conductive polymer matrix, PEDOT:PSS doped with DMSO, in a SWCNTs dispersion they obtained promising ZT values around 0.02 [109]. The addition of 35 wt% of SWCNT to PEDOT:PSS give values of σ increasing up to 400 S cm^{-1} , while keeping constant $S \approx 20 \text{ } \mu\text{VK}^{-1}$, and the thermal conductivity $\kappa \sim 0.2 - 0.4 \text{ W m}^{-1}\text{K}^{-1}$ [109]. The addition of polyvinyl acetate to single-wall carbon nanotubes and PEDOT:PSS gives high electrical conductivity of the order of 10^3 S cm^{-1} , keeping constant the thermal conductivity, $\kappa \sim 0.2 - 0.4 \text{ W m}^{-1}\text{K}^{-1}$, the thermopower $S = 41 \text{ } \mu\text{VK}^{-1}$ and large thermoelectric power factors of about $PF = 160 \text{ } \mu\text{W/mK}^2$ with 60 wt % SWCNT. The presence of PVAc in the composites improves the CNTs dispersion in the polymer matrix (Figure 5.1, image taken from [110]), thus enhancing the electrically connected junctions in the nanotube network and yielding high thermoelectric performance [197]. Recently, the addition of conductive stabilizer such as meso-tetra(4-carboxyphenyl) porphine (TCPP) to the PEDOT:PSS/DWCNTs dispersion clearly improves the thermoelectric properties of the composite giving very exciting values of $PF = 500 \text{ } \mu\text{W/m K}^2$, one of highest obtained for an organic flexible material [110].

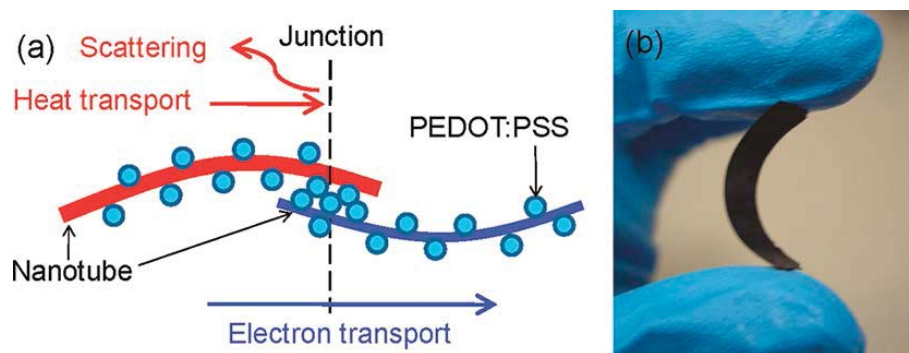


Figure 5.1 (a) CNT are coated by PEDOT:PSS particles, making nanotube-PEDOT:PSS-nanotube junctions in the composites. (b) The fully dried composite held between two fingers indicates that it is a free-standing flexible black material. Reproduced from [197] with permission of ACS Nano.

Generally, the power factor of most of the polymers used as thermoelectric materials is in the range of $1 - 10^{-4} \mu\text{W}/\text{m K}^2$, three orders of magnitude smaller than the state-of-the-art in inorganic TE materials [107]. Addition of CNTs creates an interconnected network and increases the electrical conductivity, keeping nearly constant the Seebeck coefficient and the thermal conductivity. Building highly ordered structures will improve thermoelectric efficiency, as shown in composites formed by novel 3D CNT networks with PANI [198]. These composites depict maximum values of $\sigma = 40.35 \text{ S cm}^{-1}$, $S = 23.3 \mu\text{W K}^{-1}$, $\kappa = 0.29 \text{ W m}^{-1} \text{ K}^{-1}$ that gives a ZT value of 2.2×10^{-3} . Notice that the ZT values are 6.0×10^{-4} for a 3D CNT network and 7.0×10^{-7} for PANI. Better results have been obtained for the case of SWCNTs dispersed in an aniline solution and in situ polymerization (Figure 5.2) [107].

The PANI/SWCNT nanocomposites show both higher electrical conductivity and Seebeck coefficient as compared to pure PANI, which could be attributed to the enhanced carrier mobility in the ordered chain structures of the PANI. The maximum electrical conductivity and Seebeck coefficient of composites reach $1.25 \times 10^2 \text{ Scm}^{-1}$ and $40 \mu\text{W K}^{-1}$, respectively, and the maximum power factor is up to $2 \times 10^{-5} \text{ W}/\text{m K}^2$, more than 2 orders of magnitude higher than pure polyaniline, and $ZT \sim 0.004$ [107]. The SWCNT/PANI nanocomposites show both higher electrical conductivity and Seebeck coefficient as compared to pure PANI, which could be attributed to the enhanced carrier mobility in the ordered chain structures of the PANI.

The incorporation of SWCNTs to polythiophenes derivatives, especially poly(3-hexylthiophene), has demonstrated a high increase in their thermoelectric properties [199]. The power factor significantly exceeds the values obtained with either constituent alone, provided that the conjugated polymer is sufficiently p-doped. The use of SWCNTs consistently results in a higher electrical conductivity, with a maximum value above 1000 Scm^{-1} and thus gives rise to a power factor of $25 \mu\text{W}/\text{mK}^2$ for a filler content of only 8 wt% and a maximum value of $PF = 95 \mu\text{W}/\text{mK}^2$

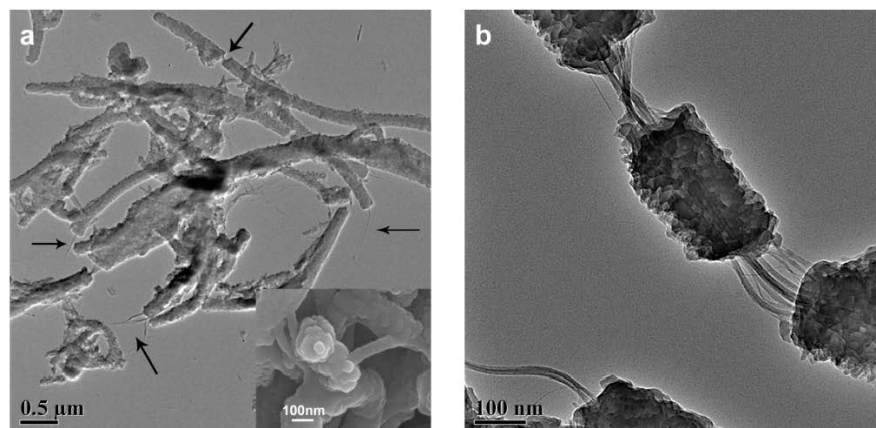


Figure 5.2 TEM images for SWCNT/PANI composites with 25 wt % SWCNT. Inset of (a) is the SEM top view of the nanowire. Reproduced from [107] with permission of ACS Nano.

for 42–81 wt%. Moreover, a CNT content of 8–10 wt% keeps the low bulk thermal conductivity of the polymer matrix, which promises a high figure of merit of at least $ZT > 0.2$ at room temperature.

5.1.2 Graphene/Graphite

Starting from 2013, a lot of research has been devoted on how to increase the thermoelectric properties by composite engineering with carbon derivatives different from CNTs-based materials as graphene, graphene nanoplatelets (GNP) or expanded graphite. Graphite in all its variants has been extensively studied [200] as it is used to increase the electrical conductivity of polymer matrices. Different groups have attempted to improve the thermoelectric efficiency or turning from p-type to n-type conduction a PANI matrix [201–204]. Lei Wang et al [201] prepared HClO_4 -doped PANI/graphite composites by mechanical ball milling and cold pressing. The Seebeck coefficient as well as the electrical conductivity increases with the graphite content giving a $PF = 4.18 \mu\text{W/m K}^2$ and a figure of merit $ZT = 1.37 \times 10^{-3}$ at 50 wt % of graphite. More recently [203], similar values have been obtained for the same system, $PF = 0.8 \mu\text{W/m K}^2$ and $ZT = 1.95 \times 10^{-3}$ for a composite containing 30 wt% GN at 453 K. Simultaneous increase in electrical conductivity and Seebeck coefficient in PANI/graphene nanosheets nanocomposites has been obtained [202] for composites prepared as pellets and films. The power factor of the pellets and films increase from 0.64 to 5.60 and from 0.05 to $1.47 \mu\text{W/m K}^2$ at 50 wt % graphene. The best value of $PF = 14 \mu\text{W/m K}^2$ [204] has been determined for exfoliated graphene nanoplatelets/PANI composites at 50 wt % GNP by mechanical blending.

A very promising paper reported values of $PF = 11.09 \mu\text{W/m K}^2$ and $ZT = 2.1 \times 10^{-2}$ measured on spin coating films obtained by incorporating 2 wt% of graphene to a solution of PEDOT:PSS

[205]. The uniformly distributed graphene increases the interfacial area by 2-3 times with respect similar CNT samples. This results in a facilitated carrier transfer between PEDOT:PSS and graphene as well as the high electron mobility of graphene. Additionally, the porous structure of the thin film decreases the thermal conductivity [205]. Films of PEDOT:PSS/expanded graphite [206] depict an exponential increase of the electrical conductivity while the Seebeck coefficient remains constant, with a maximum $PF = 5.31 \mu\text{Wm}^{-1}\text{K}^{-2}$. In order to enhance the thermoelectric properties, non-covalently functionalized graphene with fullerene [207] by $\pi - \pi$ stacking in a liquid interface was integrated into PEDOT:PSS. Graphene helps to improve the electrical conductivity while fullerene enhances the Seebeck coefficient and hinders the thermal conductivity. The electrical conductivity increases up to 700 S cm^{-1} , the thermal conductivity changed from 0.2 to $2 \text{ W m}^{-1}\text{K}^{-1}$, as usual in this kind of composites, while the Seebeck coefficient was enhanced by around 4-fold, yielding a $ZT = 6.7 \times 10^{-2}$ for 30 wt % nanohybrids-filled polymer composite where the ratio of fullerene to graphene was 3:7. Expanded graphite serves as a filler for both p- and n-type organic materials for constructing thermoelectric devices [208]. PEDOT:PSS/EG composites behave as p-type materials, However, expanded graphite dispersed in polyvinyl alcohol (PVA) with PEI gives composite films with improved n-type characteristics. Promising values of $S = -25 \mu\text{V K}^{-1}$ and $\sigma = 10 \text{ S cm}^{-1}$ have been measured.

5.1.3 Inorganic nanoparticles

Several pioneering works [209–211] studied the influence of some inorganic structures on the thermoelectric efficiency of polymer matrices. PPy- Fe_2O_3 composites depict a linear metallic behavior of the Seebeck coefficient with positive values increasing with temperature and a semiconducting-like behavior of the conductivity [209]. Thermoelectric hybrid materials like $\text{Bi}_{0.5}\text{Sb}_{1.5}\text{Te}_3$ and 1-7 wt%PANI [210] depict electrical conductivities and Seebeck coefficient 30-70% lower than the corresponding to $\text{Bi}_{0.5}\text{Sb}_{1.5}\text{Te}_3$ samples implying a decrease of the PF from 250 to $90 \mu\text{W/m K}^2$ upon addition of 7 wt % of PANI. PANI/ $\text{NaFe}_4\text{P}_{12}$ whisker and nanowire composites have also been prepared [211]. The conductivity of the whisker composite is larger than that of the PANI, although the corresponding to the nanowires is lower. However, the Seebeck coefficient of the nanowire structure is larger than the other two at high temperature. This possibly results from the quantum confinement in the nanowire and an increase in the density of states per unit volume in the nanocomposite [211].

More recently, some efforts have been reported by enhancing the thermoelectric performance of a polymer matrix with Bi_2Te_3 . By mixing Bi_2Te_3 as a powder with PEDOT:PSS results in a 2-3 fold increase of the power factor [46] indicating a promising route of making materials to be used for printing TE devices on flexible substrates. Nanorods of Bi_2Te_3 coated by PANI were created in order to generate a more ordered molecular arrangement of PANI. Thus, the electrical conductivity and thermoelectric power were enhanced with $ZT = 0.0043$ at room temperature

Table 5.1 Thermoelectric parameters of the most relevant conducting polymer composites with carbon materials at room temperature.

System	σ (S cm ⁻¹)	S (μ K ⁻¹)	κ (W m ⁻¹ K ⁻¹)	PF (μ W/m K ²)	ZT	reference
PANI/DWCNT, PE-DOT:PSS/Graphene	1900	120		2710		[39]
PANI/DWCNT, SDBS/Graphene	1000	120		1825		[38]
SWCNT/PEDOT:PSS, DMSO, GA	400	27	↑0.4	25	~0.02	[109]
CNT/PEDOT stabilizer TCPP	980	70		500		[110]
CNT/PVAc	48	45	0.34		0.006	[196]
SWCNT/PEDOT:PSS PVAc	1000	41	0.2-0.4	160		[197]
SWCNT/PEDOT:PSS Layered structure	241	38.9		21.1		[212]
SWCNT/PANI	125	40		0.2	0.004	[107]
3D-CNT/PANI	40.35	23	0.29		0.0022	[107]
CNT-PANI nanofibers	15	10		0.16	0.0022	[213]
PANI coated CNT-PANI	28	21.6	0.4		0.001	[214]
poly(3-hexylthiophene) SWCNTs	1000	29		98		[199]
MWCNT/polithiophene	6	25	0.6		8.7×10^{-4}	[215]
PANI/graphite composites	100	10	1.2	4.18	1.37×10^{-3}	[201]
PANI/graphene nanosheets pellet	~60	~30		5.6		[202]
PANI/graphene nanosheets film	~8	~42		1.47		[202]
PANI/graphene nanoplatelets mechanical blending	123	34		14		[204]
PEDOT:PSS/expanded graphite	213	15		5.31		[206]
PEDOT:PSS/graphene fullerene	700	25	0.4		0.06	[207]

[45]. PEDOT:PSS/Bi₂Te₃ composite films depict a maximum electrical conductivity of 421 S cm⁻¹ with 10 wt% Bi₂Te₃ corresponding to a PF= 9.9 μ W/m K² and $ZT = 0.04$ [44].

Other procedure to enhance the TE efficiency is by adding additives. So, flexible films of PEDOT:PSS and poly(acrylic acid) (PAA) with an additive reach values of $ZT = 0.2$ for a Bi₂Te₃ concentration of 95 wt% [216]. Other inorganic particle different from Bi₂Te₃ is tellurium. The power factor of PEDOT:PSS can be optimized by dispersing Te nanowires just changing the synthesis, the effect of nanowire morphology [40, 217, 218]. A conformationally organized PEDOT:PSS interfacial layer template by the Te nanowires produces a high conductivity and Seebeck coefficient, keeping the low thermal conductivity of the host polymer. A ZT as high as 0.1 has been obtained.

Table 5.2 Thermoelectric parameters of the most relevant conducting polymers composites with inorganic nanoparticles at room temperature.

System		σ (Scm ⁻¹)	S (μ VK ⁻¹)	κ (W m ⁻¹ K ⁻¹)	PF (μ Wm ⁻¹ K ⁻²)	ZT	reference
PEDOT:PSS	PAA	380	79	0.36	~240	0.2	[216]
Bi ₂ Te ₃							
PEDOT:PSS	Bi ₂ Te ₃	250	150	0.558	131	0.08	[46]
PANI	Bi ₂ Te ₃ nanorods	11.626	39	0.11	1.8	0.004	[46]
p-type							
PANI	Bi ₂ Te ₃ nanorods	23	-70		10		[46]
n-type							
PEDOT:PSS	Bi ₂ Te ₃	421	18.6	0.07	9.9	0.04	[44]
films							
PEDOT:PSS	Te	19.3	163	0.22-0.3	70.9	0.1	[217]
PEDOT:PSS	Te	~ 15	260		100		[40]
nanowire							
PEDOT:PSS/H ₂ SO ₄		~ 200	100		284		[42]
Te nanorod							
PEDOT:PSS	Te	~ 12	170		35		[218]
nanowire							
PEDOT:PSS	Gold	~ 2000	12		20		[218]
nanorod							
PH3T	Bi ₂ Te ₃	~ 4.5	118		6.3		[219]

Novel metal/polymer/metal structures present a new design to combine inorganic metals and organic polymers thus increasing the Seebeck coefficient up to 252 μ V/K on a Al/PEDOT:PSS/Al device [220]. Spherical gold nanoparticles rod-shaped (Au NR) have proven to be effective as increases the electrical conductivity (2000 S cm⁻¹) and decrease the Seebeck coefficient (12 μ V/K) with the increase of Au NR concentration in the PEDOT:PSS matrix [221].

Tables 5.1 and 5.2 summarize values of the main thermoelectric parameters in conductive polymers, polymer composites with carbons and inorganic materials, respectively.

5.1.4 Common methods to prepare nanocomposites and hybrid materials

The synthesis of nanocomposites and hybrid materials basically consists of the creation of a stable mixture of both compounds and a further processing step. In order to create a homogeneous mixture, firstly the inorganic nanofiller has to be dispersed into the polymer matrix. A polymer solution is usually employed. The nanofiller is added to the polymer solution (water or organic solvent) and then the mixture is subjected to a dispersion treatment using mechanical stirring and usually ultrasounds (Figure 5.3(a)). Other way is to disperse the fillers in the monomer or pre-polymer solution. After a homogeneous dispersion is obtained, the mixture is polymerized creating a composite material. This method is commonly used for thermoset polymers such as epoxy resins [222]. Figure 5.3 shows the steps followed in the two methods.

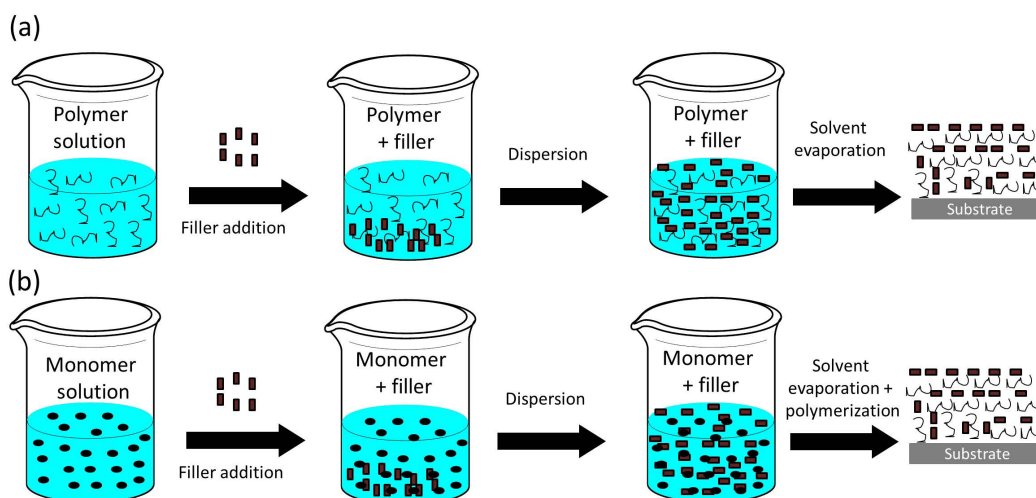


Figure 5.3 schematic of polymer nanocomposites preparation from (a) polymeric solution and (b) insitu polymerization

5.1.4.1 Surface modification of inorganic nanofillers

The big problem to get an efficient polymer composite is to obtain a good dispersion of the inorganic filler into the polymer matrix; due to their different nature, they are not compatible in general. For this reason during many years researches have been doing a lot of effort to improve the stability of inorganic additives in the polymer solutions or solvents. Surface modification is the most used method to improve the dispersion of the inorganic filler in a polymeric matrix. It is possible to classify the surface modification considering how the modifier is anchored to the inorganic particle. Using this criteria, the surface modification method can be classified in non-covalent modification and covalent modification.

The non-covalent methods consist of the adsorption of amphiphilic molecules, such as surfactants and amphiphilic copolymers or polyaromatic molecules with hydrophilic or hydrophobic groups to the nanofiller surface [223, 224]. The hydrophilic parts of the modifier can interact with polar regions of the polymer matrix and the hydrophobic parts of the modifier with the non-polar regions. Consequently, the dispersion of the filler increases due to the interaction with the polymer matrix media. This method is very common in the dispersion of CNTs in water [223, 224]. Surfactants, such as sodium dodecyl sulfate (SDS) or cetyltrimethylammonium bromide (CTAB), can be employed to stabilize CNTs in water [223, 224].

The covalent methods consist of anchoring the modifier by covalent bonding. There are a lot of methods to carry out this modification. One of those is the chemical treatment of the filler surface employing silane coupling agents to improve the compatibility between the particle and polymer surfaces and the properties of the composite materials. For example, the surface of the unmodified nanoparticle is covered only with $-OH$ groups, while the surface of the silane-modified nanoparticle is covered with 3-methacryloxypropyl trimethoxysilane molecules. The

modified nanoparticles behave differently within organic solvents or polymer matrices compared to unmodified nanoparticles, showing better dispersion the modified ones [224].

Other method is grafting of synthetic polymers. This approach consists in modifying the surfaces of inorganic based on grafting synthetic polymers to the substrate surface. This enhances the chemical functionality and alters the surface topology of the native inorganic material. This kind of functionalization reduces the aggregate formation (see Figure 5.4) . The polymer from

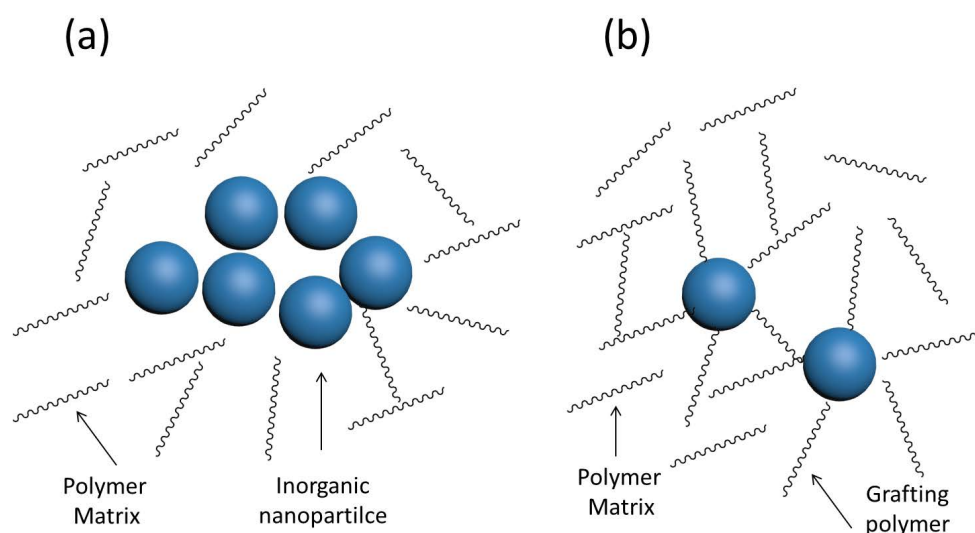


Figure 5.4 Diagram of: (a) agglomerated nanoparticles in the matrix polymer and (b) well dispersed particles due to the grafting polymer.

the surface keeps the particles separated and stables in the polymer matrix media. Two methods have been reported in the literature to covalently attach polymer chains on the surface of inorganic nanofillers. The first one is the “grafting to” in which the end-functionalized polymers react with the particle surface. The second method is the “grafting from” method in which polymer chains are grown from an initiator-terminated self-assembled monolayer [224].

In the following sections four studies related with the synthesis of polymer nanocomposites such as: PEDOT:PSS/EG, Perovskite/PEDOT, Te/PEDOT and MWCNT/PEDOT are shown.

5.2 PEDOT:PSS/EG composites⁸

5.2.1 Materials

PEDOT:PSS solution (1.3 wt % in water) with a ratio of PEDOT to PSS of 38.5 to 61.5 %, natural graphite powder of size < 20 m, nitric acid (HNO₃) and sulfuric acid (H₂SO₄) were

⁸This section is based on the publication: “Thermoelectric measurements of PEDOT: PSS/expanded graphite composites M. Culebras, C. M. Gómez, A. Cantarero, *Journal of Materials Science*, 48, 2855-2860 (2013) Reproduced with permission of Springer.

purchased from Sigma-Aldrich Co.

5.2.2 Preparation of expanded graphite

Expanded graphite was obtained by the method of chemical oxidation [19]. The natural graphite was dried at 75°C in a vacuum oven for 10 h. Then, it was mixed for 12 h with a mixture of sulfuric and nitric acid in a volume ratio 3:1 in order to form the graphite intercalated compound (GIC). The nitric acid is used as an oxidizer and the sulfuric acid to intercalate them. The mixture was stirred from time to time to get a uniform intercalation of sulfuric acid into the graphite flakes. After washing and filtrating until a neutral pH, the resulting material was dried at 60°C in vacuum for 5 h, and afterwards subjected to a thermal shock at 900°C for 20 s to form the EG.

5.2.3 Preparation of PEDOT:PSS/EG

Expanded graphite at different weight fractions from 0 to 80 wt % was introduced in the commercial solution of PEDOT:PSS. The blend was sonicated in an ultrasonic bath for 1h in order to disaggregate the EG flakes and stirred vigorously for 5 h in order to obtain a stable dispersion. The suspensions were cast on glass slides that were previously washed in an ultrasonic bath with distilled water and finally with acetone to eliminate the water. The PEDOT:PSS/EG coated glass was kept at 40°C during 24 h and then at 60°C in vacuum for 5 h. The film dimensions were (4×2.7) cm² and the thickness ranged between 20-30 μm.

5.2.4 Morphology of the PEDOT:PSS/EG composites

The morphological features of the smooth PEDOT:PSS/EG films were determined by TEM and SEM analysis. The TEM images shown in Figure 5.5 indicate a homogeneous dispersion of

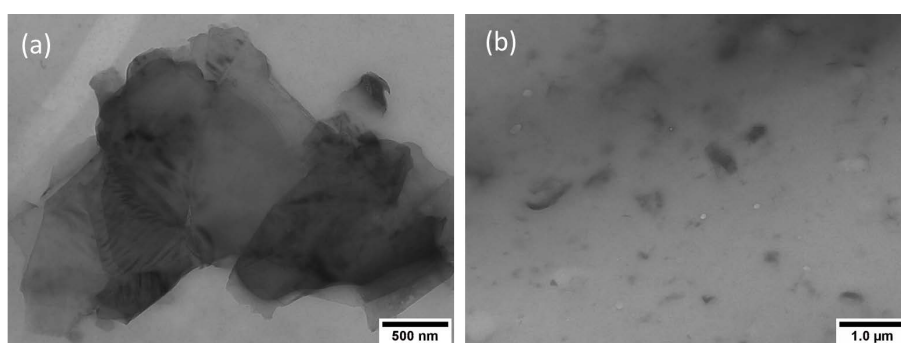


Figure 5.5 TEM images of PEDOT:PSS with 15 wt % of expanded graphite.

EG in the PEDOT:PSS polymer with a nanometric size particle dispersion. Expanded graphite

nanosheet appears exfoliated into many EG layers. The SEM images are depicted in Figure 5.6. Figures 5.6(a) and 5.6(b) show the cross-section of a sample of PEDOT:PSS without EG

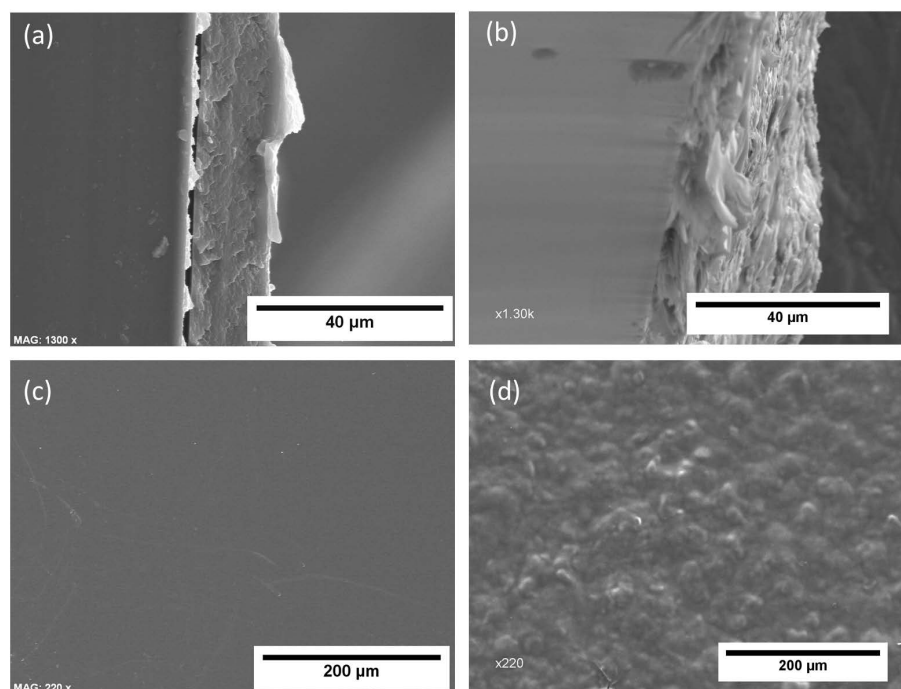


Figure 5.6 SEM images of: (a) cross section of PEDOT:PSS, (b) cross section of PEDOT:PSS with 30 wt % expanded graphite, (c) surface PEDOT:PSS and (d) surface PEDOT:PSS with 30 wt % expanded graphite.

and with 30 wt % EG, respectively. The film of PEDOT:PSS form a single layer structure, whereas introduction of EG induces the formation of a multilayer structure. The chains of PEDOT:PSS are intercalated in the galleries of the EG indicating a homogeneous composite dispersion. Figure 5.6(c) and 5.6(d) shows the surface of a film of PEDOT:PSS without EG and with 30 wt % EG respectively, with a characteristic roughness indicating the packing density of the EG at the film surface for films with EG. TEM and SEM images indicate a well-dispersed, densely packed PEDOT:PSS/EG films.

5.2.5 Thermal analysis of the PEDOT:PSS/EG composites

The thermal analysis was carried out using DSC and TGA measurements, as described in Chapter 2. Figure 5.7 shows the DSC curves of PEDOT:PSS films with no indication of a well-defined glass transition temperature, as previously reported [225]. In the first DSC scan an endothermic peak around 110°C is detected related to the melting of the PEDOT:PSS crystals [226]. An indication that the sample was free of water is revealed by the absence of a peak near to 0°C. No peaks were observed during a second temperature scan indicating that the sample did not have enough time to re-crystallize during the quick cooling. The PEDOT:PSS chains tend to form crystals during film formation or during slow cooling if there is enough time to reorganize

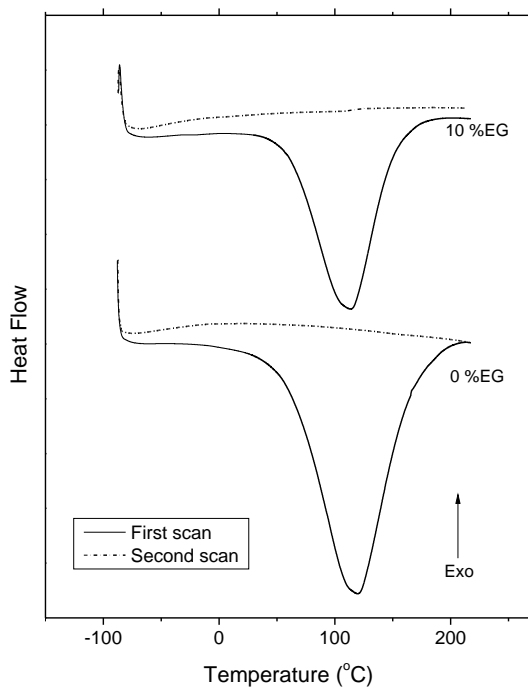


Figure 5.7 Differential scanning calorimetric patterns of PEDOT:PSS and PEDOT:PSS with 10% of EG.

themselves. Similar patterns have been obtained for the PEDOT:PSS samples modified with EG.

Figure 5.8 shows the weight loss of PEDOT:PSS, of PEDOT:PSS with 30 wt % EG and pure

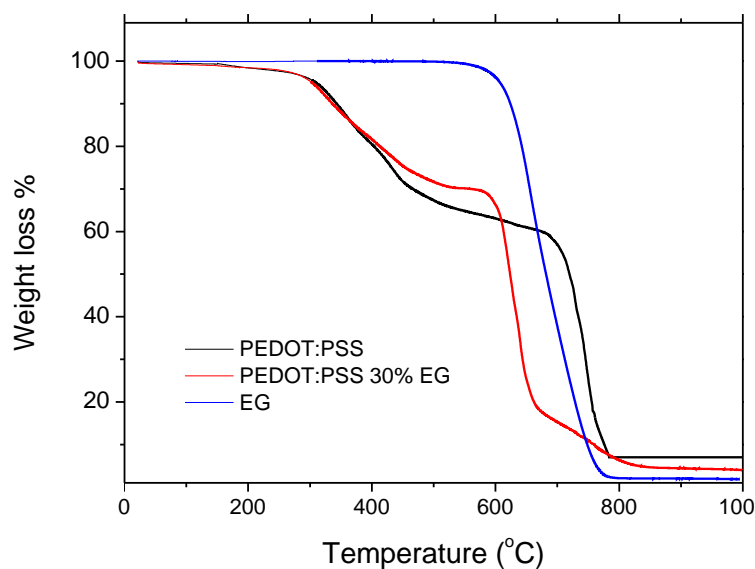


Figure 5.8 Thermogravimetric analysis of PEDOT:PSS, PEDOT:PSS with 30 wt % EG and EG powder.

EG. Good thermal stability was observed for PEDOT:PSS and PEDOT:PSS 30 wt% EG until about 270°C, similar to PPy/EG composites [20]. The sample weight significantly decreases due to the fragmentation of the PSS sulfonate group at about 250°C. At higher temperatures, larger than 575°C, other fragments due to carbon oxidation are detected. This secondary process in the PEDOT:PSS samples modified with EG is overlapped with the oxidation of carbon atoms in the EG particles. Expanded graphite is stable until around 600°C and lose weight in one step without any residual weight left [227]. The good thermal stability in PEDOT:PSS and PEDOT:PSS/EG composites, indicate that it is possible to use these materials in applications up to 200°C.

5.2.6 Thermoelectric properties of PEDOT:PSS/EG composites

Conductivity of semi-conducting polymers as PEDOT:PSS in presence of conducting fillers depends on the filler loading and its dispersion in the matrix. The electrical conductivity of the composites was measured at 25°C being this temperature the most usual in large-scale applications. Data of electrical conductivity, determined by the Van Der Pauw method, are plotted as a function of expanded graphite content in Figure 5.9. The electrical conductivity of PEDOT:PSS

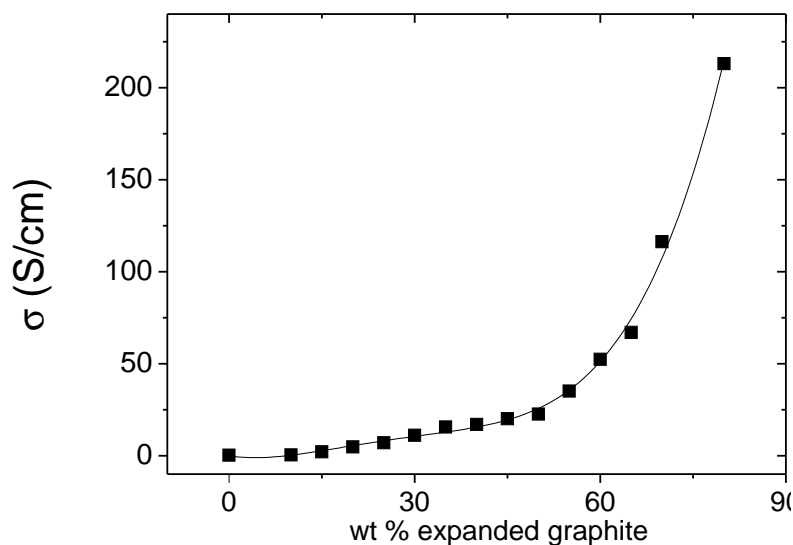


Figure 5.9 Electrical conductivity of PEDOT:PSS/ expanded graphite composites.

increases with the expanded graphite content from 0.21 S/cm to 213 S/cm, as usual in these graphite modified samples [228, 229]. A sharp increase of conductivity is attained at around 55 weight % of EG. Free movement of charge carriers above this graphite content increases more efficiently the conductivity caused by a higher connectivity between the conductive expanded graphite layers [228, 230, 231]. At lower graphite content the conductivity is mainly due to the intrinsic conductivity of the polymer. Figure 5.10 shows the results of the Seebeck coefficient

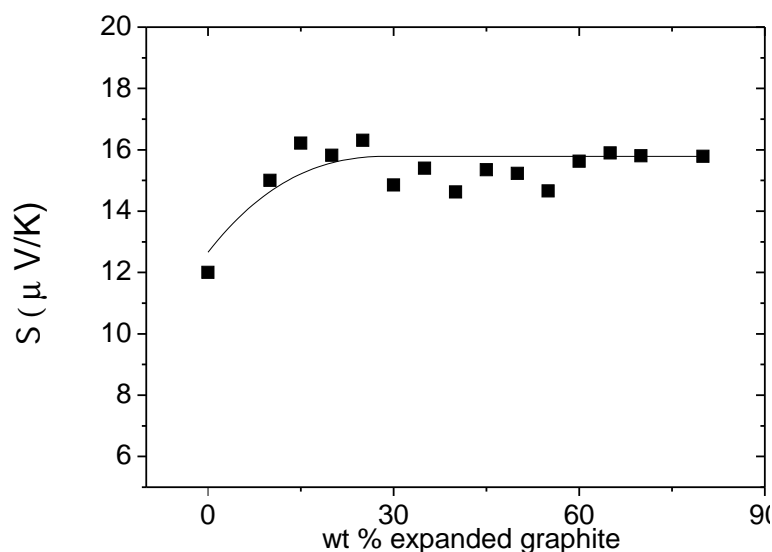


Figure 5.10 Seebeck values of PEDOT:PSS/expanded graphite composites.

measurements of PEDOT:PSS/EG composites as a function of EG content at room temperature. Values of S are positive, indicating a p-type conduction. The Seebeck coefficient increases with the first addition of EG and levels out at about $15\text{--}16 \mu\text{V/K}$ without not apparent dependence on the expanded graphite content. These values are lower than those for traditional inorganic materials such as Bi_2Te_3 and GeSi [55, 232] but in the same range of magnitude than other semi-conducting polymers [72]. The power factor as a measure of the thermoelectric potential of the samples is shown in Figure 5.11 as a function of EG content at room temperature. The

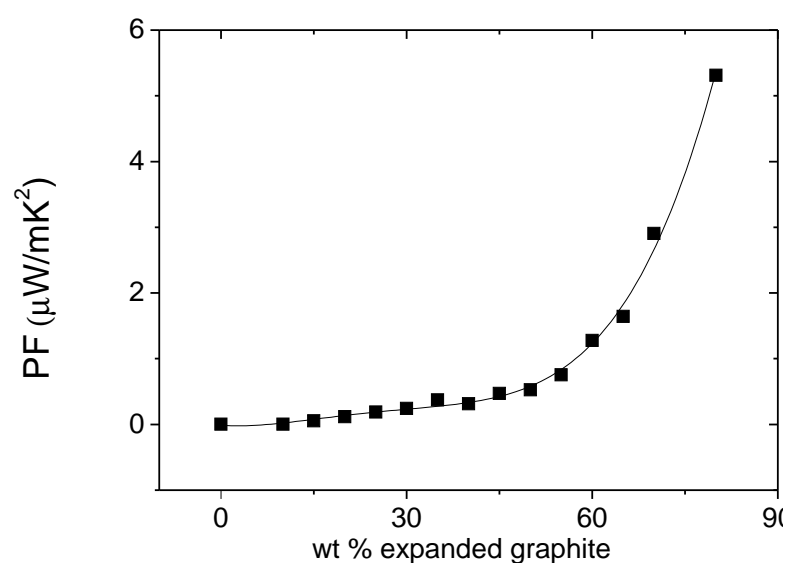


Figure 5.11 Power factor of PEDOT:PSS/expanded graphite composites.

shape of the curve is similar to that of the conductivity with a sharp increase from $0.0035\mu\text{W/m K}^2$ without EG to $5.31\mu\text{W/m K}^2$ with 80 % wt of EG. To get an idea of the value of the ZT, since we do not have experimental data, we have chosen values of thermal conductivity from the literature. The thermal conductivity for PEDOT:PSS was assumed to be approximately 0.2 W/m K [72]. This gives a value of ZT of 5.74×10^{-6} for the PEDOT:PSS used in this work. In reference [231] the value of thermal conductivity for ethylene-octene copolymer/expanded graphite composites with 50 wt % of EG was 0.676 W/mK . Since the chemical nature of the our samples is similar, for PEDOT:PSS with 50 wt % of EG the calculated ZT value would be 2.3×10^{-4} , similar to literature values [72]. The addition of EG in a PEDOT:PSS matrix increases the ZT value by three orders of magnitude with respect to PEDOT:PSS.

5.3 Hybrid composites of NCCO perovskites/PEDOT

5.3.1 Materials

Cobalt acetate tetrahydrate ($\text{Co}(\text{CH}_3\text{COO})_2\cdot 4\text{H}_2\text{O}$) 98% purity, calcium acetate monohydrate ($\text{Ca}(\text{CH}_3\text{COO})_2\cdot \text{H}_2\text{O}$) 99% purity, neodymium oxide (Nd_2O_3) 99.9%, glacial acetic acid 99.5%, tetrahydrofuran, Fe-Tos and a commercial aqueous solution of PEDOT:PSS have been purchased to Sigma Aldrich Co. (Madrid, Spain). EDOT, 97 % purity, was obtained from Alfa Aesar and butanol was bought to VWR.

5.3.2 Synthesis of the perovskite nanoparticles⁹

$\text{Nd}_{1-x}\text{Ca}_x\text{CoO}_3(\text{NCCO})(x= 0.001 \text{ and } 0.005)$ powder was obtained by a conventional thermal method: $\text{Co}(\text{CH}_3\text{COO})_2\cdot 4\text{H}_2\text{O}$ and $\text{Ca}(\text{CH}_3\text{COO})_2\cdot \text{H}_2\text{O}$ were dissolved in deionized water, and Nd_2O_3 was dissolved in acetic acid. All the solutions were combined to obtain Nd-Ca-Co solutions whose total cationic concentration was 0.30 M and subsequently, frozen with liquid nitrogen. In order to eliminate the solvent, the frozen solution was lyophilized at 10^{-4} atm with a Tesla Cryodos freeze-dryer to obtain an amorphous solid. Finally, the solid was heated during 12 h at $900\text{ }^\circ\text{C}$ under air atmosphere to obtain the perovskite phase. The powder obtained was pressed to form compact pellets (0.5" in diameter) by using a pellet die at 490 MPa. Further, the pellets were sintered at $1150\text{ }^\circ\text{C}$ for 48 h in air atmosphere.

⁹This section is based on the publication: "Hybrids composites of NCCO/PEDOT for thermoelectric applications M. Culebras, A. García-Barberá, J. F. Serrano-Claumarchirant, C. M. Gómez, A. Cantarero, *Synthetic Metals*, (2017) DOI:10.1016/j.synthmet.2016.12.016 Reproduced with permission of Elsevier.

5.3.3 Preparation of the composites

Two different series of composites were made by changing the perovskite/polymer weight ratio as follows: 80/20, 85/15, 90/10 and 95/5. Series 1: NCCO/PEDOT:PSS with $x=0.001$ and 0.005 . The NCCO powder was dispersed in the commercial aqueous solution of PEDOT:PSS by sonication with an ultrasonic bath during 1 h in order to destroy all the aggregates. The resulted dispersion was stirred for 5 h to be stabilized. Addition of THF forms a precipitate of NCCO/ PEDOT:PSS which was filtered and dried at 100°C in vacuum for 5 h. Series 2: NCCO/PEDOT:Tos with $x=0.001$ and 0.005 . The perovskite powder was dispersed in a solution of EDOT (1 wt %) in butanol. The dispersion was sonicated in an ultrasonic bath for 1h in order to disaggregate the NCCO particles and then stirred vigorously for 5 h in order to obtain a stable dispersion. Then, FeTos was added to the EDOT solution at 1:2 EDOT:Fe-Tos molar ratio, and the resultant solution was dropped on a glass substrate and heated at 100°C for 10 min. The powder obtained was washed with deionized water and ethanol several times, and subsequently dried at 100°C in vacuum for 5 h. Finally, the resulting powder was pressed to make a pellet.

5.3.4 Morphological and structural characterization of the NCCO/PEDOT perovskites nanocomposites

In this work, a p-type material, the perovskite cobalt oxide $\text{Nd}_{1-x}\text{Ca}_x\text{CoO}_3$, has been used as thermoelectric matrix due to its high Seebeck coefficient. Two different dopant concentrations, $x=0.001$ and 0.005 , were employed in order to find the best doping content in these kind of oxides. These oxides were blended with a small amount of PEDOT:PSS and PEDOT:Tos. Thus, four different composites, with different weight concentrations of perovskite/polymer=80/20, 85/15, 90/10 and 95/5, for the two calcium content were investigated. Figure 5.12 shows the morphology from SEM images of the $\text{Nd}_{1-x}\text{Ca}_x\text{CoO}_3$ ($x=0.001$) with the two different polymer matrices, PEDOT:PSS and PEDOT:Tos, under study. For the case of PEDOT:PSS (Figures 5.12(a), (c) and (e)) it is possible to observe how the polymer fills the whole space between the NCCO nanoparticles for a PEDOT content of 20% wt. However, when the NCCO content increases, the polymer content decreases giving rise to the appearance of free space between the NCCO nanoparticles, increasing the contact between them as it can be observed in Figures 5.12(c) and (e). Similarly, the PEDOT-Tos hybrids have the same morphological characteristics as shown in Figures 5.12(b), 5.12(d) and 5.12(f). The size of the NCCO nanoparticles was around 500 nm.

Figure 5.13 depicts the characteristic X-ray patterns of the fabricated $\text{Nd}_{1-x}\text{Ca}_x\text{CoO}_3$ ($x=0.001$) composites using PEDOT:PSS (Figure 5.13(a)) and PEDOT:Tos (Figure 5.13(b)). The diffraction peaks in both system are an indication of the cubic perovskite phase. This is crucial for the purpose of this work since only the cubic phase presents thermoelectric activity [143, 170, 171].

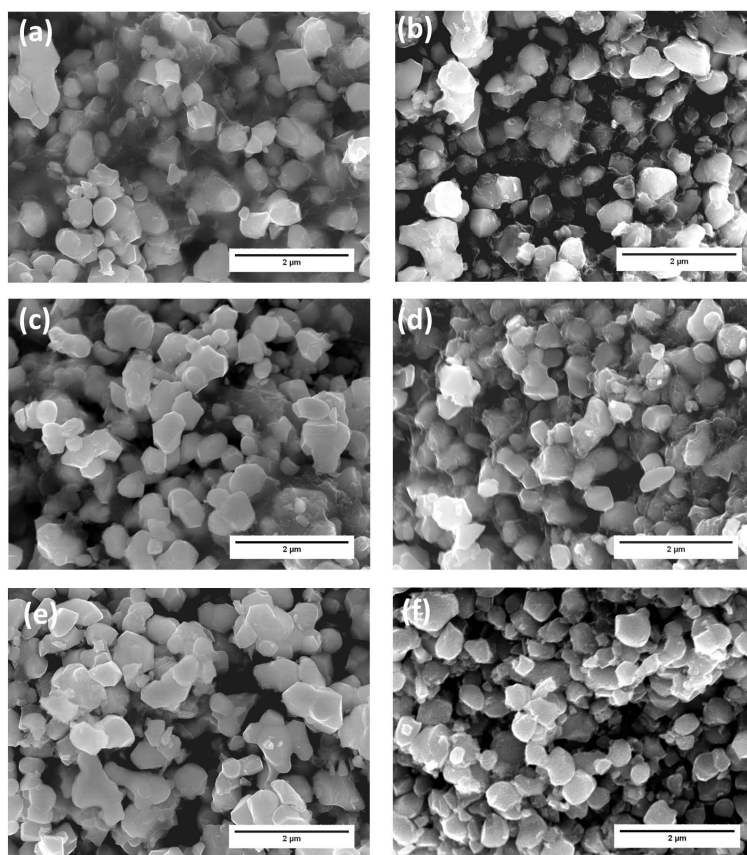


Figure 5.12 SEM images of NCCO/PEDOT:PSS composites with : (a) 80% (c) 90% and (e) 95 % of $\text{Nd}_{0.999}\text{Ca}_{0.001}\text{CoO}_3$. SEM images of NCCO/PEDOT:Tos composites with an (b) 80% (d) 90% and (f) 95 % of $\text{Nd}_{0.999}\text{Ca}_{0.001}\text{CoO}_3$.

The peak associated to the amorphous polymer phase in the composite appears between $2\theta=10^\circ$ and $2\theta=20^\circ$. The area of this peak increases proportionally to the amount of PEDOT in the blend [233].

5.3.5 Thermoelectric properties of the NCCO/PEDOT hybrids perovskites composites

In order to characterize the hybrids materials, Figure 5.14 plots values of the electrical conductivity, Seebeck coefficient, and power factor for the systems NCCO /PEDOT:PSS and NCCO/PEDOT:Tos as a function of calcium doping and proportion of perovskite. The electrical conductivity increases with the addition of polymer to the NCCO particles as it is shown in Figures 5.14(a) and 5.14(d) for PEDOT:PSS and PEDOT:Tos, respectively. The electrical conductivity for the case of pure NCCO was 5×10^{-4} S/cm and 1.5×10^{-2} S/cm for a calcium content of $x=0.001$ and $x=0.005$, respectively. The electrical conductivity is very low, which is normal because the pellet has been obtained by compressing the nanostructured powder.

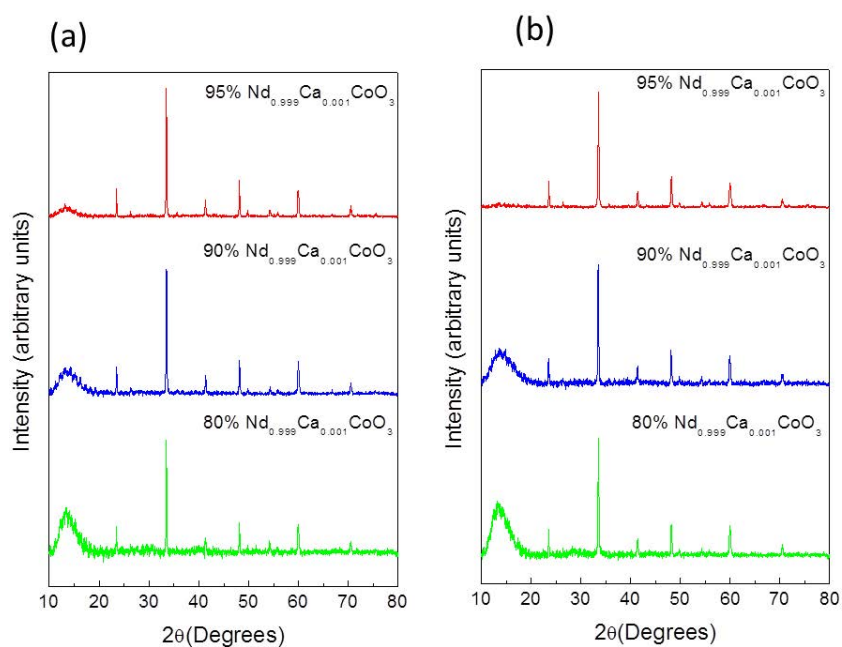


Figure 5.13 XRD spectra of $\text{Nd}_{0.999}\text{Ca}_{0.001}\text{CoO}_3$ composites with: (a) PEDOT:PSS and (b) PEDOT:Tos.

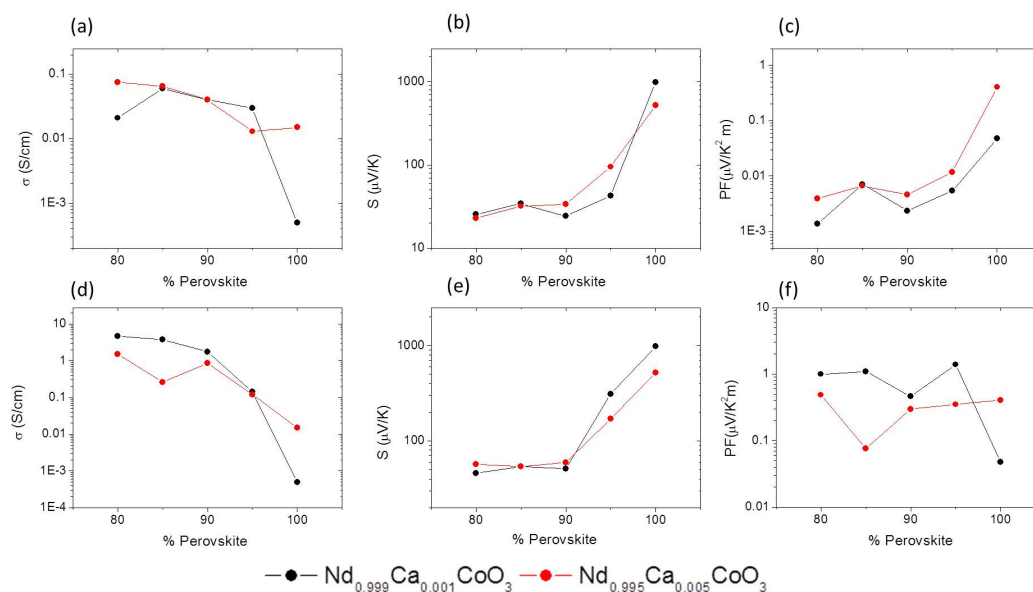


Figure 5.14 Electrical conductivity, Seebeck coefficient and power factor for the NCCO/PEDOT:PSS nanocomposites (plots a, b, and c) and for NCCO/PEDOT:Tos (plots d-f).

However, the electrical conductivity increased with the calcium content in the NCCO nanoparticles. This fact indicates a doping effect due to the presence of calcium into the perovskite phase according with previous investigations [141]. The combination of a conducting polymer with the NCCO nanoparticles produces an increase of several orders of magnitude in the electrical conductivity (4 in the case of PEDOT:Tos). The polymer acts as a conductive binder between

the NCCO nanoparticles, increasing the electric contact between the nanoparticles. The higher conductive nature of PEDOT:Tos compared with the PEDOT:PSS in combination with the in-situ polymerization produces a higher increase in the electrical conductivity, when PEDOT:Tos is used to prepare the NCCO nanocomposites. Figure 5.14(b) and 5.14(e) show the Seebeck coefficient of NCCO/PEDOT:PSS and NCCO/PEDOT:Tos as a function of calcium doping and proportion of NCCO. The NCCO exhibits large values for the case of pure nanoparticles, 979 $\mu\text{V/K}$ and 519 $\mu\text{V/K}$, typical for low doped semiconductors. The Seebeck coefficient decreases with the incorporation of PEDOT until values around 25 $\mu\text{V/K}$ for the case of PEDOT:PSS and 50 $\mu\text{V/K}$ for the case of PEDOT:Tos. In case of PEDOT:PSS the value is very similar to medium doped PEDOT [37] indicating a scanty effect in the enhancement of the Seebeck coefficient with the addition of NCCO nanoparticles. However, for the case of the PEDOT:Tos and NCCO nanoparticles it is possible to obtain intermediate values of 310 $\mu\text{V/K}$ at 5% of PEDOT load, for a calcium content of 0.001 and 170 $\mu\text{V/K}$ for 0.005. Finally, with the addition of 20 % of PEDOT, the Seebeck coefficient decreases until values around 50 $\mu\text{V/K}$ in both kind of composites. The PF has been calculated with values of the electrical conductivity and the Seebeck coefficient, in order to give an idea of the thermoelectric efficiency of these kind of hybrid composites. For the case of the composites based on PEDOT:PSS, the PF decreases with the addition of the polymer indicating that PEDOT:PSS is poor conductive additive for these kind of nanofillers. The scanty effect of PEDOT:PSS is given by their low electrical conductivity. However, for the case of the nanocomposites fabricated in-situ using PEDOT:Tos as a polymer, the power factor increases compared to the pure NCCO nanoparticles. This fact indicates a good synergy between PEDOT:Tos and the NCCO nanoparticles. The best value, 1.34 $\mu\text{W/K}^2\text{m}$, was attained for the sample with 5% of PEDOT:Tos and nanoparticles with 0.001 calcium content. The best compromise between the electrical conductivity and the Seebeck coefficient has been attained for this kind of nanocomposites.

5.4 Combining multilayer carbon nanotube assembly and electrochemical polymerization for hybrid thermoelectric materials

5.4.1 Materials

Poly(diallyldimethylammonium chloride) (PDDA), with a molecular weight of $1-2 \times 10^5$ g/mol, sodium deoxycholate (DOC) ($\text{C}_{24}\text{H}_{39}\text{NaO}_4$), EDOT, lithium perchlorate (LiClO_4), and acetonitrile were purchased from SigmaAldrich (Milwaukee, WI). All chemicals were used as received. MWCNTs were obtained from Bayer Material Science (12–15 nm outer and 4 nm inner wall diameter > 1 μm length, C 95 wt%) (Leverkusen, Germany).

5.4.2 Substrates

PET, with a thickness of 179 μm , (trade name ST 505 by DuPont Teijin, purchased from Tekra Corp, New Berlin, WI) was rinsed with water, methanol, ultra pure water, and dried with filtered air before use. Corona treatment (a BD-20C Corona Treater, Electro-Technic Products Inc., Chicago, IL) was used to improve the adhesion of the first layer by oxidizing the polymer surface. Polished Ti/Au crystals with a resonance frequency of 5MHz were purchased from Maxtek, Inc. (Cypress, CA) and used to characterize deposited mass per layer with a quartz crystal microbalance (QCM).

5.4.3 Assembly of MWCNT films

0.05 wt % MWCNT were dispersed in an aqueous solution of 0.25 wt% PDDA or 1 wt% DOC. Both MWCNT suspensions were bath sonicated for 30 min, followed by 20 min of 15 W tip sonication in an ice-water bath, and another 30 min of bath sonication to homogenize. MWCNT dispersions were then centrifuged at 4000 rpm for 20 min and the supernatant was decanted. The pH of the nanotube suspensions, in either PDDA or DOC, was left unaltered at 5.8. Each substrate was immersed into the cationic PDDA-based suspension for 5 min, followed by rinsing and drying, and then dipped into the anionic DOC suspension for another 5 min. This process results in one deposition sequence of a MWCNT-PDDA/MWCNT-DOC bilayer (BL). After the initial BL was deposited, all subsequent layers were deposited with 1 min dip times, with rinsing and drying in between. This cycle was repeated to deposit the desired number of bilayers. Deposited multilayer films were air-dried overnight and then stored in a desiccator prior to further processing or characterization.

5.4.4 Electrochemical deposition of PEDOT

A solution of 0.01 M EDOT and 0.1 M LiClO_4 was prepared in acetonitrile. The polymerization was carried out in a three-electrode electrochemical cell at 3 mA vs an Ag/AgCl reference electrode in an Epsilon 851 cyclic voltammeter (BASi Instrumentation, West Lafayette, IN). During the electrochemical polymerization of EDOT, a platinum grid was used as counter electrode and the MWCNT film acted as the working electrode. Figure 5.15 shows a scheme of the polymerization of EDOT over the MWCNTs substrates fabricated using layer by layer assembly (LBL).

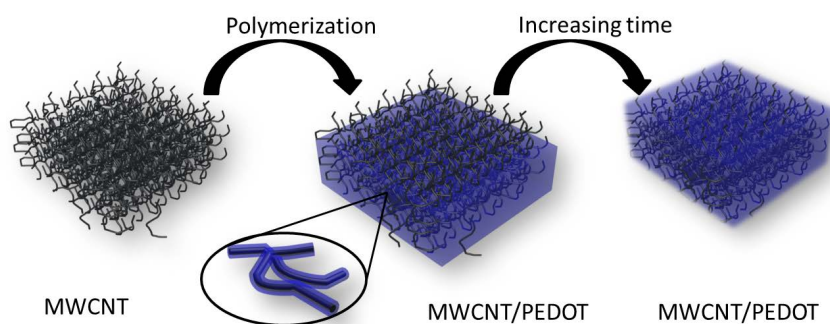


Figure 5.15 Scheme of PEDOT polymerization of MWCNTs substrates

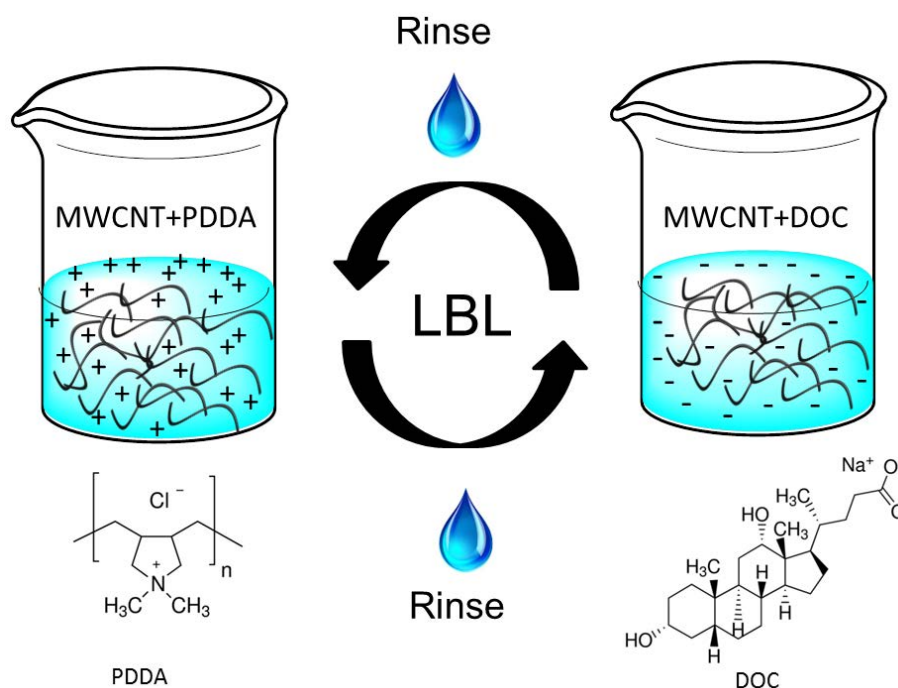


Figure 5.16 Schematic of the LBL deposition of MWCNTs stabilized by PDDA and DOC.

5.4.5 Morphology and characterization during the electrochemical deposition of PEDOT

. MWCNTs films were prepared using the LBL assembly method shown in Figure 5.16. Multilayer thin films tightly assemble due to the electrostatic interaction between PDDA and DOC molecules used to stabilize the MWCNT in the aqueous deposition suspensions. In the case of PDDA, the polymer is assumed to be adsorbed to the MWCNT, creating positively-charged nanotubes that are stable in water. In the same way, the interaction between DOC and the surface of MWCNT imparts water stability and a negative charge. Alternately, exposing a PET thick film substrate to these two oppositely-charged aqueous solutions results in the incremental growth of a nanotube-based thin film with high electrical conductivity, as shown in Figure 5.17. Figure

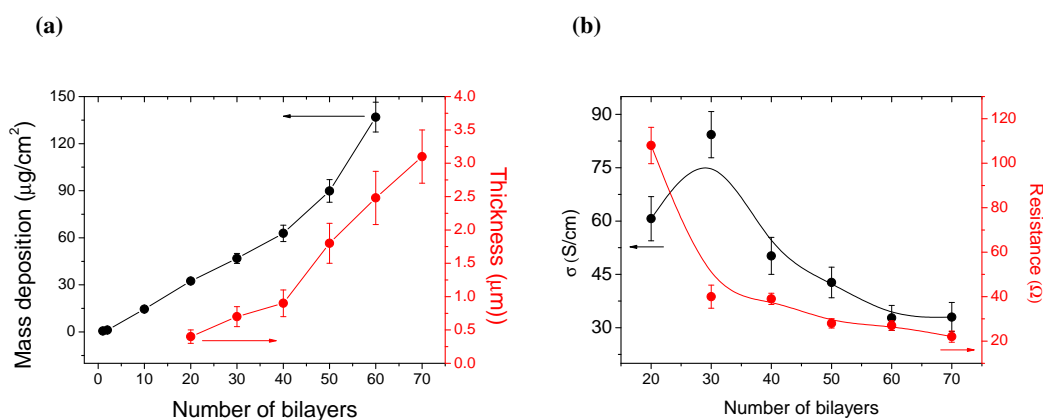


Figure 5.17 Mass deposition and thickness of MWCNT-PDDA/MWCNT-DOC films as a function of the number of bilayers deposited (a). Electrical conductivity and absolute resistance as a function of the number of bilayers deposited (b). The lines in each graph are just to guide the eyes.

5.17(a) shows the approximately linear growth in thickness and mass deposited during the LBL assembly of MWCNT-PDDA and MWCNT-DOC. The thickness increases from 400 nm at 20 BL to 3.1 μm at 70 BL. The relatively large size and complex shape of the carbon nanotubes results in a significant error associated with these values. What appears to be a change in the slope of growth beyond 40 BL is an artifact due to the high variability associated with the profilometer thickness measurements.

Electrical conductivity and resistance values for these MWCNT-based films as a function of the number of bilayers deposited are shown in Figure 5.17(b). The resistance decreases greatly from 20 to 30 BL and then decreases more gradually. In a bulk material, increasing thickness typically decreases electrical resistance, but these multilayered thin films exhibit more complex changes in the electrical behavior. During LBL deposition, diffusion of DOC and PDDA deeper into the film can increase the proportion of insulating material, which causes an increase in the resistance, although not necessarily proportional to the increase in thickness due to the reduction of the electrical conductivity. For this reason, a maximum in the electrical conductivity appears at 30 BL, when these effects are counterbalanced. The dense packing of MWCNTs, that contributes to relatively high electrical conductivity (Figure 5.17(b)), is shown in cross sections TEM images for a 50 BL MWCNT-PDDA/MWNT-DOC film (Figure 5.18). The nanotubes appear more tightly packed close to the PET substrate which may indicate greater stabilizer content (DOC and PDDA) near the multilayer film surface. This is a contributing factor to the behavior shown in Figure 5.17(b) (i.e., there is no clear trend between electrical conductivity and film thickness). Greater packing density with a smaller number of bilayers will result in the greater electrical conductivity for the 20 and 30 BL films.

Figure 5.19 shows the voltage across the electrodes as a function the polymerization time during the PEDOT synthesis over the substrate with 30 BL. The potential oscillate between 1.65-1.80

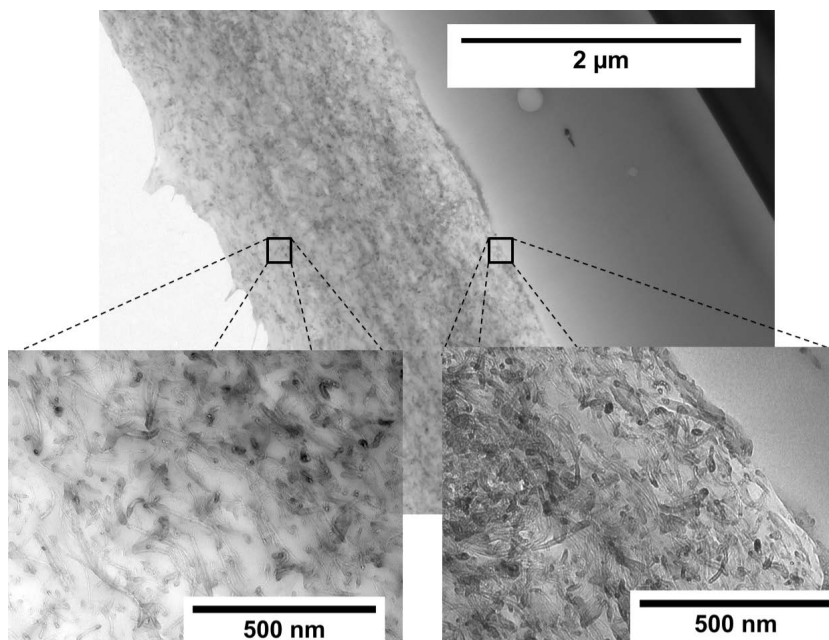


Figure 5.18 TEM images of the cross section of a film with 50 BL MWCNT-PDDA/MWCNT-DOC.

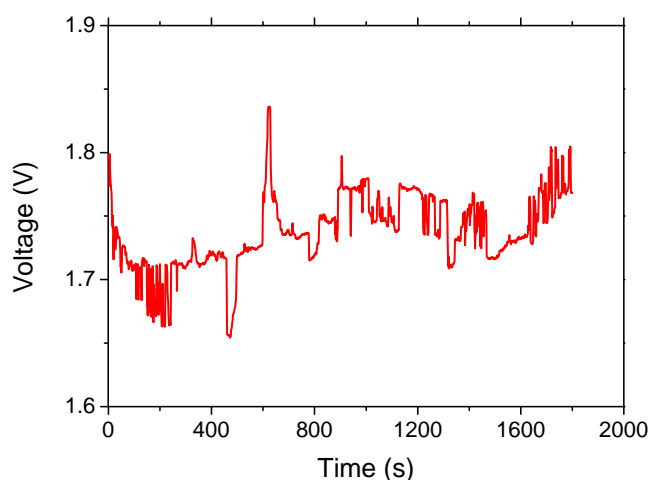


Figure 5.19 Voltage as a function of the polymerization time for the sample with 30 BL.

V. Probably these oscillations are generated by diffusion of the molecules from the electrode (PDDA and DOC) to the solution (also the electrolytes can go to the electrode), since the electrode is a layered system. This voltage is adequate to polymerize EDOT. This fact indicates that the working electrode made by a film of MWCNTs is conductive enough to keep 3 mA between the electrodes. Consequently, a homogeneous polymerization over the MWCNTs substrate was observed.

The morphology of these MWCNT-PEDOT thin films was visualized using SEM, as shown in Figure 5.20. Prior to EDOT diffusion and polymerization, the MWCNT assembly exhibits a

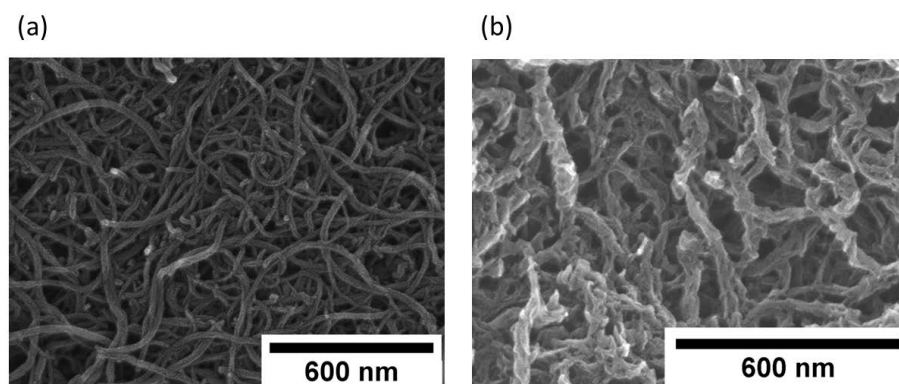


Figure 5.20 SEM images of a 50 BL of MWCNT-PDDA/MWCNT-DOC film (a) and the same film after 10 (b) of EDOT polymerization.

well-connected network, with a homogeneous distribution of nanotubes (Figure 5.20(a)). After 10 minutes of EDOT polymerization, uniform and conformal coverage of the nanotube film is observed (Figure 5.20(b)). MWCNTs are still clearly visible at this polymerization time, but longer time causes PEDOT to fill interstitial space among the nanotubes as it is observed in Figure 5.21, further improving connectivity. Filling open space in these nanotube assemblies with

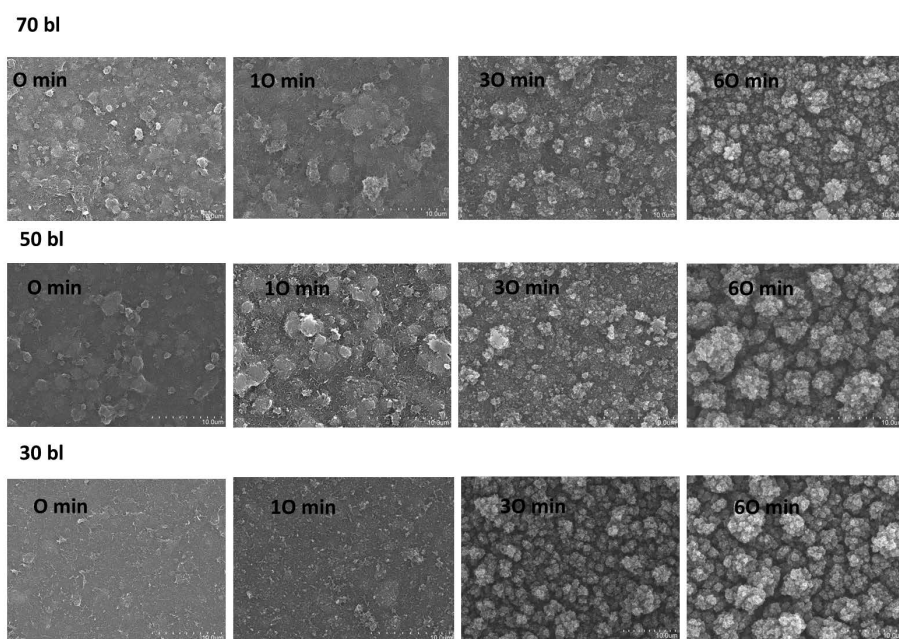


Figure 5.21 SEM images of MWCNT/PEDOT films.

ICP will improve electrical conductivity and thermoelectric performance. Figure 5.21 shows the surfaces morphology of different substrates as a function of the polymerization time. Homogeneous distribution of the MWCNTs has been observed around the substrate with a different roughness degree. For lower number of BL the surface was flatter than the films fabricated employing large number of BL as can be observed in Figure 5.21. At 10 minutes of PEDOT electropolymerization, the SEM images indicate no changes on the film surface indicating that

there was not enough PEDOT to overcome the MWCNTs film. At intermediate polymerization times for the films fabricated using 50 and 70 BL, excess of PEDOT was not observed on the film surface. However, when the number of BL was 30 some PEDOT globules were observed as show Figure 5.21 indicating that PEDOT covers the film completely. After 60 min of polymerization, all MWCNT are covered and excess PEDOT creates a layer with a globular morphology (Figure 5.21), which is commonly seen with electrochemical polymerization [27, 37, 62].

In order to study the polymerization of PEDOT over the MWCNTs substrate the cross section of the films was study as a function of the polymerization time as it has been shown in Figure 5.22 . It is possible to see how EDOT polymerize over the MWCNTs, increasing the electri-

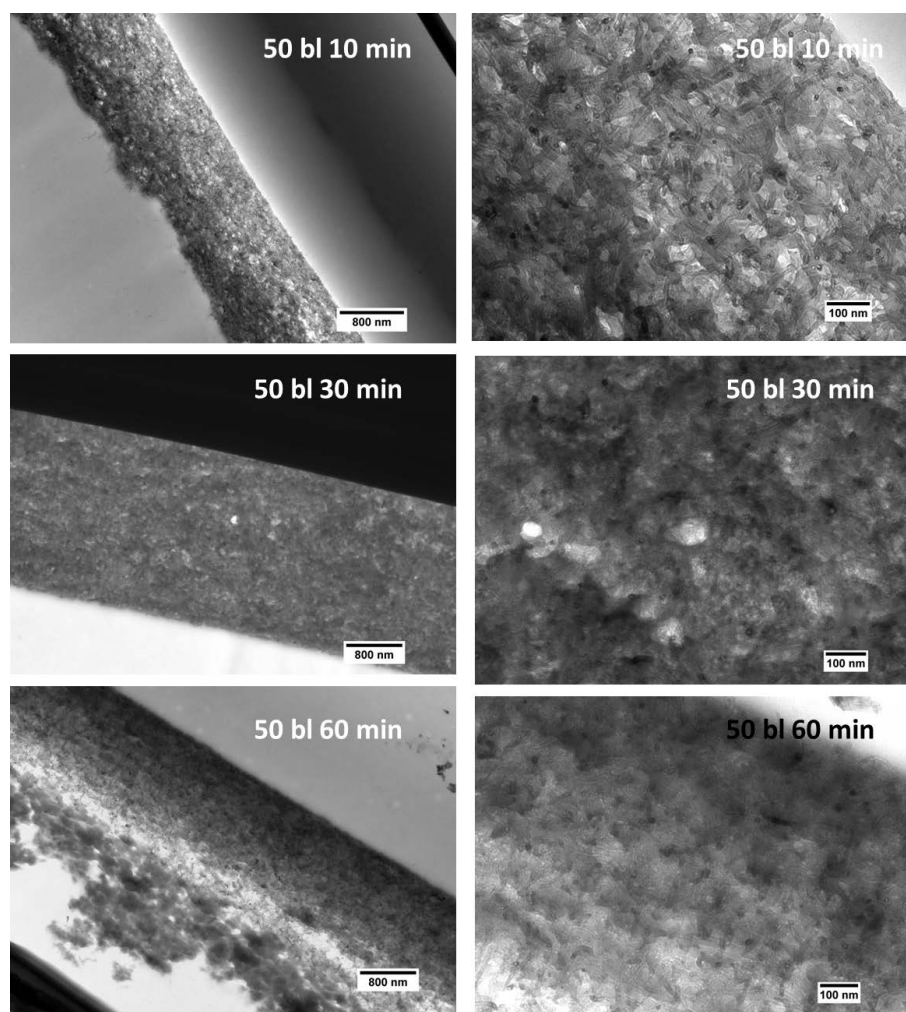


Figure 5.22 TEM images of the cross section MWCNT/PEDOT Films (50 BL).

cal connections between the MWCNTs. PEDOT is distributed homogeneously in all the film, showing a diffusion of EDOT through the carbon nanotubes during the polymerization. At long polymerization times, the PEDOT overcome the MWCNTs film creating a layer of PEDOT on the surface. In addition, the thickness of the MWCNTs film decreases during polymerization at

10 minutes due to the diffusion of the excess of PDDA and DOC from the film to the electrochemical solution.

5.4.6 Thermoelectric behavior of MWCNT-PEDOT hybrid films

Electrical conductivity, Seebeck coefficient and power factor were determined as a function of the number of bilayers deposited and PEDOT polymerization time, as shown in Figure 5.23. Conductivity increases several orders of magnitude with the addition of PEDOT to the MWCNT-

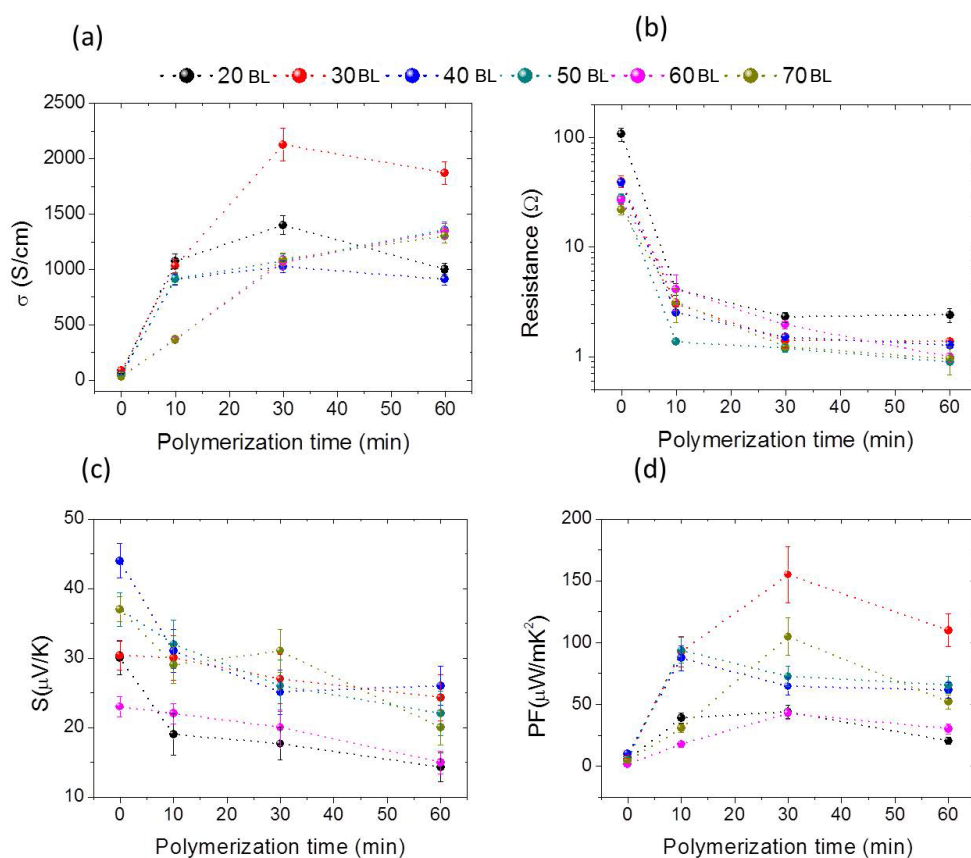


Figure 5.23 (a) Electrical conductivity, (b) resistance, (c) Seebeck coefficient and (d) power factor of MWCNT-PDDA)/MWCNT-DOC multilayers as a function of PEDOT polymerization time.

based multilayer thin films. A maximum in electrical conductivity is observed with 30 min of polymerization when the number of bilayers is smaller than 50, but 60 minutes of polymerization is needed to achieve maximum conductivity with 50 or more bilayers. In this case, electrical conductivity is primarily influenced by polymerization time and film thickness. With increasing polymerization time (i.e., more PEDOT incorporation), excess of PEDOT produces a single layer that decreases conductivity. With greater film thickness, the number of defects increases and, consequently, the electrical conductivity is reduced. For this reason, the electrical conductivity reaches a maximum when the film has an optimal number of MWCNT layers

and PEDOT covers the entire nanotube network without significant excess, which happens at 30 BL and with 30 min of polymerization. The maximum electrical conductivity of (2100 ± 100) S/cm is unprecedented for a MWCNT-based composite, which is comparable to films prepared with DWCNTs or highly doped PEDOT [39]. Figure 5.23(b) shows electrical resistance of the MWCNT-PDDA/MWCNT-DOC films as a function of PEDOT polymerization time. As expected, resistance decreases with the incorporation of more PEDOT (i.e., larger polymerization time) to the MWCNT network. Resistance below 1Ω was achieved for some films, which makes them very promising for thermoelectric module fabrication. Unfortunately, the Seebeck coefficient tends to decrease with polymerization time as well (Figure 5.23(c)). This is not an unexpected result because PEDOT has an inherently low Seebeck coefficient ($7\text{--}10 \mu\text{V/K}$) [27, 37] and longer polymerization time increases the concentration in the nanocomposite film. Power factor reaches a peak value at intermediate film thickness (30 BL) and polymerization time (30 min), as shown in Figure 5.23(d). The maximum power factor is approximately $150 \mu\text{W/m K}^2$, being the highest value for MWCNTs-polymer composite [19, 20] until the date.

5.5 Tellurium-PEDOT hybrid films synthesized by electrochemical synthesis

5.5.1 Materials

The reactants used in this study are: EDOT, 97% purity (Munich, Germany), Lithium Perchlorate (LiClO_4) 95% purity (Alfa Aesar, Karlsruhe, Germany), tellurium (IV) oxide 99% purity (Acros Organics, Geel, Belgium), acetonitrile (reagent grade) and sulphuric acid (95%) (VWR Chemicals, Llinars del Vallés, España).

5.5.2 Synthesis of Te-PEDOT films

The preparation of the Te-PEDOT films was performed in a three electrode cell by means of electrochemical polymerization. First of all, the films of PEDOT: ClO_4 were synthesized on a PET substrate ($2 \times 4 \text{ cm}^2$) with a gold coating (20 nm) obtained by metal evaporation in a Univex 300 Evaporation system. The gold layer served as the working electrode. PEDOT: ClO_4 was polymerized starting from a 0.01 M solution of EDOT and LiClO_4 0.1 M, in 100 mL of acetonitrile at a current of 3 mA versus an Ag/AgCl reference electrode for 30 s. PEDOT coated gold PET was washed with acetonitrile to remove the monomer and oligomeric species from the surface. Afterwards, the gold layer was removed with an acid solution (HNO_3 :HCl ratio 1:3). The PEDOT derivative thin films were washed several times with water and finally with ethanol (with this treatment the gold layer was removed keeping the polymer integrity and its

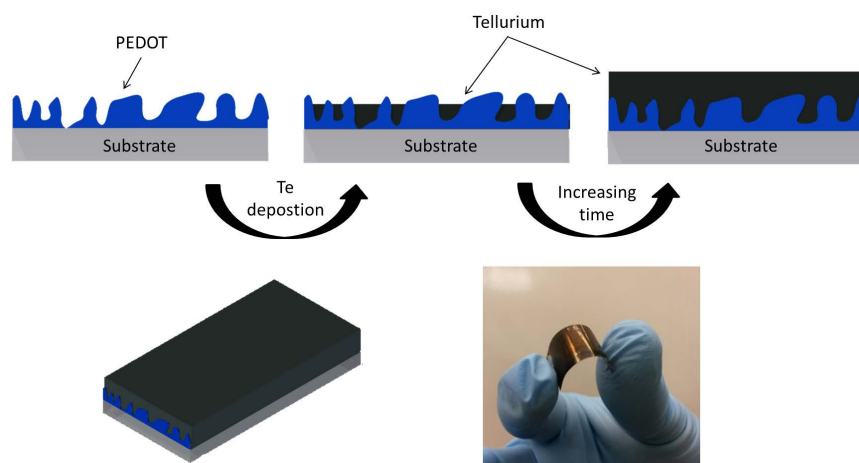
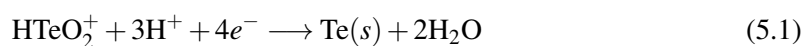


Figure 5.24 Scheme of the Te deposition over the PEDOT working electrode.

properties) [37]. Te deposited films were obtained by electrochemical deposition on the PEDOT surface using this film as the working electrode (see Figure 5.24). Tellurium deposition was carried out at -0.4 V from a 0.01 M TeO_2 and 0.1 M H_2SO_4 solution in 100 mL of ultra pure water in a ice bath. All the films obtained were washed several times with water and finally with ethanol. In all the experiments, a steel electrode was used as the counter electrode and an IVIUM n-stat equipment was employed as a potentiostat.

5.5.3 Morphology and characterization during the electrochemical deposition of Te

Cyclic voltamperometry (CV) was used to optimize and to study the deposition of tellurium over the PEDOT film as the working electrode. The starting solution was formed by the tellurium oxide (TeO_2) dissolved in sulphuric acid solution to form telluric acid (HTeO_2^+) [234], as described in the experimental part. Figure 5.25(a) shows the corresponding cyclic voltamperogram. The main reduction peak appears at -0.4 V. This cathodic peak can be associated with the reduction of HTeO_2^+ to Te, deposited over the working electrode, according with the following reaction [234, 235]:



Another reduction processes can be overcome during the Te deposition such as the hydrogen evolution:



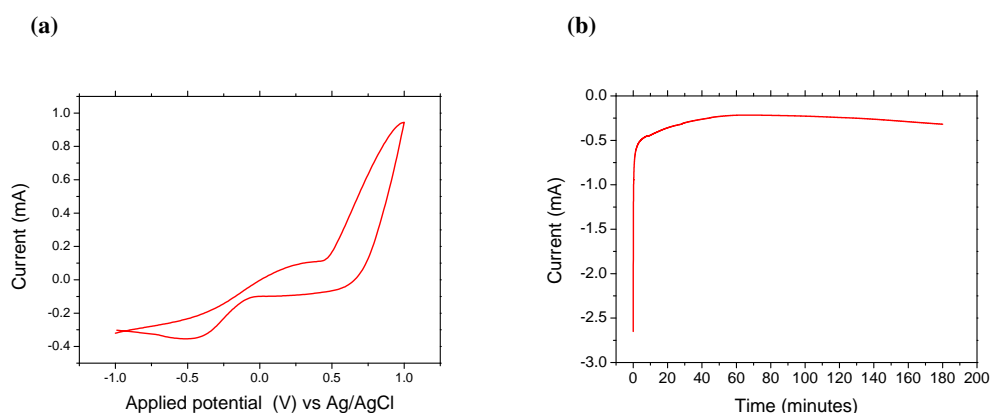


Figure 5.25 (a) Cyclic voltamperometry of HTeO_2^+ using PEDOT film as a working electrode. (b) Galvanometric curve during the Te deposition in an ice bath. Thickness of the Te-PEDOT films as a function of the Te electrodeposition time.

or other reactions that involve Te, which occurs at the same time than the Te deposition such as [234, 235]:

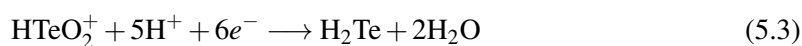


Figure 5.25(b) shows the evolution of current during Te deposition on the working electrode (PEDOT film) at $-0.4 \text{ V vs Ag/AgCl}$. A decay of the intensity is observed below 60 minutes of Te electrodeposition, probably due to the tellurium deposition on the PEDOT film. At time longer than 60 minutes the working electrode would be saturated in Te so, the electrical resistance decreases consequently, the intensity slightly increases to keep a voltage of -0.4 V between the electrodes. The occurrence of parallel reactions can be the reason of efficiency during the Te deposition [234]. Figure 5.26 plots the PEDOT-Te film thickness as a function

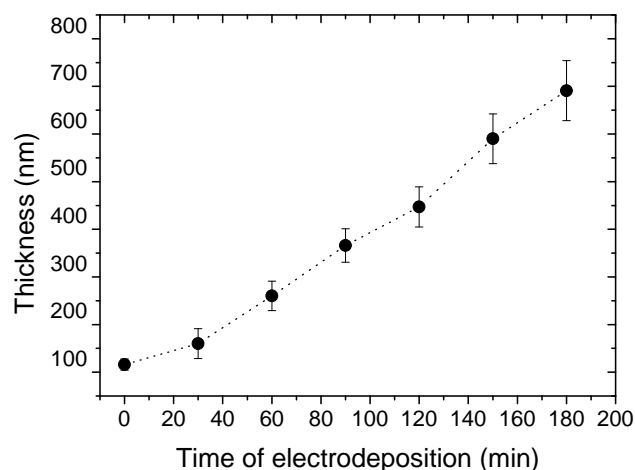


Figure 5.26 Thickness of the Te-PEDOT films as a function of the Te electrodeposition time.

of Te electrodeposition time. A progressive increment in the thickness is observed indicating a deposition of Te on the PEDOT electrode.

Figure 5.27 shows the morphology of the films as a function of the Te electrodeposition time.

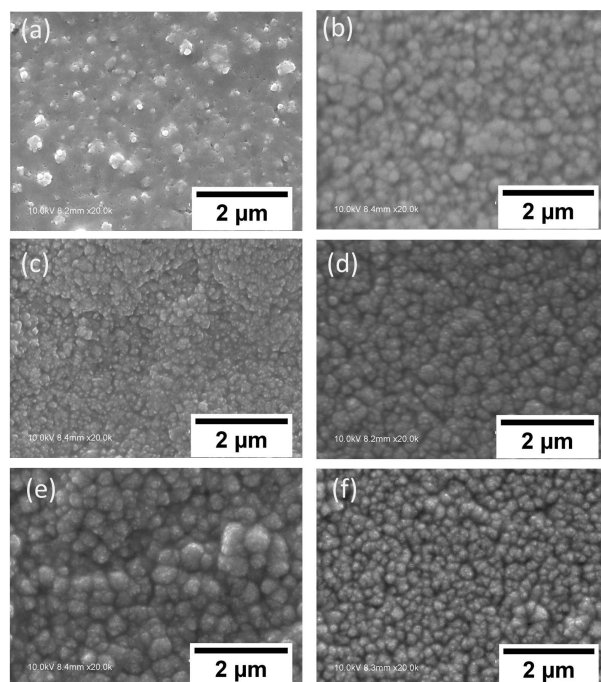


Figure 5.27 SEM images of Te-PEDOT films after: (a) 30, (b) 60, (c) 90, (d) 120, (e) 150 and (f) 180 minutes of Te electrodeposition.

All the films were homogeneous with different roughness degrees, as detected by SEM. At low deposition times (30 minutes), it is possible to observe Te crystals on the PEDOT surface (Figure 5.27(b)), the crystals were distributed homogeneously over the PEDOT film. However, the degree of interconnection between the Te crystals was really low. Figure 5.27(b) shows the surface of the PEDOT films after 60 minutes of polymerization, showing how the film surface is practically covered by Te particles. After 90 minutes of Te synthesis (Figure 5.27(c)), the amount of Te increases, creating a more compact morphology, which improves the contact among Te crystals. Figure 5.27(d), (e) and (f) show the film surface after 120, 150 and 180 minutes of Te synthesis respectively. The images show a Te film homogeneously distributed with a globular morphology typical for electrodeposited materials.

Figure 5.28 shows the surface topography of Te-PEDOT film synthesized during 2.5 hours of Te deposition measured using AFM. The figure depicts a film composed by Te crystals with certain roughness degree. It is possible to observe domains where the tellurium crystals are very close between them producing variations in the Z-direction around ± 20 nm. However narrow valleys appear corresponding with Te particle boundary in some regions of the sample. These results indicates that Te is not deposited producing a flat film. As increasing the Te deposition, the

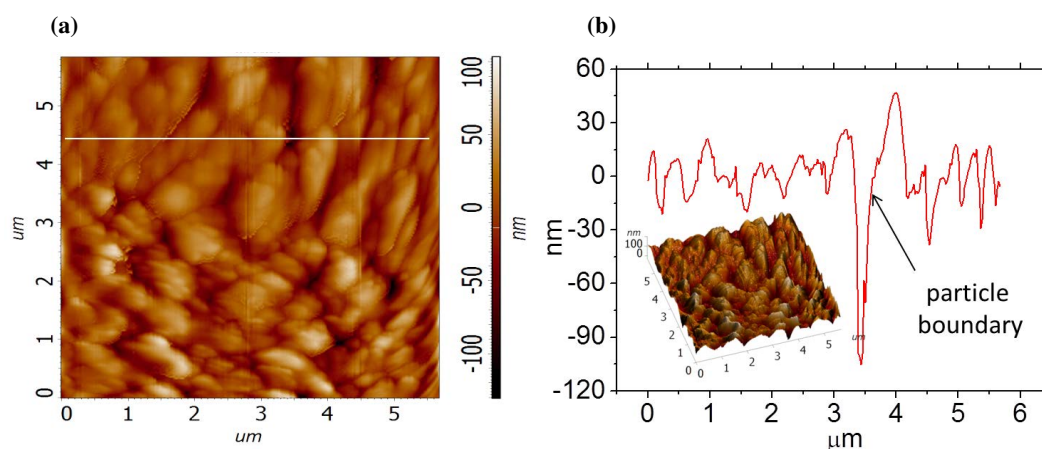


Figure 5.28 (a) AFM image of the PEDOT film after 2.5 hours of electrodeposition. (b) Roughness profile corresponding with the white line on the AFM image (the inset is a 3D view of AFM image).

particles are more tightly connected one with each other creating a rough film. The morphology obtained is typical for Te synthesized by electrodeposition [235].

Figure 5.29 shows the Raman spectra of the Te-PEDOT films. The optical characterization was

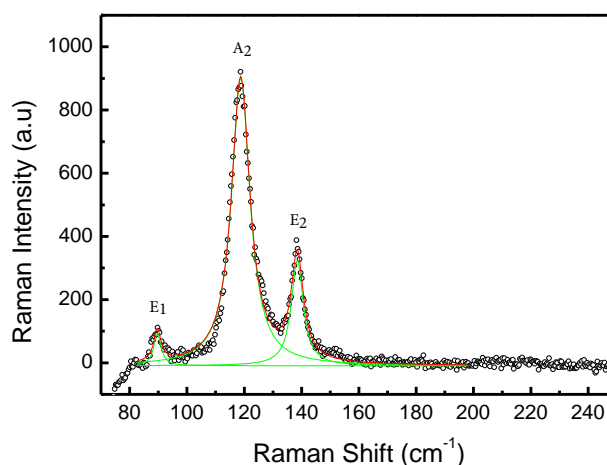


Figure 5.29 Room-temperature Raman-scattering spectra of PEDOT-Te films obtained with the 647.1 nm excitation line of an Ar-Kr laser.

performed using the triple spectrometer in subtractive mode, in order to go below 100 cm^{-1} for the purposes of measuring the phonon optical modes related to Tellurium. All measurements were calibrated with a Si sample by the characteristic phonon peak at 519.5 cm^{-1} . After measuring the Si phonon, we kept the spectrometer in this position in order to avoid displacements in the calibration, thus our experimental values have a maximum uncertainty of 0.2 cm^{-1} . The Raman spectra were de-convoluted with Lorentzians (green lines) in order to extract the contributions from individual modes and give an accurate phonon value. The red line is the cumulative

fit of the Raman Spectra. In the sample with Te content, we can observe three peaks, located at 88, 117 and 137 cm^{-1} , corresponding to the E_1 , A_1 , and E_2 optical modes respectively, in agreement with the bibliography [236].

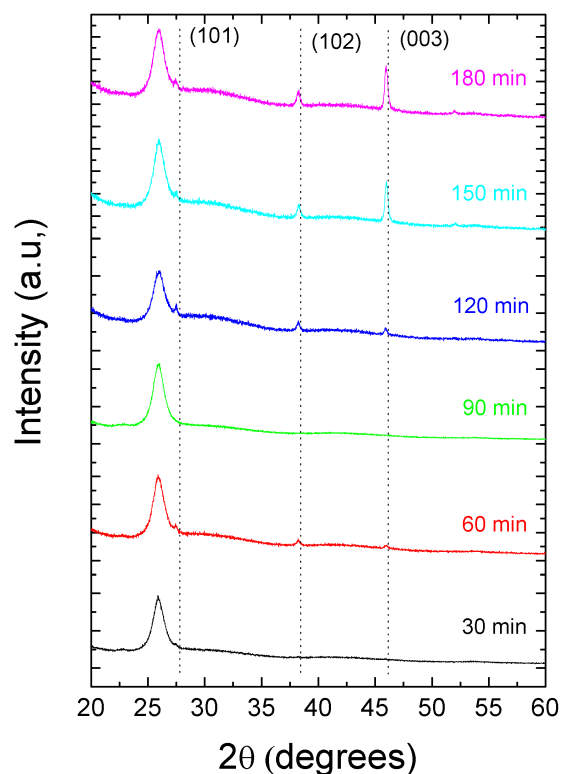


Figure 5.30 XRD analysis of Te-PEDOT films as a function Te deposition time.

Figure 5.30 shows the XRD analysis of Te-PEDOT films from 20° to 60° at different times of Te electrodeposition. All the spectra present a peak centered at $2\theta=25.8^\circ$. This peak corresponds with the crystalline domains of the PET substrate. This diffraction peak is attributed to the reflection corresponding with the (100) plane [237, 238]. The signal of the PET substrate overcome the PEDOT peaks. Several Te diffraction peaks are also observed in Figure 5.30. These peaks correspond with the diffraction of planes (101), (102), (003) centered at $2\theta=27.5^\circ$, 38.2° and 45.8° , respectively. The intensity of the Te peaks increases with electrochemical deposition time, since the Te content increases as well. The XRD results show a preferred orientation in the (003) direction during crystal growth. The crystal size, D , in this orientation was determined using the Scherrer equation:

$$D = \frac{K\lambda}{\beta \cos\theta} \quad (5.5)$$

where, λ is the X-ray wavelength; β the full-width at half-maximum in radians; and θ the Bragg angle. The samples synthesized for 180, 150 and 120 minutes had a crystal size of 26 ± 3

nm, 27 ± 3 nm and 31 ± 3 nm, respectively. These values are in agreement with the literature [235, 237, 238].

5.5.4 Thermoelectric behavior of Te-PEDOT films

As it can be seen in Figure 5.31, the electrical conductivity was determined as a function of Te deposition time. The electrical conductivity decreases with Te content from (750 ± 70) S/cm to (59 ± 5) S/cm. This change is probably due to the fact that the Te deposited using electrochemical methods is polycrystalline, creating a film with the appearance of a porous material. The PEDOT conductivity is higher than that of Te by itself due to its semi-metallic character [70]. This behavior comes from the high doping level found in the PEDOT films grown by electrochemical polymerization at oxidative potentials [27, 37]. The huge drop in the electrical conductivity is not only produced by the presence of Te nanocrystals, but also by the decrease of the doping level occurred in the PEDOT during the electrodeposition of Te, since the applied potential during the Te synthesis was -0.4 V. This negative potential produces an electrochemical dedoping of PEDOT, generated by the reduction process taken place on the working electrode [37].

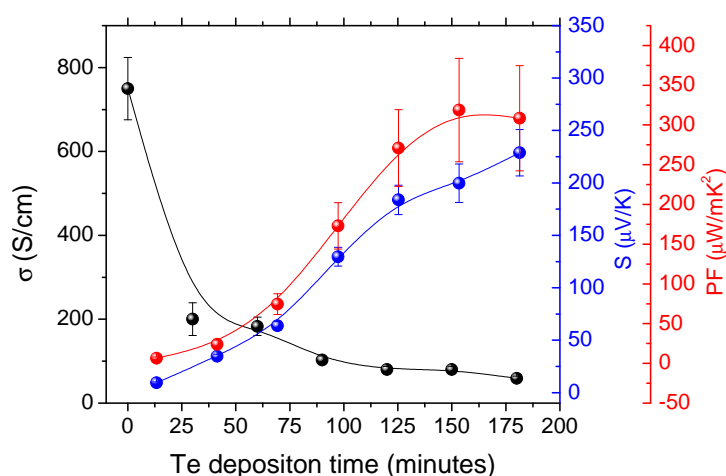


Figure 5.31 Electrical conductivity, Seebeck coefficient and Power Factor of Te-PEDOT films as a function Te deposition time.

The Seebeck coefficient was measured at room temperature as a function of the Te deposition time (see Figure 5.31). The Seebeck coefficient increases more than one order of magnitude, from (9 ± 1) $\mu\text{V/K}$ to (230 ± 20) $\mu\text{V/K}$. At lower deposition times (30 min), the Seebeck coefficient is closer to the value of the reduced PEDOT, 35-40 $\mu\text{V/K}$ [27, 37, 239]. This indicates that the Te crystals deposited on the PEDOT film are not well interconnected inhibiting the increase of the Seebeck coefficient. For this reason, at low electrodeposition times (below 60 min) the Seebeck coefficient is related with the reduced state of PEDOT [27, 37, 239]. As the deposition

time of Te increases, its properties dominate over that of PEDOT and a large increase of S is observed. At large deposition times, the Seebeck coefficient increases until values closer to $230 \mu\text{V/K}$. This value is in the same range than those achieved for Te films synthesized by electrochemical polymerization by Martín-González *et al.* [235] (around $250 \mu\text{V/K}$), although the values obtained in Ref. [235] were lower, probably due to the presence of PEDOT in the final film. The reason of the large increase observed in the Seebeck coefficient at longer deposition times is originated from the well connected Te crystals. The Te crystals produce continuous and homogeneous films as it has been shown in the SEM images (see Figure 5.27), giving very good values for the Seebeck coefficient.

The Power Factor of the Te-PEDOT films has been calculated from the electrical conductivity and the Seebeck coefficient (Figure 5.31). The Power factor increases from $6.5 \pm 1.5 \mu\text{W/m K}^2$ to $308 \mu\text{W/m K}^2$ with the Te electrodeposition time. This increment in the PF is mainly dominated by the increase of the Seebeck coefficient. The optimum Te deposition time was 150 min, giving a PF around $(320 \pm 70) \mu\text{W/m K}^2$. The values obtained in this work can be compared with previous studies done in similar composites using Te as a filler in a conductive matrix. For instance, the maximum value obtained for PEDOT:PSS-Te films treated with H_2SO_4 was $284 \mu\text{W/m K}^2$ [42], or for the case of PEDOT:PSS mixed with Te nanowires [40] they measure a value around $100 \mu\text{W/m K}^2$. Other relevant study was reported by E. W. Zaia *et al.* [43] obtaining a PF around $85 \mu\text{W/m K}^2$ for PEDOT:PSS/Te nanowires doped with copper. In this work, Te-PEDOT films have been synthesized with the largest power factor published until the present date to our knowledge, even higher than Te films previously synthesized by electrochemical deposition ($285 \mu\text{W/m K}^2$) [235]. This indicates the good synergy between PEDOT and Te in these films. The range of ZT could be estimated taking values of the thermal conductivity from the literature. The thermal conductivity of Te films is in range of $0.8\text{--}1.1 \text{ W/m K}$ [235]. Previous studies of the thermal conductivity of PEDOT:PSS mixed with Te at 85 % wt showed values around 0.22 W/m K [41]. Thus, the ZT of the Te-PEDOT films prepared in this work could be in the limiting range $0.1\text{--}0.43$.

5.6 Conclusions

In this chapter four kinds of nanocomposites have been investigated. Two of them, PEDOT:PSS/EG and PEDOT/Perovskite nanocomposites were prepared by the conventional synthesis process, mixing and dispersion. The other two systems, MWCNT/PEDOT and Te-PEDOT were prepared by electrodeposition. Homogeneous PEDOT:PSS/ expanded graphite composites have been prepared by solvent evaporation on a glass substrate at different EG contents. SEM and TEM images indicate a homogeneous dispersion. DSC analysis indicate an endothermic peak due to semi crystalline structure, independent of the graphite content. The thermal stability is

not greatly improved upon graphite addition. The electrical conductivity shows a sharp increase upon addition of the expanded graphite, whereas the Seebeck coefficient levels out after the first graphite addition. The thermoelectric power of these systems is dominated by the electrical conductivity. For the case of NCCO/PEDOT composites based on PEDOT doped with Tosylate and PSS were prepared. The addition of PEDOT to the NCCO nanoparticles increases the electrical conductivity, since the polymer acts as a conductive binder. The Seebeck coefficient increases with the NCCO content achieving higher values when Tosylate is the doping element. The best thermoelectric efficiency is given by the sample with 5 % of PEDOT:Tos and nanoparticles with a Ca content of 0.001. A method to synthesize low resistance thermoelectric films using the combination of LBL assembly and electrochemical polymerization has been developed. The electrical conductivity increases as a function of the polymerization time while the Seebeck coefficient decreases. The maximum thermoelectric efficiency was achieved at 30 BL during 30 min of polymerization. Finally, Te-PEDOT films have been synthesized by a very simple method, electrochemical deposition. Te has been deposited over PEDOT working electrodes and was characterized by XRD, Raman and SEM analysis. The electrical conductivity decreases as a function of the Te electrodeposition time while the Seebeck coefficient increases. The maximum power factor was achieved at 150 min of Te electrodeposition time giving the excellent value of $(320 \pm 70) \mu\text{W/m K}^2$, being the highest value obtained until now for this kind of systems.

Chapter 6

Devices for energy production and storage using conducting polymers

Content

In this chapter four experiments related with energy production and storage using organic semiconductors and nanocomposites will be shown. Firstly, all the concepts necessary to understand the chapter will be introduced in the first section. Then the first experiment, consists of the development of a thermoelectric generator using PEDOT as thermoelectric element. In the section 6.3 the results obtained for another thermoelectric module fabricated using MWCNTs-PEDOT nanocomposites will be shown. Then the fabrication of a thermal sensor based of PEDOT films will be discussed. Finally, in section 6.5 the implementation of several supercapacitors based on PEDOT fabricated employing different substrates such as: PET and Cotton fabric will be demonstrated.

6.1 Introduction

This section has been divided in two main topic: thermoelectrics for energy applications and supercapacitors for energy storage.

6.1.1 Thermoelectric modules

The main element in a TEG or cooler is called "thermocouple". Basically consists of a n-type and a p-type semiconductor electrically connected in series by a metallic element (commonly, copper). Figure 6.1 shows the configuration of a thermoelectric module, which consists

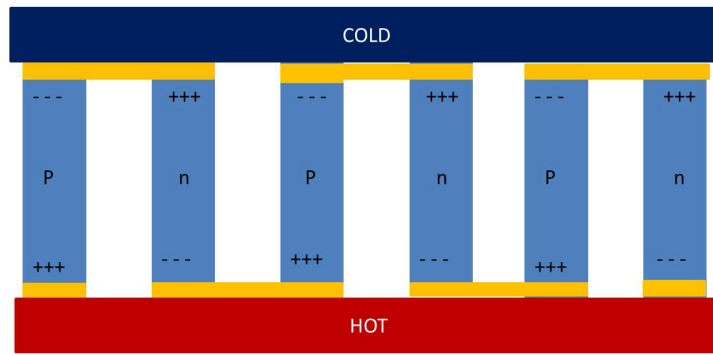


Figure 6.1 Configuration of a thermoelectric module.

of several thermocouples connected electrically in series but thermally in parallel isolated by two ceramics panel, one on the top and the other at the bottom of the device. The generating performance of a thermoelectric module is gauged primarily by the conversion efficiency and power-per-unit-area, while the cooling performance by the coefficient of performance (COP) and heat-pumping capacity. These parameters can be estimated using the proper theoretical models that can be very useful in analyzing and optimizing the design of small dimension thermoelectric modules.

6.1.2 Power output and conversion efficiency

The TEG can convert heat into electricity through the Seebeck effect. The electrical power generated from a module depends on the following parameters: number of thermocouples, configuration, thermoelectric properties of thermoelement materials, thermal and electrical properties of contact layers, and the temperature difference across the module [47]. Thinking of the module shown in Figure 6.1, and taking into account the thermal and electrical contact resistances, the output voltage V and current I are given by:

$$V = \frac{NS(T_h - T_c)}{1 + 2rl_c/l}, \quad (6.1)$$

$$I = \frac{AS(T_h - T_c)}{2\rho(n+l)(1 + 2rl_c/l)}, \quad (6.2)$$

where N is the number of thermocouples in a module, S the Seebeck coefficient of the thermoelectric element and ρ the electrical resistivity, T_h and T_c are temperatures at the hot and cold sides of the generator, respectively, A and l are the cross section area and the length of the thermoelectric material, respectively, l_c is the thickness of the contact layer, $n = 2\rho_c/\rho$ and $r = \lambda/\lambda_c$ (where ρ_c is the electrical contact resistivity, λ_c the thermal contact conductivity, and λ

the thermal conductivity of thermoelement material). n and r are usually referred to as electrical and thermal contact parameters, for commercially available Peltier modules, general common values are $n \sim 0.1$ mm and $r \sim 0.2$ [47].

The power output P and conversion efficiency ϕ of a thermoelectric module, when operated with a matched load, is given by the following equations:

$$P = \frac{S^2}{2\rho} \frac{AN(T_h - T_c)^2}{(n+a)/1 + rl_c/l)^2}, \quad (6.3)$$

$$\phi = \frac{\frac{T_h - T_c}{T_h}}{(1 + 2r\frac{l_c}{l})^2 [2 - \frac{1}{2}(\frac{T_h - T_c}{T_h}) + (\frac{4}{ZT_h})(\frac{l+n}{l+2rl_c})]}, \quad (6.4)$$

where $Z = S^2/(\lambda\rho)$ is the figure of merit of the materials used in the fabrication of the thermoelectric module. Figure 6.2 shows the power per unit area $P_A = P/AN$ and conversion efficiency

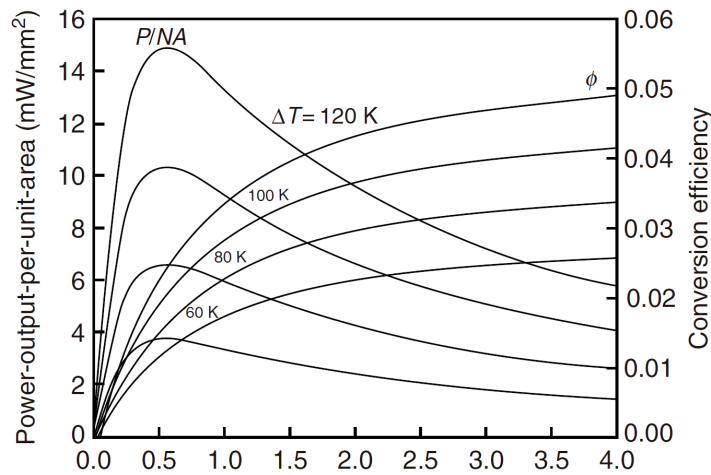


Figure 6.2 Power per unit area and conversion efficiency vs thermoelement length for different temperature differences. Reproduced from [47] with permission of TAYLOR and FRANCIS.

as a function of the length of the thermoelectric material for several temperature gradients. In order to obtain high conversion efficiency, the module should be designed with high length. However, if a large power-per-unit-area is required, the thermoelectric length should be optimized at a relatively shorter length. It is apparent that the optimum design of a thermoelectric module is likely to be a compromise between obtaining high conversion efficiency or large power output.

6.1.3 Thermoelectric module fabrication

In order to fabricate a TEG several parameters have to be considered for example: The operating temperatures T_c and T_h , the required output voltage, current, the thermoelectric properties of the

thermoelectric element and also the design parameters such as: the length of thermoelectric materials, the cross-sectional area, and the number of the thermocouples N in the generator. For this reason, it is very important to optimize all of these parameters in order to get a high performance thermoelectric modules.

Basically, the conventional thermoelectric Peltier modules are fabricated using n- and p-type Bi_2Te_3 as thermoelectric elements. The assembly process is shown in Figure 6.3. After a sintering process, Bi_2Te_3 is cutted in a small square pieces, then these pieces are electrically conected

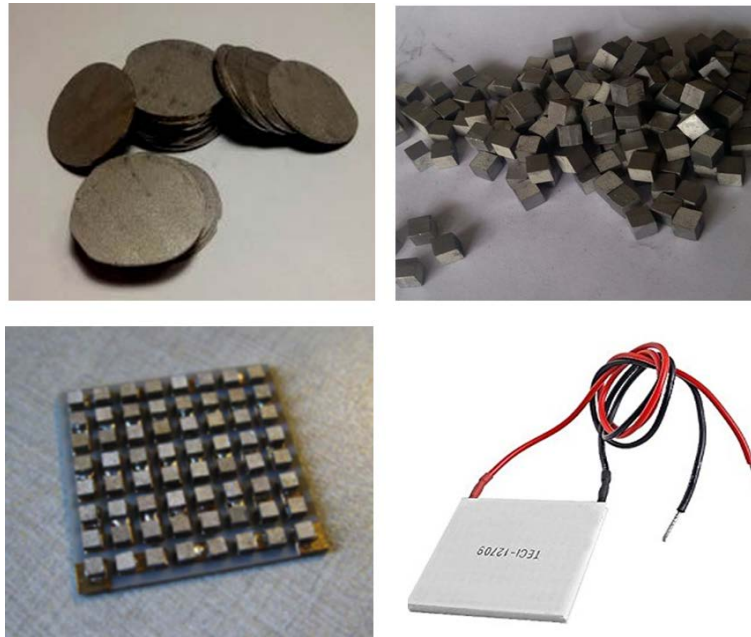


Figure 6.3 Image of a Peltier module assembly.

in a series configuration alternating n and p type material. Finally, the module is isolated using two ceramic panels (top and bottom) and two copper wires are used as a current collectors.

The thermoelectric elements in a module can be designed attending to the maximum ZT at the temperature range operation. Since the thermoelectric element will be in a temperature gradient, it is possible to create a segmented thermoelectric material with the maximum efficiency of each material in the position where this temperature appears in the thermal gradient along the thermoelectric element. In this arrangement two materials are joined or segmented together, each with its figure of merit optimized for a different temperature range. Figure 6.4 shows a multisegmented generator. Under development for applications recovering automobile waste exhaust heat, the cold-side sections of both elements are based on bismuth telluride. The hot side sections of the p- and n-type elements consist of high-performance, a cobalt filled skutterudite and a cobalt antimonide clathrate, respectively, with zinc antimonide segmented into the p-type leg to operate over the intermediate temperature range. A 15% conversion efficiency has been obtained in prototype generators when operated over a temperature difference of around 700 K [47].

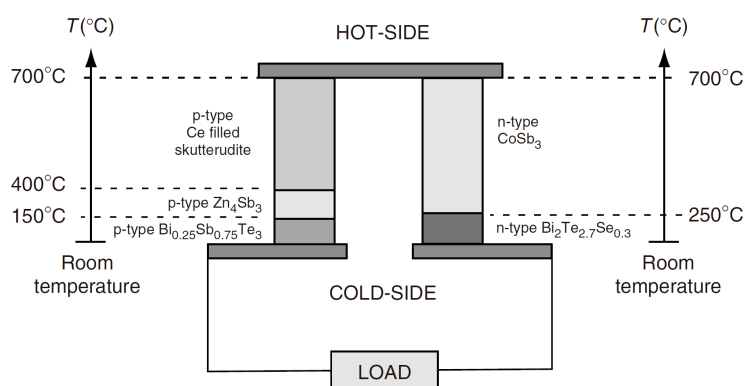


Figure 6.4 High performance multisegmented thermoelectric generator. Reproduced from [47] with permission of TAYLOR and FRANCIS.

6.1.4 Organic thermoelectric modules

There are several disadvantages that makes unsuitable the use of thermoelectric modules based on inorganic materials for energy production. One of those is the impossibility of use them in large scale applications [240], since the cost of the raw materials is too high (it has to be taken into account that Te and Bi are one of the most rare elements in the earth crust). However, organic materials can be employed advantageously into the development of thermoelectric generators [241–244]. These materials offer great possibilities in terms on large scale application fabrication in multiple geometries, interesting mechanical properties as flexibility and easy integration in different elements such as: clothes, buildings or facades [42]. Unfortunately, there are some problems to be solved in order to be competitive with the inorganic thermoelectric materials. The most important problem is the low thermoelectric efficiency of organic materials, although several approaches have been used to improve the thermoelectric efficiency of conductive polymers. Optimizing the doping level has become one of the most powerful methods to increase PF, which is a useful parameter to gauge performance when the thermal conductivity is similar amongst the materials being compared. In the case of PEDOT, $ZT \gtrsim 0.2$ and $PF \gtrsim 300 \mu\text{W}/\text{m K}^2$ has been demonstrated with various dopants [36]. The addition of nanostructured fillers to the conducting polymers has also been used to increase their thermoelectric efficiency. For example, very high power factors have been obtained for PANI/DWCNT/Graphene ($1750 \mu\text{W}/\text{m K}^2$) and PANI/DWCNT/PEDOT:PSS/Graphene ($2710 \mu\text{W}/\text{m K}^2$) multilayer thin films prepared using the LBL assembly [38, 39]. Polymer composites have also been prepared using inorganic semiconductor nanostructures such as Te nanorods [40, 41, 245] or even Bi_2Te_3 [44], but the use of inorganic fillers does not solve the problems of high cost and scarcity of raw materials. For this reason, it is more useful to develop high performance thermoelectric materials based on completely organic semiconductors. There are very promising examples of good thermoelectric performance for PEDOT:PSS films and PANI/DWCNT/PEDOT:PSS/Graphene multilayer assemblies, but these materials are very thin (60-1000 nm) [38, 39, 246]. From the

point of view of thermoelectric device fabrication, these thin films are expected to have large internal resistance in the final thermoelectric generator due to the series connections between the legs, which is challenging for energy generation. It is important to produce films with a very low electrical resistance in combination with a large power factor. In principle, it is possible to reduce the resistance just by increasing the thickness of the film, but this is not completely true for polymers. When the thickness of the polymer film increases, the number of defects also increases [247], creating a poor morphology for electrical transport through the material. As a result, the final electrical conductivity sometimes decreases with thickness, which reduces the efficiency of the thermoelectric material. This chapter describes the synthesis of the two thermoelectric modules based on organic materials studied in the previous chapters. To understand the results obtained in this chapter the most relevant results in terms of organic thermoelectric module fabrication found in the bibliography will be commented.

6.1.4.1 State-of-the-art of organic thermoelectric modules

The fabrication of thermoelectric modules using conducting polymers is one of the most important challenges in the field of organic thermoelectrics due to the necessity to find a stable and efficient n-type conducting polymer. Currently there are several studies with very interesting values of ZT, around 0.2-0.4 in PEDOT [24, 27, 36]. However, PEDOT can only be obtained as a p-type semiconductor. The problem of n-type conducting polymers is their low stability in air conditions due to that fact that they are in a reduced state that can be lost through the oxidant effect of the air. Currently, some conducting polymer air stable with n-type behavior are available. Unfortunately, the thermoelectric efficiency is very low [248]. One of the earliest work was developed by X. Crispin *et al.* [36]. After the discovery of the impressive ZT (0.25) in PEDOT:Tos optimized by chemical de-doping X. Crispin *et al.* fabricated a thermoelectric generator using PEDOT:Tos as thermoelectric p-type material and TTF-TCNQ as n-type semiconductor. The TEG is completed by depositing on the top Au contacts. The maximum power output per area of the PEDOT-Tos/TTF-TCNQ TEGs consists of 54 thermocouples with the following leg dimensions: $25\text{mm} \times 25\text{mm} \times 30\mu\text{m}$ achieving a value around $45 \mu\text{Wcm}^{-2}$. Then in 2014 with the discovery of a very high power factor of PEDOT:PSS by Pipe *et al.* [24] and Qingshuo *et al.* [242] reported an organic thermoelectric modules screen-printed on paper by using PEDOT:PSS, as shown in Figure 6.5. This research is a very good example of a solution process for a thermoelectric module fabrication. They used a highly conductive PEDOT:PSS solution to be used as an ink to cover a sheet of paper previously masked. Their results were very promising achieving a power output of $4.0 \mu\text{W}$ at 50 K temperature gradient. However the highest power output achieved for organic thermoelectric module was attained by Zhu *et al.* in 2012 [249]. They synthesized conducting polymers of n-type and p-type based on poly(metal 1,1,2,2-ethenetetrathiolate) achieving very high value of ZT, 0.1-0.2 at 400 °C for both kinds

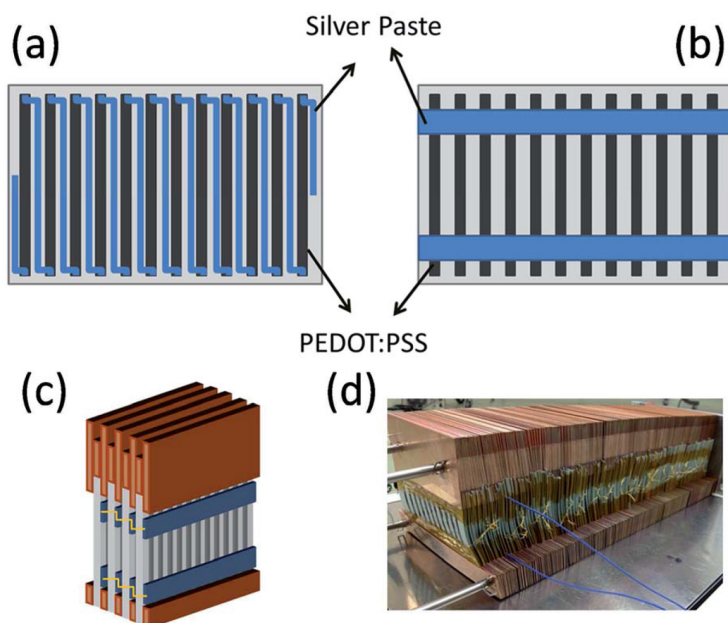


Figure 6.5 Schematic representation of the: (a) series and (b) parallel PEDOT:PSS array, (c) schematic and (d) photograph of the PEDOT:PSS modules sandwiched between copper plates. Reprinted from [242] with permission from The Royal Society of Chemistry.

of thermoelectric materials. Following the architecture of the conventional Peltier modules they made a thermoelectric generator with the impressive power output of $750 \mu\text{W}$ at 82°C temperature gradient. Against the poly(metal 1,1,2,2-ethenetetrathiolate)s derivatives are insoluble and present the same problems than the inorganic thermoelectric modules.

For the case of polymer nanocomposites there are a big number of researchers with very promising results in terms of power output being nanocomposites based on CNTs the most representatives. The advantage of using CNTs is that these materials can be n-type or p-type, so it is possible to combine several layer of n-type and p-type CNTs to fabricate the thermoelectric module. Carroll *et al.* [250] developed a thermoelectric generator based on n-type and p-type CNTs in 2012. They connected 72 layer of CNTs as shows Figure 6.6 intercalating an isolating

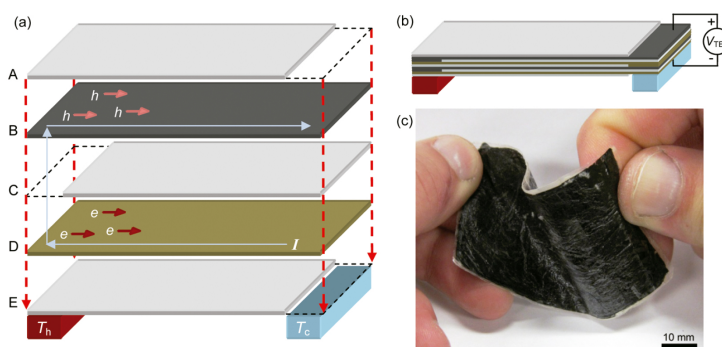


Figure 6.6 (a) and (b) 3D scheme of thermoelectric module assembly and (c) real image of the module. Reprinted from [250] with permission of ACS Nano Letters.

layer between the CNTs layer. They achieved a very interesting power output of 137 nW at a $\Delta T=50^\circ\text{C}$. Following these ideas several thermoelectric modules were fabricated. Recently, Wang *et al.* [251] reported a generator using diethylenetriamine (DETA) as n-type dopant for SWCNTs. They delivered 649 nW at $\Delta T=55^\circ\text{C}$ for 14 thermocouples generator. Other significant work was published in 2016 by Cho *et al.* [252] where a thermoelectric generator using Au-doped-CNT/PANI (p-type) and PEI/CNT (n-type) as thermoelectric elements was reported. They achieved 376 nW in 14th thermocouple module applying 10°C of temperature difference.

6.1.5 Conducting polymers as supercapacitors

Currently, there are several kinds of devices able to store energy such as: fuel cells, batteries, combustion engines, supercapacitors and capacitors [49, 253, 254]. Basically, there are two parameters characteristic of all devices employed in energy storage, one is the energy density and the other one is the power density. The energy density gives information about the amount of energy that the device can accumulate per unit mass, the power density is related with the power output that the device is able to supply per unit mass. Figure 6.7 shows the energy densities

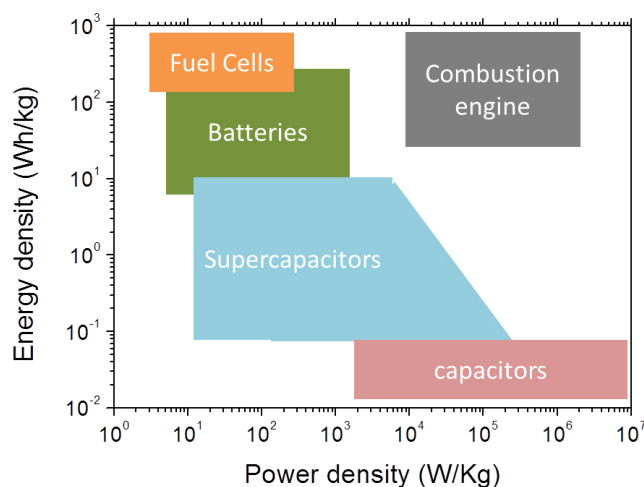


Figure 6.7 Energy densities versus power densities for various energy storage devices.

and the power densities for several energy storage devices. Batteries show high energy density however low power density; in contrast capacitors exhibit a high power density and low energy density. Consequently, the batteries can store big amount of energy, however the energy output is very low. The capacitors are able to supply energy very fast, however, they cannot store a big quantity. In the region with intermediate properties are the supercapacitors.

The most simple example of a capacitor is based on metallic parallel plates represented in the schematic of the Figure 6.8. It is made from two metallic plates separated by a dielectric material. Trough the application of a potential difference between the plates it is possible to charge

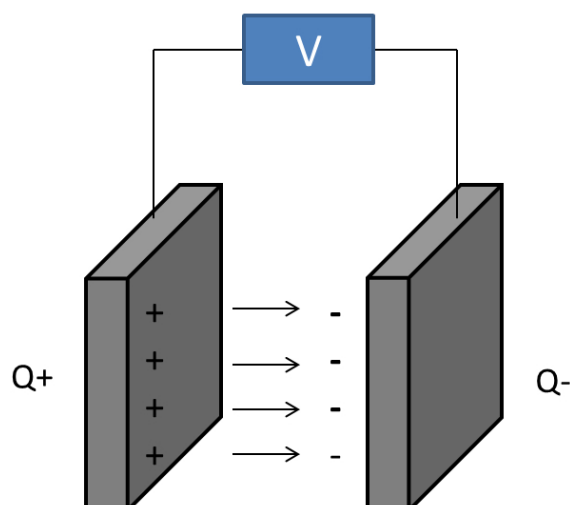


Figure 6.8 Scheme of parallel plate capacitor .

the metallic plated and the capacitor can apply charge in a passive way. The most important parameter of a capacitor is the capacitance (C). C is determined by the ratio of the charge (Q), and the potential difference (ΔV) given by the equation:

$$C = \frac{Q}{\Delta V} \quad (6.5)$$

There are several kinds of capacitors such as: ceramics with capacitances around 1 nF, polyester capacitors, with capacitances in the range of nF and electrolytic capacitors with capacitance values higher than 1 μ F. The typical electrolytic capacitors are composed by aluminium electrodes separated by an electrolyte and rolled in a cylindrical device. The electrolytic capacitors able to store energy, more than 10 KW/Kg are called supercapacitors [62, 255, 256]. Depending on the charge mechanism, they are double layer supercapacitors if the charge is given by ions, and pseudosupercapacitors if the charge process is produced by redox reactions. The capacity in the double layer supercapacitors only depends on the electrode morphology (porosity and surface area) and the electrolyte, while the pseudosupercapacitors not only depend on the electrode morphology and the kind of electrolyte, but also the material of the electrode, since these capacitors involve fast redox reactions between the electrode and the electrolyte [50]. The materials used in the fabrication of double layer supercapacitors, basically, are carbon derivatives such as: CNTs [51, 254] or graphene [256]. In contrast, the materials employed in the fabrication of the pseudosupercapacitors are electro-active compounds able to produce redox reactions such as: transition metals oxides or conducting polymers. As it has been commented in previous chapters of this thesis, there are several advantages on the use of conducting polymers in energy applications. The combination of several materials in the fabrication of the electrode is a good strategy to increase the device capacitance. For this reason it is very important the development

of nanocomposites based on carbon materials, conducting polymer and metallic oxides in order to obtain high performance supercapacitors.

As it has been commented before, the morphology of the electrode is a key point in order to obtain a high performance supercapacitor, since it is related with the surface area of the electrode. So, using nanostructured electrodes can be one solution to increase the capacitance of the fail device. Figure 6.9 shows different nanostructured composites attending to their dimensional-

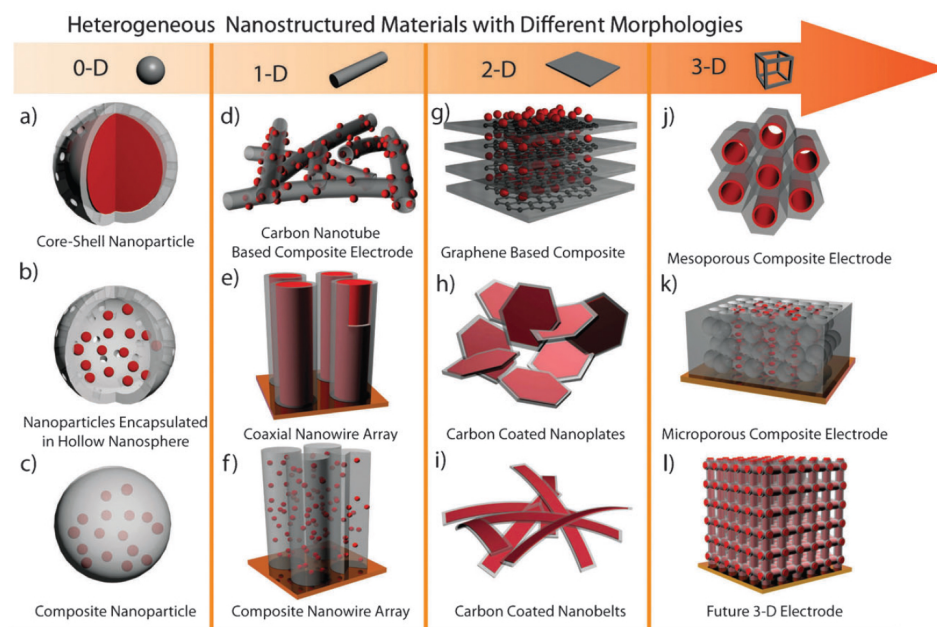


Figure 6.9 Different heterogeneous nanostructured materials based on structural complexity. Reprinted from [257] with permission from The Royal Society of Chemistry.

ity. 0-D dimensional nanostructures can be nanospheres or nanocapsules, their main problem is the low electrical conductivity of the particles weakly connected [257]. 1-D nanostructures are basically nanowires and nanotubes, they can present aleatory distribution or vertically aligned in a substrate, the mains problems of these compounds are their low stability and conductivity. 2-D nanostructures are based on laminar semiconductors such as graphene, these structures are more stable highly conductive. 3-D surface nanostructures are networks of nanowires or fibers. This kind of electrodes depict higher stability conductivity and elasticity.

In this chapter, supercapacitors devices have been developed using PEDOT as electrode material and nanocomposites of MWCNTs-PEDOT-MnO₂ over cotton fabrics in order to get a 3D electrode.

6.2 A thermoelectric module fabricated by electrochemical polymerization¹⁰

6.2.1 Materials

The reactants used in this study are: EDOT, lithium perchlorate (LiClO_4), ethanol, hydrazine and acetonitrile, all of them purchased from Sigma Aldrich Co (Madrid, Spain).

6.2.2 Device fabrication

The device fabrication was carried out in four steps. The first step was the generation of a conductive pattern in a polyethylene terephthalate (PET) substrate. In this work we used gold as conductive material. Using a mask, the gold was evaporated over the PET substrate. The shape of the gold pattern is shown in Figure 6.10. The second step consists of the electrochemical

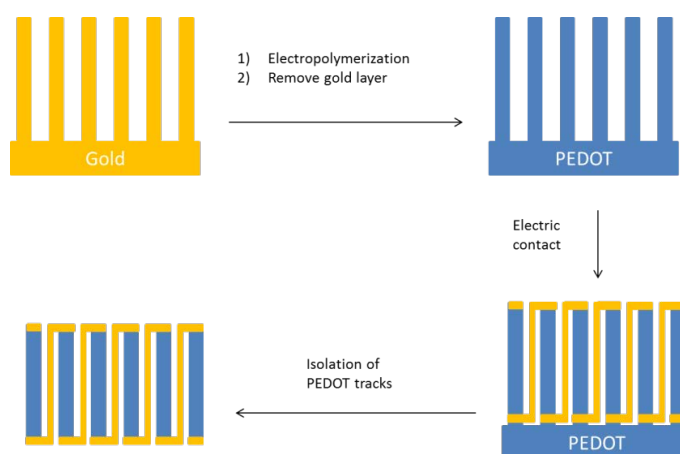


Figure 6.10 Scheme of the synthesis of PEDOT thermoelectric module.

polymerization. The gold pattern over the PET substrate was used as working electrode, a steel sheet as counter electrode and Ag/AgCl was used as the reference electrode. PEDOT was polymerized from a 0.01 M solution of EDOT and LiClO_4 0.1 M in acetonitrile. The polymerization was carried out at 3 mA during different time periods. After the polymerization, the PEDOT tracks were insulated removing the gold at the bottom of the device as shown in Figure 6.10. Finally, the PEDOT tracks were electrically connected by gold contacts using a mask deposited by metallic evaporation (see Figure 6.10).

¹⁰This section is based on the publication: "Organic thermoelectric modules produced by electrochemical polymerization M. Culebras, M. M. de Lima, C. Gómez, A. Cantarero *Journal of Applied Polymer Science*, 43927 (2017), Reproduced by permission of Wiley.

6.2.3 Electrical measurements of the thermoelectric module

The synthesis of PEDOT was carried out in galvanostatic mode, keeping constant the current between the electrodes. Previous experiments determined that the optimum current for the synthesis is 3 mA, because at this current it has been obtained the best compromise between growth velocity and good quality of the deposition of PEDOT. If the current is very low the speed of

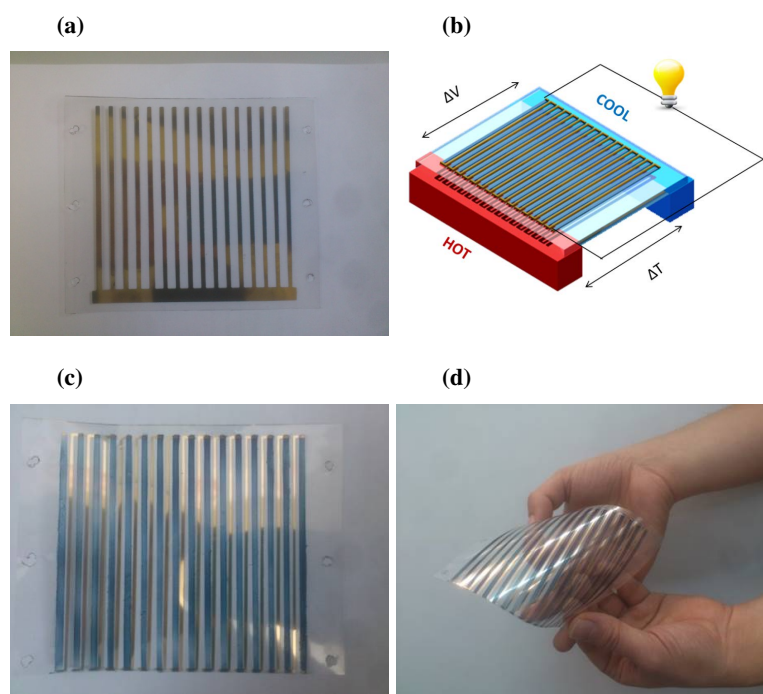


Figure 6.11 Images of: (a) Gold pattern, (b) 3D model of the thermoelectric module, (c) and (d) final device .

the reaction is also low and, if the current is higher than 3 mA the velocity of the PEDOT deposition is very fast, producing an interconnection of the PEDOT tracks. In order to isolate the PEDOT tracks, the gold layer used as a working electrode has to be removed. The gold layer (see figure 6.11(a)) has been removed using Royal water ($\text{HNO}_3:\text{HCl}$ 1:3). The PEDOT and PET substrate are not affected with this treatment, as it has been demonstrated in Chapter 3. In the fabrication of this module only a n-type semiconductor is used. For this reason the electrical contacts between the PEDOT layer have been made from the cold part to the hot part of the device to connect in series the thermoelectric elements. Figure 6.11 shows some pictures of the final device composed by 16 PEDOT tracks connected with gold layers. In addition, the PET substrate provides flexibility to the module.

Figure 6.12 shows the voltage as a function of the temperature difference applied to the sample for the module with and without chemical reduction and for one PEDOT track after the reduction treatment. The Seebeck coefficient for a single PEDOT track before chemical reduction was $10 \mu\text{V}/\text{K}$, but after 11 seconds of treatment with hydrazine vapor the Seebeck coefficient increases

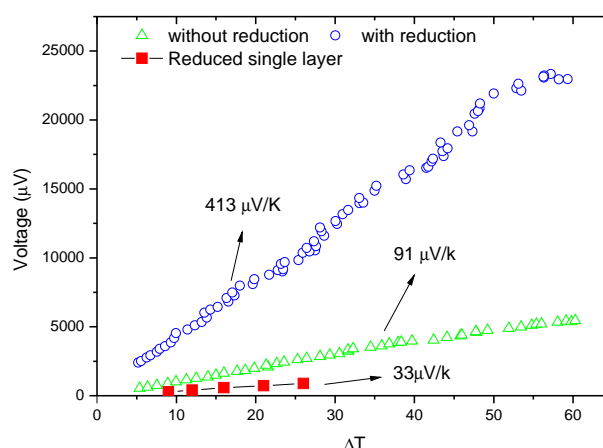


Figure 6.12 Voltage as a function of temperature.

until $33 \mu\text{V/K}$; these data are consistent with the previous values already published in [27, 37]. The hydrazine treatment affects to the doping level of the polymeric material decreasing the number of charge carriers, since the electrons, provided by the reduction agent, neutralize the positive charges along the PEDOT chains (polarons and bipolarons) [19, 27, 37]. Consequently the number of π -bands increases and the electrical conductivity of the films change from 750 S/cm to 350 S/cm at 11 s of reduction treatment. For the pristine module, the Seebeck coefficient was around $91 \mu\text{V/K}$ without the reduction treatment and it increases until $413 \mu\text{V/K}$ subjecting it to the reduction treatment with hydrazine vapor during 11 seconds. This increment in the Seebeck coefficient of the module is produced due to a reduction of the doping level of PEDOT. Figure 6.12 shows a linear behavior between the voltage and the temperature difference, indicating that the Seebeck coefficient remains constant with the temperature. Due to the absence of T_g (glass transition temperature) in PEDOT [206] the maximum temperature range application is given by the T_g of the substrate in the case of flexible substrates (for PET, $T_g \approx 85^\circ\text{C}$).

The power generation has been studied as a function of the load resistance R_L , as shown in Figure 6.13. The temperature difference was kept fixed at 60°C . In this case, the thickness of the PEDOT tracks was in the range between $2\text{--}5 \mu\text{m}$. The results show a maximum delivered power at $R_L = 30 \text{ k}\Omega$, corresponding with the impedance of the generator. The module without chemical reduction presents a maximum power around 2.7 nW , while after the reduction treatment a value of 5.03 nW has been achieved. The results indicate that the optimization of the doping level of the conducting polymer produces an increase of the power generation, since the power factor of PEDOT is higher when the polymer has the optimum doping level [27, 36, 37, 70]. The supplied voltage increases from 15 mV to 26.1 mV after the chemical reduction, since the Seebeck coefficient is higher when a de-doping process is carried out in conducting polymers [27, 36, 37, 70]. This de-doping process is very important to maximize the power generation

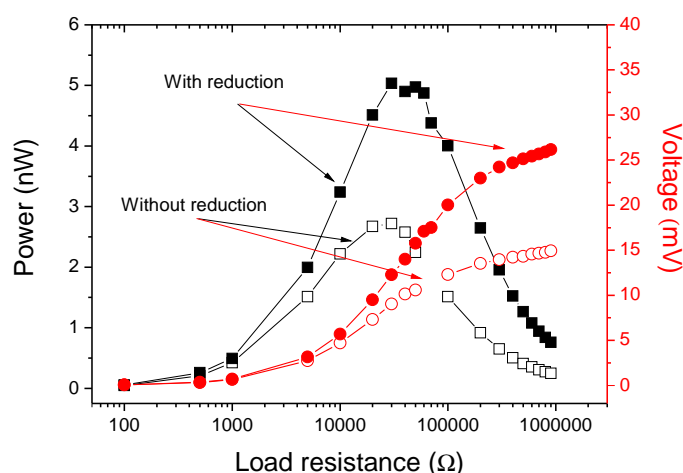


Figure 6.13 Power of the thermoelectric module as a function of the load resistance.

in the thermoelectric modules. In previous chapters, it was demonstrated that this optimization of the doping level in conducting polymers can be realized using two paths, through chemical de-doping [27] or electrochemical de-doping [37]. From the point of view of the industrial fabrication of the module, it is more appropriate to choose a process that minimizes the production costs. For this reason, the chemical de-doping, using hydrazine vapor, could be the best choice.

The impedance of the thermoelectric device is still very high. One way to reduce the impedance of the thermoelectric generator is to increase the thickness of the PEDOT track as shown in Figure 6.14(a). However, when the PEDOT film is very thick, higher than 5 μm , some cracks

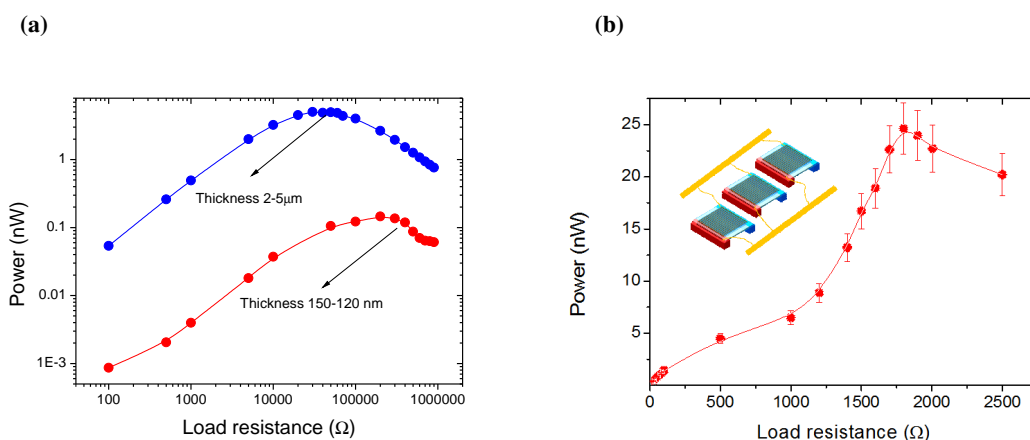


Figure 6.14 (a) Power as a function of the thickness of PEDOT tracks and (b) Power as a function of load resistance in 15 thermoelectric modules connected in parallel.

appear on the film due to the fragility of the material. Figure 6.14 shows the power of the two thermoelectric modules with different thicknesses, being higher the power when the thickness of the PEDOT track increases due to a decreasing of the impedance (30 k Ω when the thickness is around 2-5 μm and 200 k Ω when the thickness is between 120-150 nm). Another way to

reduce the impedance of the generator is to connect several modules in parallel. Following this strategy, 15 thermoelectric modules were connected in parallel using a copper tape. In this case, the maximum power was 25 nW, achieved at 1.8 k Ω , reducing significantly the impedance of the device.

Definitely, a very interesting process of fabrication of thermoelectric modules using electrochemical polymerization has been developed. This method has several advantages over the conventional procedures such as: easy scalability to industrial processes, fast synthesis, low impedance devices and low cost of production in a large scale. However, more research is needed to increase the power supplied and to decrease the impedance of the final device.

6.3 A cylindrical thermoelectric module fabricated using layer-by-layer assembly and electrochemical polymerization

6.3.1 Materials

PDDA, with a molecular weight of 10^5 - 20^5 g/mol, DOC ($C_{24}H_{39}NaO_4$), EDOT, lithium perchlorate ($LiClO_4$), and acetonitrile were purchased from Sigma Aldrich (Milwaukee, WI) All chemicals were used as received. MWCNT were obtained from Bayer MaterialScience (12–15 nm outer and 4 nm inner wall diameter, length $> 1 \mu m$, purity ≥ 95 wt%; Leverkusen, Germany).

6.3.2 Device fabrication

For thermoelectric generator fabrication, a PET substrate (8.5×15 inch²) was first masked using tape to make a striped pattern. The space between the stripes determined the width (0.6 inch in this study) of the MWCNT films. Then, a dispersion of 0.05 wt % MWCNTs were prepared in an aqueous solution of 0.25 wt% PDDA or 1 wt% DOC. Both MWCNT suspensions were bath sonicated for 30 min, followed by 20 min of 15 W tip sonication in an ice water bath, and another 30 min of bath sonication to homogenize. The MWCNT dispersion was then centrifuged at 4000 rpm for 20 min and the supernatant was decanted. The masked substrate was dipped 20 times alternatively in each solution with two washing steps after each dipping process. The polymerization process was carried out in galvanostatic mode at 3mA/inch for 60 min. In this step, the PEDOT stripes are cut to 1 inch length and electrically connected with silver paste from the bottom to the top (series connection). The thermoelectric fundamental units (30 in this case) were attached to a copper tube, using silicone as adhesive. The fundamental units were connected in groups of three in series, with all groups in parallel.

6.3.3 Characterization of the thermoelectric module

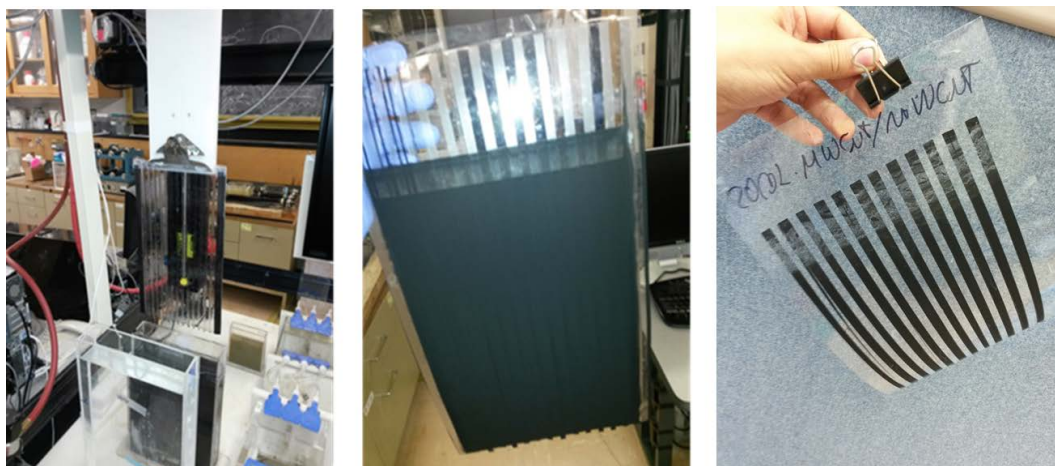


Figure 6.15 Photographs of the 20 BL of MWCNTs films preparation.

Figure 6.15 shows the PET substrate after the LBL deposition. After the tape removal the MWCNTs strips are obtained as shown in Figure 6.15. Due to the long length of the MWCNTs strips the substrate were cut in three parts to be used in the polymerization of EDOT as a working electrode. The entire substrate could not be used since, the length of the strips creates a large electrical resistance making impossible to keep 3 mA between the electrodes. Figure 6.16(a) shows the MWCNTs strips after the EDOT polymerization. PEDOT was polymerized

(a)



(b)



Figure 6.16 Pictures of: (a) 20 BL of MWCNTs/MWCNTs after PEDOT polymerization and (b) fundamental unit of thermoelectric module.

homogeneously over the MWCNTs strips decreasing the electrical resistance of the stripes. The substrates after polymerization were cut in 1 inch length and electrically connected with silver paste from the bottom to the top (series connection) as it has been shown in Figure 6.16(b). The

number of thermoelectric strips was 12, the size was (0.6×1) inch², the resistance of each strip was 3.2Ω approximately, the resistance of the silver paste contact was 4Ω , so all these factors together makes a fundamental unit of the thermoelectric generator with a total resistance of 86Ω .

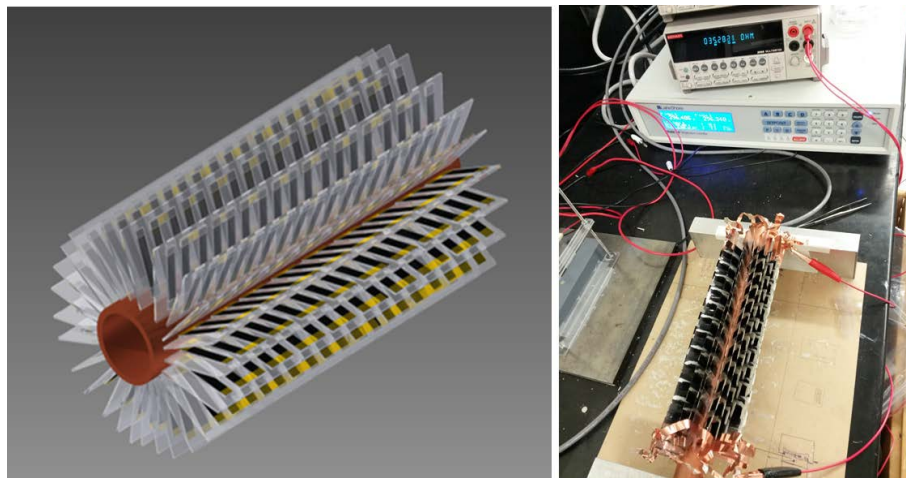


Figure 6.17 Schematic and picture of the thermoelectric module fabricated from PEDOT-infused MWCNT-based films deposited on PET.

The thermoelectric module shown in Figure 6.16 was fabricated using the 20 BL MWCNT-based films and 60 min of PEDOT polymerization. All of the thermoelectric films were connected from the hot side to the cold side because the legs have only one type of conduction (p-type). The supplied power was measured as a function of the voltage (Figure 6.18(a)) and the load

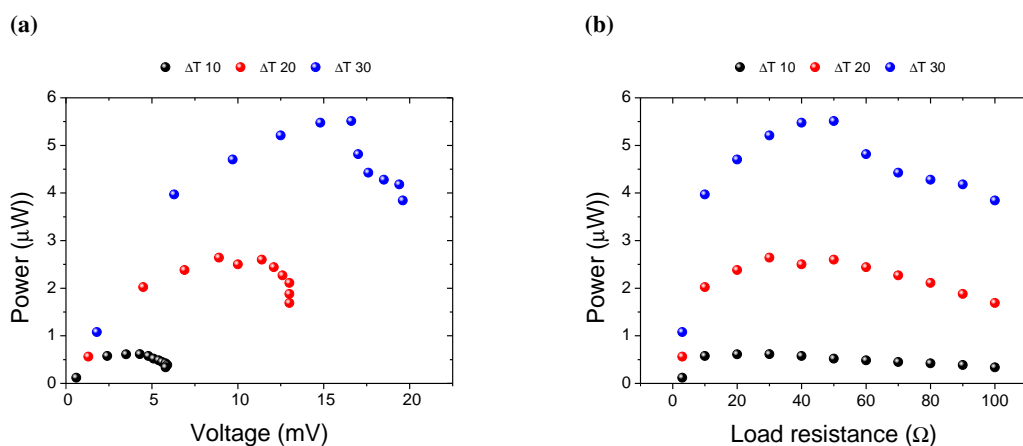


Figure 6.18 Power from cylindrical thermoelectric generator as a function of: (a) voltage and (b) load resistance, with varying temperature differential supplied.

resistance (Figure 6.18(b)). The maximum power supplied was $5.5 \mu\text{W}$ with a load of 40Ω . As expected, the power generation increases with a larger temperature difference. This cylindrical generator morphology of this device is ideal for recycling waste heat from pipes. The power

achieved here is greater than most other thermoelectric generators produced with organic materials, which range from 30 nW up to $\sim 2 \mu\text{W}$ with ΔT from 10 to 50 °C [242, 250–252, 258]. This thermoelectric generator is the first prototype, although the power output obtained is not bad, it is needed more research trying to improve the performance of the thermoelectric module, in order to be competitive with commercial Peltier modules.

6.4 Thermal sensor based on a PEDOT film ¹¹

6.4.1 Materials

The reactants used in this study were: EDOT, 1-butyl-3-methylimidazolium hexafluorophosphate, and acetonitrile, purchased from Sigma Aldrich Co (Madrid, Spain).

6.4.2 Synthesis of PEDOT nanofilms

The PEDOT films have been obtained by the electrochemical polymerization method on a gold thin film (20 nm), previously deposited on a PET substrate by metal evaporation in a Univex 300 Evaporation system. The synthesis was carried out in an Ivium-n-Stat: a multi-channel electrochemical workstation under computer control with a Pt grid as a counter electrode, a PET gold covered substrate as the working electrode and a Ag/AgCl electrode as the reference one. The PEDOT was polymerized from a 0.01 M solution of EDOT and 1-butyl-3-methylimidazolium hexafluorophosphate 0.01 M in 100 mL of acetonitrile at 3 mA during 1.5 minutes. Under these experimental conditions, the PEDOT film thickness was 110-120 nm. The gold layer of the working electrode was removed after the PEDOT synthesis with an acid solution ($\text{HNO}_3:\text{HCl}$ ratio 1:3). The PEDOT nanofilms were rinsed several times with water and ethanol to remove the untreated monomer and then dried in air at room temperature. Finally, the samples were reduced in a hydrazine (N_2H_4) vapor atmosphere during 25 seconds.

6.4.3 Sensor fabrication

Figure 6.19 shows the scheme of the electronic elements which forms the thermal sensor. This device is composed by: i) a PEDOT nanofilm attached to two blocks at different temperatures (T and T_0), ii) a circuit amplifier with a high differential gain (G_d), of about 100 dB, iii) a light emitting diode connected at the output through a load resistance and v) a power supply with an electromotive force (emf) of $\pm 5\text{V}$. The electronic circuit is composed by an ANI 129 (or an

¹¹This section is based on the publication: "Thermal sensor based on a polymer nanofilm" M. Culebras, A. M. López, C. M. Gómez, A. Cantarero, *Sensors and Actuators A: Physical*, 239, 161-165 (2016) Reproduced by permission of Elsevier.

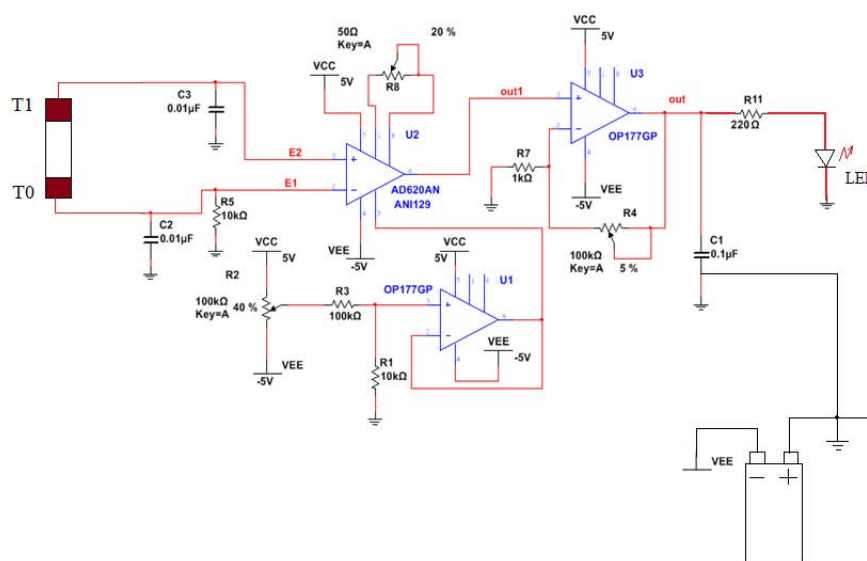


Figure 6.19 Scheme of the electronic circuit of the thermal sensor and the load.

AD620AN) OP amplifier, two OP amplifiers (OP177GP) as a voltage reference and the final fit of the gain in differential mode was performed through a non reversible structure. The negative emf is actually not necessary here for this application (since the temperature difference will be always positive), VEE can be connected to ground.

6.4.4 Sensor characterization

Among the substrates that can be used to obtain PEDOT by electrochemical polymerization, in this work, we have chosen PET since it is a polymer with good flexural properties. The flexibility was kept after the PEDOT layer was synthesized over the PET substrate. The polymerization time and intensity during the electrodeposition process determine the thickness of the film. Previous experiments [27] correlated time and intensity with the thickness of the PEDOT films. In this work, we have chosen 3 mA and 1.5 min to obtain a 120 nm thick PEDOT film as shown in Figure 6.20(a). The measurements of Seebeck coefficient were made with a homemade apparatus as shown in Figure 6.20(b). The sample (see Figure 6.20(a)) was attached between two copper blocks to guarantee a good thermal conductivity. One of these blocks was kept at room temperature (T_0) while the other one is heated to different temperatures, T being $T > T_0$. Figure 6.20(c) shows the output or Seebeck voltage as a function of the temperature difference created across the polymer nanofilm. The sample was subjected to a reduction process using hydrazine vapor to increase the Seebeck coefficient of the sample. As shown in Figure 6.20(c), the Seebeck coefficient changes from $9 \mu\text{V/K}$ to $40.1 \mu\text{V/K}$ by reducing the PEDOT. This fact is related with the doping level of the sample; since the hydrazine is a reduction agent, the oxidation level of the PEDOT chains decreases [27]. Due to this process, the polymer chains change

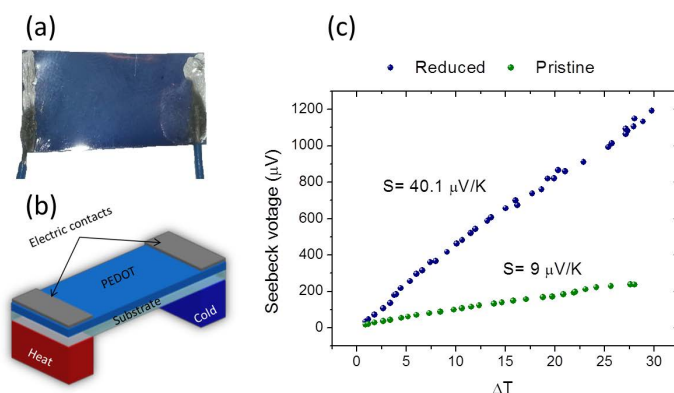


Figure 6.20 (a) Image of PEDOT nanofilm; (b) Schematic diagram of the Seebeck measurements. (c) Seebeck voltage as a function of temperature difference across the sample.

from a polaronic/bipolaronic state for the pristine sample to a neutral state for the reduced one, as have been previously reported [37, 100]. The increase of the Seebeck coefficient improves the sensitivity of the thermal sensor.

The electric behavior of the thermal polymer sensor (Figure 6.20(b)) has been simulated with a COMSOL Multiphysics Modeling Software. The following parameters have been used for the simulation: 0.2 W/m K for the thermal conductivity, 200 S/cm for the electrical conductivity and 40.1 $\mu\text{V/K}$ for the Seebeck coefficient. The sample dimensions were $20 \times 5 \text{ mm}^2$ and the thickness was 1 μm . Figure 6.21 shows the temperature mapping simulation of the polymer thin film.

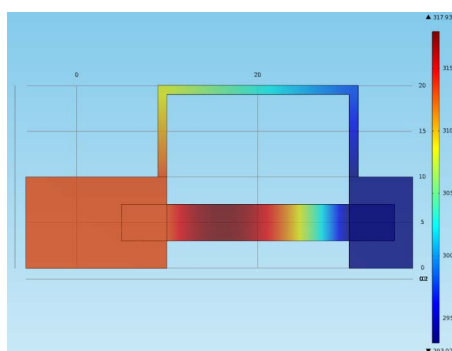


Figure 6.21 Temperature mapping of a polymer thin film simulated with COMSOL.

The film is connected to a variable load resistance in order to check the optimum impedance for the maximum energy transfer. In addition, power simulations generated by different temperature increments between the two blocks as a function of the current intensity have been obtained with the COMSOL software. Figure 6.22 shows the power generation simulations as a function of the electric current across the sample for several temperature differences. The dependence between power and current is of parabolic type. As the temperature difference increases, the maximum value of the power is shifted to higher values when the current increases. This fact is explained by an increase of the voltage across the sample produced by the Seebeck effect.

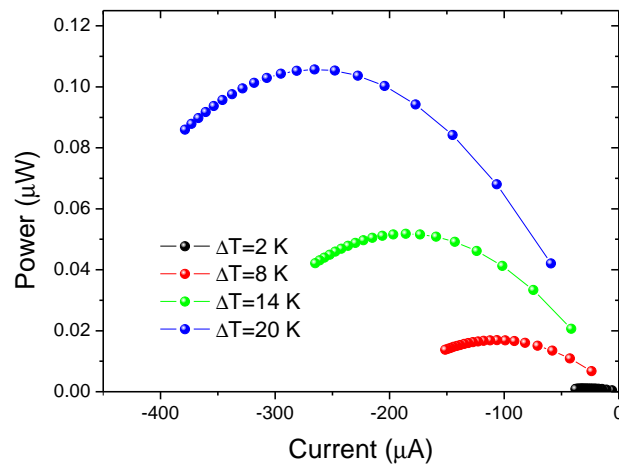


Figure 6.22 Simulation of power generation as a function of current intensity for the polymer thermal sensor at several temperature differences.

In order to check experimentally the data previously simulated, the PEDOT nanofilm (Figure 6.20a) has been successively pressed by a finger and the output signal has been recorded. Figure 6.23 shows the temperature difference and the output or Seebeck voltage generated when

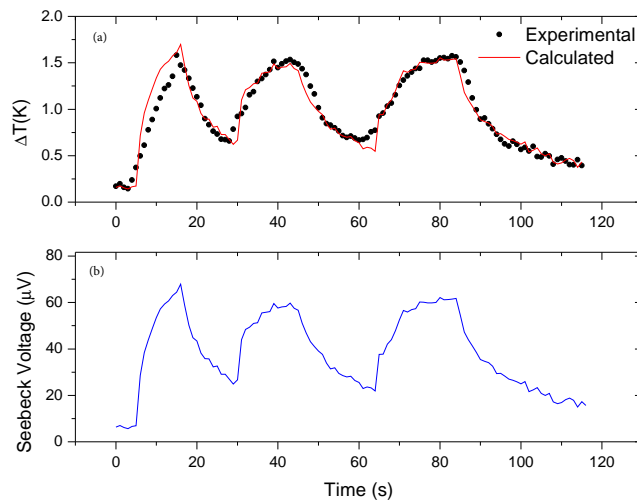


Figure 6.23 (a) Temperature increment, and (b) voltage output generated by finger pressing the thermal polymer sensor.

the PEDOT nanofilm is pressed by the finger. These results indicate that the finger creates a temperature difference of around 1.5°C (Figure 6.23(a)) on the film. The temperature gradient results show a good correlation between the data calculated from the Seebeck voltage and that measured from the PT100 resistors. A reproducible voltage of $60\text{--}65\ \mu\text{V}$ is recorded with a very good time response of $0.52\ \text{s}$.

An on-off type device that uses a PEDOT film as thermal sensor (Figure 6.24(a)) has been developed. The high CMRR (above 100 dB) of the electronic circuit in conjunction with its large differential gain (larger than 90 dB) makes it possible to use a very small input voltage (Figure 6.24(a)). For this reason, the voltage generated by the finger pressing the PEDOT film,

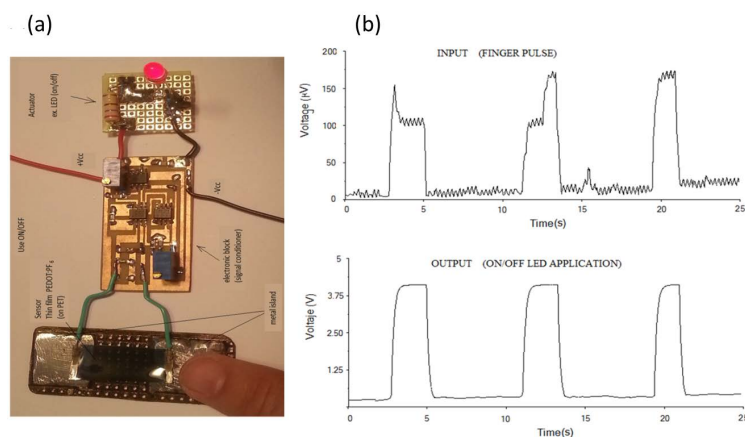


Figure 6.24 (a) Picture of the sensor device. (b) Input and output voltage during several finger pulses.

$200 \mu\text{V}$, with a temperature difference of about 5°C can be used for the device operation. The noise can be neglected because the common-mode gain (G_c) is almost zero. The output of the operational amplifier is saturated with a very low differential pressure (of the order of $80 \mu\text{V}$). When a finger pulse ($\Delta T \approx 5^\circ\text{C}$) is applied, the output voltage (Figure 6.24(b)) is enough to switch on an LED as shown in Figure 6.24(a).

6.5 Supercapacitor devices based on PEDOT nanocomposites

6.5.1 Materials

PDDA, with a molecular weight of 10^5 - 20^5 g/mol, DOC ($\text{C}_{24}\text{H}_{39}\text{NaO}_4$), EDOT, lithium perchlorate acetonitrile and propylene carbonate were purchased from Sigma Aldrich (Milwaukee, WI) All chemicals were used as received. MWCNT were obtained from Bayer Material Science (12–15 nm outer and 4 nm inner wall diameter, length $> 1 \mu\text{m}$, purity ≥ 95 wt%; Leverkusen, Germany. Cotton fabric 400 with a weight 100 g/m^2 was purchased from Testfabrics Inc, West Pittston PA USA. Poly(methyl methacrylate) (PMMA) was kindly supplied by ICI with number average molar mass $M_n = 28270$, polydispersity index $PI = 1.98$, and glass transition temperature of approximately 112°C .

6.5.2 Assembly of supercapacitors based on PEDOT films

A 20 nm gold layer was deposited in a PET substrate (4×2.7) cm² using thermal evaporation. The PET-gold substrate was used as a working electrode in a three electrode electrochemical cell, a platinum grid was used as counter electrode and Ag/AgCl electrode was used as reference electrode. EDOT polymerization was carried out at 3 mA from a solution of 0.01 M of EDOT, 0.1 M of LiClO₄ in acetonitrile using an IVIUM n-stat as a potentiostat. After the polymerization the working electrode was covered by the synthesized PEDOT films. The PET-Au-PEDOT film was cut in half to fabricate the supercapacitor device. Then these two films were connected putting in between a glass filter paper previously dipped in the electro-gel, made from 4.2 mL of acetonitrile:propylene carbonate (volume ratio 5:2) with 1 M of LiClO₄ and 0.8 g of PMMA.

6.5.3 Preparation of MWCNTs-cotton fabrics

First, cotton fabrics were washed in hot water and dried at 70 °C Then, the fabric was dipped in a solution with 0.05 wt % of MWCNTs and 0.25 wt% of PDDA. After this process the fabric was washed several times with water and drained. Then, the fabric was dipped in a solution with 0.5 wt % of MWCNTs and 0.5 wt% of DOC. The non attached elements were removed by several washing steps and drained. These two recessed correspond with one cycle called bilayer. The fabric were coated with 10, 20 and 30 BL.

6.5.4 PEDOT synthesis over MWCNTs-cotton fabrics

The synthesis of PEDOT over MWCNTs-cotton fabrics (size 4×2.7) cm² was carried out using electrochemical polymerization. A solution with 0.01 M of EDOT and 0.1 M of LiClO₄ in acetonitrile was prepared. The electrochemical cell was formed by 3 electrodes: a counter electrode (platinum grid), a reference electrode (Ag/AgCl) and the MWCNTs-cotton fabric was used as a working electrode. In order to avoid that the electrochemical solution touch the copper electrodes, the working electrode was assembled as shows Figure 6.25 . MWCNTs-cotton fabric was placed between two pieces of PET-ITO, one of them connected to a copper tape. Then the PET-ITO sheets with the fabric in between, was hold with metallic tweezer. The polymerization was carried out in a galvanostatic mode at 6 mA during 4 hours in a IVIUM n-stat in order to cover with PEDOT all the dipped part of the fabric. After the polymerization the MWCNTs-cotton-PEDOT fabric was rinsed several times with clean acetonitrile and ethanol.

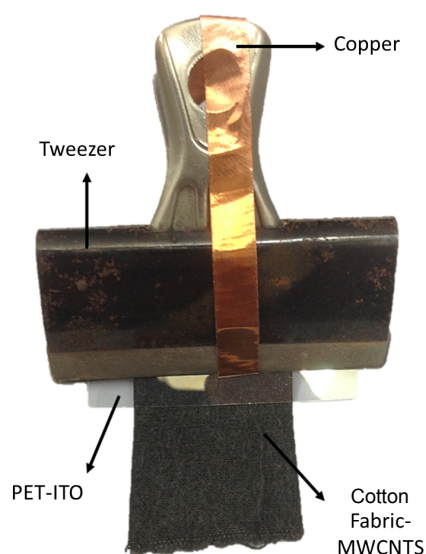


Figure 6.25 Picture of the working electrode during the PEDOT polymerization on MWCNTs-cotton fabrics.

6.5.5 MnO_2 -PEDOT co-synthesis over MWCNTs-cotton fabrics

The synthesis of MnO_2 -PEDOT-MWCNTs-cotton fabrics were carried out following the same procedure described in the previous section. However, the solution used in the synthesis was made of 0.08 M EDOT monomer, 10 mM manganese acetate, 0.16 M sodium dodecyl sulfate, and 0.1 M lithium perchlorate dissolved in water.

6.5.6 Assembly of devices based on cotton fabrics

All the devices fabricated were assembled using the following procedure. One of the sides of the fabrics was covered with a gold leaf in order to improve the electric contact. Then, a glass filter paper, previously dipped in the electro-gel solution was placed between the fabrics as shows Figure 6.26. A PET-gold sheet was employed as a current collector and finally the device was sealed with propylene tape.

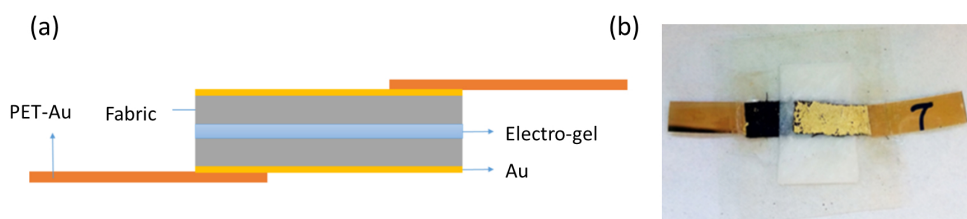


Figure 6.26 (a) Schematic of fabric supercapacitor and (b) picture of the final device.

6.5.7 Characterization of supercapacitors based on PEDOT films

The supercapacitor device using PET-Au-PEDOT films was assembled as described before. The devices were characterized by cyclic voltammetry in an IVIUM n-stat potentiostat in a two electrode mode. Figure 6.27 shows the results of the cyclic voltammetry analysis, at different scan

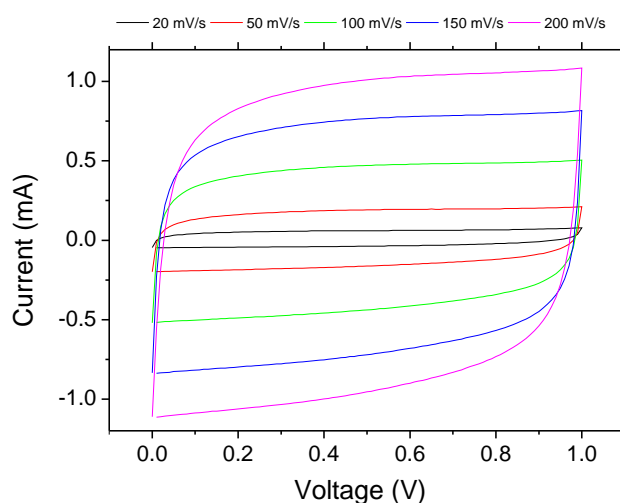


Figure 6.27 Cyclic voltammetry of PET-Au-PEDOT device at different scan ratio.

rates, from 20 mV/s to 200 mV/s, of PEDOT films synthesized during 1 minute of polymerization. These results show highly capacitance behavior with a nearly rectangular shape and highly symmetrical in the doped/de-doped states even when the scan rate is very high (200 mV/s). This fact indicates a low contribution in the equivalent internal resistance of the supercapacitor device.

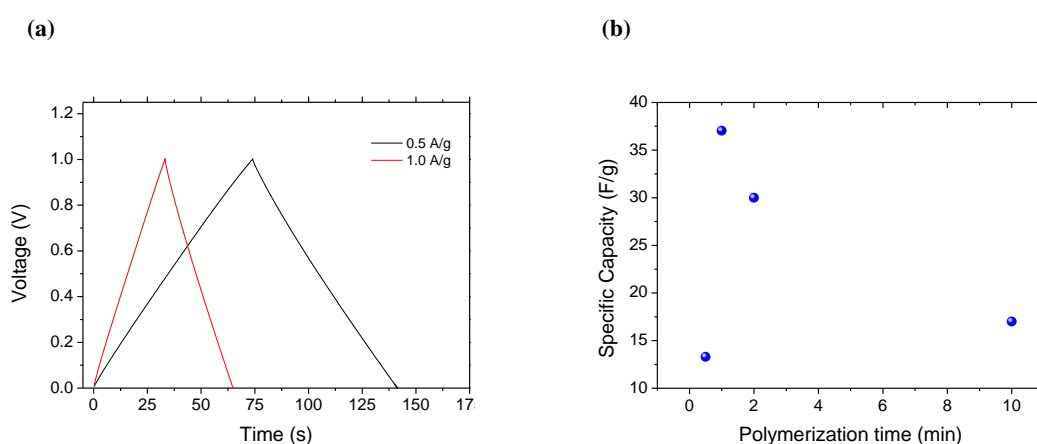


Figure 6.28 (a) Galvanostatic curves at 0.5 A/g and 1.0 A/g of PET-Au-PEDOT device. (b) Specific capacity as a function of polymerization time.

Galvanostatic analysis charge and discharge curves are shown in Figure 6.28(a). The charge and discharge processes were evaluated applying 0.5 A/g and 1.0 A/g until 1.0 V. The curves show

the typical behavior of the charge-discharge process of electrochemical supercapacitors. The discharge curves exhibit capacitance performance without ohmic drop indicating the good behavior of the device. The values of the specific capacitance were calculated using the following equation:

$$C_p = \frac{I \cdot \Delta t}{\Delta V \cdot m}, \quad (6.6)$$

where I is the constant charge current, $\Delta t/\Delta V$ is the inverse of the slope of the galvanostatic curves and m is the total mass of the electrodes. The absolute capacitance obtained for the device fabricated using a PEDOT electrode synthesized at 1 min of polymerization was 7.4 mF and 6.7 mF measured at 0.5 mA/g and 1.0 mA/g respectively. Considering the total mass of the electrodes, 0.2 mg the specific capacitance was 37.0 F/g and 33.6 F/g for 0.5 mA/g and 1.0 mA/g, respectively. The specific capacitance value decreases with the current density due to limitations with the diffusion of the electrolyte at high values of current densities.

Figure 6.29 shows the evolution of the specific capacity of the device as a function of the charge-discharge cycles at 1 mA/g. The specific capacitance decreases from 33.6 F/g to 21 F/g after 1000 cycles indicating the good behavior of the device.

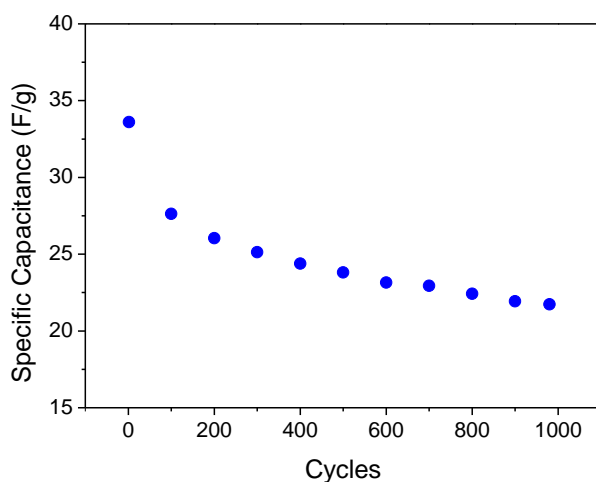


Figure 6.29 Specific capacitance of a PET-PEDOT device as a function of charge-discharge cycles.

6.5.8 Characterization of supercapacitors based on cotton fabrics

Several cotton fabric were coated with MWCNTs solutions using the LBL method (from 10 to 30 BL). As positive solution, 0.25 % of PDDA and 0.05 % of MWCNTs have been used and for negative solution 1% of DOC and 0.5 % of MWCNTs were employed. The time of dipping in each solution was 2 min with a rinse step in between. After the LBL coating, the

EDOT polymerization was performed during 4 hour, at 6 mA. The electrical conductivity was measured using Van Der Paw method as a function of the number of bilayers (see Figure 6.30). The results indicate a maximum of the electrical conductivity at 20 BL with a value around

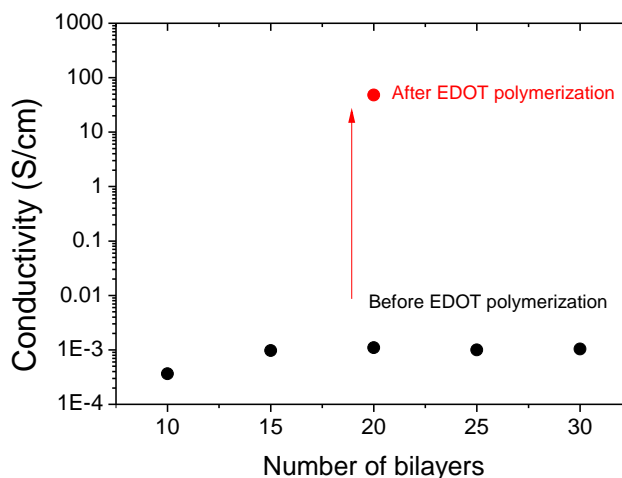


Figure 6.30 Cotton fabric/MWCNT after EDOT polymerization.

10^{-3} S/cm. After 20 BL the electrical conductivity remains in the same values, indicating no improvement in the electrical properties with the number of bilayers, probably due to a saturation of the cotton fabrics. After the synthesis of PEDOT over the fabric coated with 20 BL, the electrical conductivity increased more than 4 orders of magnitude, until values around 50 S/cm. The big increase in the electrical conductivity is due to the presence of PEDOT, that acts as an electric connector between the cotton fibers, making a highly electrically conductive fabric network.

Figure 6.31 shows several pieces of cotton fabrics coated with 10 BL and 20 BL. The image show

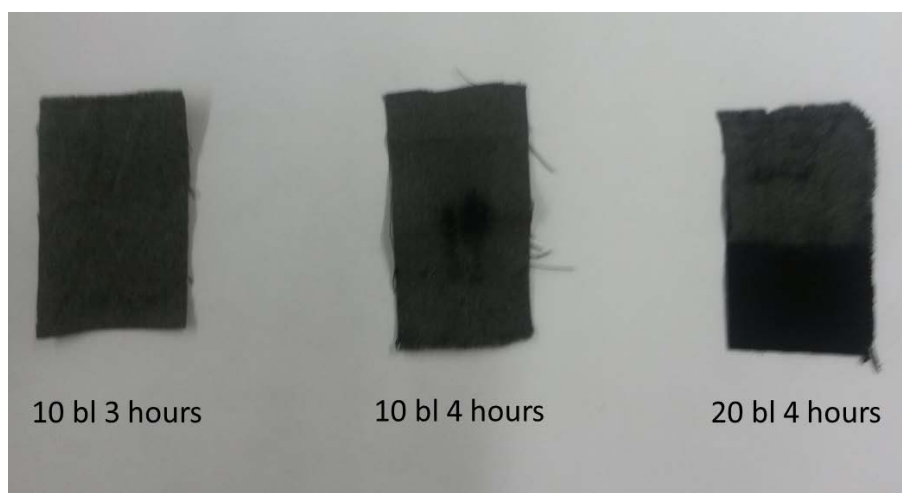


Figure 6.31 Cotton fabric/MWCNT with different number after several EDOT polymerization times.

how when the number of BL is 10 the polymerization of EDOT is not working well probably due to the high electrical resistance of the fabric, making really hard a homogeneously distribution of the current around the cotton fabric electrode. For this reason, when the time of polymerization was 4 hours only a small part of fabric was coated. However, when the number of BL was 20, the cotton fabric electrode was conductive enough to keep the current homogeneously distributed to coat completely the cotton fabric, finishing after four hours of polymerization.

SEM analysis were used to analyze the presence of PEDOT in the cotton fabrics. Figures 6.32 (a) and (b) show MWCNTs-cotton fabrics before the PEDOT synthesis. The MWCNTs layers

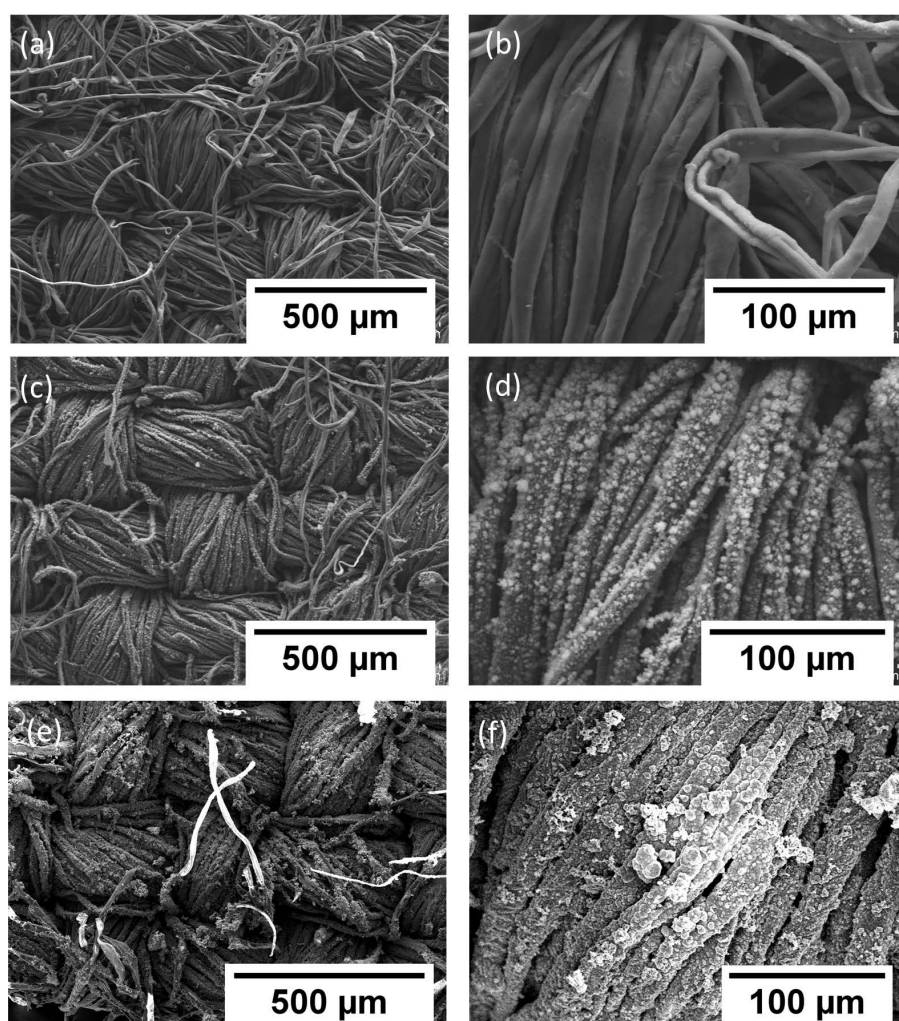


Figure 6.32 SEM images of: (a) and (b) MWCNTs-cotton fabrics, (c) and (d) MWCNTs-PEDOT cotton fabrics, (e) and (f) MWCNTs-PEDOT-MnO₂ cotton fabrics .

were homogeneously distributed around the fibers since, the SEM images did not show evidences of MWCNTs agglomerations. It is possible to observe some bridges between the cotton fabrics. These bridges are MWCNTs which electrically connect the fibers between them. Figures 6.32(c) and (d) depict the MWCNTs-cotton fabrics after the PEDOT deposition. PEDOT was homogeneously synthesized around the fabric. The SEM analysis shows that PEDOT is not

only deposited on the superficial layer but also was synthesized on the most internal fibers. The PEDOT had a globular morphology typical from the electrochemical deposition of conducting polymers. Different morphology have been obtained for the case of MWCNTs-PEDOT-MnO₂ fabrics as shown in Figures 6.32 (e) and (f). The coating was structured in spherical domains, showing some agglomerates distributed in specific parts of the sample. Obviously, the use of different reaction media in the co-deposition of PEDOT-MnO₄ produces different morphologies conditioned by the solvent (water) and the presence of a surfactant.

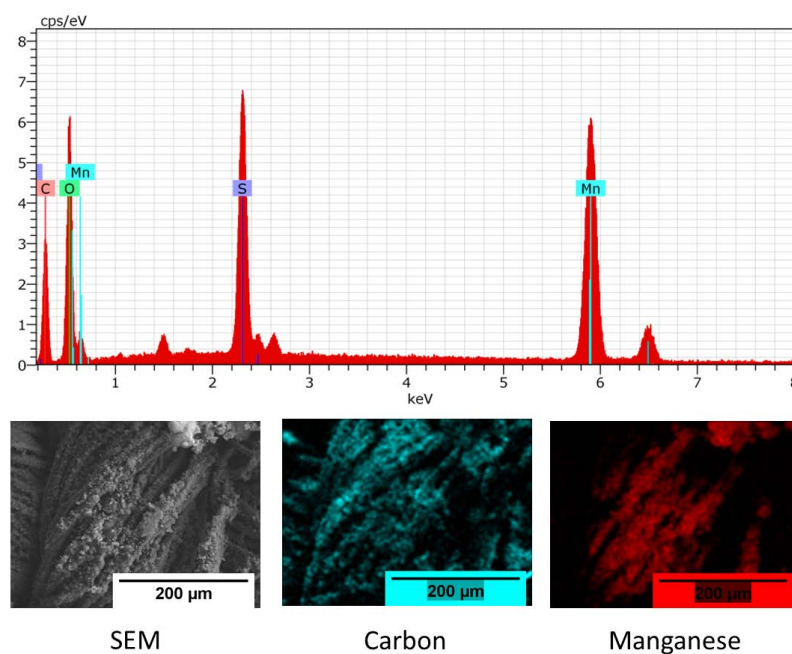


Figure 6.33 Microanalysis and mapping of MWCNTs-PEDOT-MnO₂ cotton fabrics .

EDAX elemental analysis was made to evidence the presence of Mn in the fabrics as shown in the Figure 6.33. The results indicate the presence of Mn in the cotton fabrics, with a (28 ± 5) %wt on the sample surface. The mapping images show the element distribution of carbon and manganese. The image of Mn distribution (red) shows how the Mn is concentrated in the middle of the sewing, probably because the reduction of Mn ions is dominating in this area of the fabric.

The devices using MWCNTs-PEDOT-cotton fabric and MWCNTs-PEDOT-MnO₂-cotton fabric were assembled as it has been described in the previous section. The devices were characterized by cyclic voltametry in an IVIUM n-stat potentiostat in a two electrode mode. Figure 6.34 shows the cyclic voltametry curves of the devices fabricated using MWCNTs-PEDOT and MWCNTs-PEDOT-MnO₂ over cotton fabrics between 0 and 1 V at 20 mV/s. The curves do not show a rectangular shape indicating a non ideal capacitance behavior. Probably this behavior is given by the poor electrical connection between the electro-active region (MWCNTs-PEDOT and MWCNTs-PEDOT-MnO₂) and the current collector (PET-Au). However, the curves show some capacitance behavior at low scan rate such as 20 mV/s which decreases when the scan rate is higher.

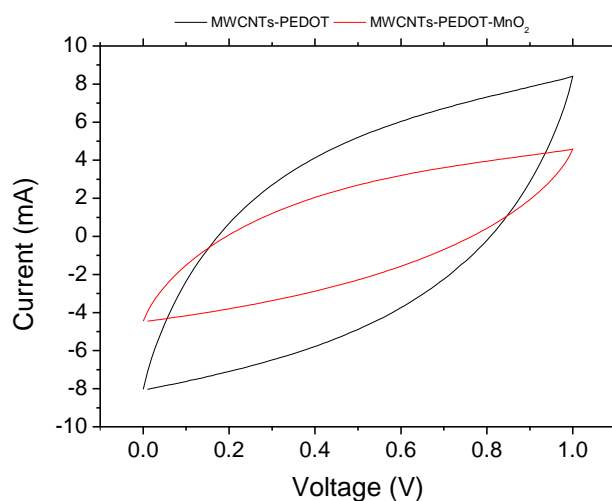


Figure 6.34 Cyclic voltammetry of MWCNTs-PEDOT-cotton fabric and MWCNTs-PEDOT-MnO₂-cotton fabric devices at 20 mV/s.

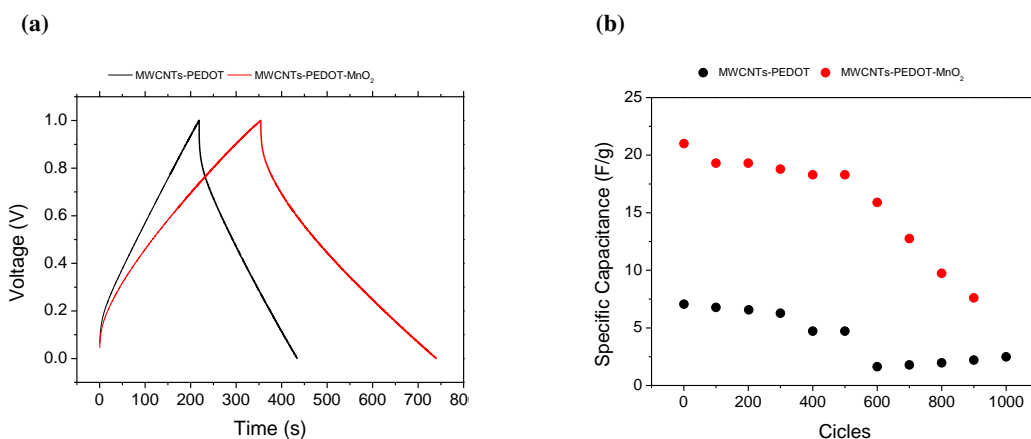


Figure 6.35 (a) Galvanostatic curves of CNTs-PEDOT-Cotton fabric and MWCNTs-PEDOT-MnO₂-cotton fabric devices. (b) Specific capacity as a function of cycles.

Galvanostatic analysis charge and discharge curve are shown in Figure 6.35(a). The charge and discharge process was evaluated applying 1 mA until 1.0 V. The curves show the typical behavior of charge-discharge process of electrochemical supercapacitors. The discharge curves exhibit capacitance performance with an ohmic drop indicating that the behavior of the device can be improved. The values of the specific capacitance were calculated using Eq. 6.6. The absolute capacitance values obtained for CNTs-PEDOT-cotton fabric and MWCNTs-PEDOT-MnO₂-cotton fabric devices were 406 and 294 mF, respectively. Taken into account the mass of the electro-active part of the electrodes (54 mg for CNTs-PEDOT and 14 mg for MWCNTs-PEDOT-MnO₂) the specific capacitance was 7.0 F/g and 21 F/g for CNTs-PEDOT-cotton fabric and MWCNTs-PEDOT-MnO₂-cotton fabric devices, respectively. The specific capacitance was evaluated as a function of the number of cycles as shown in the Figure 6.35(b). In both cases the

specific capacity decreases with the number cycles, being important after 500 cycles, probably given by a degradation of the electro-gel.

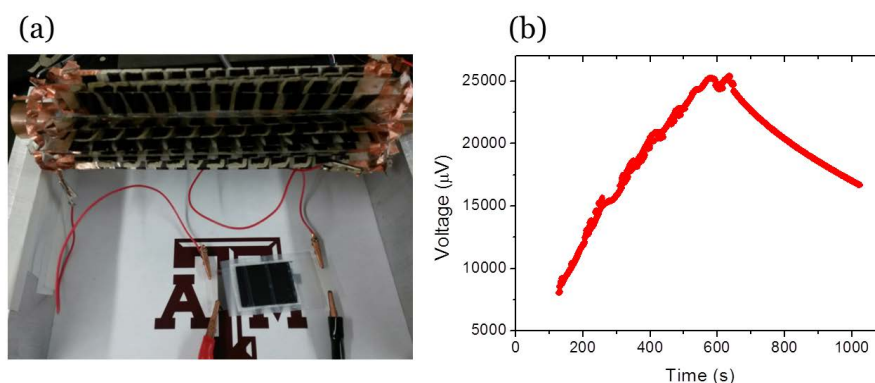


Figure 6.36 (a) Picture of the cylindrical thermoelectric generator charging one of the supercapacitors developed. (b) Charge and discharge curve using the thermoelectric generators as power supply.

Figure 6.36 shows a proof of concept of the cylindrical thermoelectric (fabricated with MWC-NTS/PEDOT nanocomposites) generator charging one supercapacitor device fabricated using PEDOT electrodes. The temperature gradient applied to thermoelectric generator was 30 K. The Figure 6.36(b) shows how the voltage arrives until 26 mV after 600 s. Obviously, this experiment is a small proof of concept, and it could be the starting point for future research.

6.6 Conclusions

In this chapter, several devices have been developed using the materials synthesized in previous chapters. On the one hand, two thermoelectric generators were fabricated. The first was made using PEDOT synthesized by electrochemical polymerization. The chemical de-doping using hydrazine vapor increases the power generation. By increasing the thickness of the PEDOT tracks, it is possible to increase the power generation. Connecting 15 modules in parallel, the supplied power has been incremented until 25 nW. The second thermoelectric generator was fabricated combining layer by layer assembly and electrochemical polymerization using MWC-NTs and PEDOT achieving a power of $5.5 \mu\text{W}$ at $\Delta T=30 \text{ K}$. In addition it has been developed a thermal sensor based on the thermoelectric effect acting on a polymeric materials. A PEDOT nanofilm has been obtained from electrochemical polymerization from EDOT monomers on a PET substrate covered with gold. The PEDOT nanofilm has been used as thermal sensor based on the Seebeck effect. A simulation using COMSOL Multiphysics indicates the temperature and voltages differences that can be generated. An electronic device that uses the voltage generated by the temperature difference due to a finger pressing the polymer has been constructed. The device can switch on a LED.

On the other hand, several supercapacitors devices based on PEDOT were prepared by electrochemical polymerization of PEDOT. The supercapacitors based on PEDOT films show an excellent capacitance behavior according to the cyclic voltametry results achieving 37 F/g of specific capacitance. Also supercapacitors devices were made over cotton fabrics combining layer by layer deposition and electrochemical deposition of PEDOT and MnO_2 . The devices based on cotton fabrics showed higher values in terms of absolute capacitance however the specific capacitance were smaller, 7.0 F/g and 21 F/g for CNTs-PEDOT-cotton fabric and MWCNTs-PEDOT- MnO_2 -cotton fabric devices respectively. This fact can be explained because the devices based on cotton fabrics were not well optimized due to the high ohmic drop showed in the galvanostatic curves. However, the purpose of this research was to create as starting point for future research lines. Finally, a proof of concept of the charge of a supercapacitor using thermoelectric generator based on organic materials was developed.

Chapter 7

General conclusions

The thermoelectric properties have been evaluated in several materials of different nature (organic, inorganic and hybrids). The addition of polar solvents as DMSO to PEDOT:PSS solution increases the electrical conductivity due to a secondary doping effect in the polymer chains. The electrochemical polymerization is a powerful method to synthesize highly conductive polymers such as PEDOT and PPy. Using chemical de-doping, through hydrazine vapor it is possible to optimize ZT of PEDOT. The electrical conductivity decreases with the exposure time to hydrazine vapor while the Seebeck coefficient increases. In addition, the thermoelectric properties were evaluated in PEDOT films synthesized using different counter-ions, achieving the best thermoelectric efficiency ($ZT = 0.2$) in PEDOT:BTfMSI at 5 seconds of reduction time. Also the electrochemical de/doping is a very promising way to optimize the thermoelectric efficiency in conducting polymers, the results obtained for PEDOT and PPy depict optimum values at intermediate potentials for the case of PEDOT and at negative potentials for PPy. In addition PEDOT nanoparticles showed thermoelectric behavior. The electrical conductivity increases with the contraction of the oxidant salt (Fe-Tos), however the spherical morphology only is obtained when H_2O_2 is used during the synthesis, generating some losses in terms of electrical conductivity due to secondary reactions. The synthesis of PEDOT nanoparticles using a positive charged surfactant (DTAB) produces a transition between p-type to n-type semiconductor. In addition higher concentrations of DTAB inhibits the PEDOT polymerization. Finally, PEDOT nanowires with a 200 nm of diameter have been synthesized using alumina templates. For the case of inorganic materials, $La_{1-x}Ca_xMnO_3$ and $Nd_{1-x}Ca_xCoO_3$ only the perovskite phase is obtained at $650^\circ C$, producing a change in the morphology in the $La_{1-x}Ca_xMnO_3$. The thermoelectric properties are strongly dependent on the calcium content in both materials. In the case of $La_{1-x}Ca_xMnO_3$ nanostructures there is change from p-type to n-type conduction with calcium content, and in $Nd_{1-x}Ca_xCoO_3$ perovskite nanowires the electrical conductivity is higher at lower calcium content. In addition, several carbon derivatives were evaluated as thermoelectric materials (carbon black, vitreous carbon and charcoal), showing that the irradiation

process can alter the semiconductor behavior, for example the samples of vitreous carbon change from p-type to n-type after irradiation. Hybrids and nanocomposites materials showed excellent thermoelectric behavior. The nanocomposites prepared by solution process methods such as PEDOT:PSS-EG and PEDOT-Perovskites nanocomposites showed an increase in their thermoelectric efficiency. The addition of EG to PEDOT:PSS polymer matrix increases the electrical conductivity 3 orders of magnitude. The addition of PEDOT to perovskites nanocomposites improves the electrical conductivity achieving higher PF than the raw materials. PEDOT can be synthesized using LBL MWCNTs films as working electrode. The electrochemical polymerization over these films creates hybrids materials with a high thermoelectric efficiency giving a maximum, $150 \mu\text{W}/\text{m K}^2$, using 30 BL MWCNTs film and polymerized during 30 min. The same strategy was followed for Te-PEDOT films. The thermoelectric properties were evaluated as a function of Te decomposition time. The electrical conductivity decreases as a function of the Te electrodeposition time while the Seebeck coefficient increases. The maximum power factor was achieved at 150 min of Te electrodeposition time giving the excellent value of $(320 \pm 70) \mu\text{W}/\text{m K}^2$. Figure 7.1 shows the evolution of the thermoelectric efficiency given by the PF, for the most representative materials studied during this doctoral thesis. The trend is clear, there has been an impressive increase as result of the continuous research carry out during these years. Finally, two thermoelectric modules, one thermal sensor and supercapacitors devices were fabricated based on the materials studied in this thesis.

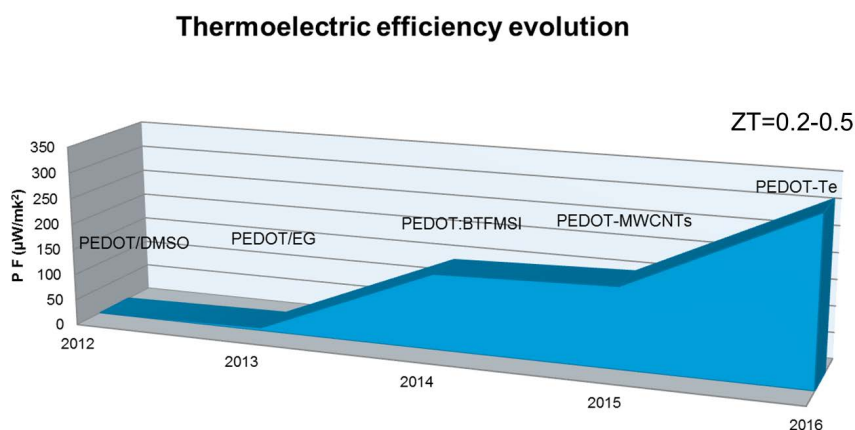


Figure 7.1 Thermoelectric efficiency evolution during the period of this thesis o during the last four years.

Bibliography

- [1] H. Lund and B. V. Mathiesen. Energy system analysis of 100% renewable energy systems the case of denmark in years 2030 and 2050. *Energy*, 34(5):524–531, 2009.
- [2] D. Connolly, H. Lund, B. V. Mathiesen, and M. Leahy. A review of computer tools for analysing the integration of renewable energy into various energy systems. *App. Ener.*, 87(4):1059–1082, 2010.
- [3] H. Lund. Renewable energy strategies for sustainable development. *Energy*, 32(6):912–919, 2007.
- [4] A. R. M. Siddique and B. Mahmud, S. and Van Heyst. A comprehensive review on vibration based micro power generators using electromagnetic and piezoelectric transducer mechanisms. *Energy Conv. Manag.*, 106:728–747, 2015.
- [5] G. M’bougui, K. Adendorff, R. Naidoo, A. A. Jimoh, and D. E. Okojie. A hybrid piezoelectric micro-power generator for use in low power applications. *Renew. Sust. Energ. Rev.*, 49:1136–1144, 2015.
- [6] G. Liu, Q. Leng, J. Lian, H. Guo, X. Yi, and C. Hu. Notepad-like Triboelectric Generator for Efficiently Harvesting Low-Velocity Motion Energy by Interconversion between Kinetic Energy and Elastic Potential Energy. *ACS Appl. Mater. Interfaces*, 7(2):1275–1283, 2015.
- [7] S. H. Shin, Y. H. Kwon, Y. H. Kim, J. Y. Jung, M. H. Lee, and J. Nah. Triboelectric Charging Sequence Induced by Surface Functionalization as a Method To Fabricate High Performance Triboelectric Generators. *ACS Nano*, 9(4):4621–4627, 2015.
- [8] T. J. Seebeck. Ueber die magnetische polarisation der metalle und erze durch temperatur-differenz. *Annalen der Physik*, 82(2):133–160, 1826.
- [9] G. J. Snyder and E. S. Toberer. Complex thermoelectric materials. *Nat. Mater*, 7(2):105–114, 2008.
- [10] C. Goupil, W. Seifert, K. Zabrocki, E. Mueller, and G. J. Snyder. Thermodynamics of Thermoelectric Phenomena and Applications. *Entropy*, 13(8):1481–1517, 2011.

- [11] A. Cantarero and F. X. Alvarez . Thermoelectric effects: Semiclassical and quantum approaches from the boltzmann transport equation. In *Nanoscale Thermoelectrics*, pages 1–39. Springer International Publishing, 2014.
- [12] J. P. Heremans. Low dimensional thermoelectricity. *Acta Phys. Pol. A*, 108:609–634, 2005.
- [13] L. D. Hicks and M. S. Dresselhaus. Effect of quantum-well structures on the thermoelectric figure of merit. *Phys. Rev. B*, 47:12727–12731, 1993.
- [14] M. Martín-González, O. Caballero-Calero, and P. Díaz-Chao. Nanoengineering thermoelectrics for 21st century: Energy harvesting and other trends in the field. *Renewable Sustainable Energy Rev.*, 24:288–305, 2013.
- [15] J. Yang, L. Xi, W. Qiu, L. Wu, X. Shi, L. Chen, J. Yang, W. Zhang, C. Uher, and D. J. Singh. On the tuning of electrical and thermal transport in thermoelectrics: an integrated theory–experiment perspective. *npj Comput. Mater.*, 2:15015, 2016.
- [16] R. Venkatasubramanian, E. Siivola, T. Colpitts, and B. O’Quinn. Thin-film thermoelectric devices with high room-temperature figures of merit. *Nature*, 413(6856):597–602, 2001.
- [17] T. C. Harman, P. J. Taylor, M. P. Walsh, and B. E. LaForge. Quantum dot superlattice thermoelectric materials and devices. *Science*, 297(5590):2229–2232, 2002.
- [18] B. Poudel, Q. Hao, Y. Ma, Y. Lan, A. Minnich, B. Yu, X. Yan, D. Wang, A. Muto, D. Vashaee, X. Chen, J. Liu, M. S. Dresselhaus, G. Chen, and Z. Ren. High-thermoelectric performance of nanostructured bismuth antimony telluride bulk alloys. *Science*, 320(5876):634–638, 2008.
- [19] M. Culebras, C. M. Gómez, and A. Cantarero. Review on Polymers for Thermoelectric Applications. *Materials*, 7(9):6701–6732, 2014.
- [20] Y. Du, S. Z. Shen, K. Cai, and P. S. Casey. Research progress on polymer-inorganic thermoelectric nanocomposite materials. *Prog. Polym. Sci.*, 37(6):820–841, 2012.
- [21] C. de Tomás, A. Cantarero, A. Lopeandia, and F. X. Álvarez. From kinetic to collective behavior in thermal transport on semiconductors and semiconductor nanostructures. *J. Appl. Phys.*, 115:0000, 2014.
- [22] M. Wagner, G. Span, S. Holzer, and T. Grasser. Thermoelectric power generation using large-area Si/SiGe pn-junctions with varying Ge content. *Semicond. Sci. Technol.*, 22(1): S173–S176, 2007.
- [23] T. Park, C. Park, B. Kim, H. Shin, and E. Kim. Flexible pedot electrodes with large thermoelectric power factors to generate electricity by the touch of fingertips. *Energy Environ. Sci.*, 6:788–792, 2013.

- [24] M. Y. Kim and T. Sung. Oh. Thermoelectric Power Generation Characteristics of a Thin-Film Device Consisting of Electrodeposited n-Bi₂Te₃ and p-Sb₂Te₃ Thin-Film Legs. *J. Electron. Mater.*, 42(9):2752–2757, 2013.
- [25] Byeonggwon Kim, Haijin Shin, Teahoon Park, Hanwhuy Lim, and Eunkyong Kim. NIR-Sensitive Poly(3,4-ethylenedioxy-selenophene) Derivatives for Transparent Photo-Thermo-Electric Converters. *Adv. Mater.*, 25(38):5483–5489, 2013.
- [26] S. H. Lee, H. Park, S. Kim, W.n Son, I. W. Cheong, and J. H. Kim. Transparent and flexible organic semiconductor nanofilms with enhanced thermoelectric efficiency. *J. Mater. Chem. A*, 2:7288–7294, 2014.
- [27] M. Culebras, A. Cantarero, and C. M. Gómez. Enhanced thermoelectric performance of pedot with different counter ions optimized by chemical reduction. *J. Mater. Chem. A*, 2: 10109–10115, 2014.
- [28] O. Bubnova, M. Berggren, and X. Crispin. Tuning the Thermoelectric Properties of Conducting Polymers in an Electrochemical Transistor. *J. Am. Chem. Soc.*, 134(40):16456–16459, 2012.
- [29] K-C. Chang, M-S. Jeng, C-C. Yang, Y-W. Chou, S-K. Wu, M. A. Thomas, and Y.-C. Peng. The Thermoelectric Performance of Poly(3,4-ethylenedioxythiophene)/Poly(4-styrenesulfonate) Thin Films. *J. Electron. Mater.*, 38(7):1182–1188, 2009.
- [30] Q. Yao, Q. Wang, L. Wang, Y. Wang, J. Sun, H. Zeng, Z. Jin, X. Huang, and L. Chen. The synergic regulation of conductivity and Seebeck coefficient in pure polyaniline by chemically changing the ordered degree of molecular chains. *J. Mater. Chem. A*, 2(8): 2634–2640, 2014.
- [31] P. Limelette, B. Schmaltz, D. Brault, M. Guineau, C. Autret-Lambert, S. Roger, V. Grimal, and F. Tran Van. Conductivity scaling and thermoelectric properties of polyaniline hydrochloride. *Journal of Applied Physics*, 115(3):033712/1–033712/6, 2014.
- [32] B. Lu, S. Chen, J. Xu, and G. Zhao. Thermoelectric performances of different types of polyselenophene and its copolymers with 3-methylthiophene via electropolymerization. *Synth. Met.*, 183:8–15, 2013.
- [33] P. S. Taylor, L. Korugic-Karasz, E. Wilusz, P. M. Lahti, and F. E. Karasz. Thermoelectric studies of oligophenylenevinylene segmented block copolymers and their blends with MEH-PPV. *Synth. Met.*, 185:109–114, 2013.
- [34] R. Yue, S.i Chen, C. Liu, B. Lu, J. Xu, J. Wang, and G. Liu. Synthesis, characterization, and thermoelectric properties of a conducting copolymer of 1,12-bis(carbazolyl)dodecane and thieno3,2-bthiophene. *J. Solid State Electrochem.*, 16(1):117–126, 2012.

- [35] H.i Shi, C. Liu, J. Xu, H. Song, B. Lu, F. Jiang, W. Zhou, G. Zhang, and Q. Jiang. Facile Fabrication of PEDOT:PSS/Polythiophenes Bilayered Nanofilms on Pure Organic Electrodes and Their Thermoelectric Performance. *ACS Appl. Mater. Interfaces*, 5(24): 12811–12819, 2013.
- [36] O. Bubnova, Z. U. Khan, A. Malti, S. Braun, M. Fahlman, M. Berggren, and X. Crispin. Optimization of the thermoelectric figure of merit in the conducting polymer poly(3,4-ethylenedioxythiophene). *Nat Mater*, 10(6):429–433, 2011.
- [37] M. Culebras, B. Uriol, C. M. Gomez, and A. Cantarero. Controlling the thermoelectric properties of polymers: application to PEDOT and polypyrrole. *Phys. Chem. Chem. Phys*, 17(23):15140–15145, 2015.
- [38] C. Cho, B. Stevens, J-H. Hsu, R. Bureau, D. A. Hagen, O. Regev, C. Yu, and J. C. Grunlan. Completely Organic Multilayer Thin Film with Thermoelectric Power Factor Rivaling Inorganic Tellurides. *Adv. Mater*, 27(19):2996–3001, 2015.
- [39] C. Cho, K. L. Wallace, P. Tzeng, J-H. Hsu, C. Yu, and J. C. Grunlan. Outstanding Low Temperature Thermoelectric Power Factor from Completely Organic Thin Films Enabled by Multidimensional Conjugated Nanomaterials. *Adv. Energy Mater*, 6(7):1502168, 2016.
- [40] S. K. Yee, N. E. Coates, A. Majumdar, J. J. Urban, and R. A. Segalman. Thermoelectric power factor optimization in PEDOT:PSS tellurium nanowire hybrid composites. *Phys. Chem. Chem. Phys*, 15(11):4024–4032, 2013.
- [41] Kevin C. See, Joseph P. Feser, Cynthia E. Chen, Arun Majumdar, Jeffrey J. Urban, and Rachel A. Segalman. Water-Processable Polymer-Nanocrystal Hybrids for Thermoelectrics. *Nano Lett.*, 10(11):4664–4667, 2010.
- [42] E. J. Bae, Y. H. Kang, K-S. Jang, and S. Y. Cho. Enhancement of Thermoelectric Properties of PEDOT:PSS and Tellurium-PEDOT:PSS Hybrid Composites by Simple Chemical Treatment. *Sci Rep*, 6:18805, 2016.
- [43] E. W. Zaia, A. Sahu, P. Zhou, M. P. Gordon, J. D. Forster, S. Aloni, Y-S. Liu, J. Guo, and J. J. Urban. Carrier Scattering at Alloy Nanointerfaces Enhances Power Factor in PEDOT:PSS Hybrid Thermoelectrics. *Nano Lett*, 16(5):3352–3359, 2016.
- [44] H. Song, C. Liu, H. Zhu, F. Kong, B. Lu, J. Xu, J. Wang, and F. Zhao. Improved Thermoelectric Performance of Free-Standing PEDOT:PSS-Bi₂Te₃ Films with Low Thermal Conductivity. *J. Electron. Mater*, 42(6):1268–1274, 2013.
- [45] K. Chatterjee, M. Mitra, K. Kargupta, S. Ganguly, and D. Banerjee. Synthesis, characterization and enhanced thermoelectric performance of structurally ordered cable-like novel polyaniline-bismuth telluride nanocomposite. *Nanotechnology*, 24(21):215703, 2013.

- [46] B. Zhang, J. Sun, H. E. Katz, F. Fang, and R. L. Opila. Promising Thermoelectric Properties of Commercial PEDOT:PSS Materials and Their Bi₂Te₃ Powder Composites. *ACS Appl. Mater. Interfaces*, 2(11):3170–3178, 2010.
- [47] D.M. Rowe. *Thermoelectrics Handbook Macro to Nano*. CRC Press 2005. Taylor and Francis group, 2010.
- [48] M. Hyland, H. Hunter, J. Liu, E. Veety, and D. Vashaee. Wearable thermoelectric generators for human body heat harvesting. *Appl. Energy*, 182:518–524, 2016.
- [49] G. A. Snook, P. Kao, and A. S. Best. Conducting-polymer-based supercapacitor devices and electrodes. *J. Power Sources*, 196(1, SI):1–12, 2011.
- [50] B. E. Conway. *Electrochemical supercapacitors: scientific fundamentals and technological applications*. Springer Science & Business Media, 2013.
- [51] B. Guo, Z. Hu, Y. An, N. An, P. Jia, Y. Zhang, Y. Yang, and Z. Li. Nitrogen-doped heterostructure carbon functionalized by electroactive organic molecules for asymmetric supercapacitors with high energy density. *RSC Adv*, 6(46):40602–40614, 2016.
- [52] L. J. Van Der Pauw. A method of measuring the resistivity and Hall coefficient on lamellae of arbitrary shape. *Philips Technical Review*, 20:220–224, 1958.
- [53] H. L. Phuoc, C-N. Liao, C. W. Luo, and J. Leu. Thermoelectric properties of nanostructured bismuth-telluride thin films grown using pulsed laser deposition. *J. Alloy. Compd*, 615:546–552, 2014.
- [54] Th C. Hasapis, S. N. Girard, E. Hatzikraniotis, K. M. Paraskevopoulos, and M. G. Kanatzidis. On the Study of PbTe-Based Nanocomposite Thermoelectric Materials. *J. Nano Res*, 17:165–174, 2012.
- [55] N. Stein, N. Petermann, R. Theissmann, G. Schierning, R. Schmechel, and H. Wiggers. Artificially nanostructured n-type SiGe bulk thermoelectrics through plasma enhanced growth of alloy nanoparticles from the gas phase. *J. Mater. Res*, 26(15):1872–1878, 2011.
- [56] G. S. Nolas, D. T. Morelli, and Terry M. Tritt. Skutterudites: A phonon-glass-electron crystal approach to advanced thermoelectric energy conversion applications. *Ann. Rev. Mater. Sci*, pages 1–29, 1999.
- [57] V. L. Kuznetsov, L. A. Kuznetsova, A. E. Kaliazin, and D. M. Rowe. Preparation and thermoelectric properties of A₈B₁₆^{III}B₃₀^{IV} clathrate compounds. *J. Appl. Phys.*, 87:7871–7875, 2000.
- [58] P. A. Cox. *The elements. Their origin, abundance, and distribution*. 1989.

- [59] A. Slikkerveer and F. A. Dewolff. Pharmacokinetics and Toxicity of Bismuth Compounds. *Med Toxicol Adverse Drug Exp*, 4(5):303–323, 1989.
- [60] M. C. Yarema and S. C. Curry. Acute tellurium toxicity from ingestion of metal-oxidizing solutions. *Pediatrics*, 116(2):319–321, 2005.
- [61] S. Sakurai, Y. Kawamata, M. Takahashi, and K. Kobayashi. Improved Photocurrent of a Poly (3,4-ethylenedioxythiophene)-ClO₄-/TiO₂ Thin Film-modified Counter Electrode for Dye-sensitized Solar Cells. *J. Oleo Sci*, 60(12):639–646, 2011.
- [62] G. P. Pandey and A. C. Rastogi. Synthesis and characterization of pulsed polymerized poly(3,4-ethylenedioxythiophene) electrodes for high-performance electrochemical capacitors. *Electrochim. Acta*, 87:158–168, 2013.
- [63] S. Guenes, H. Neugebauer, and N. S. Sariciftci. Conjugated polymer-based organic solar cells. *Chem. Rev*, 107(4):1324–1338, 2007.
- [64] C. Adachi, M. A. Baldo, M. E. Thompson, and S. R. Forrest. Nearly 100% internal phosphorescence efficiency in an organic light-emitting device. *J. Appl. Phys*, 90(10):5048–5051, 2001.
- [65] Rasit A. and Hayati M. A review: Thermoelectric generators in renewable energy. *Int. J. Renew. Energy Res*, 4:128–136, 2014.
- [66] N. Paradee and A. Sirivat. Synthesis of poly(3,4-ethylenedioxythiophene) nanoparticles via chemical oxidation polymerization. *Polym. Int*, 63(1):106–113, 2014.
- [67] A. Aydin and I. Kaya. Syntheses, characterizations and electrochromic applications of polymers derived from carbazole containing thiophene rings in side chain with electrochemical and FeCl₃ methods. *Org. Electron.*, 14(3):730–743, 2013.
- [68] A. F. Diaz, K. K. Kanazawa, and G. P. Gardini. Electrochemical polymerization of pyrrole. *J. Chem. Soc.-Chem. Commun*, (14):635–636, 1979.
- [69] J. V. Thombare, M. C. Rath, S. H. Han, and V. J. Fulari. The influence of monomer concentration on the optical properties of electrochemically synthesized polypyrrole thin films. *J. Semicond*, 34(10):103002, 2013.
- [70] O. Bubnova, Z. U. Khan, H. Wang, S. Braun, D. R. Evans, M. Fabretto, P. Hojati-Talemi, D. Dagnelund, J-B. Arlin, Y. H. Geerts, S. Desbief, D. W. Breiby, J. W. Andreasen, R. Lazzaroni, W. M. Chen, I. Zozoulenko, M. Fahlman, P. J. Murphy, M. Berggren, and X. Crispin. Semi-metallic polymers. *Nat Mater*, 13(2):190–194, 2014.
- [71] A. N. Aleshin, S. R. Williams, and A. J. Heeger. Transport properties of poly(3,4-ethylenedioxythiophene)/poly(styrenesulfonate). *Synth. Met*, 94(2):173–177, 1998.

- [72] F-X. Jiang, J-K. Xu, B-Y. Lu, Y. Xie, R-J. Huang, and L-F. Li. Thermoelectric performance of poly(3,4-ethylenedioxythiophene): Poly(styrenesulfonate). *Chin. Phys. Lett*, 25(6):2202–2205, 2008.
- [73] J. Jin, Q. Wang, and M. A. Haque. Doping dependence of electrical and thermal conductivity of nanoscale polyaniline thin films. *J. Phys. D-Appl. Phys*, 43(20):205302, 2010.
- [74] Q. Yao, L. D. Chen, X. C. Xu, and C. F. Wang. The high thermoelectric properties of conducting polyaniline with especial submicron-fibre structure. *Chem. Lett*, 34(4):522–523, 2005.
- [75] B. S. Sydulu, S. Palaniappan, and P. Srinivas. Nano fibre polyaniline containing long chain and small molecule dopants and carbon composites for supercapacitor. *Electrochim. Acta*, 95:251–259, 2013.
- [76] Q-Z. Yu, M.-M. Shi, M. Deng, and H-Z. Chen. Morphology and conductivity of polyaniline sub-micron fibers prepared by electrospinning. *Mater. Sci. Eng. B-Adv. Funct. Solid-State Mater*, 150(1):70–76, 2008.
- [77] J. Li, X. Tang, H. Li, Y. Yan, and Q. Zhang. Synthesis and thermoelectric properties of hydrochloric acid-doped polyaniline. *Synth. Met*, 160(11-12):1153–1158, 2010.
- [78] K. Liu, H. Pang, J. Zhang, H. Huang, Q. Liu, and Y. Chu. Synthesis and characterization of a highly stable poly (3,4-ethylenedioxythiophene)-gold nanoparticles composite film and its application to electrochemical dopamine sensors. *RSC Adv*, 4(17):8415–8420, 2014.
- [79] L. Astratine, E. Magner, J. Cassidy, and A. Betts. Electrodeposition and Characterisation of Copolymers Based on Pyrrole and 3,4-Ethylenedioxythiophene in BMIM BF₄ Using a Microcell Configuration. *Electrochim. Acta*, 115:440–448, 2014.
- [80] C-W. Hu, K-M. Lee, R. Vittal, D-J. Yang, and K-C. Ho. A High Contrast Hybrid Electrochromic Device Containing PEDOT, Heptyl Viologen, and Radical Provider TEMPO. *J. Electrochem. Soc*, 157(7):75–78, 2010.
- [81] C. K. Yoon, G. Chitnis, and B. Ziaie. Impact-triggered thermoelectric power generator using phase change material as a heat source. *J. Micromech. Microeng*, 23(11):114004, 2013.
- [82] R. Michalski, A. Sikora, J. Adamus, and A. Marcinek. Mechanistic Aspects of Radiation-Induced Oligomerization of 3,4-Ethylenedioxythiophene in Ionic Liquids. *J. Phys. Chem. A*, 114(43):11552–11559, 2010.

- [83] I. Levesque, X. Gao, D. D. Klug, J. S. Tse, C. I. Ratcliffe, and M. Leclerc. Highly soluble poly(2,7-carbazolenevinylene) for thermoelectrical applications: From theory to experiment. *React. Funct. Polym.*, 65(1-2):23–36, 2005.
- [84] R. Zuzok, A. B. Kaiser, W. Pukacki, and S. Roth. Thermoelectric-power and conductivity of iodine-doped new polyacetylene. *J. Chem. Phys.*, 95(2):1270–1275, 1991.
- [85] K. Bi, A. Weathers, S. Matsushita, M. T. Pettes, M. Goh, K. Akagi, and L. Shi. Iodine doping effects on the lattice thermal conductivity of oxidized polyacetylene nanofibers. *J. Appl. Phys.*, 114(19):194302, 2013.
- [86] A.J. Heeger, N.S. Sariciftci, and E.B. Namdas. *Semiconducting and Metallic Polymers*. Oxford Graduate Texts. OUP Oxford, 2010.
- [87] A. J. Epstein, H. Rommelmann, R. Bigelow, H. W. Gibson, D. M. Hoffmann, and D. B. Tanner. Role of solitons in nearly metallic polyacetylene. *Phys. Rev. Lett.*, 50(23), 1983.
- [88] D. Moses, A. Denenstein, A. Pron, A. J. Heeger, and A. G. Macdiarmid. Specific heats of pure and doped polyacetylene. *Solid State Commun.*, 36(3):219–224, 1980.
- [89] S. Stafstroem and J. L. Bredas. Evolution of the electronic structure of polyacetylene and polythiophene as a function of doped level and lattice conformation. *Phys. Rev. B*, 38(6): 4180–4191, 1988.
- [90] M. Winokur, Y. B. Moon, A. J. Heeger, J. Barker, D. C. Bott, and H. Shirakawa. X-ray scattering from sodium-doped polyacetylene: incommensurate-commensurate and order-disorder transformations. *Phys. Rev. Lett.*, 58(22):2329–2332, 1987.
- [91] R. d’Agosta. Towards a dynamical approach to the calculation of the figure of merit of thermoelectric nanoscale devices. *Phys. Chem. Chem. Phys.*, 15:1758–1765, 2012.
- [92] A. I. Boukai, Y. Bunimovich, J. Tahir-Kheli, J-K. Yu, W. A. Goddard, and J. R. Heath. Silicon nanowires as efficient thermoelectric materials. *Nature*, 451(7175):168–171, 2008.
- [93] K. Gregorczyk and M. Knez. Hybrid nanomaterials through molecular and atomic layer deposition: Top down, bottom up, and in-between approaches to new materials. *Prog. Mater. Sci.*, 75:1–37, 2016.
- [94] I. W. Hamley. Nanotechnology with soft materials. *Angew. Chem.-Int. Edit.*, 42(15): 1692–1712, 2003.
- [95] J. Y. Cheng, C. A. Ross, H. I. Smith, and Edwin L. Thomas. Templated self-assembly of block copolymers: Top-down helps bottom-up. *Adv. Mater.*, 18(19):2505–2521, 2006.
- [96] J. Henzie, J. E. Barton, C. L. Stender, and T. W. Odom. Large-area nanoscale patterning: Chemistry meets fabrication. *Accounts Chem. Res.*, 39(4):249–257, 2006.

- [97] L. J. Guo. Nanoimprint lithography: Methods and material requirements. *Adv. Mater*, 19(4):495–513, 2007.
- [98] C. Mijangos, R. Hernandez, and J. Martin. A review on the progress of polymer nanostructures with modulated morphologies and properties, using nanoporous AAO templates. *Prog. Polym. Sci*, 54-55:148–182, 2016.
- [99] A. García-Barberá, M. Culebras, S. Roig-Sánchez, C. M. Gómez, and A. Cantarero. Three dimensional pedot nanowires network. *Synth. Met.*, 220:208–212, 2016.
- [100] S. Garreau, G. Louarn, J. P. Buisson, G. Froyer, and S. Lefrant. In situ spectroelectrochemical Raman studies of poly(3,4-ethylenedioxythiophene) (PEDT). *Macromolecules*, 32(20):6807–6812, 1999.
- [101] S. Garreau, J. L. Duvail, and G. Louarn. Spectroelectrochemical studies of poly(3,4-ethylenedioxythiophene) in aqueous medium. *Synth. Met*, 125(3):325–329, 2001.
- [102] X. W. Chen and O. Inganäs. Three-step redox in polythiophenes: Evidence from electrochemistry at an ultramicroelectrode. *J. Phys. Chem*, 100(37):15202–15206, 1996.
- [103] A. O. Patil, A. J. Heeger, and F. Wudl. Optical properties of conducting polymers. *Chem. Rev*, 88(1):183–200, 1988.
- [104] M. Scholdt, H. Do, J. Lang, A. Gall, A. Colmann, U. Lemmer, J. D. Koenig, M. Winkler, and H. Boettner. Organic Semiconductors for Thermoelectric Applications. *J. Electron. Mater*, 39(9):1589–1592, 2010.
- [105] F. Yakuphanoglu, B. F. Senkal, and A. Sarac. Electrical conductivity, thermoelectric power, and optical properties of organo-soluble polyaniline organic semiconductor. *J. Electron. Mater.*, 37(6):930–934, 2008.
- [106] N. Kuramoto. Preparation of processable and highly conductive polyaniline and its application as a counter electrode of dye sensitized solar cell. *Abstr. Pap. Am. Chem. Soc*, 243, MAR 25 2012. 11th International Biorelated Polymer Symposium / 243rd National Spring Meeting of the American-Chemical-Society (ACS), San Diego, CA, MAR 25-29, 2012.
- [107] Q. Yao, L. Chen, W. Zhang, S. Liufu, and X. Chen. Enhanced Thermoelectric Performance of Single-Walled Carbon Nanotubes/Polyaniline Hybrid Nanocomposites. *ACS Nano*, 4(4):2445–2451, 2010.
- [108] Y. Du, K. Cai, Z. Qin, S. Z. Shen, and P. S. Casey. Preparation and thermoelectric properties of Bi(2)Te(3)/Polythiophene nanocomposite materials. In Ma, M, editor, *Mechanical, industrial, and manufacturing engineering*, Lecture Notes in Information Technology,

- pages 457–460, 2011. International Conference on Mechanical, Industrial, and Manufacturing Engineering, Melbourne, Australia, JAN 15-16, 2011.
- [109] D. Kim, Y. Kim, K. Choi, J. C. Grunlan, and C. Yu. Improved Thermoelectric Behavior of Nanotube-Filled Polymer Composites with Poly(3,4-ethylenedioxythiophene) Poly(styrenesulfonate). *ACS Nano*, 4(1):513–523, 2010.
- [110] G. P. Moriarty, K. Briggs, B. Stevens, C. Yu, and J. C. Grunlan. Fully organic nanocomposites with high thermoelectric power factors by using a dual-stabilizer preparation. *Energy Technology*, 1(4):265–272, 2013.
- [111] D. Ge, J. Mu, S. Huang, P. Liang, O. U. Gcilitshana, S. Ji, V. Linkov, and W. Shi. Electrochemical synthesis of polypyrrole nanowires in the presence of gelatin. *Synth. Met*, 161(1-2):166–172, 2011.
- [112] H. Randriamahazaka. Electrodeposition mechanisms and electrochemical behavior of poly(3,4-ethylenedithiathiophene). *J. Phys. Chem. C*, 111(12):4553–4560, 2007.
- [113] P. Anjaneyulu, V. Varade, C. S. Suchand Sangeeth, K. P. Ramesh, and R. Menon. Field dependent and disorder-induced nonlinear charge transport in electrochemically doped polypyrrole devices. *J. Phys. D-Appl. Phys*, 47(50):505106, 2014.
- [114] H. J. Ahonen, J. Lukkari, and J. Kankare. n- and p-doped poly(3,4-ethylenedioxythiophene): Two electronically conducting states of the polymer. *Macromolecules*, 33(18):6787–6793, 2000.
- [115] P. Rapta, A. Neudeck, A. Petr, and L. Dunsch. In situ EPR/UV-VIS spectroelectrochemistry of polypyrrole redox cycling. *J. Chem. Soc.-Faraday Trans*, 94(24):3625–3630, 1998.
- [116] J. Wang, K. Cai, and S. Shen. A facile chemical reduction approach for effectively tuning thermoelectric properties of pedot films. *Org. Electron*, 17(0):151 – 158, 2015.
- [117] K. Sato, M. Yamaura, T. Hagiwara, K. Murata, and M. Tokumoto. Study on the electrical-conduction mechanism of polypyrrole films. *Synth. Met*, 40(1):35–48, 1991.
- [118] J. Wang, K. Cai, S. Shen, and J. Yin. Preparation and thermoelectric properties of multi-walled carbon nanotubes/polypyrrole composites. *Synth. Met*, 195:132–136, 2014.
- [119] S. Han, W. Zhai, G. Chen, and X. Wang. Morphology and thermoelectric properties of graphene nanosheets enwrapped with polypyrrole. *RSC Adv*, 4(55):29281–29285, 2014.
- [120] A. Weathers, Z. U. Khan, R. Brooke, D. Evans, M. T. Pettes, J. W. Andreasen, X. Crispin, and L. Shi. Significant electronic thermal transport in the conducting polymer poly(3,4-ethylenedioxythiophene). *Adv. Mater*, 27:2101–2106, 2015.

- [121] J. Liu, X. Wang, D. Li, N. E. Coates, R. A. Segalman, and D. G. Cahill. Thermal conductivity and elastic constants of pedot:pss with high electrical conductivity. *Macromolecules*, 48:585–591, 2015.
- [122] J. Wu, Y. Sun, W. B. Pei, L. Muang, W. Xu, and Q. Zhang. Polypyrrole nanotube film for flexible thermoelectric application. *Synth. Met.*, 196:173–177, 2014.
- [123] C-H. Wu, T-M. Don, and W-Y. Chiu. Characterization and conversion determination of stable PEDOT latex nanoparticles synthesized by emulsion polymerization. *Polymer*, 52(6):1375–1384, 2011.
- [124] C-H. Wu, W-Y. Chiu, and T-M. Don. Conductive composite particles synthesized via pickering emulsion polymerization using conductive latex of poly(3,4-ethylenedioxythiophene) (PEDOT) as stabilizer. *Polymer*, 53(5):1086–1092, 2012.
- [125] T. Chen, J. Qiu, K. Zhu, J. Li, J. Wang, S. Li, and X. Wang. Ultra high permittivity and significantly enhanced electric field induced strain in PEDOT:PSS-RGO-PU intelligent shape-changing electro-active polymers. *RSC Adv*, 4(109):64061–64067, 2014.
- [126] L-D. Zhao, V. P. Dravid, and M. i G. Kanatzidis. The panoscopic approach to high performance thermoelectrics. *Energy Environ. Sci*, 7(1):251–268, 2014.
- [127] V. Potula and W. Kaye. The impact of menopause and lifestyle factors on blood and bone lead levels among female former smelter workers: The Bunker Hill study. *Am. J. Ind. Med*, 49(3):143–152, 2006.
- [128] C. Cros, M. Pouchard, and P. Hagemuller. Sur une nouvelle famille de clathrates minéraux isotopes des hydrates de gaz et de liquides. interprétation des résultats obtenus. *J. Solid State Chem*, 2(4):570 – 581, 1970.
- [129] J. S. Kasper, P. Hagemuller, M. Pouchard, and C. Cros. Clathrate structure of silicon AnaNAXSII36 (X11). *Science*, 150(3704):1713, 1965.
- [130] M. Beekman and G. S. Nolas. *Synthetic Approaches to Intermetallic Clathrates*, pages 65–90. Springer Netherlands, Dordrecht, 2014.
- [131] A. Shakouri. Recent Developments in Semiconductor Thermoelectric Physics and Materials. In D. R. Clarke and P. Fratzl , editor, *Ann. Rev. Mater. Res*, volume 41 of *Annual Review of Materials Research*, pages 399–431. 2011.
- [132] G. P. Meisner. Superconductivity and magnetic order in ternary rare-earth transition metal phosphides. *Physica B*, 108(1-3):763–764, 1981.
- [133] M. E. Danebrock, C. B. H. Evers, and W. Jeitschko. Magnetic properties of alkaline earth and lanthanoid iron antimonides AFe_4Sb_{12} ($A=Ca, Sr, Ba, La-Nd, Sm, Eu$) with the $LaFe_4P_{12}$ structure. *J. Phys. Chem. Solids*, 57(4):381–387, 1996.

- [134] D. A. Gajewski, N. R. Dilley, E. D. Bauer, E. J. Freeman, R. Chau, M. B. Maple, D. Mandrus, B. C. Sales, and A. H. Lacerda. Heavy fermion behaviour of the cerium-filled skutterudites $\text{CeFe}_4\text{Sb}_{12}$ and $\text{Ce}_{0.9}\text{Fe}_3\text{CoSb}_{12}$. *J. Phys.-Condes. Matter*, 10(31) : 6973 – 6985, 1998.
- [135] N. Takeda and M. Ishikawa. The effect of La substitution and magnetic field on non-Fermi-liquid behaviour in $\text{CeRu}_4\text{Sb}_{12}$. *J. Phys.-Condes. Matter*, 13(26):5971–5980, 2001.
- [136] E. Bauer, A. Galatanu, H. Michor, G. Hilscher, P. Rogl, P. Boulet, and H. Noel. Physical properties of skutterudites $\text{Yb}_x\text{M}_4\text{Sb}_{12}$, $\text{M} = \text{Fe, Co, Rh, Ir}$. *Eur. Phys. J. B*, 14(3):483–493, 2000.
- [137] I. Terasaki, Y. Sasago, and K. Uchinokura. Large thermoelectric power in NaCo_2O_4 single crystals. *Phys. Rev. B*, 56:R12685–R12687, 1997.
- [138] Y. Miyazaki. Crystal structure and thermoelectric properties of the misfit-layered cobalt oxides. *Solid State Ion*, 172(1):463–467, 2004.
- [139] A. Nag and V. Shubha. Oxide thermoelectric materials: A structure–property relationship. *J. Electron. Mater*, 43(4):962–977, 2014.
- [140] K. Berggold, M. Kriener, C. Zobel, A. Reichl, M. Reuther, R. Müller, A. Freimuth, and T. Lorenz. Thermal conductivity, thermopower, and figure of merit of $\text{La}_{1-x}\text{Sr}_x\text{Co}_3$. *Phys. Rev. B*, 72:155116, 2005.
- [141] A. Inagoya, D. Sawaki, Y. Horiuchi, S. Urata, R. Funahashi, and I. Terasaki. Thermoelectric module made of perovskite cobalt oxides with large thermopower. *J. Appl. Phys*, 110(12), 2011.
- [142] M. Culebras, R. I. Toran, C. M. Gomez, and A. Cantarero. $\text{La}_{1-x}\text{Ca}_x\text{MnO}_3$ semiconducting nanostructures: morphology and thermoelectric properties. *Nanoscale Res. Lett*, 9, 2014.
- [143] T. Shimura, T. Hayashi, Y. Inaguma, and M. Itoh. Magnetic and electrical properties of $\text{La}_y\text{A}_x\text{Mn}_w\text{O}_3$ ($\text{A}=\text{Na, K, Rb, and Sr}$) with perovskite-type structure. *J. Solid State Chem*, 124(2):250–263, 1996.
- [144] X. Zhu, J. Wang, Z. Zhang, J. Zhu, S. Zhou, Z. Liu, and N. Ming. Perovskite nanoparticles and nanowires: Microwave-hydrothermal synthesis and structural characterization by high-resolution transmission electron microscopy. *J. Am. Ceram. Soc*, 91(8):2683–2689, 2008.

- [145] Ai. Wang, Y. Zeng, L. Han, C. Ding, L. Cao, and R. Li. Highly dispersed spherical $\text{Bi}_{3.25}\text{La}_{0.75}\text{Ti}_3\text{O}_{12}$ nanocrystals via topotactic crystallization of aggregation-free gel particles from an effective inverse miniemulsion sol-gel approach. *J. Nanopart. Res*, 17(9): 1–11, 2015.
- [146] F. Heusler. Über manganbronze und über die synthese magnetisierbarer legierungen aus unmagnetischen metallen. *Angew. Chem*, 17(9):260–264, 1904.
- [147] F. Casper, T. Graf, S. Chadov, B. Balke, and C. Felser. Half-heusler compounds: novel materials for energy and spintronic applications. *Semicond. Sci. Technol*, 27(6):063001, 2012.
- [148] C. Evangeli, K. Gillemot, M. Leary, E. and Teresa G., G. Rubio-Bollinger, C. J. Lambert, and N. Agrait. Engineering the Thermopower of C-60 Molecular Junctions. *Nano Lett.*, 13(5):2141–2145, 2013.
- [149] A. Fugallo, G. and Cepellotti, L. Paulatto, M. Lazzeri, N. Marzari, and F. Mauri. Thermal Conductivity of Graphene and Graphite: Collective Excitations and Mean Free Paths. *Nano Lett*, 14(11):6109–6114, 2014.
- [150] C. J. Vineis, A. Shakouri, A. Majumdar, and M. G. Kanatzidis. Nanostructured Thermoelectrics: Big Efficiency Gains from Small Features. *Adv. Mater*, 22(36):3970–3980, 2010.
- [151] W. Takeuchi, M. Ura, M. Hiramatsu, Y. Tokuda, H. Kano, and M. Hori. Electrical conduction control of carbon nanowalls. *Appl. Phys. Lett*, 92(21), 2008.
- [152] G. Chen W. Liu, X. Yan and Z. Ren. Recent Advances in thermoelectric nanocomposites. *Nano Energy*, 1(-):42–56, 2012.
- [153] T. Peczalski. Effect of hydrogen on the electrical resistivity of carbon. *Phys. Rev*, 11(5): 363–371, 1918.
- [154] D. I. Jones and A. D. Stewart. Properties of hydrogenated amorphous-carbon films and the effects of doping. *Philos. Mag. B-Phys. Condens. Matter Stat. Mech. Electron. Opt. Magn. Prop*, 46(5):423–434, 1982.
- [155] O. A. Williams, M. D. Whitfield, R. B. Jackman, J. S. Foord, J. E. Butler, and C. E. Nebel. Carrier generation within the surface region of hydrogenated thin film polycrystalline diamond. *Diam. Relat. Mat*, 10(3-7, SI):423–428, 2001.
- [156] T. X. Nguyen and S. K. Bhatia. Characterization of heat-treated porous carbons using argon adsorption. *Carbon*, 44(4):646–652, 2006.

- [157] G. Gundiah, A. Govindaraj, N. Rajalakshmi, K. S. Dhathathreyan, and C. N. R. Rao. Hydrogen storage in carbon nanotubes and related materials. *J. Mater. Chem*, 13(2): 209–213, 2003.
- [158] A. D. Lueking, C. E. B. Clifford, and D. L. Narayanan. Induced defects in carbonaceous materials for hydrogen storage. *Abstr. Pap. Am. Chem. Soc*, 228(Part 1):678, 2004.
- [159] B. Safibonab, A. Reyhani, A. Nozad Golikand, S. Z. Mortazavi, S. Mirershadi, and M. Ghoranneviss. Improving the surface properties of multi-walled carbon nanotubes after irradiation with gamma rays. *Appl. Surf. Sci*, 258(2):766–773, 2011.
- [160] D. H. Galvan, I. L. Garzon, P. Santiago, and M. Jose-Yacaman. Structural changes and electronic properties of gamma irradiated graphite: An experimental and theoretical study. *Fullerene Sci. Technol*, 6(5):867–883, 1998.
- [161] J. V. Sharp and S. G. Burnay. Effect of gamma-irradiation on carbon-fiber properties. *Radiat. Eff. Defects Solids*, 22(1):45–48, 1974.
- [162] V. Skakalova, U. Dettlaff-Weglikowska, and S. Roth. Gamma-irradiated and functionalized single wall nanotubes. *Diam. Relat. Mat*, 13(2):296–298, 2004.
- [163] D. Kleut, S. Jovanovic, Z. Markovic, D. Kepic, D. Totic, N. Romcevic, M. Marinovic-Cincovic, M. Dramicanin, I. Holclajtner-Antunovic, V. Pavlovic, G. Drazic, M. Milosavljevic, and B. Todorovic Markovic. Comparison of structural properties of pristine and gamma irradiated single-wall carbon nanotubes: Effects of medium and irradiation dose. *Mater. Charact*, 72:37–45, 2012.
- [164] S. M. Lee, K. H. An, Y. H. Lee, G. Seifert, and T. Frauenheim. A hydrogen storage mechanism in single-walled carbon nanotubes. *J. Am. Chem. Soc*, 123(21):5059–5063, 2001.
- [165] L. D. Hicks and M. S. Dresselhaus. Effect of quantum-well structures on the thermoelectric figure of merit. *Phys. Rev. B*, 47(19):12727–12731, 1993.
- [166] Y. M. Lin, X. Z. Sun, and M. S. Dresselhaus. Theoretical investigation of thermoelectric transport properties of cylindrical Bi nanowires. *Phys. Rev. B*, 62(7):4610–4623, 2000.
- [167] Y. Wang and H. J. Fan. Improved Thermoelectric Properties of $\text{La}_{1-x}\text{Sr}_x\text{CoO}_3$ Nanowires. *J. Phys. Chem. C*, 114(32):13947–13953, 2010.
- [168] T. Zhang, C. G. Jin, T. Qian, X. L. Lu, J. M. Bai, and X. G. Li. Hydrothermal synthesis of single-crystalline $\text{La}_{0.5}\text{Ca}_{0.5}\text{MnO}_3$ nanowires at low temperature. *J. Mater. Chem*, 14(18):2787–2789, 2004.

- [169] J. Deng, L. Zhang, H. Dai, H. He, and C. T. Au. Single-crystalline $\text{La}_{0.6}\text{Sr}_{0.4}\text{CoO}_{3-\delta}$ nanowires/nanorods derived hydrothermally without the use of a template: Catalysts highly active for toluene complete oxidation. *Catal. Lett.*, 123(3-4):294–300, 2008.
- [170] R. Mahendiran, S. K. Tiwary, A. K. Raychaudhuri, T. V. Ramakrishnan, R. Mahesh, N. Rangavittal, and C. N. R. Rao. Structure, electron-transport properties, and giant magnetoresistance of hole-doped LaMnO_3 systems. *Phys. Rev. B*, 53(6):3348–3358, 1996.
- [171] J. Mizusaki, Y. Yonemura, H. Kamata, K. Ohyama, N. Mori, H. Takai, H. Tagawa, M. Dokiya, K. Naraya, T. Sasamoto, H. Inaba, and T. Hashimoto. Electronic conductivity, Seebeck coefficient, defect and electronic structure of nonstoichiometric $\text{La}_{1-x}\text{Sr}_x\text{MnO}_3$. *Solid State Ion*, 132(3-4):167–180, 2000.
- [172] X. Y. Huang, Y. Miyazaki, and T. Kajitani. High temperature thermoelectric properties of $\text{Ca}_{1-x}\text{Bi}_x\text{Mn}_{1-y}\text{V}_y\text{O}_{3-\delta}$ ($0 \leq x = y \leq 0.08$). *Sol. State Commun*, 145(3):132–136, 2008.
- [173] R. Koc and H. U. Anderson. Electrical conductivity and seebeck coefficient of $(\text{La,Ca})(\text{Cr,Co})\text{O}_3$. *J. Mater. Sci.*, 27(20):5477–5482, 1992.
- [174] J. H. Kuo, H. U. Anderson, and D. M. Sparlin. Oxidation reduction behavior of undoped and sr-doped LaMnO_3 - defect structure, electrical-conductivity, and thermoelectric power. *J. Solid State Chem*, 87(1):55–63, 1990.
- [175] C. Ritter, M. R. Ibarra, J. M. DeTeresa, P. A. Algarabel, C. Marquina, J. Blasco, J. Garcia, S. Oseroff, and S. W. Cheong. Influence of oxygen content on the structural, magneto-transport, and magnetic properties of $\text{LaMnO}_{3+\delta}$. *Phys. Rev. B*, 56(14), 1997.
- [176] Z. Zeng, M. Greenblatt, and M. Croft. Large magnetoresistance in antiferromagnetic $\text{CaMnO}_{3-\delta}$. *Phys. Rev. B*, 59(13) : 8784–8788, 1999.
- [177] J. J. Neumeier and J. L. Cohn. Possible signatures of magnetic phase segregation in electron-doped antiferromagnetic CaMnO_3 . *Phys. Rev. B*, 61(21):14319–14322, 2000.
- [178] C. O. Yoon, J. H. Kim, H. K. Sung, and H. Lee. Electrical conductivity and thermopower of phosphoric acid doped polyaniline. *Synth. Met*, 84(1-3):789–790, 1997.
- [179] T. Okuda, K. Nakanishi, S. Miyasaka, and Y. Tokura. Large thermoelectric response of metallic perovskites: $\text{Sr}_{1-x}\text{La}_x\text{TiO}_3$ ($0 < x < 0.1$). *Phys. Rev. B*, 63:113104, 2001.
- [180] E. Papirer, S. LI, H. Balard, and J. Jagiello. Surface energy and adsorption energy distribution measurements on some carbon blacks. *Carbon*, 29(8):1135–1143, 1991.
- [181] A. Anson, J. Jagiello, J. B. Parra, M. L. Sanjuan, A. M. Benito, WK Maser, and MT Martinez. Porosity, surface area, surface energy, and hydrogen adsorption in nanostructured carbons. *J. Phys. Chem. B*, 108(40):15820–15826, 2004.

- [182] V. Jimenez, A. Ramirez-Lucas, P. Sanchez, J. L. Valverde, and A. Romero. Hydrogen storage in different carbon materials: Influence of the porosity development by chemical activation. *Appl. Surf. Sci.*, 258(7):2498–2509, 2012.
- [183] Z. Xu, L. Chen, L. Liu, X. Wu, and L. Chen. Structural changes in multi-walled carbon nanotubes caused by gamma-ray irradiation. *Carbon*, 49(1):350–351, 2011.
- [184] C. Marliere, P. Poncharal, L. Vaccarini, and A. Zahab. Effect of gas adsorption on the electrical properties of single walled carbon nanotubes mats. In Sullivan, J. P. and Robertson, J. and Zhou, O. and Allen, T. B. and Coll, B. F., editor, *Amorphous and nanostructured carbon*, volume 593 of *Materials research society symposium proceedings*, pages 173–177, 2000.
- [185] B. Campbell and A. Mainwood. Radiation damage of diamond by electron and gamma irradiation. *Phys. Status Solidi A-Appl. Res.*, 181(1):99–107, 2000.
- [186] M. A. Obolensky, A. V. Basteev, and L. A. Bazyma. Hydrogen Storage in Irradiated Low-Dimensional Structures. *Fuller. Nanotub. Carbon Nanostruct.*, 19(1-2):133–136, 2011.
- [187] A. Madroñero and J. Robla and J. García-Hierro and M. S. Martín-González and P. Díaz and A. López. Variation of the Seebeck coefficient with hydrogen content in carbon microfilaments. *J. Mater. Sci: Mater. Electron*, 23:1470–1476, 2012.
- [188] A. Braun, M. Bartsch, B. Schnyder, R. Kotz, O. Haas, H. G. Haubold, and G. Goerigk. X-ray scattering and adsorption studies of thermally oxidized glassy carbon. *J. Non-Cryst. Solids*, 260(1-2):1–14, 1999.
- [189] B.G. Hyde M. O’Keeffe. Crystal structures; I. Patterns and Symmetry. *Mineralogical Society of América*, Whashington DC , 1996.
- [190] S. Rodrigues, I. Suarez-Ruiz, M. Marques, I. Camean, and D. Flores. Microstructural evolution of high temperature treated anthracites of different rank. *Int. J. Coal Geol.*, 87(3-4):204–211, 2011.
- [191] T. Saito and Y. Sasaki. Effect of high-temperature neutron-irradiation on the crystallites of graphite materials. *Carbon*, 18(6):407–411, 1980.
- [192] J. C. Bokros and R. J. Price. Radiation-induced dimensional changes in pyrolytic carbons deposited in a fluidized bed. *Carbon*, 4(3):441–449, 1966.
- [193] J. C. Bokros and A. S. Schwartz. A model to describe neutron-induced dimensional changes in pyrolytic carbon. *Carbon*, 5(5):481–493, 1967.
- [194] A. P. Goncalves, E. B. Lopes, G. Delaizir, J. B. Vaney, B. Lenoir, A. Piarristeguy, A. Pradel, J. Monnier, P. Ochin, and C. Godart. Semiconducting glasses: A new class of thermoelectric materials. *J. Solid State Chem.*, 193(SI):26–30, 2012.

- [195] M. Meyyappan. *Carbon nanotubes. Science and applications*. CRC Press, Florida, 2005.
- [196] C. Yu, Yeon S. Kim, D. Kim, and J. C. Grunlan. Thermoelectric Behavior of Segregated-Network Polymer Nanocomposites. *Nano Lett*, 9(3):1283, 2009.
- [197] C. Yu, K. Choi, L. Yin, and J. C. Grunlan. Light-Weight Flexible Carbon Nanotube Based Organic Composites with Large Thermoelectric Power Factors. *ACS Nano*, 5(10):7885–7892, 2011.
- [198] J. Chen, X. Gui, Z. Wang, Z. Li, R. Xiang, K. Wang, D. Wu, X. Xia, Y. Zhou, Q. Wang, Z. Tang, and L. Chen. Superlow Thermal Conductivity 3D Carbon Nanotube Network for Thermoelectric Applications. *ACS Appl. Mater. Interfaces*, 4(1):81–86, 2012.
- [199] C. Bounioux, P. Diaz-Chao, M. Campoy-Quiles, M. Martin-Gonzalez, A. R. Goni, R.I Yerushalmi-Rozene, and C. Mueller. Thermoelectric composites of poly(3-hexylthiophene) and carbon nanotubes with a large power factor. *Energy Environ. Sci*, 6(3):918–925, 2013.
- [200] M. Rastegaralam, M. Piao, G. Kim, U. Dettlaff-Weglikowska, and S. Roth. Influence of chemical treatment on the electrical conductivity and thermopower of expanded graphite foils. volume 10 of *Physica Status Solidi C-Current Topics in Solid State Physics*, pages 1183–1187, 2013.
- [201] L. Wang, D. Wang, G. Zhu, J. Li, and F. Pan. Thermoelectric properties of conducting polyaniline/graphite composites. *Mater. Lett*, 65(7):1086–1088, 2011.
- [202] Y. Du, S. Z. Shen, W. Yang, R. Donelson, K. Cai, and P. S. Casey. Simultaneous increase in conductivity and Seebeck coefficient in a polyaniline/graphene nanosheets thermoelectric nanocomposite. *Synth. Met*, 161(23-24):2688–2692, 2012.
- [203] Y. Lu, Y. Song, and F. Wang. Thermoelectric properties of graphene nanosheets-modified polyaniline hybrid nanocomposites by an in situ chemical polymerization. *Mater. Chem. Phys*, 138(1):238–244, 2013.
- [204] B. Abad, I. Alda, P. Diaz-Chao, H. Kawakami, A. Almarza, D. Amantia, D. Gutierrez, L. Aubouy, and M. Martin-Gonzalez. Improved power factor of polyaniline nanocomposites with exfoliated graphene nanoplatelets (GNPs). *J. Mater. Chem. A*, 1(35):10450–10457, 2013.
- [205] G. H. Kim, D. H. Hwang, and S. I Woo. Thermoelectric properties of nanocomposite thin films prepared with poly(3,4-ethylenedioxythiophene) poly(styrenesulfonate) and graphene. *Phys. Chem. Chem. Phys*, 14(10):3530–3536, 2012.
- [206] M. Culebras, C. M. Gomez, and A. Cantarero. Thermoelectric measurements of PEDOT:PSS/expanded graphite composites. *J. Mater. Sci.*, 48(7):2855–2860, 2013.

- [207] K. Zhang, Y. Zhang, and S. Wang. Enhancing thermoelectric properties of organic composites through hierarchical nanostructures. *Sci Rep*, 3: 3448, 2013.
- [208] M. Piao, G. Kim, Gary P. Kennedy, S. Roth, and U. Dettlaff-Weglikowska. Preparation and characterization of expanded graphite polymer composite films for thermoelectric applications. *Phys. Status Solidi B-Basic Solid State Phys*, 250(12):2529–2534, 2013.
- [209] R. Gangopadhyay, A. De, and S. Das. Transport properties of polypyrrole-ferric oxide conducting nanocomposites. *J. Appl. Phys*, 87(5):2363–2371, 2000.
- [210] X. B. Zhao, S. H. Hu, M. J. Zhao, and T. J. Zhu. Thermoelectric properties of $\text{Bi}_{0.5}\text{Sb}_{1.5}\text{Te}$ polyaniline hybrids prepared by mechanical blending. *Mater. Lett*, 52(3): 147–149, 2002.
- [211] H. Liu, J. Y. Wang, X. B. Hu, R. I. Boughton, S. R. Zhao, Q. Li, and M. H. Jiang. Structure and electronic transport properties of polyaniline $\text{NaFe}_4\text{P}_{12}$ composite. *Chem. Phys. Lett*, 352(3-4):185–190, 2002.
- [212] H. Song, C. Liu, J. Xu, Q. Jiang, and H. Shi. Fabrication of a layered nanostructure PEDOT:PSS/SWCNTs composite and its thermoelectric performance. *RSC Adv*, 3(44): 22065–22071, 2013.
- [213] Q. Wang, Q. Yao, J. Chang, and L. Chen. Enhanced thermoelectric properties of CNT/PANI composite nanofibers by highly orienting the arrangement of polymer chains. *J. Mater. Chem*, 22(34):17612–17618, 2012.
- [214] H. Yan and K. Kou. Enhanced thermoelectric properties in polyaniline composites with polyaniline-coated carbon nanotubes. *J. Mater. Sci*, 49(3):1222–1228, 2014.
- [215] L. Wang, X. Jia, D. Wang, G. Zhu, and J. Li. Preparation and thermoelectric properties of polythiophene/multiwalled carbon nanotube composites. *Synth. Met*, 181:79–85, 2013.
- [216] K. Kato, H. Hagino, and K. Miyazaki. Fabrication of bismuth telluride thermoelectric films containing conductive polymers using a printing method. *J. Electron. Mater*, 42(7): 1313–1318, 2013.
- [217] K. C. See, J. P. Feser, C. E. Chen, A. Majumdar, J. J. Urban, and R. A. Segalman. Water-Processable Polymer-Nanocrystal Hybrids for Thermoelectrics. *Nano Lett*, 10(11):4664–4667, 2010.
- [218] N. E. Coates, S. K. Yee, B. McCulloch, K. C. See, A. Majumdar, R. A. Segalman, and J. J. Urban. Effect of Interfacial Properties on Polymer-Nanocrystal Thermoelectric Transport. *Adv. Mater*, 25(11):1629–1633, 2013.

- [219] M. He, J. Ge, Z. Lin, X. Feng, X. Wang, H. Lu, Y. Yang, and F. Qiu. Thermopower enhancement in conducting polymer nanocomposites via carrier energy scattering at the organic-inorganic semiconductor interface. *Energy Environ. Sci*, 5(8):8351–8358, 2012.
- [220] M. Stanford, H. Wang, I. Ivanov, and B. Hu. High Seebeck effects from conducting polymer: Poly(3,4-ethylenedioxythiophene): poly(styrenesulfonate) based thin-film device with hybrid metal/polymer/metal architecture. *Appl. Phys. Lett*, 101(17):173304, 2012.
- [221] A. Yoshida and N. Toshima. Gold nanoparticle and gold nanorod embedded PEDOT:PSS thin films as organic thermoelectric materials. *J. Electron. Mater.*, 43(6):1492–1497, 2014.
- [222] A. Nohales, D. Lopez, M. Culebras, and C. M. Gomez. Rheological study of gel phenomena during epoxide network formation in the presence of sepiolite. *Polym. Int*, 62(3):397–405, 2013.
- [223] S. W. Kim, T. Kim, Y. S. Kim, H. S. Choi, H. J. Lim, S. J. Yang, and C. R. Park. Surface modifications for the effective dispersion of carbon nanotubes in solvents and polymers. *Carbon*, 50(1):3–33, 2012.
- [224] S. Kango, S. Kalia, A. Celli, J. Njuguna, Y. Habibi, and R. Kumar. Surface modification of inorganic nanoparticles for development of organic-inorganic nanocomposites-A review. *Prog. Polym. Sci*, 38(8):1232–1261, 2013.
- [225] H-E. Yin, C-H. Wu, K-S. Kuo, W-Y. Chiu, and H-J. Tai. Innovative elastic and flexible conductive PEDOT:PSS composite films prepared by introducing soft latexes. *J. Mater. Chem*, 22(9):3800–3810, 2012.
- [226] X. Zhang, C. Li, and Y. Luo. Aligned/Unaligned Conducting Polymer Cryogels with Three-Dimensional Macroporous Architectures from Ice-Segregation-Induced Self-Assembly of PEDOT-PSS. *Langmuir*, 27(5):1915–1923, 2011.
- [227] M. Fang, K. Wang, H. Lu, Y. Yang, and S. Nutt. Covalent polymer functionalization of graphene nanosheets and mechanical properties of composites. *J. Mater. Chem*, 19(38):7098–7105, 2009.
- [228] S. Konwer, J. Maiti, and S. K. Dolui. Preparation and optical/electrical/electrochemical properties of expanded graphite-filled polypyrrole nanocomposite. *Mater. Chem. Phys*, 128(1-2):283–290, 2011.
- [229] S. R. Dhakate, S. Sharma, M. Borah, R. B. Mathur, and T. L. Dhami. Expanded graphite-based electrically conductive composites as bipolar plate for PEM fuel cell. *Int. J. Hydrog. Energy*, 33(23):7146–7152, 2008.

- [230] A. Celzard, J. F. Mareche, G. Furdin, and S. Puricelli. Electrical conductivity of anisotropic expanded graphite-based monoliths. *J. Phys. D-Appl. Phys.*, 33(23):3094–3101, 2000.
- [231] P. Svoboda, R. Theravalappil, S. Poongavalappil, J. Vilcakova, D. Svobodova, P. Mokrejs, and A. Blaha. A study on electrical and thermal conductivities of ethylene-octene copolymer/expandable graphite composites. *Polym. Eng. Sci.*, 52(6):1241–1249, 2012.
- [232] M. Saleemi, M. S. Toprak, S. Li, M. Johnsson, and M. Muhammed. Synthesis, processing, and thermoelectric properties of bulk nanostructured bismuth telluride (Bi_2Te_3). *J. Mater. Chem.*, 22(2):725–730, 2012.
- [233] G. Greczynski, T. Kugler, and W. R. Salaneck. Characterization of the PEDOT-PSS system by means of X-ray and ultraviolet photoelectron spectroscopy. *Thin Solid Films*, 354(1-2):129–135, 1999.
- [234] R. Kowalik, D. Kutyla, K. Mech, T. Tokarski, and P. Zabinski. Electrowinning of Tellurium from acidic solutions. *Arch. Metall. Mater.*, 60:591–596, 2015.
- [235] B. Abad, M. Rull-Bravo, S. L. Hodson, X. Xu, and M. Martin-Gonzalez. Thermoelectric properties of electrodeposited tellurium films and the sodium lignosulfonate effect. *Electrochim. Acta*, 169:37–45, 2015.
- [236] C. Rodríguez-Fernández, C. V. Manzano, A. H. Romero, J. Martín, M. Martín-González, M. Morais de Lima Jr, and A. Cantarero. The fingerprint of te-rich and stoichiometric bi_2te_3 nanowires by raman spectroscopy. *Nanotechnology*, 27(7):075706, 2016.
- [237] R. A. Nunes, V. C. Costa, V. M. de Araujo Calado, and J. R. Tavares. Wear, Friction, and Microhardness of a Thermal Sprayed PET - Poly (Ethylene Terephthalate) Coating. *Mater. Res.-Ibero-am. J. Mater.*, 12(2):121–125, 2009.
- [238] I. N. Strain, Q. Wu, A. M. Pourrahimi, M. S. Hedenqvist, R. T. Olsson, and R. L. Anderson. Electrospinning of recycled PET to generate tough mesomorphic fib membranes for smoke filtration. *J. Mater. Chem. A*, 3(4):1632–1640, 2015.
- [239] M. Culebras, A. M. Lopez, C. M. Gomez, and A. Cantarero. Thermal sensor based on a polymer nanofilm. *Sens. Actuator A-Phys*, 239:161–165, 2016.
- [240] S. LeBlanc, S. K. Yee, M. L. Scullin, C. Dames, and K. E. Goodson. Material and manufacturing cost considerations for thermoelectrics. *Renew. Sust. Energ. Rev.*, 32:313–327, 2014.

- [241] N. Toshima, K. Oshima, H. Anno, T. Nishinaka, S. Ichikawa, A. Iwata, and Y. Shiraishi. Novel Hybrid Organic Thermoelectric Materials: Three-Component Hybrid Films Consisting of a Nanoparticle Polymer Complex, Carbon Nanotubes, and Vinyl Polymer. *Adv. Mater.*, 27(13):2246, 2015.
- [242] Q. Wei, M. Mukaida, K. Kirihara, Y. Naitoh, and T. Ishida. Polymer thermoelectric modules screen-printed on paper. *RSC Adv*, 4(54):28802–28806, 2014.
- [243] Y. Chen, Y. Zhao, and Z. Liang. Solution processed organic thermoelectrics: towards flexible thermoelectric modules. *Energy Environ. Sci*, 8(2):401–422, 2015.
- [244] C. Yu, A. Murali, K. Choi, and Y. Ryu. Air-stable fabric thermoelectric modules made of N- and P-type carbon nanotubes. *Energy Environ. Sci*, 5(11):9481–9486, 2012.
- [245] J. Gao, C. Liu, L. Miao, X. Wang, C. Li, R. Huang, Y. Chen, and S. Tanemura. Power factor enhancement via simultaneous improvement of electrical conductivity and Seebeck coefficient in tellurium nanowires/reduced graphene oxide flexible thermoelectric films. *Synth. Met.*, 210(B):342–351, 2015.
- [246] B. Kim, H. Shin, T. Park, H. Lim, and E. Kim. NIR-Sensitive Poly(3,4-ethylenedioxy-selenophene) Derivatives for Transparent Photo-Thermo-Electric Converters. *Adv. Mater.*, 25(38):5483–5489, 2013.
- [247] C. Liu, F. Jiang, M. Huang, R. Yue, B. Lu, J. Xu, and G. Liu. Thermoelectric Performance of Poly(3,4-Ethylenedioxy-thiophene)/Poly(Styrenesulfonate) Pellets and Films. *J. Electron. Mater.*, 40(5):648–651, 2011.
- [248] I. Yamaguchi and T. Nagano. Synthesis, chemical, and thermoelectric properties of n-type -conjugated polymer composed of 1,2,4-triazole and pyridine rings and its metal complexes. *J. Appl. Polym. Sci*, 131(4):39928/1–39928/7.
- [249] Y. Sun, P. Sheng, C. Di, F. Jiao, W. Xu, D. Qiu, and D. Zhu. Organic Thermoelectric Materials and Devices Based on p- and n-Type Poly(metal 1,1,2,2-ethenetetrathiolate)s. *Adv. Mater.*, 24(7):932–937, 2012.
- [250] C. A. Hewitt, A. B. Kaiser, S. Roth, M. Craps, R. Czerw, and D. L. Carroll. Multilayered Carbon Nanotube/Polymer Composite Based Thermoelectric Fabrics. *Nano Lett.*, 12(3):1307–1310, 2012.
- [251] G. Wu, C. Gao, G. Chen, X. Wang, and H. Wang. High-performance organic thermoelectric modules based on flexible films of a novel n-type single-walled carbon nanotube. *J. Mater. Chem. A*.

- [252] C. J. An, Y. H. Kang, A-Y. Lee, K-S. Jang, Y. Jeong, and S-Y. Cho. Foldable Thermoelectric Materials: Improvement of the Thermoelectric Performance of Directly Spun CNT Webs by Individual Control of Electrical and Thermal Conductivity. *ACS Appl. Mater. Interfaces*, 8(34):22142–22150, 2016.
- [253] H. Wang, Q. Hao, X. Yang, L. Lu, and X. Wang. Graphene oxide doped polyaniline for supercapacitors. *Electrochem. Commun*, 11(6):1158–1161, 2009.
- [254] K. Wang, P. Zhao, X. Zhou, H. Wu, and Z. Wei. Flexible supercapacitors based on cloth-supported electrodes of conducting polymer nanowire array/SWCNT composites. *J. Mater. Chem*, 21(41):16373–16378, 2011.
- [255] Z. Zhao, G. F. Richardson, Q. Meng, S. Zhu, H-C. Kuan, and J. Ma. PEDOT-based composites as electrode materials for supercapacitors. *Nanotechnology*, 27(4):042001, 2016.
- [256] L. Chen, Y. Liu, Y. Zhao, N. Chen, and L. Qu. Graphene-based fibers for supercapacitor applications. *Nanotechnology*, 27(3):032001, 2016.
- [257] R. Liu, J. Duay, and S. B. Lee. Heterogeneous nanostructured electrode materials for electrochemical energy storage. *Chem. Commun*, 47(5):1384–1404, 2011.
- [258] S. W. Finefrock, X. Zhu, Y. Sun, and Y. Wu. Flexible prototype thermoelectric devices based on Ag₂Te and PEDOT:PSS coated nylon fibre. *Nanoscale*, 7(13):5598–5602, 2015.

Abbreviations

AAOM	Anodized alumina membranes
AFM	Atomic force microscopy
APS	Ammonium persulfate
BTFMSI	1- ethyl- 3-methylimidazolium bis(trifluoromethylsulfonyl) imide
CNT	Carbon nanotube
CTAB	Cetyltrimethylammonium bromide
DMSO	Dimethylsulfoxide
DOS	Density of states
DSC	Differential scanning calorimetry
DTA	Diethylenetriamine
DTAB	Decyltrimethylammonium bromide
DWCNT	Double-wall carbon nanotube
EDOT	3,4-ethylenedioxythiophene
EG	Expanded graphite
Fe-Tos	Iron(III) p-toluenesulfonate
FTIR	Fourier transform infrared spectroscopy
GIC	Graphite intercalated compound
GNP	Graphene nanoplatelets
GPHS-RTG	General-Purpose Heat Source-Radioisotope Thermoelectric Generator
ICP	Intrinsically conductive polymers
LBL	Layer by layer
MDSC	Modulated differential scanning calorimetry
MWCNT	Multi-wall carbon nanotube
NCCO	NdCaCoO perovskites
NMR	Nuclear magnetic resonance spectroscopy

OECCD	Open electrode charge-coupled device
P3HT	Poly(3-hexylthiophene-2,5-diyl)
PANI	Polyaniline
PEDOT	Poly(3,4-ethylenedioxythiophene)
PEI	Polyethylenimine
PET	Polyethylene terephthalate
PPP	Poly-p-phenylene
PPy	Polypyrrole
PSS	Poly(styrenesulfonate)
PVA	Polyvinyl alcohol
PVAc	Poly(vinyl acetate)
SEM	Scanning electron microscopy
SSH	Schrieffer-Heeger Hamiltonian
SWCNT	Single-wall carbon nanotube
T CPP	Meso-tetra(4-carboxyphenyl) porphine
TEG	Thermo electric Generator
TEM	Transmission electron microscope
TGA	Thermogravimetric analysis
XRD	X-ray diffraction

List of Figures

1.1	Historical energy demand. Image taken from BP Statistical Review of World Energy, London, 2015.	1
1.2	Diagram of energy losses. Image taken from U.S. Department of Energy Midwest.	2
1.3	Scheme of the thermoelectric effect.	3
1.4	Thermoelectric module.	4
1.5	γ as a function of ZT	5
1.6	Evolution of ZT in some thermoelectric materials. Reproduced from [15] image under a Creative Commons CC-BY license	7
1.7	GPHS-RTG thermoelectric generator. Reproduced from [47] with permission of TAYLOR and FRANCIS	10
1.8	Commercial: (a) Peltier module and (b) portable thermoelectric refrigerator. . .	10
1.9	Specific capacitance of some materials. Reprinted from [49] with permission from Elsevier.	11
2.1	Contacts configurations to measure (a) R_1 , (b) R_2 and (c) voltage as function of the current for a PEDOT:PSS film.	14
2.2	(a) Seebeck measurement system, (b) scheme of sample measurement and (c) Seebeck voltage as a function of the temperature gradient.	15
2.3	(a) Scheme of the power measurements, and (b) box with the connections for the load resistance.	16
2.4	Picture of (a) Ivium-n-Stat: multi-channel electrochemical analyzer and (b) electrochemical cell with the three electrodes.	16
3.1	Conducting polymers (a) articles and (b) number of cites in thermoelectricity during the last 19 years. Data taken from Web of Science TM	23
3.2	Mechanism for EDOT polymerization using APS as oxidant.	24
3.3	Diagram of energy levels in conjugated systems	26
3.4	Tight-binding band structure of the uniform chain $(CH)_N$. Reprinted from [86] with permission of Oxford University Press.	29
3.5	Tight-binding band structure of dimerized $(CH)_N$. Reprinted from [86] with permission of Oxford University Press.	30
3.6	Scheme of the electrochemical cell.	31
3.7	Electrical conductivity (σ), Seebeck coefficient (α), thermal conductivity (κ), PF and ZT as a function of the carrier concentration. Reprinted from [9] with permission of NPG.	32
3.8	Structure of a soliton on a polyacetylene chain.	33
3.9	Band scheme of the midgap state associated with the soliton. Left neutral soliton, center positive soliton and right negative soliton.	33

3.10	Bonding and antibonding pair of gap states associated with confined soliton pairs. (a) Lower gap doubly occupied and (b) two states occupied with electrons with a different spin.	34
3.11	(a) Molecular structure of negative polaron (left) and positive polaron (right) in PPP. Electronic structures and gap state occupancies of the (b) negative polaron and (c) positive polaron.	34
3.12	(a) Molecular structure of negative bipolaron (left) and positive bipolaron (right). Electronic structures and gap state occupancies of the (b) negative bipolaron and (c) positive bipolaron.	35
3.13	(a) Coil conformation, (b) extended coil conformation, and (c) linear conformation.	36
3.14	Scheme of a reaction using the soft template method.	37
3.15	SEM images of AAOM: (a) top view and (b) cross section.	38
3.16	SEM images of PEDOT:PSS films (a) top view and (b) cross section. (c) Photograph of PEDOT:PSS film with gold contacts.	40
3.17	Electrical conductivity as a function of DMSO content.	40
3.18	PEDOT at (a) benzoind and (b) quinoid conformation	41
3.19	Seebeck coefficient of PEDOT:PSS films as a function of DMSO content.	41
3.20	Power Factor of PEDOT:PSS films as a function of DMSO content.	42
3.21	Molecular structure of (a) 1-Butyl-3-methylimidazolium hexafluorophosphate and (b) 1-Ethyl-3-methylimidazolium bis(trifluoromethylsulfonyl)imide.	43
3.22	Scheme of the sample preparation sequence.	44
3.23	PEDOT:ClO ₄ with the gold layer (left) and after removing the gold layer (right)	44
3.24	SEM images of (a) native PEDOT:ClO ₄ , (b) PEDOT:ClO ₄ after 20s of reduction treatment, (c) native PEDOT:PF ₆ , (d) PEDOT:PF ₆ after 20s of reduction treatment, (e) native PEDOT:BTfMSI and (f) PEDOT:BTfMSI after 20s of reduction treatment showing the different morphologies.	45
3.25	Raman spectra of PEDOT:ClO ₄ , PEDOT:PF ₆ and PEDOT:BTfMSI at several reduction times.	47
3.26	UV-Vis-NIRs spectra of: (a) PEDOT:ClO ₄ , PEDOT:PF ₆ and PEDOT:BTfMSI at several reduction times and (b) PPEDOT:ClO ₄ , before and after acid treatment.	48
3.27	Electrical conductivity (σ), Seebeck coefficient S, and power factor (PF) , of: (a) PEDOT:ClO ₄ , (b) PEDOT:PF ₆ and (c) PEDOT:BTfMSI, as a function of chemical reduction time.	49
3.28	PEDOT conformation under the presence of different counter-ions.	51
3.29	ZT values of PEDOT:ClO ₄ , PEDOT:PF ₆ and PEDOT:BTfMSI as a function of chemical reduction time at 25 °C.	51
3.30	SEM images of: (a) PEDOT and (b) PPy films surfaces after electrochemical polymerization.	54
3.31	Cyclic voltammetry of: (a) PEDOT and (b) PPy. (c) Scheme of polymer electronic states as a function of the oxidation/reduction level.	54
3.32	UV-Vis spectra of: (a) PEDOT and (b) PPy as a function of different applied voltages vs Ag/AgCl on ITO coated glass electrode deposited polymer films.	56
3.33	Electrical conductivity, Seebeck coefficient and power factor of (a) PEDOT and (b) PPy as a function of voltage referred to the Ag/AgCl electrode.	57
3.34	ZT of PEDOT and PPy as a function of applied potential at 300 K.	58
3.35	Molecular structure of Lutensol AT50 and DTAB.	59
3.36	TEM images of PEDOT nanoparticles with a molar ratio: (a) EDOT:Fe-Tos 1:0.5, (b) EDOT:Fe-Tos 1:1, (c) EDOT:Fe-Tos 1:2, (d) EDOT:Fe-Tos 1:3.5	62

3.37	Scheme of PEDOT polymerization in miniemulsion	63
3.38	TEM images of PEDOT nanoparticles with H ₂ O ₂ : (a) 7.5 · 10 ⁻³ M, (b) 1.5 · 10 ⁻² M, (c) 3.7 · 10 ⁻² M, (d) 7.5 · 10 ⁻² M. (e) Particle size distribution.	64
3.39	Scheme of PEDOT polymerization in miniemulsion with H ₂ O ₂	64
3.40	TEM images of PEDOT nanoparticles with 0.5 ml of H ₂ O ₂ and: (a) 0.5 ml, (b) 1.0 ml, (c) 2.5 ml and (d) 5 ml of HCl.	65
3.41	TEM images of PEDOT nanoparticles with a molar ration EDOT:Fe-Tos 1:1 using: (a) 0.05 g, (b) 0.5 g, (c) 1.0 g and (d) 3.0 g of DTAB	66
3.42	TEM images of PEDOT nanoparticles with a molar ratio EDOT:Fe-Tos 1:2 using:(a) 0.05 g, (b) 0.5 g, (c) 1.0 g and (d) 3.0 g of DTAB	67
3.43	Electrical conductivity, and Seebeck coefficient of PEDOT nanoparticles as a fuction of Fe-Tos concentration.	68
3.44	(a) Raman and (b) Uv-Vis spectra of PEDOT at different EDOT:Fe-Tos molar ratios.	68
3.45	(a) Electrical conductivity and (b) Seebeck coefficient of PEDOT as a function of H ₂ O ₂ concentration.	69
3.46	(a) Raman and (b) Uv-Vis spectra of PEDOT at different H ₂ O ₂ content H ₂ O ₂	69
3.47	Broken conjugation of PEDOT due to the ·OH radicals	70
3.48	FTIR spectra of PEDOT nanoparticles with 0.5 ml and without H ₂ O ₂	71
3.49	Electrical conductivity, and Seebeck coefficient, of PEDOT nanoparticles as a function of HCl concentration.	71
3.50	(a) Raman and (b) Uv-Vis spectra of PEDOT as a function of HCl volume added during the synthesis.	72
3.51	Electrical conductivity and Seebeck coefficient of PEDOT nanoparticles as a function of DTAB concentration using a molar ratio EDOT:Fe-Tos (a) 1:1 and (b) 1:2	73
3.52	Raman spectra of PEDOT nanoparticles as a function of DTAB concentration using a molar ratio EDOT:Fe-Tos: (a) 1:1 and (b) 1:2	73
3.53	Uv-Vis spectra of PEDOT nanoparticles as a function of DTAB concentration using a molar ratio EDOT:Fe-Tos: (a) 1:1 and (b) 1:2.	74
3.54	Scheme of PEDOT-NW synthesis.	75
3.55	SEM images of the cross section of the alumina templates used in the PEDOT nanowires synthesis: (a) native membrane, (b) 4 hours at 3 mA, (c) 8 hours at 3 mA and (d) 8 hours at 6 mA.	76
3.56	SEM images of PEDOT nanowires (a), (b), (c) after template removal and (d) after dispersion.	77
3.57	Scheme of electrical conductivity (left image) and Seebeck coefficient (right image) measurement of a single PEDOT nanowire.	78
4.1	ZT of inorganic thermoelectric materials used for different temperature applications over the years. Reprinted from [126] with permission from The Royal Society of Chemistry.	80
4.2	The building-blocks of the type I (top) and II (bottom) clathrates with guest atoms inside the polyhedra that form the unit cell of these two structure types. Reproduced from [47] with permission of TAYLOR and FRANCIS.	81
4.3	Crystal structure of skutterudites with the metal atoms M (open circles), the pnictogen atoms X (solid circles) arranged in planar, near-square four-membered rings. The other two circles are voids, which are often found by other elements to form a completely filled structure. Reprinted from [131].	82

4.4	Crystal structure of layered cobalt oxides Na_xCoO_2 . Reprinted from [138] with permission of Elsevier.	84
4.5	Crystal structure of SrTiO_3 perovskite. Reprinted from [139] with permission of Springer.	84
4.6	Density of states for (a) a bulk 3D crystalline semiconductor: (b) a 2D quantum well, (c) a 1D nanowire or nanotube, and (d) a 0D quantum dot. Reproduced from [47] with permission of TAYLOR and FRANCIS.	88
4.7	Seebeck coefficient of Bi nanowires of various diameters. Reproduced from [47] with permission of TAYLOR and FRANCIS.	89
4.8	Photograph of a Teflon autoclave with its steel holder	90
4.9	SEM images of $\text{La}_{1-x}\text{Ca}_x\text{MnO}_3$ ($x=0.05$) after different temperature treatments during 12 h: (a) 230 °C, (b) 650 °C, (c) 900 °C and (d) after sintering.	91
4.10	TEM images and particle size distribution of $\text{La}_{1-x}\text{Ca}_x\text{MnO}_3$ ($x=0.05$) after different temperature treatments during 12 h: (a) and (b) 230°C, (c) and (d) 650°C, (e) and (f) 900°C.	92
4.11	X-ray diffraction spectra of $\text{La}_{1-x}\text{Ca}_x\text{MnO}_3$ nanostructures (a) as a function of the calcination temperature ($x = 0.05$) and (b) as a function of the composition. The red lines refer to the perovskite phase diffraction pattern.	93
4.12	Electrical conductivity of $\text{La}_{1-x}\text{Ca}_x\text{MnO}_3$ (a) ($x = 0.05$) before and after sintering and (b) for different Ca contents as a function of the temperature.	94
4.13	(a) Seebeck coefficient and (b) power factor of $\text{La}_{1-x}\text{Ca}_x\text{MnO}_3$ for different calcium contents as a function of the temperature.	95
4.14	SEM images of $\text{Nd}_{1-x}\text{Ca}_x\text{CoO}_3$ ($x=0.005$) at: (a) 230 °C and (b) 650 °C. (c) TEM images of $\text{Nd}_{1-x}\text{Ca}_x\text{CoO}_3$. (d) Histogram of the diameter of the nanowires.	97
4.15	X-ray diffraction spectra of $\text{Nd}_{1-x}\text{Ca}_x\text{CoO}_3$ nanostructures (a) at 230°C for the composition $x = 0.005$ and (b) at 650°C as a function of the composition. The vertical lines correspond to the diffraction patterns.	98
4.16	Electrical conductivity of $\text{Nd}_{1-x}\text{Ca}_x\text{CoO}_3$ ($x = 0.005$) before and after sintering.	99
4.17	(a) Electrical conductivity and (b) Seebeck coefficient of $\text{Nd}_{1-x}\text{Ca}_x\text{CoO}_3$ as a function of the temperature.	100
4.18	(a) Thermal conductivity and (b) ZT of $\text{Nd}_{1-x}\text{Ca}_x\text{CoO}_3$ as a function of the temperature.	101
4.19	XRD plot of (a) non-hydrogenated samples and (b) hydrogenated samples.	103
4.20	SEM images of: (a) the surface of sample P, (b) the surface of sample PA.	105
4.21	Electrical conductivity of charcoal samples as a function of the treatment	106
4.22	Seebeck coefficient of charcoal samples as a function of the treatment.	106
4.23	PF of charcoal samples after the different treatment.	107
4.24	X-Ray results for glassy-carbon.	109
5.1	(a) CNT are coated by PEDOT:PSS particles, making nanotube-PEDOT:PSS-nanotube junctions in the composites. (b)The fully dried composite held between two fingers indicates that it is a free-standing flexible black material. Reproduced from [197] with permission of ACS Nano.	117
5.2	TEM images for SWCNT/PANI composites with 25 wt % SWCNT. Inset of (a) is the SEM top view of the nanowire. Reproduced from [107] with permission of ACS Nano.	118
5.3	schematic of polymer nanocomposites preparation from (a) polymeric solution and (b) insitu polymerization	122

5.4	Diagram of: (a) agglomerated nanoparticles in the matrix polymer and (b) well dispersed particles due to the grafting polymer.	123
5.5	TEM images of PEDOT:PSS with 15 wt % of expanded graphite.	124
5.6	SEM images of: (a) cross section of PEDOT:PSS, (b) cross section of PEDOT:PSS with 30 wt % expanded graphite, (c) surface PEDOT:PSS and (d) surface PEDOT:PSS with 30 wt % expanded graphite.	125
5.7	Differential scanning calorimetric patterns of PEDOT:PSS and PEDOT:PSS with 10% of EG	126
5.8	Thermogravimetric analysis of PEDOT:PSS, PEDOT:PSS with 30 wt % EG and EG powder.	126
5.9	Electrical conductivity of PEDOT:PSS/ expanded graphite composites	127
5.10	Seebeck values of PEDOT:PSS/expanded graphite composites.	128
5.11	Power factor of PEDOT:PSS/expanded graphite composites.	128
5.12	SEM images of NCCO/PEDOT:PSS composites with : (a) 80% (c) 90% and (e) 95 % of $\text{Nd}_{0.999}\text{Ca}_{0.001}\text{CoO}_3$. SEM images of NCCO/PEDOT:Tos composites with an (b) 80% (d) 90% and (f) 95 % of $\text{Nd}_{0.999}\text{Ca}_{0.001}\text{CoO}_3$	131
5.13	XRD spectra of $\text{Nd}_{0.999}\text{Ca}_{0.001}\text{CoO}_3$ composites with: (a) PEDOT:PSS and (b) PEDOT:Tos.	132
5.14	Electrical conductivity, Seebeck coefficient and power factor for the NCCO/PEDOT:PSS nanocomposites (plots a, b, and c) and for NCCO/PEDOT:PSS (plots d-f).	132
5.15	Scheme of PEDOT polymerization of MWCNTs substrates	135
5.16	Schematic of the LBL deposition of MWCNTs stabilized by PDDA and DOC.	135
5.17	Mass deposition and thickness of MWCNT-PDDA/MWCNT-DOC films as a function of the number of bilayers deposited (a). Electrical conductivity and absolute resistance as a function of the number of bilayers deposited (b). The lines in each graph are just to guide the eyes.	136
5.18	TEM images of the cross section of a film with 50 BL MWCNT-PDDA/MWCNT-DOC.	137
5.19	Voltage as a function of the polymerization time for the sample with 30 BL.	137
5.20	SEM images of a 50 BL of MWCNT-PDDA/MWCNT-DOC film (a) and the same film after 10 (b) of EDOT polymerization.	138
5.21	SEM images of MWCNT/PEDOT films.	138
5.22	TEM images of the cross section MWCNT/PEDOT Films (50 BL).	139
5.23	(a) Electrical conductivity, (b) resistance, (c) Seebeck coefficient and (d) power factor of MWCNT-PDDA)/MWCNT-DOC multilayers as a function of PEDOT polymerization time.	140
5.24	Scheme of the Te deposition over the PEDOT working electrode.	142
5.25	(a) Cyclic voltamperometry of HTeO_2^+ using PEDOT film as a working electrode. (b) Galvanometric curve during the Te deposition in an ice bath. Thickness of the Te-PEDOT films as a function of the Te electrodeposition time.	143
5.26	Thickness of the Te-PEDOT films as a function of the Te electrodeposition time.	143
5.27	SEM images of Te-PEDOT films after: (a) 30, (b) 60, (c) 90, (d) 120, (e) 150 and (f) 180 minutes of Te electrodeposition.	144
5.28	(a) AFM image of the PEDOT film after 2.5 hours of electrodeposition. (b) Roughness profile corresponding with the white line on the AFM image (the inset is a 3D view of AFM image).	145

5.29	Room-temperature Raman-scattering spectra of PEDOT-Te films obtained with the 647.1 nm excitation line of an Ar-Kr laser.	145
5.30	XRD analysis of Te-PEDOT films as a function Te deposition time.	146
5.31	Electrical conductivity, Seebeck coefficient and Power Factor of Te-PEDOT films as a function Te deposition time.	147
6.1	Configuration of a thermoelectric module.	152
6.2	Power per unit area and conversion efficiency vs thermoelement length for different temperature differences. Reproduced from [47] with permission of TAYLOR and FRANCIS.	153
6.3	Image of a Peltier module assembly.	154
6.4	High performance multisegmented thermoelectric generator. Reproduced from [47] with permission of TAYLOR and FRANCIS.	155
6.5	Schematic representation of the: (a) series and (b) parallel PEDOT:PSS array, (c) schematic and (d) photograph of the PEDOT:PSS modules sandwiched between copper plates. Reprinted from [242] with permission from The Royal Society of Chemistry.	157
6.6	(a) and (b) 3D scheme of thermoelectric module assembly and (c) real image of the module. Reprinted from [250] with permission of ACS Nano Letters.	157
6.7	Energy densities versus power densities for various energy storage devices.	158
6.8	Scheme of parallel plate capacitor	159
6.9	Different heterogeneous nanostructured materials based on structural complexity. Reprinted from [257] with permission from The Royal Society of Chemistry.	160
6.10	Scheme of the synthesis of PEDOT thermoelectric module	161
6.11	Images of: (a) Gold pattern, (b) 3D model of the thermoelectric module, (c) and (d) final device	162
6.12	Voltage as a function of temperature	163
6.13	Power of the thermoelectric module as a function of the load resistance.	164
6.14	(a) Power as a function of the thickness of PEDOT tracks and (b) Power as a function of load resistance in 15 thermoelectric modules connected in parallel	164
6.15	Photographs of the 20 BL of MWCNTs films preparation.	166
6.16	Pictures of: (a) 20 BL of MWCNTs/MWCNTs after PEDOT polymerization and (b) fundamental unit of thermoelectric module.	166
6.17	Schematic and picture of the thermoelectric module fabricated from PEDOT-infused MWCNT-based films deposited on PET.	167
6.18	Power from cylindrical thermoelectric generator as a function of: (a) voltage and (b) load resistance, with varying temperature differential supplied	167
6.19	Scheme of the electronic circuit of the thermal sensor and the load	169
6.20	(a) Image of PEDOT nanofilm; (b) Schematic diagram of the Seebeck measurements. (c) Seebeck voltage as a function of temperature difference across the sample.	170
6.21	Temperature mapping of a polymer thin film simulated with COMSOL.	170
6.22	Simulation of power generation as a function of current intensity for the polymer thermal sensor at several temperature differences.	171
6.23	(a) Temperature increment, and (b) voltage output generated by finger pressing the thermal polymer sensor.	171
6.24	(a) Picture of the sensor device. (b) Input and output voltage during several finger pulses.	172

6.25	Picture of the working electrode during the PEDOT polymerization on MWCNTs-cotton fabrics.	174
6.26	(a) Schematic of fabric supercapacitor and (b) picture of the final device.	174
6.27	Cyclic voltammetry of PET-Au-PEDOT device at different scan ratio.	175
6.28	(a) Galvanostatic curves at 0.5 A/g and 1.0 A/g of PET-Au-PEDOT device. (b) Specific capacity as a function of polymerization time	175
6.29	Specific capacitance of a PET-PEDOT device as a function of charge-discharge cycles.	176
6.30	Cotton fabric/MWCNT after EDOT polymerization.	177
6.31	Cotton fabric/MWCNT with different number after several EDOT polymerization times.	177
6.32	SEM images of: (a) and (b) MWCNTs-cotton fabrics, (c) and (d) MWCNTs-PEDOT cotton fabrics, (e) and (f) MWCNTs-PEDOT-MnO ₂ cotton fabrics . . .	178
6.33	Microanalysis and mapping of MWCNTs-PEDOT-MnO ₂ cotton fabrics	179
6.34	Cyclic voltammetry of MWCNTs-PEDOT-cotton fabric and MWCNTs-PEDOT-MnO ₂ - cotton fabric devices at 20 mV/s.	180
6.35	(a) Galvanostatic curves of CNTs-PEDOT-Cotton fabric and MWCNTs-PEDOT-MnO ₂ -cotton fabric devices. (b) Specific capacity as a function of cycles.	180
6.36	(a) Picture of the cylindrical thermoelectric generator charging one of the supercapacitors developed. (b) Charge and discharge curve using the thermoelectric generators as power supply.	181
7.1	Thermoelectric efficiency evolution during the period of this thesis o during the last four years.	184

List of Tables

1.1	Thermoelectric parameters of the most relevant conducting polymers at room temperature.	9
3.1	Molecular structures of typical conducting polymers	22
3.2	Dopants of the most typical semiconducting polymers	25
3.3	Typical vibrational modes of PEDOT.	46
3.4	Amounts of the reactants during the study of the EDOT:Fe-Tos molar ratio influence.	60
3.5	Amounts of the reactants during the study of the H ₂ O ₂ concentration influence.	60
3.6	Amounts of the reactants during the study of the pH influence.	60
3.7	Reactants during the study of the DTAB influence on PEDOT polymerization with a molar ratios EDOT:Fe-Tos 1:1 and 1:2.	61
4.1	Treatments in the carbon black samples.	102
4.2	Determination of crystalline size using Scherrer's formula	103
4.3	Results of the measurements of electric conductivity and Seebeck effect on the carbon black samples	104
4.4	Treatments performed on the charcoal samples	105
4.5	Treatments performed on the samples.	108
4.6	Results of electrical conductivity and Seebeck effect in vitreous-carbon samples subjected to different treatments.	108
4.7	XRD parameters of all samples.	111
5.1	Thermoelectric parameters of the most relevant conducting polymer composites with carbon materials at room temperature.	120
5.2	Thermoelectric parameters of the most relevant conducting polymers composites with inorganic nanoparticles at room temperature.	121

Appendix A

Resumen en castellano

A.1 Motivación

Debido a la gran demanda energética que actualmente presenta la sociedad es necesario apostar por el desarrollo de nuevos dispositivos energéticos que permitan satisfacer las necesidades de la sociedad actual. El inherente agotamiento de las fuentes de energía no renovables, a parte de los problemas medioambientales que presenta el abuso de estas fuentes, crea la necesidad de buscar y construir nuevos dispositivos más eficientes capaces de producir energía. La existencia de materiales con alta eficiencia termoeléctrica puede ser de especial interés para aprovechar las pérdidas en forma de calor y transformarlas en energía eléctrica; muy interesante para ámbitos industriales y, en particular, en la industria del automóvil. Un material termoeléctrico ideal consiste en un conductor eléctrico perfecto que al mismo tiempo sea un aislante térmico perfecto.

Los materiales termoeléctricos se caracterizan mediante una cantidad adimensional denominada Figura de Mérito (ZT) que se expresa mediante el producto de un parámetro Z , que depende de las propiedades intrínsecas del material, por la temperatura T a la que se encuentra el mismo. ZT viene definida por: el coeficiente de Seebeck, S , la conductividad eléctrica, σ , la conductividad térmica, κ y la temperatura absoluta, T según la ecuación $ZT = S^2\sigma/T$. El valor máximo de ZT se obtiene en un corto rango de temperaturas, de manera que un material termoeléctrico idóneo para aplicaciones de alta temperatura no lo es en aplicaciones de baja temperatura y vice-versa. En los años 90 se disponía de un conjunto de materiales con una figura de mérito en torno a la unidad. En esos momentos, nos encontramos con tres familias entre los materiales termoeléctricos. En primer lugar, el Bi_2Te_3 para aplicaciones en torno a temperatura ambiente.

En segundo lugar, materiales basados en PbTe para aplicaciones a temperaturas intermedias. Finalmente, SiGe para el uso a temperaturas elevadas, fundamentalmente en generadores termoeléctricos de radioisótopos, utilizados en las naves espaciales. La situación realmente había cambiado poco desde los años 60. Cualquier proyecto de investigación que propusiera como meta la obtención de ZT del orden de 3 hubiera sido rechazado por cualquier Agencia de Financiación como no creíble. A mediados de los años 90 la situación cambió drásticamente. L.D Hicks y M.S Dresselhaus propusieron la utilización de pozos cuánticos y superredes para la mejora de las propiedades termoeléctricas de los materiales. El confinamiento cuántico y el aumento en la densidad de estados hicieron posible el aumento del coeficiente Seebeck del material. La misma idea fue desarrollada por una serie de investigadores y en unos años T.L. Harman et al obtuvo un considerable aumento de ZT utilizando puntos cuánticos de PbTe. En el caso de materiales basados en carbono la situación es también esperanzadora. Un estudio reciente de H. Sevinçli y G. Cuniberti estima que en el caso de láminas de grafeno la figura de mérito podría ser del orden de 20 (Resultado teórico no comprobado experimentalmente). Resultados incluso mejores se han predicho en el caso de polímeros conductores y sistemas híbridos. El uso de polímeros conductores (ICP) sobre materiales de índole inorgánica presenta varias ventajas como, por ejemplo, la abundancia de materias primas, el bajo coste de las mismas, fácil modificación química para ajustarse a la finalidad deseada, fácil procesado a escala industrial, ausencia de toxicidad etc. En particular destaca la familia de polímeros en basados en poli-(3-4 etilendioxitiofeno) conocido como PEDOT. Algunos investigadores han obtenido valores bastante altos de ZT, en torno a 0.2-0.4, para PEDOT: Tosilato (PEDOT:Tos) y PEDOT:Poliestiren-sulfonato (PEDOT:PSS).

Por otro lado, la utilización de ICP para supercondensadores presenta un alto potencial, debido a su alto poder de capacidad con unos valores alrededor de 100-500 F/g y a su rápida absorción y desorción de iones. En este caso, la utilización de ICP abarataría el coste en la fabricación de dispositivos debido a la abundancia de las materias primas y a su fácil procesado. Nuevamente, la formación de nanoestructuras poliméricas puede ser clave para incrementar las prestaciones de dichos dispositivos, ya que el uso de materiales nanoestructurados conlleva un incremento del área superficial, de modo que el contacto electrodo-electrolito es mayor, aumentando la velocidad de carga y descarga, acortándose los caminos para el transporte electrónico.

A.2 Objetivos

El objetivo principal de la presente tesis doctoral ha sido el desarrollo de materiales orgánicos para ser usados en dispositivos termoeléctricos, que se han logrado a través de objetivos secundarios tales como:

1. Diseño, formulación y síntesis de polímeros conductores y su completa caracterización
2. Diseño, formulación y síntesis de materiales híbridos (orgánicos-inorgánicos) y su completa caracterización.
3. Síntesis de nanoestructuras semiconductoras y su caracterización.
4. Fabricación de módulos termoeléctricos y supercondensadores basados en polímeros conductores.

A.3 Metodología y estructura de la tesis

Se han utilizado diferentes métodos de síntesis para obtener polímeros conductores y materiales nanoestructurados, como la polimerización oxidativa y la electropolimerización. En cuanto a los métodos de síntesis de materiales nanoestructurados se han empleado técnicas como: la síntesis hidrotermal y miniemulsión. También se realizó una caracterización estructural mediante técnicas espectroscópicas, como Raman, FTIR, Uv-Vis y difracción de rayos-X, una caracterización morfológica, como microscopía de fuerza atómica y microscopía electrónica de barrido y de transmisión, una caracterización eléctrica y térmica mediante medidas de efecto Seebeck, conductividad eléctrica y térmica, con equipos experimentales desarrollados durante la tesis. La conductividad eléctrica es uno de los factores que determinan la eficiencia termoeléctrica del material, ya que se encuentra en el numerador de la expresión de ZT. Por lo tanto se diseñó un montaje experimental para llevar a cabo dichas medidas. La conductividad eléctrica de las muestras se ha medido siguiendo el método de Van Der Paw. El método de Van Der Paw es muy indicado para la medida de la conductividad eléctrica en películas delgadas. Para ello se realizan 6 contactos metálicos de un 200 nm de espesor de Au mediante un equipo de evaporación de metales, Leybold Univex 300, sobre la superficie de las muestras. Se sitúan 4 contactos en el centro equidistantes entre sí (a, b, c y d), que son los que se utilizarán para la medida de conductividad eléctrica, ya que éste método utiliza medida de resistencias eléctricas a 4 hilos.

Los otros de los extremos son usados posteriormente para la medida del efecto Seebeck. Según la ecuación de Van Der Pauw:

$$e^{-\pi d R_1 \sigma} + e^{-\pi d R_2 \sigma} = 1 \quad (\text{A.1})$$

donde d , es el espesor de la película y σ , es la conductividad eléctrica. Para el cálculo de las resistencias R_1 y R_2 se utilizaron las siguientes ecuaciones, según la ley de Ohm: $R_1 = V_{bd}/I_{ac}$ y $R_2 = V_{ab}/I_{cd}$. Para el cálculo de R_1 se pasa una corriente entre los contactos a y c y se registra la tensión entre los contactos b y d, de igual modo se procede para el cálculo de R_2 salvo que, la corriente se inyecta entre los contactos A y B y se registra la tensión en los contactos c y d. Para el registro de las medidas se ha utilizado un multímetro Keithely 2400. Para la medida del efecto Seebeck se diseñó un dispositivo experimental que fue desarrollado en el laboratorio para la realización de la presente tesis doctoral. El dispositivo para determinar el coeficiente de Seebeck consta de un multímetro para registrar la diferencia de potencial, un controlador de temperatura, dos bloques de cobre, uno refrigerado por un corriente de agua y el otro calentado por una resistencia eléctrica, dos sensores de temperatura PT100 y dos cables que contactan los extremos de la muestra. Para la obtención del coeficiente Seebeck, la muestra es sometida a una diferencia de temperatura entre los extremos, de modo que se registra la tensión entre los contactos de los extremos de la muestra en función de la diferencia de temperatura. La pendiente de la recta obtenida es el coeficiente de Seebeck de acuerdo con la expresión:

$$S = \Delta V / \Delta T. \quad (\text{A.2})$$

La presente tesis doctoral se ha estructurado en 7 capítulos. El primer capítulo consiste en una introducción general donde se introducen conceptos básicos y generales de la tesis. El segundo capítulo se dedica a la descripción de las técnicas experimentales empleadas. El tercer capítulo consiste en varios desarrollos experimentales relacionados con el estudio de las propiedades termoeléctricas de polímeros conductores y nanoestructuras poliméricas basadas en PEDOT. El segundo capítulo está dedicado al estudio de las propiedades termoeléctricas de nanohilos de óxidos metálicos $\text{Nd}_{1-x}\text{Ca}_x\text{CoO}_3$ y $\text{La}_{1-x}\text{Ca}_x\text{MnO}_3$ además de materiales basados en carbono como, negro de humo, carbón vegetal y vitrografito. El capítulo 5 está dedicado a la síntesis y caracterización de materiales híbridos basados en PEDOT (PEDOT-Grafito expandido, PEDOT-MWCNTs, PEDOT- $\text{Nd}_{1-x}\text{Ca}_x\text{CoO}_3$ y PEDOT-Te). El Capítulo 6 describe la fabricación de dos generadores termoeléctricos, un sensor térmico y supercondensadores basados en los materiales

estudiados en los capítulos posteriores. Por último, el Capítulo 7 está dedicado a las conclusiones generales de la tesis.

A.4 Resultados y conclusiones más relevantes

En el Capítulo 3, se obtuvieron películas de una disolución comercial de PEDOT:PSS mediante deposición por casting en sustratos de vidrio. Se midieron las propiedades termoeléctricas (conductividad eléctrica y efecto Seebeck) en función de la cantidad de DMSO en la disolución de PEDOT:PSS, obteniéndose un incremento de 3 órdenes de magnitud (desde 0.14 S/cm hasta 177 S/cm), sin embargo, el coeficiente de Seebeck disminuyó con la adición de DMSO. Para dar una idea de la eficiencia termoeléctrica de las películas se calculó el Power Factor ($PF = S^2\sigma$) obteniéndose un valor máximo de $0.722 \mu\text{W}/\text{mK}^2$. Por otra parte se sintetizaron películas de PEDOT por vía electroquímica en presencia de varios contraiones. Se observó una dependencia de la conductividad eléctrica en función del tipo de contraión utilizado. En dichas películas se evaluaron las propiedades termoeléctricas en función del tiempo de reducción en presencia de hidracina para optimizar el nivel de dopado de las películas de PEDOT. Se observó una disminución de la conductividad eléctrica y un aumento del coeficiente de Seebeck con el tiempo de reducción. El valor óptimo de eficiencia dado por el PF se obtuvo después de 11 s para PEDOT: ClO_4 y PEDOT: PF_6 con valores de 41 y $60 \mu\text{W}/\text{mK}^2$ respectivamente y después de 5 s para las muestras de PEDOT:BTFMSI obteniendo un valor de $PF=147 \mu\text{W}/\text{mK}^2$. Además, se realizó un estudio de las propiedades termoeléctricas de PEDOT y PPy en función del potencial en una celda electroquímica. Se observó un aumento de la conductividad eléctrica a potenciales donde predominaban las especies oxidadas mientras que el coeficiente de Seebeck aumentó a potenciales donde predominaban las especies reducidas de PEDOT y PPy. Para el caso del PEDOT se obtuvo un valor de máximo de PF de alrededor de $16 \mu\text{W}/\text{mK}^2$ a un potencial de 0.01 V mientras que para las muestras de PPy el valor máximo de PF fue $3.9 \mu\text{W}/\text{mK}^2$ a un potencial de -2.0 V. En este capítulo se muestran también los resultados obtenidos para la polimerización de PEDOT en miniemulsión. Para ello se emplearon dos surfactantes, Lutensol AT50 y DTAB y como oxidantes Fe-Tos y agua oxigenada. Para el caso de las muestras sintetizadas en presencia de Lutensol AT 50 se consiguió obtener una morfología esférica con un tamaño de partícula entre 30 y 40 nm. La conductividad eléctrica aumento con el contenido de Fe-Tos pero disminuyó con el contenido de agua oxigenada probablemente debido a reacciones secundarias en la cadena polimérica que rompen la conjugación. La síntesis de nanopartículas de PEDOT utilizando un

surfactante catiónico (DTAB) produce una transición de tipo de conducción, es decir, se produce un cambio de semiconductor de tipo p a semiconductor de tipo n. Además una concentración elevada de DTAB provocó una inhibición de la reacción de polimerización de PEDOT. Finalmente también se obtuvieron nanohilos de PEDOT utilizando Alúminas porosas de 200 nm de diámetro de Poro.

En el Capítulo 4 se sintetizaron nanoestructuras de tipo nanohilo de compuestos basados en $\text{Nd}_{1-x}\text{Ca}_x\text{CoO}_3$ y $\text{La}_{1-x}\text{Ca}_x\text{MnO}_3$. Para el caso de los materiales de composición $\text{La}_{1-x}\text{Ca}_x\text{MnO}_3$ se observó un cambio en la morfología de nanohilo a nanopartícula tras el tratamiento de calcinado. La fase de tipo perovskita se obtuvo a 650 °C. Tras el proceso de sinterizado a alta temperatura, la conductividad eléctrica aumentó varios órdenes de magnitud. Dependiendo del contenido en calcio se observó un cambio en el tipo de conducción obteniéndose un comportamiento de tipo n para $x=0.005$ y p desde $x=0.01$ hasta $x=0.5$. En el caso de las muestras de composición $\text{Nd}_{1-x}\text{Ca}_x\text{CoO}_3$ la fase de perovskita se alcanzó a 650 °C con la morfología de tipo nanohilo. Al igual que en las muestras de composición $\text{La}_{1-x}\text{Ca}_x\text{MnO}_3$ la conductividad eléctrica aumentó con el proceso de sinterizado. Se obtuvieron valores de coeficiente de Seebeck en el rango de 600-700 $\mu\text{V/K}$. El contenido en calcio está fuertemente relacionado con la conductividad eléctrica, siendo ésta mayor a bajos contenidos en calcio. Además, se obtuvieron los valores de ZT para las muestras de $\text{Nd}_{1-x}\text{Ca}_x\text{CoO}_3$, alzando un valor máximo de 0.012 a 520 °C. Finalmente, para los materiales basados en carbono (negro de humo, carbón vegetal y vitrografito) el proceso de irradiación puede alterar su comportamiento termoeléctrico como, por ejemplo, cambios en el signo de del coeficiente de Seebeck como es el caso de las muestras de vitrografito produciendo un cambio de tipo de semiconductor tipo p a tipo n.

En el Capítulo 5 se estudiaron cuatro tipos de nanocomposites híbridos orgánico-inorgánico tales como: PEDOT-grafito expandido, PEDOT-MWCNTs, PEDOT- $\text{Nd}_{1-x}\text{Ca}_x\text{CoO}_3$ y PEDOT-Te. Las películas de PEDOT-grafito expandido se prepararon mediante dispersión de partículas de grafito expandido en una disolución de PEDOT:PSS y posterior evaporación del disolvente sobre sustratos de vidrio. Los resultados obtenidos indicaron un aumento de la conductividad eléctrica con el contenido en grafito expandido, llegando a alcanzar valores de 200 S/cm a altos contenidos de grafito expandido. El coeficiente de Seebeck aumentó con la primera adición de grafito expandido a un valor de 15-16 $\mu\text{V/K}$ que se mantuvo constante con el contenido en grafito expandido. Se obtuvo un valor máximo de PF de 5.31 $\mu\text{W/mK}^2$ a un contenido en grafito expandido de 80 %. Las muestras de PEDOT- $\text{Nd}_{1-x}\text{Ca}_x\text{CoO}_3$ fueron realizadas utilizando PEDOT:PSS y PEDOT:Te como componente orgánico y nanopartículas de $\text{Nd}_{1-x}\text{Ca}_x\text{CoO}_3$ con

$x=0.001$ y $x=0.005$. Las imágenes de SEM muestran una distribución homogénea de ambos componentes. En cuanto a las propiedades termoeléctricas, los resultados de conductividad eléctrica mostraron un aumento de la misma con el contenido en PEDOT, sin embargo, las muestras con PEDOT:Tos mostraron valores mayores. En el caso del coeficiente de Seebeck se observó la tendencia contraria, el valor del coeficiente de Seebeck aumentó con el contenido de $\text{Nd}_{1-x}\text{Ca}_x\text{CoO}_3$. Para las nanopartículas puras el coeficiente de Seebeck fue de $979 \mu\text{V/K}$ y $519 \mu\text{V/K}$ para las composiciones $x=0.001$ y $x=0.005$, respectivamente. Este disminuyó hasta $25 \mu\text{V/K}$ para el caso de PEDOT:PSS y $50 \mu\text{V/K}$ para el caso de PEDOT:Tos. Los resultados óptimos fueron alcanzados a un 5 % de contenido en PEDOT:Tos y un 95 % de $\text{Nd}_{1-x}\text{Ca}_x\text{CoO}_3$ con $x=0.005$ obteniendo un power factor de $1.34 \mu\text{W/mK}^2$. Otro tipo de materiales desarrollados fueron nanocompuestos híbridos basados en PEDOT-MWCNTs. La síntesis de estos materiales se llevó a cabo mediante deposición electroquímica de PEDOT sobre electrodos de MWCNTs fabricados utilizando la técnica de capa a capa (layer by layer en inglés). Para la fabricación de los electrodos se utilizó dos suspensiones de MWCNTs. En una de ellas se utilizó un surfactante de tipo catiónico (PDDA) mientras que en la otra suspensión se utilizó un surfactante de tipo aniónico, de tal manera que el sustrato de PET fue sumergido alternativamente en ambas disoluciones con etapas de lavado entre cada inmersión. Se realizaron varias síntesis de PEDOT utilizando estos electrodos de MWCNTs, fabricados con distinto número de bicapas (desde 20 hasta 60 BL). La polimerización se llevó a cabo durante 10, 30, y 60 minutos. Los resultados de microscopía electrónica (SEM y TEM) muestran una distribución homogénea de ambos componentes obteniendo unas películas donde los componentes están íntimamente mezclados ya que el PEDOT es sintetizado sobre de los MWCNTs. Con el fin de encontrar el óptimo número de bicapas y el tiempo de polimerización, se midieron en las muestras la conductividad eléctrica y el efecto Seebeck. En líneas generales la conductividad eléctrica tiende a aumentar con el tiempo de polimerización siendo óptima en la mayoría de los casos a 30 minutos utilizando electrodos con un número de bicapas intermedia (30-40 BL). En cuanto al coeficiente de Seebeck se observó una disminución con el tiempo de polimerización. El valor óptimo de power factor fue hallado en la muestra sintetizada durante 30 minutos con un electrodo de 30 bicapas dando un valor de $155 \mu\text{W/mK}^2$. Por último, en este capítulo se sintetizaron muestras de PEDOT-Te. Este tipo de películas fueron sintetizadas mediante electrodeposición de Te a -0.4 V sobre una película de PEDOT previamente sintetizada por vía electroquímica. Los resultados de difracción de rayos X y Raman confirmaron la presencia de Te en la película de PEDOT. El análisis morfológico de la superficie llevado a cabo mediante SEM y AFM mostró una superficie de morfología globular con una rugosidad de $\pm 20 \text{ nm}$. La conductividad eléctrica

y el coeficiente de Seebeck se estudió en función del tiempo de electrodeposición de Te sobre las películas de PEDOT. Se observó un aumento del coeficiente de Seebeck con el tiempo de electrodeposición, mientras que se observó una disminución de la conductividad eléctrica con el tiempo de electrodeposición. El valor máximo de power factor se determinó en la muestra con un tiempo de electrodeposición de Te de 150 minutos alcanzando un valor de $320 \mu\text{W}/\text{mK}^2$.

En el Capítulo 6, se presentaron los resultados de fabricación y caracterización de dos generadores termoeléctricos, un sensor térmico y supercondensadores basados en los materiales desarrollados en los capítulos anteriores. El primer generador termoeléctrico presentado fue fabricado mediante un proceso único de deposición electroquímica de PEDOT como elemento termoeléctrico en una geometría planar. Para ello se empleó un sustrato flexible de PET con un patrón de oro, depositado mediante evaporación metálica. Las medidas de efecto Seebeck en el dispositivo dieron un valor de $91 \mu\text{V}/\text{K}$, debido a la conexión en serie de 16 pistas de PEDOT. El dispositivo se sometió a un tratamiento de optimización del nivel de dopado mediante vapor de hidracina, ocasionando un incremento en el coeficiente de Seebeck del dispositivo hasta un valor de $413 \mu\text{V}/\text{K}$. Se realizaron medidas de potencia en el dispositivo manteniendo un diferencia de temperatura de 60°C . El valor máximo de potencia fue 2.7 nW a una resistencia de carga de $30 \text{ K}\Omega$. Dicho valor se aumentó hasta 5.03 nW tras la optimización del dopado mediante vapor de hidracina. La conexión de 15 módulos en paralelo dio lugar a una disminución de la resistencia interna del dispositivo incrementando el valor de potencia hasta 25 nW a una resistencia de carga de $1.8 \text{ K}\Omega$. El segundo dispositivo descrito en el capítulo fue desarrollado utilizando el material híbrido sintetizado a partir de MWCNTs y PEDOT. Los sustratos de MWCNTs se obtuvieron mediante el proceso de capa a capa (layer by layer) sobre láminas flexibles de PET con dimensiones de (8.5×15) pulgadas. Previamente en las láminas de PET, se dibujó un patrón a modo de tiras mediante el empleo de cinta adhesiva. Una vez se obtuvo el patrón, los sustratos se emplearon como electrodos de trabajo para la electropolimerización de PEDOT. Los elementos termoeléctricos consistieron en 12 pistas de MWCNTs/PEDOT con una altura de 1 pulgada conectados eléctricamente mediante laca conductora de plata, a este conjunto de elementos termoeléctrico se le llamó unidad fundamental. Alrededor de 30 unidades fundamentales fueron ensambladas a una tubería de cobre creando así un generador con geometría cilíndrica. Con este dispositivo se obtuvo una potencia máxima de $5.5 \mu\text{W}$ con una diferencia de temperatura de 30°C en circuito cerrado a una resistencia de carga de 50Ω . El tercer dispositivo desarrollado ha sido un sensor térmico basado en el efecto termoeléctrico de una película de PEDOT, de tal manera que se ha desarrollado una aplicación del tipo on-off. El alto CMRR (superior a 100 dB)

del circuito electrónico realizado junto con su gran ganancia diferencial (superior a 90 dB) hace posible poder utilizar una entrada de tensión muy pequeña. En concreto, el sensor proporciona en circuito abierto una tensión de unos $200 \mu\text{V}$ con una diferencia de temperatura de unos $5 \text{ }^\circ\text{C}$. El ruido es suficientemente rechazado debido a que la ganancia en modo común (G_c) es casi nula. La salida del amplificador de instrumentación (AI) se satura con una tensión diferencial muy baja (del orden de $80 \mu\text{V}$). Cuando se aplica, por ejemplo, un dedo al extremo del sensor ($\Delta T \sim 5 \text{ }^\circ\text{C}$) la salida del (AI) presenta una tensión aproximada a la tensión de alimentación capaz de habilitar una carga (load) determinada. Por ejemplo, un led (funcionamiento ON). Cuando el dedo se retira se deshabilita el led (funcionamiento OFF). Como el circuito electrónico (AI) es muy sensible a la tensión diferencial requiere que el sensor esté situado en un entorno en donde sus extremos (T y T_0) tengan la misma temperatura en ausencia de excitación externa. Por último, en este capítulo se desarrollaron varios dispositivos para almacenamiento de energía basado en supercondensadores mediante el uso de materiales obtenidos y caracterizados en esta tesis. Los primeros dispositivos fueron fabricados con películas de PEDOT depositadas vía electroquímica en sustratos de PET con un capa delgada de Au (20 nm) previamente depositada mediante evaporación metálica. Las películas de PEDOT sobre los sustratos de PET-Au se utilizaron como electrodos en el supercondensador, de tal manera que entre los electrodos se colocó un trozo de papel de filtro, hecho con fibra de vidrio, previamente humedecido con un electro-gel, fabricado a partir de: 4.2 mL 1 M de perclorato de litio en una relación volumen 5:2 de acetonitrilo:carbonato de propileno y 0.8 g de PMMA. Siendo el primer paso la realización de la disolución 5:2 de acetonitrilo:carbonato de propileno y adicionar sobre esta disolución 0.8 g de PMMA, luego se adicionan 4.2 mL de perclorato de litio 1 M sobre la disolución 5:2 por último se agita y se calienta a $105 \text{ }^\circ\text{C}$ hasta formación de un gel. Los resultados de voltamperometría cíclica mostraron un buen comportamiento del dispositivo como condensador, también se evaluó la capacidad específica del dispositivo alcanzando un valor de 33.6 F/g que disminuyó hasta 21 F/g después de 1000 ciclos de carga y descarga en el dispositivo. Se fabricaron otros dispositivos basado en un tejido de algodón, MWCNTs y PEDOT. En primer lugar, las telas se impregnaron con 20 BL de MWCNTs mediante el proceso de capa a capa. Los tejidos de algodón se sumergieron en dos suspensiones de MWCNTs en una de ellas se utilizó un surfactante de tipo catiónico (PDDA) mientras que en la otra suspensión se utilizó un surfactante de tipo aniónico, de tal manera que el trozo de tela de algodón se sumergió alternativamente en ambas disoluciones con etapas de lavado entre cada inmersión. Una vez obtenida la deposición de MWCNTs sobre el algodón, se procedió a la síntesis de PEDOT y PEDOT-MnO₂ mediante

un proceso de co-electrodeposición. Las imágenes de microscopia electrónica mostraron un recubrimiento homogéneo de las fibras que conforman el tejido de algodón por parte del PEDOT. En el caso de la co-electrodeposición junto con MnO_2 se observó la presencia de partículas de MnO_2 distribuidas en las fibras de algodón. Se ensamblaron dos dispositivos de igual modo que para las películas de PEDOT. En este caso se obtuvieron capacidades absolutas muy elevadas 406 mF y 294 mF para los dispositivos de MWCNTs-PEDOT-algodón y MWCNTs-PEDOT- MnO_2 -algodón respectivamente. Sin embargo, la capacidad específica fue de 7.0 F/g and 21 F/g para para los dispositivos de MWCNTs-PEDOT-algodon y MWCNTs-PEDOT- MnO_2 -algodón respectivamente, mostrando un valor inferior que el obtenido para los dispositivos fabricados con películas de PEDOT sobre sustratos de Au y PET. Este hecho puede ser debido a que el proceso de fabricación de este tipo de electrodos fabricados a partir de tejidos de algodón requiere de una optimización. Por último se desarrolló una prueba de concepto en la cual uno de los condensadores desarrollados en este capítulo se cargó mediante el módulo cilíndrico desarrollado a partir de los materiales híbridos de MWCNTs-PEDOT.

En conclusión, la presente tesis doctoral ha contribuido muy positivamente al estado del arte en el ámbito de la termoelectricidad tanto en materiales orgánicos híbridos abriendo así nuevos horizontes para futuras líneas de investigación.

Appendix B

Publication list

Journal publications

1. M. J. Sanchis, M. Carsí, C. M. Gómez, M. Culebras, K. N. Gonzales, and F. G. Torres. Monitoring molecular dynamics of bacterial cellulose composites reinforced with graphene oxide by carboxymethyl cellulose addition. *Carbohydr. Polym.*, 157:353–360, 2017
2. C. Cho, M. Culebras, K. L. Wallace, Y. Song, J-H. Holder, K. and Hsu, C. Yu, and J. C. Grunlan. Stable n-type thermoelectric multilayer thin films with high power factor from carbonaceous nanofillers. *Nano Energy*, 28:426–432, 2016
3. A. García-Barberá, M. Culebras, S. Roig-Sánchez, C. M. Gómez, and A. Cantarero. Three dimensional pedot nanowires network. *Synth. Met.*, 220:208–212, 2016
4. M. Culebras, M. Morais de Lima, C. Gómez, and A. Cantarero. Organic thermoelectric modules produced by electrochemical polymerization. *J. Appl. Polym. Sci.*, 2016
5. M. Culebras, A. M. Lopez, C. M. Gomez, and A. Cantarero. Thermal sensor based on a polymer nanofilm. *Sens. Actuator A-Phys*, 239:161–165, 2016
6. M. J. Sanchis, B. Redondo-Foj, M. Carsí, P. Ortiz-Serna, M. Culebras, C. M. Gómez, A. Cantarero, and R. Muñoz-Espí. Controlling dielectrical properties of polymer blends through defined pedot nanostructures. *RSC Adv*, 6(66):62024–62030, 2016

7. M. Culebras, C. J. Grande, F. G. Torres, O. P. Troncoso, C. M. Gomez, and M. C. Bañó. Optimization of cell growth on bacterial cellulose by adsorption of collagen and poly-L-lysine. *Int. J. Polymer. Mater.*, 64(8):411–415, 2015
8. P. Ortiz-Serna, M. Carsi, B. Redondo-Foj, M. J. Sanchis, M. Culebras, C. M. Gómez, and A. Cantarero. Thermal and dielectric properties of polycarbonatediol polyurethane. *J. Appl. Polym. Sci.*, 132(22), 2015
9. B. Redondo-Foj, P. Ortiz-Serna, M. Carsí, M. J. Sanchis, M. Culebras, C. M. Gómez, and A. Cantarero. Electrical conductivity properties of expanded graphite–polycarbonatediol polyurethane composites. *Polym. Int.*, 64(2):284–292, 2015
10. M. Culebras, B. Uriol, C. M. Gomez, and A. Cantarero. Controlling the thermoelectric properties of polymers: application to PEDOT and polypyrrole. *Phys. Chem. Chem. Phys.*, 17(23):15140–15145, 2015
11. M. Culebras, A. Cantarero, and C. M. Gómez. Enhanced thermoelectric performance of pedot with different counter ions optimized by chemical reduction. *J. Mater. Chem. A*, 2: 10109–10115, 2014
12. M. Culebras, C. M. Gómez, and A. Cantarero. Review on Polymers for Thermoelectric Applications. *Materials*, 7(9):6701–6732, 2014
13. M. Culebras, R.I Toran, C. M. Gomez, and A. Cantarero. $\text{La}_{1-x}\text{Ca}_x\text{MnO}_3$ semiconducting nanostructures: morphology and thermoelectric properties. *Nanoscale Res. Lett.*, 9, 2014
14. M. Culebras, A. Madroñero, C. Mota, C. M. Gómez, J. M. Amo, and A. Cantarero. Changes in the thermoelectric response of vitreous carbon due to the irradiation by γ -rays. *Radiat Eff. Defects Solids*, 169(7):620–627, 2014
15. M. Culebras, C. Gomez, A. Gomez, F. Sapina, and A. Cantarero. Synthesis of $\text{Nd}_{1-x}\text{Ca}_x\text{CoO}_3$ perovskite nanowires for thermoelectric applications. *J. Elect. Eng.*, 2:59–64
16. D. Granda-Restrepo, Y. Medina-Pineda, M. Culebras-Rubio, and C. Gomez-Clari. Desarrollo y caracterización de una película activa biodegradable con antioxidantes (alfa-tocoferol) a partir de las proteínas del lactosuero. *Vitae*, 21(1):11–19, 2014
17. M. Culebras, C. M. Gomez, and A. Cantarero. Thermoelectric measurements of PEDOT:PSS/expanded graphite composites. *J. Mater. Sci.*, 48(7):2855–2860, 2013

18. C. Mota, M. Culebras, A. Cantarero, A. Madro, C. M. Gómez, J. M. Amo, and J. I. Robla. Effects of gamma irradiation on the kinetics of the adsorption and desorption of hydrogen in carbon microfibres. *Adv. Mater. Chem. Phys*, 2013
19. A. Madro, M. Culebras, A. Cantarero, C. M. Gómez, C. Mota, J. M. Amo, and J. I. Robla. An approach on the hydrogen absorption in carbon black after gamma irradiation. *Adv. Mater. Chem. Phys*, 2013, 2013
20. C. M. Gómez, M. Culebras, A. Cantarero, B. Redondo-Foj, P. Ortiz-Serna, M. Carsí, and M. J. Sanchis. An experimental study of dynamic behaviour of graphite–polycarbonatediol polyurethane composites for protective coatings. *Appl. Surf. Sci*, 275:295–302, 2013
21. A. Nohales, D. Lopez, M. Culebras, and C. M. Gomez. Rheological study of gel phenomena during epoxide network formation in the presence of sepiolite. *Polym. Int*, 62(3): 397–405, 2013
22. M. Culebras, C. M. Gomez, and A. Cantarero. Thermoelectric materials based on poly (3, 4-ethylenedioxythiophene). *Journal of Thermoelectricity*, (4):36–42, 2013
23. C. Mota, A. Madroño, J. M. Amo, J. I. Robla, M. Culebras, and A. Cantarero. Variations in the electrical resistivity of vapour grown carbon fibres by effect of successive operations of intake and outgassing of hydrogen. *J. Mater. Sci. Res*, 2(1):163, 2013
24. M. Culebras, A. Madroño, A. Cantarero, J. M. Amo, C. Domingo, and A. López. Confident methods for the evaluation of the hydrogen content in nanoporous carbon microfibers. *Nanoscale Res. Lett*, 7(1):1–5, 2012
25. M. Culebras. Materiales con aplicaciones termoeléctricas. *MoleQla: revista de Ciencias de la Universidad Pablo de Olavide*, (5):109–111, 2012

Conference contributions

1. M. Culebras. Thermoelectric properties of pedot-tellurium films synthesized by electrochemical method. EMN Polymer (Hong kong, China), Invited talk, 2016
2. M. Culebras. Pedot-tellurium films synthesized by electrochemical method for hybrid thermoelectric material. ICOT (Kyoto, Japan), Poster, 2016

3. M. Culebras. New organic thermoelectric device based on conducting polymers. E-MRS Spring Meeting, (Lille, France), Oral presentation, 2015
4. M. Culebras. New organic thermoelectric device based on conducting polymers. MRS Fall Meeting Exhibit, (Boston, Spain), Oral presentation, 2015
5. M. Culebras. Semiconducting polymers with high figure of merit. GEFES, (Ciudad Real, Spain), Oral presentation, 2014
6. M. Culebras. Surface morphology effect on electrical properties in conducting polymers. Porous Semiconductors, (Benidorm, Spain), Poster, 2014
7. M. Culebras. PEDOT a high efficient thermoelectric material. 12th European Conference on Thermoelectrics, (Madrid, Spain), Oral presentation, 2014
8. M. Culebras. Synthesis of semimetallic polymers thin films by electrochemical polymerization for electronic applications. XIII Reunión del Grupo Especializado de Polímeros de la RSEQ y RSEF, (Gerona, Spain), Oral presentation, 2014
9. M. Culebras. Improved thermoelectric figure of merit in PEDOT:ClO₄ thin films. European polymer congress, (Pisa, Italy), Oral presentation, 2013
10. M. Culebras. Thermoelectric measurements of PEDOT:PSS- expanded graphite composite. E-MRS Spring Meeting, (Strasbourg, France), Oral presentation, 2012
11. M. Culebras. Estudio termodinámico de separación de fases de mezclas resina epoxi-termoplástico. XXXIII Reunión bienal de la RSEQ, (Valencia, Spain), Poster, 2012

Other presentations in conferences (presenting author underlined)

1. L. Villar, M. Culebras, C. M Gómez, and A. Cantarero. Synthesis of PEDOT/dWCNT nanocomposites for thermoelectric applications. XXXV Reunión Bienal RSEQ, (La Coruña, Spain), Poster, 2016
2. M. Culebras, R. Torán, A. Cantarero, and C. M. Gómez. Synthesis of La_{1-x}Ca_xCO₃ perovskites nanostructures for thermoelectric applications. 12th European Conference on Thermoelectrics, (Madrid, Spain), Poster, 2014

3. C. M. Gómez, M. Culebras, and A. Cantarero. Thermoelectric properties in poly(3,4-ethylenedioxythiophene). XIII Reunión del Grupo Especializado de Polímeros de la RSEQ y RSEF, (Gerona, Spain), Poster, 2014
4. Mario C., L. Laconcepcion, C. M. Gómez, and A. Cantarero. Study of doping level in pedot:clo₄ thin films for high thermoelectric performance. XV International Forum on Thermoelectricity, (Tallin, Estonia), Poster, 2013
5. M. Culebras, M. M. de Lima Jr, C. M. Gomez, and A. Cantarero. Polymer nanowires with a high figure of merit. MRS Fall Meeting, (Boston, United States), Poster, 2013
6. M. Culebras, C.M. Gómez, and A. Cantarero. New polymers with a high figure of merit: rescaling thermoelectricity. Energy Materials Nanotechnology East Meeting, (Beijing, China), Invited talk, 2013
7. C. M. Gómez, M. Culebras, A. Gómez, F. Sapiña, and A. Cantarero. Synthesis of Nd_{1-x}Ca_xCO₃ perovskites nanowires for thermoelectric applications. 11th European Conference on Thermoelectrics, (Noordwijk, The Netherlands), Oral presentation, 2013
8. David Gutiérrez, M. Culebras, A. Cantarero, A. Nohales, V. Costa, and C. M Gómez. Thermal study of polycarbonatediol polyurethanes/expanded graphite composites. European polymer congress, (Pisa, Italy), Poster, 2013
9. C. M. Gómez, M. Culebras, A. Gómez, F. Sapiña, and A. Cantarero. New polymer composites to improve thermoelectric efficiency. 3rd International Advances in Applied Physics and Materials Science Congress, (Antalya, Turkey), Oral presentation, 2013
10. A.Cantarero, M. Culebras, A. Gómez, F. Sapiña, and C. M. Gómez. Growth and thermal characterization of pedot:pss-nd_{1-x}Ca_xCO₃ perovskites nanocomposites. 1 th European Conference on Thermoelectrics, (Aalborg, Denmark), Poster, 2012
11. C. M. Gómez, M. Culebras, P. Felix, and A. Cantarero. Blends of polyurethane and graphite for thermoelectrical applications. 11th European Symposium on Polymer Blends, (Donostia, Spain), Oral presentation, 2012

Patents and utility models

1. M. Culebras, C. Gómez, A. Cantarero, and M. Morais. Organic thermoelectric device, thermoelectric system, method for manufacturing the device, coating enclosure, enclosure and thermoelectric solar hybrid system. Pct 2015000059, Universitat de Val`encia, 2015.

Research Projects as Participating Scientist

1. **CSD2010-0044** Conducting nanowires and polymers for energy applications. Economy and Competitiveness Ministry of Spain, 2013-2016.
2. **MAT2012-33483** Tailoring electronic and phononic properties of nanomaterials: towards ideal thermoelectricity. Economy and Competitiveness Ministry of Spain, 2011-2016.
3. **MAT2016-63955-R** Semiconductor nanostructures and nanocomposites for energy recovery, Economy and Competitiveness Ministry of Spain, 2016-2019.